

Investigating and controlling charge carrier behavior in p-type delafossite CuFeO_2 photocathodes for solar fuel production

THÈSE N° 7915 (2017)

PRÉSENTÉE LE 11 AOÛT 2017

À LA FACULTÉ DES SCIENCES DE BASE

LABORATOIRE D'INGÉNIERIE MOLÉCULAIRE DES NANOMATÉRIAUX OPTOÉLECTRONIQUES
PROGRAMME DOCTORAL EN CHIMIE ET GÉNIE CHIMIQUE

ÉCOLE POLYTECHNIQUE FÉDÉRALE DE LAUSANNE

POUR L'OBTENTION DU GRADE DE DOCTEUR ÈS SCIENCES

PAR

Mathieu Steven PRÉVOT

acceptée sur proposition du jury:

Prof. O. Kröcher, président du jury
Prof. K. Sivula, directeur de thèse
Prof. D. Bahnemann, rapporteur
Dr S. Giménez, rapporteur
Prof. A. Boghossian, rapporteuse



ÉCOLE POLYTECHNIQUE
FÉDÉRALE DE LAUSANNE

Suisse
2017

*À Alizée,
pour ton extraordinaire intelligence
et ta patience infinie,
pour nos aventures
passées et futures*

*À Maman et Elodie,
pour votre soutien sans faille
et les merveilleuses années
passées ensemble*

*À Papa,
avec qui j'aurais aimé pouvoir
discuter de ce travail
et de tant d'autres choses*

« — Et qu'est-ce qu'on brûlera à la place du charbon ?

— L'eau, répondit Cyrus Smith.

— L'eau, s'écria Pencroff, l'eau pour chauffer les bateaux à vapeur et les locomotives, l'eau pour chauffer l'eau !

— Oui, mais l'eau décomposée en ses éléments constitutifs, répondit Cyrus Smith, et décomposée, sans doute, par l'électricité, qui sera devenue alors une force puissante et maniable, car toutes les grandes découvertes, par une loi inexplicable, semblent concorder et se compléter au même moment. Oui, mes amis, je crois que l'eau sera un jour employée comme combustible, que l'hydrogène et l'oxygène, qui la constituent, utilisés isolément ou simultanément, fourniront une source de chaleur et de lumière inépuisables et d'une intensité que la houille ne saurait avoir. Un jour, les soutes des steamers et les tenders des locomotives, au lieu de charbon, seront chargés de ces deux gaz comprimés, qui brûleront dans les foyers avec une énorme puissance calorifique. Ainsi donc, rien à craindre. Tant que cette terre sera habitée, elle fournira aux besoins de ses habitants, et ils ne manqueront jamais ni de lumière ni de chaleur, pas plus qu'ils ne manqueront des productions des règnes végétal, minéral ou animal. Je crois donc que lorsque les gisements de houille seront épuisés, on chauffera et on se chauffera avec de l'eau. L'eau est le charbon de l'avenir. »

Jules Verne, *L'Île Mystérieuse*, 1874

Acknowledgments

Professor Kevin Sivula, thank you for involving me in the exciting adventure of this young laboratory and guiding me through this project. I certainly gained a lot of scientific knowledge – whether experimental or theoretical – during my time in LIMNO, and it was largely thanks to you. Thank you also for your trust and your support during these four years. It really was a pleasure working with you.

Dr. Néstor Guijarro Carratalá, my first teammate in LIMNO and a true mentor. Thank you for teaching so many things and helping me through the hardest parts of my research. Your scientific culture never ceases to amaze me. Thank you also for being such a good a friend. I will remember our trips – from Paris to New York City – and all the good times spent in the lab, sometimes until late at night. I will also remember your crazy stories and your endless energy. I will definitely miss working with you, and I look forward to cross paths again.

Dr. Florian Le Formal, ta réputation te précède et je connaissais déjà ton travail avant de te rencontrer. Cela a été une chance pour moi de faire de la recherche à tes côtés et de profiter de ton expertise pendant la deuxième moitié de cette thèse. Merci pour tes conseils avisés, et merci pour tous les bons moments passés en dehors du laboratoire.

Andrea, merci de m'avoir accueilli au LIMNO quand nous n'étions que trois dans le bureau. Merci pour m'avoir fait découvrir l'EPFL et Lausanne. Cela a été un vrai plaisir de participer à la construction du laboratoire avec toi. Je me souviendrai longtemps des conférences et des soirées passées ensemble.

Xavier, merci pour ton aide avec l'extraordinaire quantité d'équipement de mesure que tu as installé au laboratoire. Merci aussi pour les sorties escalade, pour m'avoir sorti du laboratoire et m'avoir fait découvrir tes montagnes.

Pauline, merci pour ta gentillesse et ta bonne humeur, malgré les difficultés du doctorat. Nos week-end à Roland Garros font partie des « highlights » de ces dernières années.

Wiktor, le scientifique businessman, j'ai vraiment apprécié partager ce projet avec toi, ne serait-ce que pour quelques mois. Ton esprit pratique et tes facultés de décision

ont permis de résoudre bien des problèmes. Merci d'avoir fait du LIMNO 5 « the place to be » pendant ton séjour parmi nous.

Xiaoyun, thanks for your kindness and your ingenuity, which made our collaboration very pleasant.

Thank you to Aiman, Jun-Ho, Sébastien, Émilie and Melissa. I certainly learned a lot working by your side in LIMNO. Finally, thank you to the new generation: Xavier, Arvindh, Xiaodi, Yongpeng, Florent and Charles for bringing a breath of fresh air – and fresh ideas – to the lab.

A word of thanks to the members of the jury for taking the time to read and evaluate my work, and another one to Kevin, Néstor, Florian, Xavier J., Pauline, Xavier D., and Alizée for proof-reading the manuscript.

Merci à Pierre et à Julien pour les moments de détente après des journées de travail parfois exténuantes.

Enfin, un immense merci à Alizée pour ces sept dernières années mais surtout pour sa patience et ses encouragements pendant ce doctorat, ainsi qu'à ma mère et à ma sœur pour leur soutien pendant toutes les années qui m'ont conduit jusqu'ici. Un merci particulier à Thierry et Catherine, ainsi qu'à Adrien et Josiane qui ont contribué de manière importante à mon parcours académique.

Summary

Humanity is facing the challenge of a global-scale energy transition over the next decades, where solar energy is set to play a crucial role. With the immense amount of sunlight reaching the surface of the Earth, and constantly decreasing manufacturing cost, photovoltaic technologies are on their way to replace unsustainable electricity sources. However, finding efficient ways to store solar energy over long periods, while necessary due to the intermittent nature of daylight, remains a challenge. A possible sustainable way to overcome this challenge is to convert solar energy into chemical energy inside a “solar fuel”, such as solar hydrogen. To accomplish this conversion, photoelectrochemical (PEC) tandem devices, composed of semiconducting n-type photoanode and p-type photocathode, are predicted to achieve high efficiencies for low manufacturing costs.

The original work presented in this thesis deals with the investigation and advancement of a novel photocathode material: p-type delafossite CuFeO_2 . The attractive structural and opto-electronic properties of the material are presented, along with a new sol-gel processing route to produce thin-film CuFeO_2 photocathodes. Then, promising PEC features – a good flat-band potential, and excellent stability – but also limitations – low photocurrents and photovoltage – are identified. Poor charge carrier transport is addressed by extrinsic doping with oxygen and magnesium on one hand, and a host-guest approach on the other hand. These approaches lead to significant improvement in photocurrents, reaching *ca.* 2.5 mA.cm^{-2} .

A more in-depth study of the material is then presented, concluding to the presence of a high density of surface states, causing Fermi level pinning at the CuFeO_2 /water junction. These states are characterized and identified as the primary cause for the limited performances of CuFeO_2 photocathodes, and their presence is addressed by surface modification of the photoelectrode. Two oxide overlayers – based on Al-doped ZnO/TiO_2 and amorphous gallium oxide – show promising preliminary results. The best-performing photoelectrode produces a photocurrent as high as 2 mA.cm^{-2} for water reduction.

Keywords: Solar fuels, photoelectrochemistry, oxide, thin film, water splitting, hydrogen, delafossite, solar energy, semiconductor, sol-gel

Résumé

L'humanité est confrontée au défi d'une transition énergétique à l'échelle mondiale au cours des prochaines décennies, au sein de laquelle l'énergie solaire jouera un rôle prépondérant. En raison de la quantité colossale de lumière solaire éclairant la surface de la Terre et de coûts de fabrications toujours plus faibles, les technologies photovoltaïques sont sur le point de remplacer les sources d'électricité non-renouvelables. Cependant, si trouver des méthodes efficaces de stockage de l'énergie solaire à long terme est nécessaire à cause de l'intermittence de cette dernière, cela reste un défi technologique important. Pour relever ce défi, une approche possible et renouvelable consiste à convertir l'énergie solaire en énergie chimique à travers la production d'un « carburant solaire » tel que l'hydrogène. Afin d'effectuer cette conversion, les cellules photoélectrochimiques en tandem, constituées d'une photoanode semi-conductrice de type n et d'une photocathode semi-conductrice de type p, sont prometteuses en terme d'efficacité et de coût de production.

Le travail de recherche original présenté dans cette thèse concerne l'exploration et le perfectionnement d'un nouveau matériau pour photocathode : la delafossite de type p CuFeO_2 . Les intéressantes propriétés structurales et opto-électroniques de ce matériau sont présentées, ainsi qu'une technique innovante de préparation sol-gel de photocathodes basées sur CuFeO_2 . Des propriétés photoélectrochimiques prometteuses – telles qu'un bon potentiel de bande plate et une excellente stabilité – mais aussi d'importantes limitations – de faibles photovoltage et photocourants – sont ensuite identifiées. Le problème du médiocre transport de porteurs de charge est abordé à travers le dopage extrinsèque du matériau avec de l'oxygène ou du magnésium, ainsi qu'au moyen d'une approche « host-guest » conduisant à la création d'une photocathode composite $\text{CuAlO}_2/\text{CuFeO}_2$. Ces approches conduisent à une amélioration significative du photocourant, atteignant *ca.* 2.5 mA.cm^{-2} .

Une étude plus approfondie du matériau est ensuite présentée, concluant à la présence d'une densité élevée d'états électroniques de surface causant un « clouage » du niveau de Fermi à la jonction entre CuFeO_2 et l'eau. Ces états de surface sont caractérisés et identifiés comme étant la source principale des performances photoélectrochimiques limitées des photocathodes basées sur CuFeO_2 , et leur présence est traitée par des

traitements de surface. Deux types de couches protectrices – basées sur ZnO dopé à l'aluminium et sur de l'oxyde de gallium – ont produit des résultats préliminaires prometteurs, lorsqu'ils sont utilisés en combinaison avec des nanoparticules de Pt électrocatalytiques. La photoélectrode la plus performante produit des photocourants atteignant 2 mA.cm^{-2} pour la photoreduction de l'eau.

Mots-clés : Carburant solaire, photoélectrochimie, oxyde, couche mince, électrolyse de l'eau, hydrogène, delafossite, énergie solaire, semiconducteur, sol-gel

Table of contents

Acknowledgments	i
Summary.....	iii
Résumé	v
Table of contents	vii
Table of figures and tables	xi
List of abbreviations and symbols.....	xxv
Chapter 1 – General background and motivation	1
1.1 The need for an energy transition.....	2
1.2 The quest for an alternative energy.....	4
1.3 Solar energy: a global challenge.....	6
1.4 Solar hydrogen from water splitting	9
1.5 References.....	14
Chapter 2 – Photoelectrochemical water splitting	17
2.1 Semiconductor fundamentals	18
2.2 The semiconductor-liquid junction	23
2.3 Photoelectrochemical water splitting.....	29
2.4 D4 tandem cells for PEC water splitting.....	32
2.5 References.....	35
Chapter 3 – Experimental methods.....	39
3.1 Synthetic methods.....	40
3.1.1 CuFeO ₂ thin film preparation (Chapters 4 - 7)	40
3.1.2 CuAlO ₂ scaffold preparation (Chapter 5)	40
3.1.3 SiO ₂ scaffold preparation (Chapter 5)	41
3.1.4 Overlayer deposition (chapter 7)	41

3.2 Physical characterization methods	42
3.2.1 UV-Visible spectroscopy (Chapters 4 and 5)	42
3.2.2 X-Ray diffraction measurements (Chapters 4 and 5)	45
3.2.3 Raman spectroscopy (Chapters 4 and 6)	47
3.2.4 Optical microscopy & Scanning electron microscopy (Chapters 4 to 6)	48
3.2.5 Energy dispersive X-Ray spectroscopy (Chapter 7)	49
3.2.6 Thermogravimetric analysis (Chapter 4)	49
3.2.7 Time-resolved microwave conductivity measurement (Chapter 6)	50
3.2.8 Atomic and Kelvin probe force microscopy (Chapter 6)	52
3.2.9 X-Ray photoelectron spectroscopy (Chapter 6)	54
3.3 Photoelectrochemical characterization methods	55
3.3.1 Voltammetry and chronoamperometry (Chapters 4 to 7)	57
3.3.2 Incident photon-to-electron conversion efficiency (Chapters 4 and 5)	58
3.3.3 Lamp calibration	59
3.3.4 Electrochemical impedance spectroscopy (Chapters 4 to 6)	60
3.3.5 Electrolyte preparation (Chapter 6)	62
3.3.6 Gartner model for the estimation of photocurrent (Chapter 6)	63
3.3.7 Gas chromatography and Faradaic efficiency measurement (Chapter 7)	64
3.4 References	66
Chapter 4 – CuFeO₂: a promising photocathode material for solar H₂ production	67
4.1 Structural and opto-electronic properties of CuFeO ₂	68
4.2 Early reports of CuFeO ₂ photocathodes	69
4.3 A robust sol-gel-processed CuFeO ₂ photocathode	71
4.3.1 Thin-film preparation and characterization	71
4.3.2 Photoelectrochemical characterization	74
4.3.3 Thickness optimization and performance consistency	75

4.3.4 Electrochemical Impedance spectroscopy	77
4.3.5 Photoelectrode stability	79
4.4 Conclusions	80
4.5 References	81
Chapter 5 – Improving charge separation and collection in sol-gel CuFeO₂ photocathodes	85
5.1 Extrinsic doping of CuFeO ₂ photocathodes	86
5.1.1 Oxygen intercalation	86
5.1.2 Iron substitution by Mg ²⁺	89
5.2 A Host-Guest CuAlO ₂ /CuFeO ₂ photocathode	91
5.2.1 CuAlO ₂ /CuFeO ₂ electrode preparation	92
5.2.2 Electrochemical Impedance spectroscopy	94
5.2.3 Photoelectrochemical characterization	96
5.2.4 Thickness optimization	97
5.2.5 Origin of photocurrent enhancement	100
5.3 Conclusions	103
5.4 References	105
Chapter 6 – Evaluating charge carrier transport and surface states in CuFeO₂ photocathodes	107
6.1 Thin film preparation and phase-purity assessment	108
6.2 Time-resolved microwave conductivity	110
6.3 Photoelectrochemical properties	113
6.3.1 Linear Sweep Voltammetry measurements	114
6.3.2 Open-circuit potential measurements	116
6.4 Electrochemical impedance spectroscopy	118
6.5 Surface analysis	123

6.5.1 Kelvin probe force microscopy.....	123
6.5.2 X-Ray Photoelectron Spectroscopy	124
6.6 Discussion	126
6.7 Conclusion	129
6.8 References.....	129
Chapter 7 – Surface modification of CuFeO₂ photocathodes	133
7.1 Surface modification of oxide photoelectrodes.....	134
7.2 CuFeO ₂ modification with a AZO/TiO ₂ /Pt overlayer	136
7.3 CuFeO ₂ modification with a GaO _x /Pt overlayer	139
7.4 Conclusion	143
7.5 References.....	144
Chapter 8 – Final comments and outlook.....	147
8.1 Processing of thin-film CuFeO ₂ photoelectrodes.....	148
8.2 Photoelectrochemical properties of thin-film CuFeO ₂ photocathodes	149
8.3 Surface states characterization and surface treatments of thin-film CuFeO ₂ electrodes	150
8.4 Outlook.....	151
8.5 References.....	153
Appendix.....	155
Curriculum Vitae.....	157

Table of figures and tables

Figure 1.1 a) World energy consumption for the period 1990 – 2040, as reported by the U.S. Department of Energy in 2016. b) Geographical repartition of known fossil fuel reserves (oil, natural gas and coal) by region and in percentage of the global resources, as reported by BP in their Statistical review of World energy from 2016. Countries with the largest resources in each region are indicated. TKM = Turkmenistan.....2

Figure 1.2 Estimated finite and renewable planetary energy reserves, in Terawatt years (TWy) and Terawatt years per year (TWy/y) respectively, adapted from a 2015 report of the International Energy Agency.¹³ The reported energy values are proportional to the volumes of the corresponding spheres.....5

Figure 1.3 a) Discharge time and storage capacity of several energy storage technologies. b) Example of a carbon-neutral renewable energy grid providing for electricity, heat and transportation fuels at all times by means of power-to-gas storage. Adapted from a white paper of the California Hydrogen Business Council from 2015.²¹8

Figure 1.4 a) Simplified representation of a PV + electrolyzer configuration, where a PV module produces a voltage ΔE and a current I to power an electrolyzer generating H_2 and O_2 from H_2O . Two types of electrolyzers can be found: the alkaline electrolyzer (b) and the PEM electrolyzer (c) represented with the corresponding electrochemical reactions occurring at each electrode.²⁷ 11

Figure 1.5 Alternative configurations for solar hydrogen production: a) suspension of photocatalyst particles producing a mixture of H_2 and O_2 and b) photoelectrochemical cell producing separate streams of O_2 and H_2 13

Figure 2.1 a) Type s atomic orbital and electronic energy levels arising from the combination of these atomic orbitals for a 1D chain of 2, 3, 4 and an infinity of atoms. Blue and grey spheres represent positive and negative atomic contributions respectively. For an infinity of atoms, the energy levels form an energy band, with its lowest energy corresponding to a fully bonding configuration, and its highest energy corresponding to a fully anti-bonding configuration. b) Band structure and electron filling for N atoms of

conducting sodium and insulating (semiconducting) silicon. The atomic orbitals contributing to the formation of the band and the number of states available (in brackets) are reported in each band. c) Band diagram of a semiconductor, restricted to its valence band and conduction band. EV = valence band edge; EC = conduction band edge; EF = Fermi level; Eg = band gap. 19

Figure 2.2 Simplified band diagram of an intrinsic, a p-type and an n-type semiconductors under thermal equilibrium. The acceptor and donor levels are represented after ionization. For p-type and n-type semiconductors, one type of charge carrier has a much higher concentration inside the bands, resulting in the existence of majority and minority carriers. 22

Figure 2.3 Formation of a SCLJ between a p-type (top row) or an n-type (bottom row) semiconductor and a liquid containing an electrolyte with a chemical potential E_{redox} . Before equilibrium (a) the bands of the semiconductor are flat. Once it is put in contact with the liquid phase, majority carriers flow from the semiconductor to the electrolyte until its Fermi level E_F equilibrates with E_{redox} , causing the formation of a depletion region of width W_D inside the semiconductor and of a Helmholtz layer of width W_{HL} inside the liquid. This results in a band bending in the depletion region of the semiconductor (downward in the p-type case or upward in the n-type case). c) Under illumination the production of photogenerated charge carriers induces the splitting of E_F into two quasi Fermi levels $E_{F,n}$ and $E_{F,p}$ for the electrons and holes respectively. 23

Figure 2.4 Parametrization of the SCLJ at equilibrium (a), under flat-band conditions (b), an under applied external voltage (c). Energies are referenced to the vacuum level (E_{vac}). The origin of potentials and the boundary conditions are represented only at equilibrium. EC = conduction band edge; EF = Fermi level; Eg = band gap, x = depth inside the semiconductor from the SCLJ. 25

Figure 2.5 Illustration of the origin of (a) photovoltage and (b) photocurrent at the SCLJ. The photovoltage V_{ph} is defined by the splitting of quasi Fermi levels. It is maximum when the bands are fully flattened under illumination, and is then equal to $E_{FB} - E_{redox}/q$. The photocurrent J_{ph} is maximum and equal to the generation rate G when the junction is ideal. However, in practice it is hindered by recombination processes: bulk recombination (J_{br}), recombination in the depletion region (J_{dr}), tunneling through the

SCLJ (J_t), thermionic emission through the SCLJ (J_{et}), and recombination at surface states (J_{ss}).⁶..... 28

Figure 2.6 Band alignment of a) S2 PEC cell, b) D4 PEC cell and c) PV-biased PEC cell with the redox potentials of water for direct PEC water splitting. The light source is located on the left-hand side of each device: the blue arrow represent the high-energy photons of the incident light, while the red arrow represents the low-energy photons..... 30

Figure 2.7 a) Comparison of the amount of light absorbed from the AM 1.5G solar spectrum by single-absorber vs dual-absorber configurations. The shading represents the photons that could be harvested and used to drive solar water splitting by an S2 PEC device (yellow) and a tandem D4 PEC device (brown and purple). b) Contour plot showing the maximum predicted STH efficiencies with AM 1.5G incident irradiation (1000 W.m^{-2}) and a total overpotential of 2 V for the water splitting reaction (1 V per photoelectrode) as a function of the chosen semiconductor bandgap energies with $E_{g1} > E_{g2}$. Reproduced from reference 1..... 31

Figure 2.8 Overlaid $J - V$ curves of a photocathode (brown) and a photoanode (orange). $J_{ph, op}$ is the photocurrent delivered by the tandem cell under operation, while $V_{ph, c}$ and $V_{ph, a}$ are the photovoltages delivered by the photocathode and the photoanode respectively..... 33

Figure 3.1 Integrating sphere configurations for the determination of the transmittance (a), diffuse reflectance (b) and total (diffuse + specular) reflectance (c) of a solid-state sample. Reproduced from the Shimadzu user manual.⁴ 44

Figure 3.2 a) Illustration of the diffraction of X-Rays (red lines) by a crystalline lattice of ions (blue spheres). The difference in optical path between two beams reflected by two crystalline planes separated by a distance d is $2d \sin\theta$, and therefore constructive interferences between these two beams are obtained for $2d \sin\theta \propto \lambda$ (Bragg's law). b) Locked-couple configuration: the X-Ray gun and detectors have the same angle with respect to the surface of the sample at all time. C) Pseudo-grazing incidence configuration: the X-Ray gun forms a constant small angle with the surface of the sample, and only the detector is moving..... 46

Figure 3.3 Simplified sketch of a TRMC setup. The Nd:Yag Laser provides the high-energy light to excite the sample (pump). The subsequent change in the reflective power of the sample is monitored with a microwave light provided by a Gunn diode (probe). P_{in} represents the power of the incident microwave signal, while P_{out} represents the power of the reflected light. A power meter and a detector are used to create the TRMC spectrum. Adapted from Killedar et al.⁵..... 50

Figure 3.4 Electronic diagram of a sample and a conductive AFM tip in different situations: a) sample and tip separated by a distance d without electrical contact, b) sample and tip in electrical contact, resulting in $VCPD$, c) sample and tip are in electrical contact and an external bias equal to $VCPD$ is applied to neutralize the electric field between the tip and the sample. E_{vac} is the vacuum energy, while $E_{F,S}$ and $E_{F,T}$ are the Fermi levels at the surface of the sample and the tip respectively. Adapted from Melitz et al.¹² 53

Figure 3.5 Calibration curve obtained for the conductive tip of the KPFM setup. The metals used for the calibration are indicated on the graph. The work function of the tip was taken as the intercept of the line with the y-axis. 54

Figure 3.6 a) “Cappuccino” PEC cell design. The arrows indicate the positioning of the different electrodes and the path of the light through a quartz window. b) PEC setup used in this study: a solar simulator – made of a Xenon arc lamp and appropriate optics – produces the light illuminating the PEC cell connected to a potentiostat..... 56

Figure 3.7 a) Input signal and typical output signal of a LSV experiment conducted on a photocathode. The output current is modulated by chopped illumination of the electrode, as indicated by the orange arrows. b) Input signal and typical output signal of a CV experiment. The output curve corresponds to what is observed for a reversible redox couple with a peak reduction potential E_c and a peak oxidation potential E_a (only one cycle is represented). The value $E_{1/2} = (E_c + E_a)/2$ gives an estimation of the standard redox potential of the electrolyte..... 57

Figure 3.8 a) Xe arc lamp emission spectrum (red line) calibrated with the solar AM 1.5 spectrum (blue line) for the number of incident photons between 300 nm and 850 nm. b) IPCE of the silicon photodiode as a function of the incident wavelength..... 59

Figure 3.9 Equivalent circuits commonly used in EIS and typical shapes of the associated Nyquist and Bode plots. The charge carrier pathway inside the electrode is modeled using electrical components: resistors (R), capacitors (C), constant phase elements (CPE), inductance (L) or Warburg element (W, for diffusion processes). Adapted from Cesiulis et al. ¹³	61
Figure 3.10 Parametrization of the system for Electrolyte-side and Substrate-side illuminations (left-hand side and right-hand side respectively).	63
Figure 3.11 a) Sketch of the configuration used to measure the FE of CuFeO ₂ photoelectrodes. The PEC cell was hermetically sealed to avoid contamination from the outer atmosphere, and a trap was setup on the output gas line to avoid the introduction of liquid electrolyte inside the GC. B) Calibration curve obtained with a platinum foil showing the area of the H ₂ peak on the output chromatogram as a function of the current flowing through the Pt foil.	65
Figure 4.1 The 3R polytype (a) and 2H polytype (b) of the delafossite structure ABO ₂ , reproduced from reference 1, with permission of Elsevier. c) Absorption spectra (solid lines) of CuMO ₂ (M = Sc, Cr, Mn, Fe, and Co) thin films measured at 10 K. Dashed lines represent fits of the experimental data based on a modified Elliott model. Schematic energy diagrams, derived from first-principles calculations, are shown in the right panel. Arrows indicate transitions corresponding to the observed absorption peaks. Reproduced from reference 7 with permission of the American Physical Society.	68
Figure 4.2 a) XRD trace of a CuFeO ₂ thin film deposited on FTO collected under pseudograzing incidence geometry. Blue and red lines correspond to SnO ₂ and CuFeO ₂ signals, respectively, from the ICDD database. b) Surface Raman spectrum of the same film.	71
Figure 4.3 a) Optical images of the FTO substrate (1), one layer of the dried gel (2), a six-layer film annealed at 450°C in air for one hour (3), and the final six-layer CuFeO ₂ film annealed at 700°C in argon for 12 hours (4). SEM top (b and c) and cross-sectional (d) views of a six-layer CuFeO ₂ film on FTO.....	72

Figure 4.4 a) UV-vis absorption spectrum of a CuFeO₂ film on FTO, corrected for the substrate. Corresponding direct (b) and indirect (c) Tauc plots for optical transition determination. 73

Figure 4.5 a) LSV of a ~ 300 nm-thick CuFeO₂ photocathode in 1M NaOH under intermittent one sun illumination, with argon-purged electrolyte (red trace) and oxygen-saturated electrolyte (blue trace). b) Wider potential range scan in oxygen-saturated electrolyte. The sweep rate was 10 mV.s⁻¹ towards negative potentials..... 74

Figure 4.6 Photocurrent densities obtained with electrodes of varying thicknesses at 0.4 V vs RHE (blue markers) and 0.6 V (red markers) vs RHE under electrolyte-side (a) and substrate-side (b) illumination. The data was recorded in oxygen-purged 1M NaOH. 76

Figure 4.7 IPCE measurement performed on an optimized CuFeO₂ electrode in O₂-purged 1M NaOH electrolyte. The blue circles represent experimental data, while the broken red trace represents the smoothed curve obtained from these data..... 77

Figure 4.8 Mott-Schottky diagram of a CuFeO₂ thin film on FTO in O₂-saturated 1M NaOH. The red line indicates the linear region that corresponds to the depletion regime of the semiconductor: it intercepts the x-axis at *EFB*. The equivalent circuit used to extract the values of *CSC* is represented in the top-right corner. 78

Figure 4.9 Cyclic voltammograms of a CuFeO₂ electrode in Ar-purged (a) and O₂-purged (b) 1M NaOH (scan rate: 10 mV/s). The arrows indicate the starting voltage and the direction of the voltage scans. The blue trace shows the evolution of the voltammogram over 10 scans between +0.9 V and -0.2 V vs RHE. The red trace corresponds to the same evolution between +0.9 V and +0.3 V vs RHE. The insets show a comparison of the latter and the bare FTO substrate under the same conditions. The redox peak in (a) are labeled and identified in Table 4.1. c) Raman spectra of a CuFeO₂ electrode before (red trace) an after (blue trace) being subjected to a voltage sweep from 0.9 to 0.3 V vs RHE in O₂-purged 1M NaOH under 1 sun illumination. d) Chronoamperometry of a CuFeO₂ electrode during 40 hours at +0.4 V vs RHE in 1M NaOH under O₂ bubbling and chopped illumination. Oxygen bubbles caused the noise present when the electrode was under illumination. 79

Figure 5.1 Thermogravimetric analysis of CuFeO₂ powder in air, showing the percentage of mass variation as a function of the temperature 86

Figure 5.2 a) Absolute photocurrent (total current minus dark current) density $|j_{ph}|$ as a function of applied potential for a 300 nm-thick CuFeO₂ thin films on FTO in O₂-saturated 1M NaOH under one sun illumination before (red) and after (blue) post-annealing at 300°C in air. b) Linear regions of the Mott-Schottky diagram for the same electrodes under the same conditions. c) and d) represent the same data than a) and b) respectively, but for a 100 nm-thick electrode. 87

Figure 5.3 XRD traces of a CuFeO₂ thin film on FTO before (red trace) and after (blue trace) post-annealing at 300°C in air. The diffractograms were collected under pseudo-grazing incidence. 88

Figure 5.4 a) Absolute photocurrent (total current minus dark current) density $|j_{ph}|$ as a function of applied potential under one sun illumination for nine different atomic ratios of Mg in the precursor (see caption). b) Measured photocurrent density at 0.4 V vs RHE (blue) and 0.6 V vs RHE (red) under one sun illumination as a function of the atomic ratio of Mg. c) Mott-Schottky diagram of an undoped electrode (red) and an electrode doped with 0.125% of Mg. All three graphs were obtained for = 300 nm-thick CuFeO₂ thin films on FTO in O₂-saturated 1M NaOH. 90

Figure 5.5 XRD spectra of CuAlO₂ powder (blue trace), CuFeO₂ film on FTO (red trace) and CuAlO₂/CuFeO₂ film on FTO (black trace). Films on FTO were measured under pseudo grazing incidence, whereas the CuAlO₂ powder was measured under locked-coupled conditions, causing a difference in peak broadness. Corresponding peak signals from the IPCC database are shown at the bottom of the figure. 92

Figure 5.6 a) Top-view scanning electron micrograph of a 2 µm-thick CuAlO₂ scaffold on FTO. b) Top-view micrograph of the same electrode after the deposition of 6 layers of CuFeO₂ on the CuAlO₂ scaffold. Inset: zoomed-in top view of the same sample. c) Cross-sectional view of the same CuAlO₂/CuFeO₂ composite electrode. In each micrograph, CuAlO₂ is colorized in grey and CuFeO₂ is colorized in brown. 93

Figure 5.7 Tauc plots of the CuAlO₂ scaffold (a), a bare CuFeO₂ film (b) and a CuFeO₂/CuAlO₂ electrode (c) 94

Figure 5.8 a) Mott-Schottky plot obtained for CuAlO₂ (blue trace) and CuFeO₂ (red trace) on FTO. The measurement was done in 1M NaOH, using the equivalent circuit shown in

the top right corner. b) Simplified energy diagram of the host-guest $\text{CuAlO}_2/\text{CuFeO}_2$ electrode. Colorized areas represent energy bands, arrows indicate spontaneous charge transfer under illumination, and dashed lines mark the position of the water redox couples..... 95

Figure 5.9 a) Comparison of LSV curves obtained for optimized $\text{CuAlO}_2/\text{CuFeO}_2$ (blue trace) and CuFeO_2 (red trace) electrodes, under O_2 bubbling. Electrolyte: 1M NaOH, scan rate: 10 mV.s^{-1} , illumination : 1 sun. b) IPCE spectra of CuAlO_2 (green solid line), CuFeO_2 (red solid line), and $\text{CuFeO}_2/\text{CuAlO}_2$ (blue solid line) electrodes. Corresponding integrated photocurrents are represented by the dotted lines, and referenced to the right-hand side y-axis. 96

Figure 5.10 Photocurrent densities obtained for composite electrodes with several CuAlO_2 and CuFeO_2 contents, under front (a) and back (b) illumination and under an applied bias of +0.4 V vs RHE. Electrolyte: 1M NaOH purged with O_2 , illumination: 1 sun. 98

Figure 5.11 a) Absorbance of composite electrodes with several CuAlO_2 and CuFeO_2 contents at 750 nm. c) Dependence of the absorbance of composite electrodes made with 6 successive depositions of CuFeO_2 as a function of the scaffold thickness..... 99

Figure 5.12 Absorption spectra of $\text{CuAlO}_2/\text{CuFeO}_2$ (blue solid line) and CuFeO_2 (red solid line) electrodes, and the associated APCE spectra (dotted lines), superimposed with the solar emission spectrum in photon density. Electrolyte: 1M NaOH purged with O_2 , illumination: 1 sun.100

Figure 5.13 Cross-sectional and top views of a $\text{SiO}_2/\text{CuFeO}_2$ composite electrode.....101

Figure 5.14 a) Comparison of J-V curves obtained for optimized $\text{CuAlO}_2/\text{CuFeO}_2$ (blue trace) and $\text{SiO}_2/\text{CuFeO}_2$ (black trace) electrodes, under O_2 bubbling. Electrolyte: 1M NaOH, scan rate: 10 mV.s^{-1} , illumination: 1 sun. The inset provides a detail on the J-V curve of the $\text{SiO}_2/\text{CuFeO}_2$ electrode for the potential range 0.35-0.45 V vs RHE b) Scheme of the possible pathways that photogenerated charges can take inside a $\text{CuAlO}_2/\text{CuFeO}_2$ electrode. The brown layer represents CuFeO_2 . Holes can travel either inside the CuFeO_2 layer or through the CuAlO_2 scaffold. c) Scheme of the possible pathways that photogenerated charges can take inside a $\text{SiO}_2/\text{CuFeO}_2$ electrode. Holes are blocked at the

surface of the insulating SiO₂ that acts as a recombination center. The only possible pathway for holes to reach the substrate is to travel exclusively inside the CuFeO₂ layer.

.....102

Figure 6.1 a) Optical microscope image of a typical CuFeO₂ electrode. The inset shows an image obtained at higher magnification. Both images were obtained in transmission (the incident light was going through the transparent sample). No presence of bright red hematite was observed. b) Top view SEM image of the surface of the same electrode c) Cross-sectional SEM image of the same electrode: the CuFeO₂ layer is colored in brown.

.....108

Figure 6.2 a) Optical microscope image of the surface of a CuFeO₂ thin film. The colored dots indicate the locations at which the Raman spectra displayed in (b) were acquired. For each of the five measurements, only the two peaks associated with CuFeO₂ were observed, with no trace of secondary phase.....109

Figure 6.3 Typical LSV curve obtained for a CuFeO₂ photocathode under chopped 1 sun illumination in O₂-purged 1M NaOH. Scan rate: 10 mV/s.109

Figure 6.4 a) TRMC spectra obtained for a CuFeO₂ thin film for different pump intensities. b) Peak TRMC signal values measured for two duplicate CuFeO₂ thin films (red and blue markers, respectively), at different flux of incident photons per pulse. Inset: typical TRMC signal produced by a thin film of CuFeO₂ after a pulse of 8.15×10^{12} photons cm⁻². The red trace represents the biexponential fit. The pulse wavelength was 330 nm for all measurements. AM1.5 illumination is equivalent to ~ 109 cm⁻² pulse⁻¹.....111

Figure 6.5 Schematic representation of the potential regions probed by the different redox couples used in this study shown next to the band position of CuFeO₂, under flat-band conditions, in water (left side) and in acetonitrile (right side). Note: the band bending induced by the junction is not represented. MV = Methyl Viologen, DMFc = decamethylferrocene, E_{FB} = Flat-band potential of CuFeO₂.113

Figure 6.6 Cyclic voltammograms obtained at different pH (indicated on each graph) in water for a) 0.05 M Fe(CN)₆^{3-/4-} b) 0.001 M Ru(acac)₃^{0/-}, c) 0.005 M Ru(NH₃)₆^{3+/2+} and d) 0.01 M MV^{2+/+}. e) Cyclic voltammograms obtained for 0.01 M FeCp₂^{+/0}, 0.01 M Chloranil^{0/2-}

, 0.003 M $\text{Fe}(\text{C}_5\text{Me}_5)^{+/-}$ and 0.001 M $\text{MV}^{2+/-}$ in 0.1 M TBAP/ CH_3CN . All the scans were obtained on a Pt electrode at 5 mV/s.114

Figure 6.7 LSV curves of CuFeO_2 under intermittent 1 sun illumination (10 mV s^{-1} scan) in a) 50mM $\text{Fe}(\text{CN})_6^{4-/3-}$ and b) $\sim 1 \text{ mM}$ $\text{Ru}(\text{acac})_3^{0/-}$ (saturated) at different pH, referenced to the redox potential of the electrolyte. For each curve, the red star represents a fixed potential on the RHE scale, to help visualize the apparent FLP. For c) the LSV curves were obtained for different redox systems at concentration 0.01 M in CH_3CN , except for $\text{MV}^{2+/-}$ which saturated at $\sim 1 \text{ mM}$115

Figure 6.8 OCP measured in the dark and under 10 suns front illumination at different pH for a CuFeO_2 electrode in contact with a) 50 mM $\text{Fe}(\text{CN})_6^{3-/4-}$, b) 1 mM $\text{Ru}(\text{NH}_3)_6^{3+/2+}$ and c) 10 mM $\text{MV}^{2+/-}$ (see Chapter 3, section 3.3.5 for details on the concentration of the buffers). d) $\Delta\text{OCP} = \text{OCP}_{10\text{suns}} - \text{OCP}_{\text{dark}}$ measured as a function of the redox potential of the electrolyte, referenced to the RHE. The expected ΔOCP value, in absence of FLP, is shown as the dotted line that intercepts the x-axis at $E = E_{\text{FB}}$117

Figure 6.9 Sketches of the band energies of a p-type semiconductor a) without surface states and b) with surface states, referenced to the potential scale (E). In each case, three situations are depicted: (i) band diagram before the semiconductor is put in contact with the electrolyte, (ii) band diagram after equilibration between the semiconductor and two different electrolytes of different redox potentials – such that $E_{\text{redox},1} > E_{\text{redox},2}$ in the dark (top) and under illumination (bottom), and (iii) Expected evolution of photocurrent (J_{ph}) with the applied potential (top) E and of the photovoltage V_{ph} with the redox potential of the electrolyte (bottom). In the absence of surface states, as the redox potential of the electrolyte becomes more negative (i.e. higher in energy), the band bending at equilibrium increases, and so does the photovoltage under illumination. On the contrary, when surface states are present with a high density, the Fermi level is pinned to their energy, and therefore the band bending and the photovoltage are independent of the potential of the electrolyte. As a result, if the surface states are close to the conduction band, a constant and small photovoltage is measured, and any additional voltage provided to the system occurs inside the electrolyte (across the Helmholtz layer) until the trap states are completely full or empty.119

Figure 6.10 a) Equivalent circuit used to fit the EIS data. b) Typical Nyquist plots representing EIS data for a CuFeO₂ electrode collected at 0.7 V vs RHE, in 1M NaOH, in the dark, under 0.5 sun and 1 sun illumination. Markers represent experimental data, and lines represent the fit. c) and d) Plots of the extracted values of C_{trap} and $R_{\text{ct,trap}}$ respectively, as a function of the applied potential, referenced to the RHE.....120

Figure 6.11 a) Mott-Schottky plots of a CuFeO₂ electrode in 1M NaOH in the dark, as well as under half a sun and 1 sun illuminations. b) Corresponding plot of the corrected density of surface states (DOS) extracted from C_{trap} after removal of the background capacitance.122

Figure 6.12 KPFM measurements. a) Height image of the surface of a bare CuFeO₂ electrode by AFM b) Dark KPFM mapping of the value of E_F at the surface for the same region. b) Shift in E_F ($\Delta E_F = E_{F,\text{light}} - E_{F,\text{dark}}$) measured upon illumination of the surface of the sample.124

Figure 6.13 a) XPS spectra as a function of depth of Cu 2p. b) XPS spectra as a function of depth of Cu LMM. c) XPS spectra as a function of depth of Fe 2p. d) XPS spectra as a function of depth of O 1s. The scans were performed at 0 nm, 2 nm, 4 nm, 6 nm, 8nm, 40 nm and 60 nm from the surface of the sample, starting from the bottom scan (red trace).125

Figure 6.14 Proposed energy band diagram for an isolated CuFeO₂ electrode in the dark. E_{CB} = Conduction band edge, E_{VB} = Valance band edge, E_F = Fermi level, N_A = Acceptor density, τ = carrier lifetime, L_D = carrier diffusion length, W = depletion width, N_{ss} = density of surface states.....127

Figure 7.1 a) Sketch of the structure of the layered CuFeO₂/AZO/TiO₂/Pt electrode. The relative thicknesses of the layers are not to scale. b) Predicted band alignment of the semiconducting layers of the electrode in equilibrium with the reduction potential of water. The structure exhibits a buried CuFeO₂/AZO type-II p-n heterojunction, a buried AZO/TiO₂ type-II n-n heterojunction, and a SCLJ. The band structure of AZO and TiO₂ are reproduced from Paracchino et al.⁷.....137

Figure 7.2 a) LSV curves obtained under chopped 1 sun illumination for a 300 nm-thick CuFeO₂ electrode ALD-coated with an AZO/TiO₂ overlayer before (black trace) and after

(blue trace) Pt deposition. Scan rate: 10 mV.s⁻¹. Electrolyte: 0.5 M Na₂SO₄ buffered at pH 6.1. b) Stability measurement performed for 800 seconds at 0 V vs RHE in the same electrolyte and under chopped 1 sun illumination.138

Figure 7.3 Chronoamperometry of a CuFeO₂/AZO/TiO₂/Pt electrode at -0.2 V vs RHE under constant illumination in Ar-purged pH 6.1 buffered electrolyte. The effective illumination of the photoelectrode was well below 1 sun illumination as the light has to pass through the CE before reaching the WE (as described in Chapter 3 section 3.3.7). The intense noise in the data was due to Ar purging of the electrolyte, and a mean value of the current is therefore provided. The illuminated surface area of the photoelectrode was 0.238 cm².139

Figure 7.4 SEM pictures of a) a bare 200 nm-thick CuFeO₂ thin film on FTO and b) the same electrode after GaO_x coating. c) EDX elemental mapping of the same electrode for Cu, Fe and Ga.140

Figure 7.5 LSV curves obtained under chopped 1 sun illumination for a 200 nm-thick CuFeO₂ electrode coated with a GaO_x overlayer before (black trace) and after (blue trace) Pt deposition. Scan rate: 10 mV.s⁻¹. Electrolyte: 0.5 M Na₂SO₄ buffered at pH 6.0.141

Figure 7.6 Predicted electronic band alignment for the CuFeO₂/GaO_x heterojunction before equilibration, based on the study presented in Chapter 6 for CuFeO₂ and on a previous report by Lee et al. for GaO_x.¹⁴ It reveals that, instead of forming the desired type-II heterojunction, CuFeO₂ and GaO_x are more likely to form a type-I heterojunction, with an offset of ~ 0.7 eV between the conduction band edges.142

Figure 8.1 LSV curves of the best-performing CuFeO₂ photocathode developed during this PhD thesis in the presence of O₂ as an electron scavenger (blue trace, Chapter 5) and in deaerated electrolyte (green trace, Chapter 7). These curves are overlaid with the LSV of the best performing oxide photoanode reported in the literature⁹ (yellow trace). The red trace represents the LSV needed for an optimized CuFeO₂ photocathode to reach about 5% STH conversion efficiency when combined with this photoanode. To reach this target, surface engineering could help improve the photovoltage (i.e. the onset of photocurrent), while morphology control (e.g. nanostructuring) could benefit the photocurrent densities.152

Table 1.1 Electrochemical half-reaction in acidic and alkaline media and associated redox potentials for the oxygen evolution reaction and hydrogen evolution reaction. NHE = Normal Hydrogen Electrode	10
Table 4.1 Identified peaks on the CV (Figure 4.9a). The copper peaks are taken from reference and while the iron peaks are from reference	80
Table 6.1 CuFeO ₂ semiconductor parameters derived from EIS data ^a	123

List of abbreviations and symbols

Symbol	Definition [typical unit]
acac	Acetylacetone or acetylacetonate
AFM	Atomic force microscopy
ALD	Atomic layer deposition
AM 1.5	Air mass 1.5: characterizes solar illumination at the surface of the Earth with a zenith angle of 48.2°. Standard conditions for solar energy conversion measurements.
APCE	Absorbed photon to current efficiency [%]
AZO	Aluminum-doped zinc oxide
CE	Counter electrode
CV	Cyclic voltammetry
D_i	Diffusivity ($i = n$ for electrons, $i = p$ for holes) [$\text{m}^2.\text{s}^{-1}$]
DOS	Density of surface states [cm^{-2}]
\mathcal{E}	Electric field [$\text{V}.\text{m}^{-1}$]
\mathcal{E}_{FB}	Flat-band energy [eV]
\mathcal{E}_{redox}	Chemical potential of a redox couple [eV]
e^-	Electron
E	Applied potential [V]
E^0	Standard potential [V]
E_{redox}^0	Standard potential of a redox couple [V]
$E_{1/2}$	Half-wave potential in cyclic voltammetry [V]
E_a	Anodic peak potential in cyclic voltammetry [V]
E_C	Conduction band edge [eV]
E_c	Cathodic peak potential in cyclic voltammetry [V]
E_F	Fermi level [eV]
E_{FB}	Flat-band potential [V]
E_g	Bandgap energy [eV]

E_V	Valence band edge [eV]
EDX	Energy dispersive X-Ray spectroscopy
EIS	Electrochemical impedance spectroscopy
F	Faraday constant [96500 C.mol ⁻¹]
FE	Faradaic efficiency [%]
FLP	Fermi level pinning
FTO	Fluorine-doped tin oxide
GC	Gas chromatography
h	Planck constant [6.62×10^{-34} J.s]
\hbar	Reduced Planck constant [1.05×10^{-34} J.s]
h^+	Hole
HER	Hydrogen evolution reaction
HL	Helmholtz layer
HPC	Hydroxypropyl cellulose
IPCE	Incident photon to current efficiency [%]
J	Current density [mA.cm ⁻²]
J_{ph}	Photocurrent density [mA.cm ⁻²]
$J_{ph,op}$	Photocurrent density delivered by a PEC cell under operation [mA.cm ⁻²]
k_B	Boltzmann constant [1.38×10^{-23} J.K ⁻¹]
KPFM	Kelvin probe force microscopy
ℓ	Azimuthal quantum number
L_i	Diffusion length (i = n for electrons, i = p for holes) [nm]
LCOE	Levelized cost of energy
LSV	Linear sweep voltammetry
m_c	Effective mass of electrons in the conduction band [kg]
m_v	Effective mass of holes in the valence band [kg]
MV	Methyl viologen
N_A	Acceptor density in a p-type semiconductor [cm ⁻³]
N_c	Effective density of states for electrons in the conduction band [cm ⁻³]
n_c	Density of electrons in the conduction band [cm ⁻³]

N_D	Donor density in an n-type semiconductor [cm^{-3}]
n_i	Charge carrier concentration in an intrinsic semiconductor [cm^{-3}]
N_V	Effective density of states for holes in the valence band [cm^{-3}]
NHE	Normal hydrogen electrode
OER	Oxygen evolution reaction
p_V	Density of holes in the valence band [cm^{-3}]
PEC	Photoelectrochemical
PEM	Proton exchange membrane
PV	Photovoltaic
q	Elementary charge [1.6×10^{-19} C]
Ref	Reference electrode
RHE	Reversible hydrogen electrode
S	Irradiance [mW.cm^{-2}]
SCLJ	Semiconductor-liquid junction
SEM	Scanning electron microscopy
STH	Solar-to-hydrogen
TRMC	Time-resolved microwave conductivity
T	Temperature [K]
TW _y	Terawatt-year
TW _y /y	Terawatt-year per year
UV-Vis	UV – visible light
V_H	Voltage drop across the Helmholtz layer inside the electrolyte [V]
V_{ph}	Photovoltage [V]
V_{SC}	Voltage drop across the depletion region inside the semiconductor [V]
W_D	Depletion width [nm]
W_{HL}	Width of the Helmholtz layer [nm]
WE	Working electrode
XPS	X-Ray photoelectron spectroscopy
XRD	X-Ray diffraction

α	Absorption coefficient [cm^{-1}]
ΔG^0	Variation in standard Gibbs free energy [$\text{kJ}\cdot\text{mol}^{-1}$]
ΔH^0	Variation in standard enthalpy [$\text{kJ}\cdot\text{mol}^{-1}$]
ε_0	Vacuum permittivity [$8.85 \times 10^{-12} \text{ F}\cdot\text{m}^{-1}$]
ε_r	Dielectric constant [dimensionless]
η_{PV}	Conversion efficiency of a photovoltaic device [%]
η_{STH}	Solar-to-hydrogen efficiency [%]
η_a	Overpotential associated with an oxidation process at the anode [V]
η_c	Overpotential associated with a reduction process at the cathode [V]
$\eta_{\text{electrolyzer}}$	Conversion efficiency of an electrolyzer [%]
η_{mt}	Overpotential associated with mass transport [V]
η_{ohm}	Overpotential associated with electrical resistance [V]
λ	Wavelength [nm]
μ_h	Hole mobility [$\text{m}^2\cdot\text{V}^{-1}\cdot\text{s}^{-1}$]
μ_e	Electron mobility [$\text{m}^2\cdot\text{V}^{-1}\cdot\text{s}^{-1}$]
ν	Frequency [s^{-1}]
ρ	Charge density [m^{-3}]
$\Sigma\mu$	Sum of the mobilities of charge carriers [$\text{m}^2\cdot\text{V}^{-1}\cdot\text{s}^{-1}$]
τ	Lifetime [ns]
Φ	Incident photon flux in TRMC measurements [$\text{cm}^{-2}\cdot\text{pulse}^{-1}$]
ϕ	Electrostatic potential [V]
χ	Electron affinity [eV]
ω	Angular frequency [Hz]

Chapter 1

General background and motivation

This chapter provides context and arguments for the necessity of a global energy transition away from a society powered by fossil fuels and towards a more sustainable model over the next decades. Possible sustainable energy sources are presented as an alternative to carbon-based fuels, and solar energy is established as a major participant of this transition.

The advantages and shortcomings of solar energy are exposed, concluding in the necessity to develop solar energy storage technologies. Solar energy conversion into chemical energy – inside solar fuels – is presented as a long-term storage option, and an overview of electrochemical solar water splitting process – a candidate technology for solar hydrogen production – is provided.

The technological aspects of hydrogen production from sunlight and its implementation in the current energy grid are briefly discussed. The current first generation of device, consisting in connecting an electrolyzer to a solar panel, is presented. Finally, the motivation for the development of new technologies for solar fuel production is brought up, highlighting photoelectrochemical water splitting as a promising candidate.

1.1 The need for an energy transition

Since the Industrial Revolution of the 19th century, countries have relied almost exclusively on fossil fuels to industrialize their societies, and these resources still represented 84% of the World's total energy consumption in 2012.¹ However, while this model has been successfully used over the last 150 years to propel the world at an unprecedented pace through the machine, atomic and space ages, and into the current information age, it seems to quickly approach its limits for several important reasons discussed in this section.

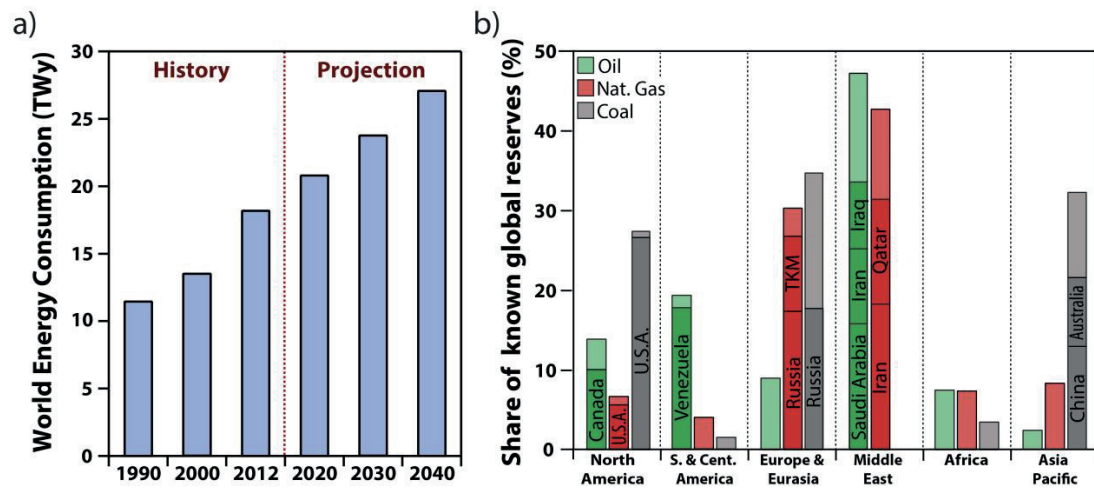


Figure 1.1 a) World energy consumption for the period 1990 – 2040, as reported by the U.S. Department of Energy in 2016. b) Geographical repartition of known fossil fuel reserves (oil, natural gas and coal) by region and in percentage of the global resources, as reported by BP in their Statistical review of World energy from 2016. Countries with the largest resources in each region are indicated. TKM = Turkmenistan.

As global life expectancy keeps increasing, due to a continuous improvement in healthcare worldwide and a decrease in armed conflicts since the second half of the 20th century, the world's population has recently skyrocketed and is projected to reach ca. 11 billion people over the next century, according to the UN Population Division.² This demographic increase coupled with the industrialization of China and India is expected to result in a steep rise in the global energy consumption over the next decades: from 18 terawatt year (TWy) in 2012 to 27 TWy in 2040, according to the International Energy Outlook 2016 published by the U.S. Department of Energy ¹ (see Figure 1.1a). Considering that the combined known reserves of fossil fuels (coal, oil and natural gas) amount to ca.

1400 TWy of energy (see Figure 1.2), they can only power the planet for an additional 50 years. Therefore, the unsustainable nature of fossil resources alone – even considering potential unknown fossil fuels reservoir – makes a good argument in favor of the diversification of the energy mix.

Moreover, oil and natural gas reserves are very unevenly distributed across the planet,³ placing most of the World's primary energy supply between the hands of only a few countries (see Figure 1.1b). These localized resources have arguably played – and keep playing – a significant role in the geopolitical instability and armed conflicts that have developed in the Middle East, North Africa and Eastern Europe over the last decades. Furthermore, the centralized production and distribution of energy currently adopted in the developed world seems inadequate for developing countries, where 1.4 billion people are still lacking access to electricity. In fact, the development of decentralized energy production units has been identified as an efficient way to provide electricity access to the underserved,^{4,5} a prerequisite for decent healthcare, education, and communication. This new energy strategy therefore represents an important step towards the accomplishment of the Sustainable Development Goals set by the UN Development Program.⁶ Therefore, better-distributed alternative energy resources granting energetic independence to every country down to a regional level are desirable to build a more stable global geopolitical situation, as well as a more advanced global society.

Finally, the most pressing concern with the use of fossil fuels is their proven detrimental effect on the climate and environment. Indeed, carbon dioxide, produced through the combustion process, has accumulated in the atmosphere at an unprecedented rate over the past 150 years, triggering a fast global increase in temperature across the planet. In an ominous report from 2013, the Intergovernmental Panel on Climate Change (IPCC) warned that this increase of +0.8°C compared to pre-industrial temperatures is already going to result in lasting environmental changes, considered irreversible on a human time scale.^{7,8} Among them the disappearance of a significant portion of the Greenland⁹ and Antarctic¹⁰ ice sheets, a concomitant raise in sea level, weakened ocean circulation and increased frequency of extreme weather patterns⁸ are particularly worrying. Importantly, further uncontrolled increase in atmospheric CO₂ levels, leading to an increase in temperature of more than 4°C relative to pre-industrial conditions, could have consequences hard to predict but almost certainly catastrophic for the future of

humanity. In fact, there is already evidence of the harmful effects of this anthropogenic climate change on human societies on a global scale. For instance, the 3-year severe drought that plagued the Fertile Crescent between 2007 and 2010, and most likely caused by the current climate change, is believed to be partly responsible for the social unrest that led to the current Syrian civil war.¹¹ In an effort to mitigate this ongoing climate change and its consequences, 134 countries have ratified the Paris Agreement in 2016, committing to reduce global CO₂ emissions quickly, with the objective of limiting the temperature increase to 1.5°C above pre-industrial levels.¹² To achieve this goal, the world has to shift a significant portion of its primary energy supply away from fossil resources in the coming years.

Overall, while our current fossil fuel-based economy has been the foundation of the 20th century and all the technological breakthroughs it brought, it has reached its limits and needs to quickly be replaced. The world needs to rely on a more diverse, more sustainable and better-distributed energy mix to face the challenges of the 21st century.

1.2 The quest for an alternative energy

Nuclear energy generated by the fission of radioactive Uranium – a potential alternative to fossil fuels – supplied 5% of the World's Energy consumption in 2012.¹ While it does not produce significant amounts of carbon dioxide, and therefore does not contribute to the previously discussed anthropogenic climate change, this technology represents several critical drawbacks that prevent it to be an adequate candidate to replace fossil fuels. (i) It produces harmful radioactive byproducts that need to be safely stored for decades. (ii) In the event of a generator explosion, it can result in lethal radiative poisoning of extended areas, as illustrated by the Chernobyl disaster and more recently by the Fukushima disaster. (iii) Like fossil resources, Uranium is not sustainable, and is in fact scarcer than any of the major fossil fuels (see Figure 1.2). (iv) To meet the additional projected energy requirements of 2040 (see Figure 1.1a), the world would need to build more than one 1 GW reactor per day, which is clearly impractical. Despite these drawbacks, because the nuclear technology is already well mastered and carbon-free, it could play a role in the early stages of the transition towards renewable energy sources, and even potentially ultimately be part of a global energy mix.

Renewable alternatives to fossil fuels and their respective known amount are represented in Figure 1.2, along with the unsustainable energy sources discussed previously and the world energy consumption of the year 2012 (18.3 TWy). Importantly, while the integrality of the known reserves of non-renewable sources are represented in Figure 1.2, renewables are associated with the energy they can potentially generate yearly. All of the renewable sources of energy listed here have the advantage of generating carbon-free power, except for biomass combustion, which can be carbon-neutral. While the majority of renewable are not sufficiently abundant to power the planet on their own, they can – and probably will – be included in a more varied energy mix with respective contributions optimized depending on the location where energy is to be generated.

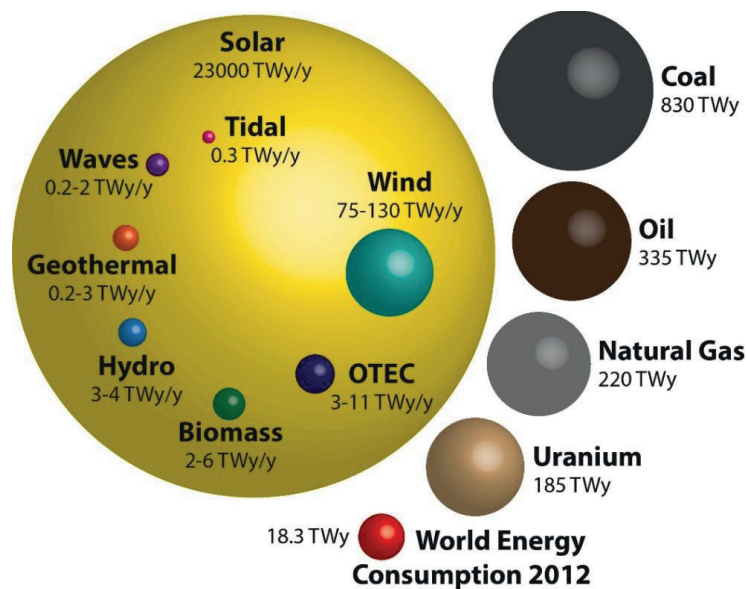


Figure 1.2 Estimated finite and renewable planetary energy reserves, in Terawatt years (TWy) and Terawatt years per year (TWy/y) respectively, adapted from a 2015 report of the International Energy Agency.¹³ The reported energy values are proportional to the volumes of the corresponding spheres.

Strikingly, solar energy is overwhelmingly more abundant than any other energy source available on Earth. Each year, an estimated 23 000 TWy of solar energy reaches emerged continents, dwarfing the annual world energy consumption by three orders of magnitude. Moreover, solar energy is a very evenly distributed resource, even favoring developing countries, mostly located in the southern hemisphere. Finally, it can be accessed without environmental destruction, as opposed to shell gas and coal, and can be exploited without the generation of CO₂ as a byproduct. For these reasons, sunlight is a very attractive source of energy and is bound to play a leading role in the energy

landscape of the next decades. However, bringing solar energy conversion technologies to a global scale presents several challenges.

1.3 Solar energy: a global challenge

Photovoltaic (PV) technologies relying on light-absorbing semiconductors for the conversion of sunlight into electricity represents one of the main approach to solar energy conversion. Since the 1950's, this technology has come a long way to become one of the cheapest sources of electricity. Especially, over the last two decades, innovations in the manufacturing of PV systems combined with environmental policies from the biggest energy consumers (USA, EU, China) allowed to quickly reduce the cost of PV electricity. In 2016, Lazard calculated a median unsubsidized levelized cost of energy (LCOE) of *ca.* \$50/MWh for PV on a utility scale in the USA,¹⁴ which is significantly lower than the \$68 – \$101/MWh calculated for natural gas, or the \$60 - \$143/MWh calculated for coal. In fact, in this study, only wind power reaches a LCOE as low as PV electricity. A similar trend has been calculated for energy systems in Europe.^{15,16} Therefore, from an economic standpoint, renewable solar and wind energies are currently the two most attractive options for the generation of electricity. Moreover, in an NREL report from 2012,¹⁷ PV power plants are calculated to produce *ca.* 40 g of CO₂eq/kWh, compared to 1000 g of CO₂eq/kWh, showing the dramatic decrease in greenhouse gas emission that would result from a transition to solar energy. Consequently, according to the New Energy Outlook 2016 from Bloomberg New Energy Finance,¹⁸ as its cost keeps dropping, solar energy will be the predominant technology in China, the USA, and Europe by 2040. Moreover, from a technological standpoint, PV technologies have known a lot of diversification over the last ten years, as evidenced by the regularly updated NREL chart.¹⁹ The improvement of thin-films technologies – based on amorphous silicon, Cu(In,Ga)Se₂ and CdTe – and the appearance of emerging technologies such as organic cells, quantum dot cells or the hybrid organic/inorganic perovskite cells are opening possibilities for the introduction of solar energy at every level in our societies. Indeed, thin-film technologies allow, for instance, the creation of flexible solar cells for incorporation in clothing or small devices, or semi-transparent modules for applications in smart windows for buildings or vehicles. Overall, the diversification and improvement of PV technologies is an extremely active field of research in both academia and the industrial sector, which prefigures a flourishing future for their application in powering our world over the next decades.

However, while solar energy holds a great potential to overcome the limits of our current global energy model, it also presents its own limitations. PV electricity production is directly tied to the intensity of the sunlight reaching the PV modules at a given time, and this intensity is highly dependent on atmospheric conditions, geographical location, the time of the day and the year. Consequently, the energy output of PV technologies is highly intermittent, and does not necessarily meet the energy needs of the population at any point in time – the most obvious situation being that no solar electricity can be produced at night, i.e. when energy demands peak in the winter. To develop solar energy on a global scale, it is therefore necessary to develop innovative technologies capable of storing the excess energy produced by solar power plants during sunny days, and effectively solving the mismatch between supply and demand. Currently, the most efficient and therefore most used storage technology consists in pumping water uphill into a dam, converting electrical energy into potential energy. However, this can only be performed in mountainous environments, and the stored energy cannot be transported. Among other available energy storage systems, batteries currently represent the most mature technology versatile enough to achieve this purpose regardless of the location of the solar power plant. Already, high capacity batteries are developed for the rapidly growing electric vehicle industry, and for household energy storage – such as the Tesla Powerwall. However, batteries are limited by their relatively small capacities and by their discharge time, typically ranging from minutes to hours (see Figure 1.3a) making them appropriate for daily storage, but unfit for long-term seasonal storage or for the displacement of large quantities of energy.

Power-to-gas technologies have been identified as a potential tool for managing solar energy intermittency on larger quantities and longer timescales. They consist in using renewable electricity to produce a combustible gas, such as hydrogen. In practical applications, solar electricity coming from PV installations is fed to an electrolyzer, where water is electrochemically converted to oxygen and hydrogen. Through this process, solar energy is therefore converted into chemical energy, under the form of an energetic solar fuel: the hydrogen molecule. Hydrogen can then either be injected in the natural gas grid, transported by vehicle or used at the site of production. Importantly, the amount of water consumed by this process is relatively small: to store 1 MWh of energy, less than 200 liters of water are necessary. In comparison, a typical European household consumed 2 to 8 MWh of electricity in 2014.²⁰ The energy stored in hydrogen molecules can last for months

and be released at will by combustion inside an engine, or more efficiently inside a fuel cell. This technology can therefore potentially complement the short term, fast-response storage technologies to create a completely carbon-neutral energy grid, running on renewable electricity and renewable fuels, as shown in Figure 1.3. This figure further illustrates the possibility of converting hydrogen and carbon dioxide to methane – a fuel safer and easier to handle in the currently existing natural gas grid.

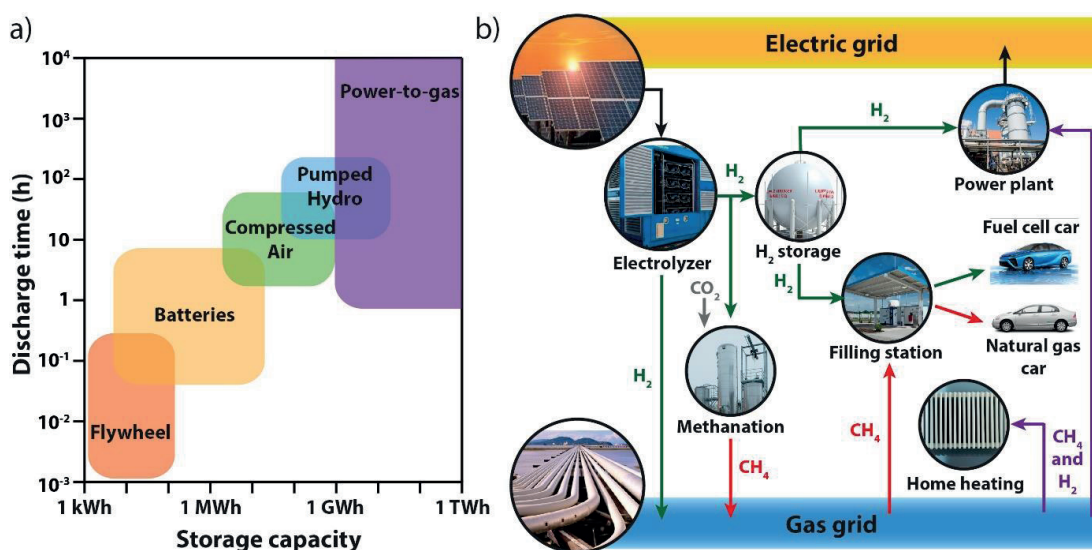


Figure 1.3 a) Discharge time and storage capacity of several energy storage technologies. b) Example of a carbon-neutral renewable energy grid providing for electricity, heat and transportation fuels at all times by means of power-to-gas storage. Adapted from a white paper of the California Hydrogen Business Council from 2015.²¹

Hydrogen therefore represents a promising carbon-free energy vector, which could be the basis of a new energetic model for our societies. Moreover, power-to-gas technologies can also be applied to off-grid energy generation by simply producing and storing hydrogen on site. Already, *ca.* forty power-to-gas demonstration projects are operational or planned in Europe, the vast majority of them in Germany,²² and a similar number can be found in the USA.²³ However, the cost of the fuels produced using this technology are still high compared to competing technologies, such as methane reforming or biomass gasification, which can produce H_2 at a cost of 1\$/kg and 1.6\$/kg respectively.²⁴ Importantly, these two technologies also generate undesirable carbon dioxide, which would require their combination with capture devices likely to increase significantly the final cost of the produced hydrogen. Regarding hydrogen generation by

electrolysis, the US Department of Energy aims for a production cost of 2.30 \$/kg by 2020,²⁵ while the European Commission targets a distribution price of 3 €/kg by 2030.²⁶ Therefore, considerable industrial and scientific research efforts have been engaged to improve currently existing electrolysis technologies for hydrogen production, meet these targets, and develop solar hydrogen as a global energy vector.

1.4 Solar hydrogen from water splitting

As discussed in the previous section, water electrolysis, or water splitting, and the resulting production of hydrogen, is a promising approach for long-term storage and transportation of solar energy. It consists in using solar energy to drive the water splitting reaction:



The standard free energy associated with this reaction is $\Delta G^0 = +237.18 \text{ kJ} \cdot \text{mol}^{-1}$ at 25°C. This also incidentally represents the maximum amount of energy one can extract from one mole of H_2 by reacting it with O_2 inside a fuel cell. The corresponding standard enthalpy of formation at 25°C is $\Delta H^0 = +286 \text{ kJ} \cdot \text{mol}^{-1}$, which corresponds to the maximum amount of energy that can be extracted by combustion of H_2 in air. These relatively high energies make H_2 one of the most energy-dense fuels, with a specific energy of $142 \text{ MJ} \cdot \text{kg}^{-1}$, a value three times higher than for regular gasoline ($46.4 \text{ MJ} \cdot \text{kg}^{-1}$), and validating its use as an efficient energy vector. However, because H_2 is a gas under standard conditions, it further requires the development of storage techniques, such as compression or adsorption in hydrides, to improve its volumetric energy density.

Since solar energy is most commonly converted into electricity, the next paragraphs will focus more specifically on electrochemical water splitting. In this process, the water splitting reaction is performed inside an electrolyzer where it is divided into two electrochemical half-reactions: the water oxidation reaction, or oxygen evolution reaction (OER) performed at the anode and the water reduction reaction or hydrogen evolution reaction (HER) performed at the cathode, each associated with a different standard redox potential (see Table 1.1).

Table 1.1 Electrochemical half-reaction in acidic and alkaline media and associated redox potentials for the oxygen evolution reaction and hydrogen evolution reaction. NHE = Normal Hydrogen Electrode

Oxygen Evolution Reaction	Hydrogen Evolution Reaction
Acidic conditions:	Acidic conditions:
$\text{H}_2\text{O}_{(l)} \rightarrow \frac{1}{2}\text{O}_{2(g)} + 2\text{H}^+_{(aq)} + 2\text{e}^-$ (1.2a)	$2\text{H}^+_{(aq)} + 2\text{e}^- \rightarrow \text{H}_{2(g)}$ (1.3a)
Alkaline conditions:	Alkaline conditions:
$2\text{OH}^-_{(aq)} \rightarrow \frac{1}{2}\text{O}_{2(g)} + \text{H}_2\text{O}_{(l)} + 2\text{e}^-$ (1.2b)	$2\text{H}_2\text{O}_{(l)} + 2\text{e}^- \rightarrow \text{H}_{2(g)} + 2\text{OH}^-_{(aq)}$ (1.3b)
Standard Redox potential at 298 K:	Standard Redox potential at 298 K:
$E^0(\text{O}_2/\text{H}_2\text{O}) = 1.23 \text{ V vs NHE}$ (1.2c)	$E^0(\text{H}^+/\text{H}_2) = 0.00 \text{ V vs NHE}$ (1.3c)

In principle, the water splitting process can therefore be thermodynamically driven inside an electrolyzer with an electromotive force of:

$$\Delta E^0 = E^0(\text{O}_2/\text{H}_2\text{O}) - E^0(\text{H}^+/\text{H}_2) = 1.23 \text{ V} \quad (1.4)$$

This voltage relates to the free energy of the water splitting reaction mentioned previously through the relationship:

$$\Delta G^0 = nF\Delta E^0 = 237.18 \text{ kJ} \cdot \text{mol}^{-1} \quad (1.5)$$

where n is the number of electrons involved in the creation of each molecule of H_2 ($n = 2$) and $F = 96500 \text{ C} \cdot \text{mol}^{-1}$ is the Faraday constant. However, in a practical device, it is necessary to apply a significant overpotential in addition to ΔE^0 in order to overcome the electrical resistivity of the system (η_{ohm}), the mass transport of the ions (η_{mt}) and the activation energy of the electrochemical reactions. This last kinetic overpotential can be divided into the cathodic overpotential (η_{c}) for the HER and the anodic overpotential (η_{a}) for the OER, and typically represents the main voltage loss. In summary, to drive the reaction, one needs to apply at least the following voltage to the electrolyzer:

$$\Delta E = \Delta E^0 + \eta_{\text{ohm}} + \eta_{\text{mt}} + \eta_{\text{a}} + \eta_{\text{c}} \quad (1.6)$$

One can therefore convert solar energy to solar hydrogen by using a PV module – where light is absorbed and converted into electrical current – delivering a voltage of ΔE

and a current I to an electrolyzer – where the electrical current is converted into chemical energy through the electrochemical water splitting process. This “PV + electrolyzer” approach is illustrated in Figure 1.4, along with the two main types of industrial electrolyzers: the alkaline electrolyzer operating in alkaline conditions, and the proton exchange membrane (PEM) electrolyzer operating in acidic conditions.

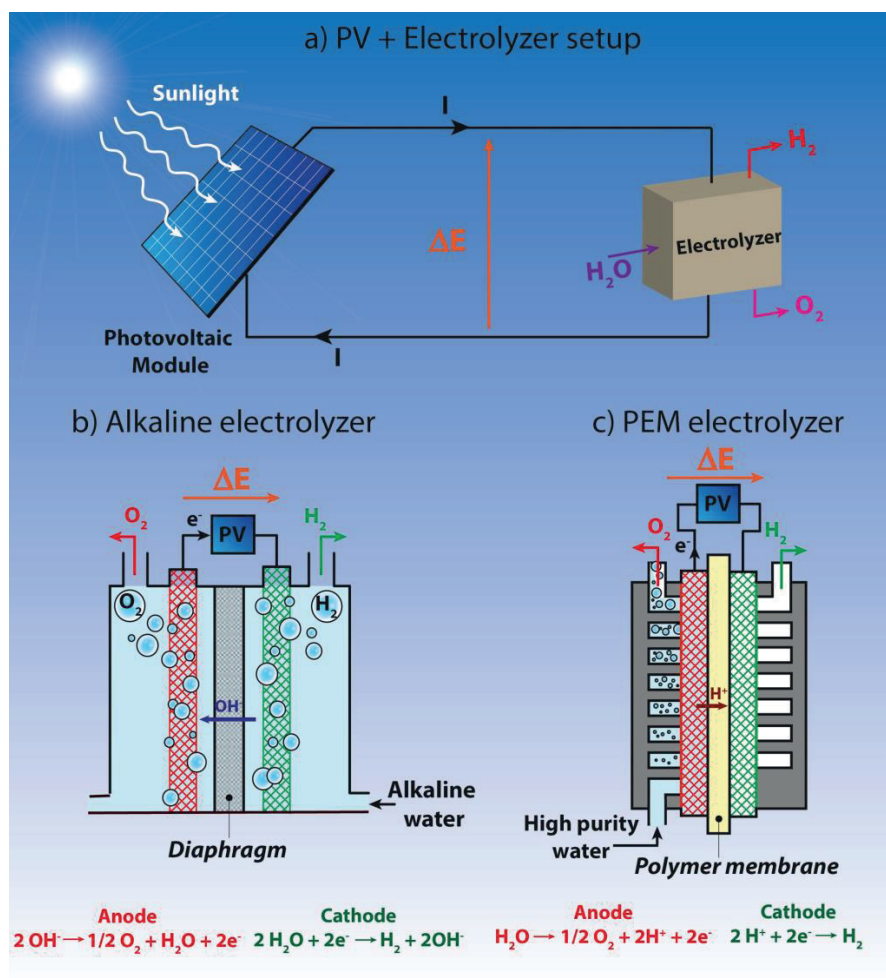


Figure 1.4 a) Simplified representation of a PV + electrolyzer configuration, where a PV module produces a voltage ΔE and a current I to power an electrolyzer generating H_2 and O_2 from H_2O . Two types of electrolyzers can be found: the alkaline electrolyzer (b) and the PEM electrolyzer (c) represented with the corresponding electrochemical reactions occurring at each electrode.²⁷

These two technologies have been and are still the focus of a lot of research, in particular concerning the development of new generations of robust Earth-abundant catalysts able to lower η_a and η_c , and therefore to increase the efficiency of the

electrolyzer by decreasing $\Delta E/\Delta E^0$. The solar-to-hydrogen efficiency (η_{STH}) of the overall PV + electrolyzer system is given by:

$$\eta_{\text{STH}} = \eta_{\text{PV}} \times \eta_{\text{electrolyzer}} \quad (1.7)$$

where η_{PV} is the efficiency of the PV module and $\eta_{\text{electrolyzer}}$ the efficiency of the electrolyzer. Triple-junction PV cells can yield a η_{PV} up to 44.7% under concentrated sunlight, but more affordable and commercially available technologies typically provide a η_{PV} around 20% (Si, CIGS, CdTe).¹⁹ Regarding the electrolyzer, state-of-the-art systems can achieve $\eta_{\text{electrolyzer}}$ close to 80%.²⁸ Therefore, a PV + electrolyzer configuration can typically perform with a η_{STH} in the 15-30% range, depending mostly on the choice of PV technology. The record efficiency for this type of system has been improving over the last years and is currently held by a device reported by Jia *et al.* performing with a η_{STH} of 30% for over 50 hours, and involving a triple-junction InGaP/GaAs/GaInNAs(Sb) solar cell connected to two PEM electrolyzers in series.²⁹ While the PV + electrolyzer approach is promising in terms of efficiency, it still presents important drawbacks. Expensive but efficient systems, based on III-V solar cells, can potentially produce hydrogen at a price low enough to meet the target set by the EU and the US DOE (see section 1.3), but only under concentrated light.³⁰ This therefore limits their use to places where the sunlight intensity is very stable and seldom altered by the presence of clouds or haze. More affordable PV systems with lower efficiency, based for instance on Si p-n junctions, can in principle meet the targets without light concentration,³⁰ but their efficiency is still very much dependent on the light intensity.

Moreover, having two independent parts in the device – the PV module and the electrolyzer – connected in series implies the necessity for optimizing and matching the current density flowing through each of them to avoid additional losses. These challenges do not entirely question the viability of the PV+electrolyzer approach, and a lot of research is still devoted to the advancement of this technology that remains the most mature, but they are however significant enough to justify the development of alternative routes towards solar hydrogen generation. Photocatalytic and photoelectrochemical water splitting represent two alternative approaches and are illustrated in Figure 1.5. On one hand, photocatalytic water splitting is performed by suspending a particulate semiconductor photocatalyst in water. This photocatalyst can absorb visible light to produce charge carriers, which can drive electrochemical water splitting at the surface of

the material, producing H_2 and O_2 *in situ*. This approach eliminates the need for external wiring and probably represents the cheapest option in the long term. However its efficiency is still lacking, and separation of the gas products remains a challenge.³¹ On the other hand, photoelectrochemical (PEC) water splitting relies on two electrodes plunged into water, like in a regular electrolyzer, but one or both of these electrodes are made of semiconductor materials capable of generating free charge carriers upon absorption of light. The charges created inside of these so-called photoelectrodes then move to the semiconductor/water interface, where they participate in electrochemical water splitting. In a PEC device, O_2 and H_2 are produced in different locations, facilitating their separation, while the overall charge balance is maintained through an ohmic contact between the two electrodes.

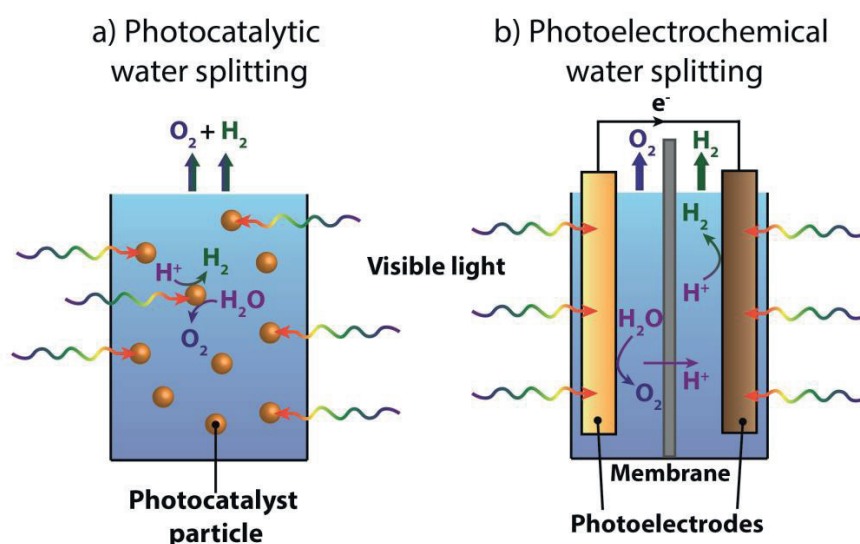


Figure 1.5 Alternative configurations for solar hydrogen production: a) suspension of photocatalyst particles producing a mixture of H_2 and O_2 and b) photoelectrochemical cell producing separate streams of O_2 and H_2 .

PEC water splitting is considered a promising technology for the second generation of solar hydrogen generators, with a much more compact design than the current PV + electrolyzer devices, as charge generation and electrochemical processes occur inside the same integrated unit. This technology is the focus of many research efforts supported by public large-scale joint programs – such as the Joint Center for Artificial Synthesis (JCAP)³² in the US, the Advanced Material and Processes for Energy Applications (AMPEA) program³³ in the EU, or the Swiss Competence Center for Energy Research (SCCER)³⁴ in

Switzerland – as well as by private companies. The work conducted during the PhD thesis was part of this global effort for the advancement of PEC water splitting, as will be developed in the next chapters.

1.5 References

- (1) U.S. Energy Information Administration. *International Energy Outlook 2016*; 2016.
- (2) United Nations, Department of Economic and Social Affairs, Population Division. December 2015.
- (3) BP. *Statistical Review of World Energy*; 2016.
- (4) Edenhofer, O.; Pichs-Madruga, R.; Sokona, Y.; Seyboth, K.; Kadner, S.; Zwickel, T.; Eickemeier, P.; Hansen, G.; Schlömer, S.; Stechow, C. von; Matschoss, P. *Renewable Energy Sources and Climate Change Mitigation: Special Report of the Intergovernmental Panel on Climate Change*; Cambridge University Press, 2011.
- (5) Alstone, P.; Gershenson, D.; Kammen, D. M. *Nat. Clim. Change* **2015**, 5 (4), 305–314.
- (6) Sustainable Development Goals: Sustainable Development Knowledge Platform <https://sustainabledevelopment.un.org/?menu=1300> (accessed Mar 16, 2017).
- (7) Solomon, S.; Plattner, G.-K.; Knutti, R.; Friedlingstein, P. *Proc. Natl. Acad. Sci.* **2009**, 106 (6), 1704–1709.
- (8) Stocker, T. F.; Qin, D.; Plattner, G.-K.; Tignor, M.; Allen, S. K.; Boschung, J.; Nauels, A.; Xia, Y.; Bex, V.; Midgley, P. M. *IPCC, 2013: Summary for Policy Makers in: Climate Change 2013: The Physical Science Basis. Contribution of Working Group I to the Fifth Assessment Report of the Intergovernmental Panel on Climate Change*; Cambridge University Press, 2014.
- (9) Straneo, F.; Heimbach, P. *Nature* **2013**, 504 (7478), 36–43.
- (10) Joughin, I.; Smith, B. E.; Medley, B. *Science* **2014**, 344 (6185), 735–738.
- (11) Kelley, C. P.; Mohtadi, S.; Cane, M. A.; Seager, R.; Kushnir, Y. *Proc. Natl. Acad. Sci.* **2015**, 112 (11), 3241–3246.
- (12) The Paris Agreement - main page http://unfccc.int/paris_agreement/items/9485.php (accessed Mar 16, 2017).
- (13) Perez, M.; Perez, R. *IEA-SHCP Newsletter*; 2015; Vol. 62.
- (14) Lazard. *Lazard's levelized cost of energy analysis*; 2016.
- (15) VGB PowerTech. *Levelized Cost of Electricity (LCOE 2015)*; 2015.
- (16) PhotoVoltaic Technology Platform. *PV LCOE in Europe 2014-30*; 2015.

- (17) Life Cycle Greenhouse Gas Emissions from Solar Photovoltaics (Fact Sheet), NREL (National Renewable Energy Laboratory) - 56487.pdf
<http://www.nrel.gov/docs/fy13osti/56487.pdf> (accessed Jun 28, 2017).
- (18) Bloomberg New Energy Finance. New Energy Outlook 2016
<https://www.bnef.com/dataview/new-energy-outlook-2016/index.html#section-0>
 (accessed Mar 21, 2017).
- (19) National Renewable Energy Laboratory. Best Research-Cell Efficiencies
<https://www.nrel.gov/pv/assets/images/efficiency-chart.png> (accessed Mar 21, 2017).
- (20) Electricity use per household | Electricity Consumption Efficiency| WEC
<https://www.wec-indicators.enerdata.eu/household-electricity-use.html> (accessed Mar 22, 2017).
- (21) California Hydrogen Business Council. *CHBC Hydrogen Energy Storage White Paper*; 2015.
- (22) Power-to-Gas Demonstration Projects
<https://www.google.com/maps/d/viewer?mid=1G6iHbCZd91DCmJEliv2EmGVDDno>
 (accessed Mar 22, 2017).
- (23) NREL: Hydrogen and Fuel Cells Research - Hydrogen Production Cost Analysis
http://www.nrel.gov/hydrogen/production_cost_analysis.html (accessed Mar 22, 2017).
- (24) Rongé, J.; Bosserez, T.; Huguenin, L.; Dumortier, M.; Haussener, S.; Martens, J. A. *Oil Gas Sci. Technol. – Rev. D'IFP Energ. Nouv.* **2015**, 70 (5), 863–876.
- (25) DOE Technical Targets for Hydrogen Production from Electrolysis | Department of Energy <https://energy.gov/eere/fuelcells/doe-technical-targets-hydrogen-production-electrolysis> (accessed Mar 22, 2017).
- (26) European Commission. *HyWays - The European Hydrogen Roadmap*; 2008.
- (27) Formal, F. L.; Bourée, W. S.; Prévot, M. S.; Sivula, K. *Chim. Int. J. Chem.* **2015**, 69 (12), 789–798.
- (28) Bertuccioli, L.; Chan, A.; Hart, D.; Lehner, F.; Madden, B.; Standen, E. *Development of Water Electrolysis in the European Union - Fuel Cells and Hydrogen Joint Undertaking*; 2014.
- (29) Jia, J.; Seitz, L. C.; Benck, J. D.; Huo, Y.; Chen, Y.; Ng, J. W. D.; Bilir, T.; Harris, J. S.; Jaramillo, T. F. *Nat. Commun.* **2016**, 7, 13237.

- (30) Dumortier, M.; Tembhurne, S.; Haussener, S. *Energy Environ. Sci.* **2015**, *8* (12), 3614–3628.
- (31) Hisatomi, T.; Kubota, J.; Domen, K. *Chem. Soc. Rev.* **2014**, *43* (22), 7520–7535.
- (32) JCAP <http://solarfuelshub.org/> (accessed Mar 29, 2017).
- (33) Advanced Materials and Processes for Energy Application (AMPEA) | EERA
<http://www.eera-set.eu/eera-joint-programmes-jps/advanced-materials-and-processes-for-energy-application-ampea/> (accessed Mar 29, 2017).
- (34) SCCER Heat and Electricity Storage <http://www.sccer-hae.ch/> (accessed Mar 29, 2017).

Chapter 2

Photoelectrochemical water splitting

In this chapter, the fundamental energetic structure and properties of semiconductor materials – the core elements of PV and PEC devices – are detailed. After introducing the band theory, the concept of semiconductor materials is defined. Then the equations governing charge carrier concentration and general electronics in semiconductors are then presented, as well as how they can be influenced by extrinsic doping.

In a second part, the physico-chemical properties of the semiconductor-liquid junction are explained, introducing important concepts: depletion regime, band bending, flat-band potential, photovoltage and photocurrent. The results derived in these first sections are then used to establish possible architectures for photoelectrochemical devices: single-absorber S2, tandem D4, and tandem PV+photoelectrode. The advantages and drawbacks of each architecture are briefly discussed.

In the last section, a more detailed attention is given to D4 tandem devices – the configuration of interest for the project presented in this manuscript. State-of-the-art photoelectrode materials are presented, and finally current challenges of the technology are discussed, motivating the original research work presented in the following chapters.

Part of the last section has been adapted from “Photoelectrochemical Tandem Cells for Solar Water Splitting” (Prévot, M.S.; Sivula K.; *J. Phys. Chem. C*, **2013**, 117, 17879-17883).¹

2.1 Semiconductor fundamentals

PEC devices, like PV devices rely on semiconductors for light absorption and charge generation. This section describes the basic properties of these particular materials, which have to be established in the framework of the band theory. Contrary to molecular species, whose electrons are localized into molecular orbitals of quantified energy, extended solids develop a so called “band structure”. This phenomenon can be illustrated from the Molecular Orbital Theory for a 1D arrangement of atoms, as shown in Figure 2.1a in the case of 1s orbitals. If a linear chain of atoms contains n atoms, n molecular orbitals arise from one type of atomic orbital, and with increasing n , the molecular orbitals are increasingly closer in energy. Therefore, for a very long chain of atoms, the resulting “molecular orbitals” are so close in energy that they form an energy continuum called “energy band”, and dispersion in energy of the resulting band depends on the strength of the interaction between the atomic orbitals of the atoms. Moreover, when other atomic orbitals are involved, this results in a band structure where energy bands accessible to the electrons are separated by other “forbidden” energy bands (see Figure 2.1b).

The filling of this band structure with electrons determines if the crystal is conductive or insulating. For a system of N atoms, each band can contain $N \times 2(2\ell+1)$ electrons, where ℓ is the azimuthal quantum number of the atomic orbitals making up the band. For instance, a crystal of N atoms of sodium has $11N$ electrons that fill four bands, with the band of highest energy is only partially filled. This partial filling allow the electrons to move freely in the band, making the material conducting. On the contrary, silicon has $14N$ electrons that completely fill 4 bands, leaving the one of immediately higher energy completely empty. Since the highest occupied band is completely filled, the electrons it contains cannot move freely and the material is insulating. For an insulator, the highest-occupied band is called the valence band, and the lowest-unoccupied band is called the conduction band. The valence band edge of energy E_V is separated from the conduction band edge of energy E_C by the band gap ($E_g = E_C - E_V$). Now, if an insulating material is provided with an energy higher than E_g , electrons can be promoted from the valence band to the conduction band, where they can move freely, making the material conducting. Such a material, which can transition from insulating to conducting under an

external source of energy, is called a semiconductor. For opto-electronic application – where the electrons are excited across the band gap by light absorption – a material is typically considered semi-conducting when its band gap is lower than ~ 4 eV, a radiation corresponding to the transition between UV-A and UV-B in the electromagnetic spectrum.

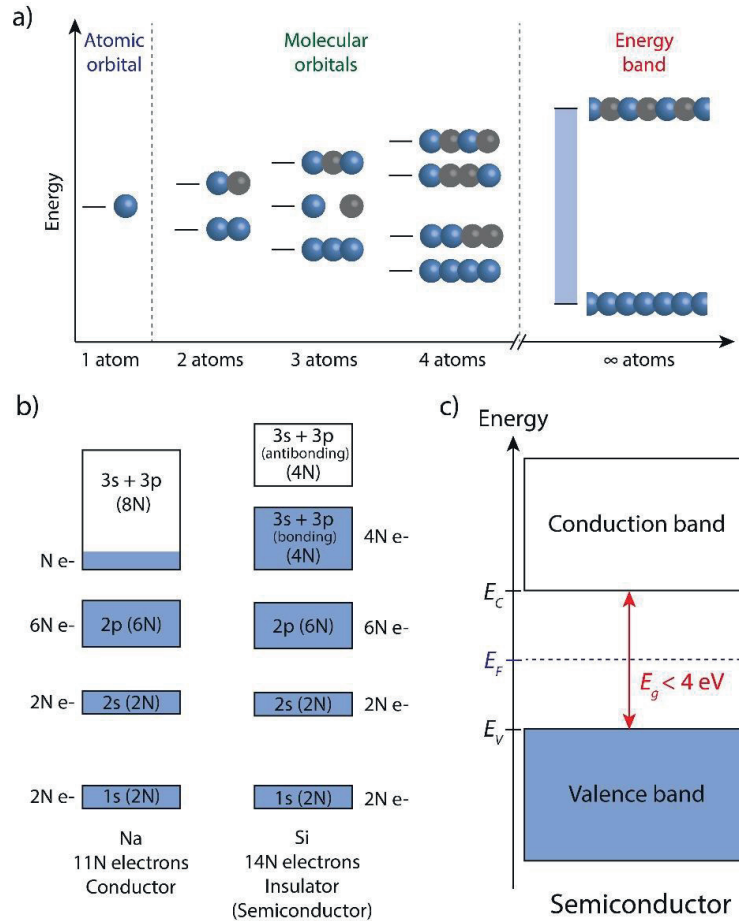


Figure 2.1 a) Type s atomic orbital and electronic energy levels arising from the combination of these atomic orbitals for a 1D chain of 2, 3, 4 and an infinity of atoms. Blue and grey spheres represent positive and negative atomic contributions respectively. For an infinity of atoms, the energy levels form an energy band, with its lowest energy corresponding to a fully bonding configuration, and its highest energy corresponding to a fully anti-bonding configuration. b) Band structure and electron filling for N atoms of conducting sodium and insulating (semiconducting) silicon. The atomic orbitals contributing to the formation of the band and the number of states available (in brackets) are reported in each band. c) Band diagram of a semiconductor, restricted to its valence band and conduction band. E_V = valence band edge; E_C = conduction band edge; E_F = Fermi level; E_g = band gap.

The following paragraphs give an analytic description of the band structure of semiconductors, adapted from *Solid State Physics* by Ashcroft and Mermin.² The Fermi

level (E_F) is defined as the energy corresponding to a 50% probability of occupancy in a conducting material, or as the energy of the highest occupied state at 0K. Since this definition cannot rigorously be applied to a semiconductor (as E_F could be identified with any energy inside the band gap), it is usually identified as the chemical potential for electrons. This chemical potential is defined as the change in free energy brought by the addition of one electron to the system, which also corresponds to the Gibbs energy of one electron. Thus, inside a semiconductor, electrons follow a Fermi-Dirac distribution:

$$f(E, E_F) = \frac{1}{e^{\frac{E-E_F}{k_B T}} + 1} \approx e^{-\frac{E-E_F}{k_B T}} \quad (2.1)$$

where $f(E, E_F)$ is the probability to find an electron of energy E inside a system with a Fermi level E_F , k_B is the Boltzmann constant, and T is the temperature. Since $E - E_F \gg k_B T$ inside the bands, the equation can be further simplified as shown above. Furthermore, for a semiconductor at thermal equilibrium in the dark, the concentration of electrons in the conduction band n_c is given by:

$$n_c(T) = \int_{E_c}^{\infty} g_c(E) \times f(E, E_F) dE \quad (2.2)$$

$$g_c(E) = \sqrt{2|E - E_c|} \frac{m_c^{3/2}}{\hbar^3 \pi^2} \quad (2.3)$$

where $g_c(E)$ is the density of available states at the conduction band edge, m_c is the effective mass of electrons inside the conduction band, and \hbar is the reduced Planck constant. This yields the following expression for n_c :

$$n_c(T) = N_c(T) e^{-\frac{E_c - E_F}{k_B T}} \quad \text{with} \quad N_c(T) = \frac{1}{4} \left(\frac{2m_c k_B T}{\pi \hbar^2} \right)^{3/2} \quad (2.4)$$

where N_c is called the effective density of states for electrons in the conduction band. One can similarly derive the concentration of holes – quasiparticles representing the vacancies of electrons – inside the valence band p_v and obtain:

$$p_v(T) = N_v(T) e^{-\frac{E_F - E_v}{k_B T}} \quad \text{with} \quad N_v(T) = \frac{1}{4} \left(\frac{2m_v k_B T}{\pi \hbar^2} \right)^{3/2} \quad (2.5)$$

where m_v is the effective mass of holes inside the valence band, and N_v is the effective density of states for holes in the valence band.

From Equations 2.4 and 2.5, one can derive the analytical expression for the Fermi level of the semiconductor:

$$E_F = \frac{E_C + E_V}{2} + \frac{3k_B T}{4} \ln \left(\frac{m_V}{m_C} \right) \quad (2.6)$$

Since $\frac{m_V}{m_C}$ is typically small, this indicates that the Fermi level of the semiconductor is located close to the center of the bandgap (see Figure 2.1c). Moreover, since each electrons inside the conduction band corresponds to a hole inside the valence band:

$$n_C(T) = p_V(T) = n_i(T) \quad (2.7)$$

and from Equations 2.4 and 2.5:

$$n_i^2 = N_V N_C e^{-\frac{E_g}{k_B T}} \quad (2.8)$$

Finally, it is possible to dope a semiconductor by introducing impurities in its crystalline structure. If these impurities present a lack of electron compared to the lattice (*e.g.* B impurities in Si), they are called acceptors and they produce a p-type semiconductor. On the contrary, if the impurities present an excess of electrons compared to the lattice (*e.g.* P in Si), they are called donors and they produce an n-type semiconductor. Introducing impurities has a direct effect on some of the previously discussed parameters and Equations 2.4, 2.5 and 2.6 are no longer valid. The effect of doping on the filling of the bands is shown in Figure 2.2. For a p-type semiconductor, the presence of acceptors produces an acceptor energy level close to the valence band, which induces the ionization of these acceptors by electrons from the valence band, where holes are consequently produced. Therefore, if there is a concentration N_A of acceptors in the lattice, and if they are fully ionized, the concentration of holes in the valence band will be equal to N_A and much higher than n_C :

$$p_V = N_A \gg n_C \quad (2.9)$$

Therefore, for a p-type semiconductor, the Fermi level position is given by:

$$E_F = E_V + k_B T \ln \left(\frac{N_A}{N_V} \right) \quad (2.10)$$

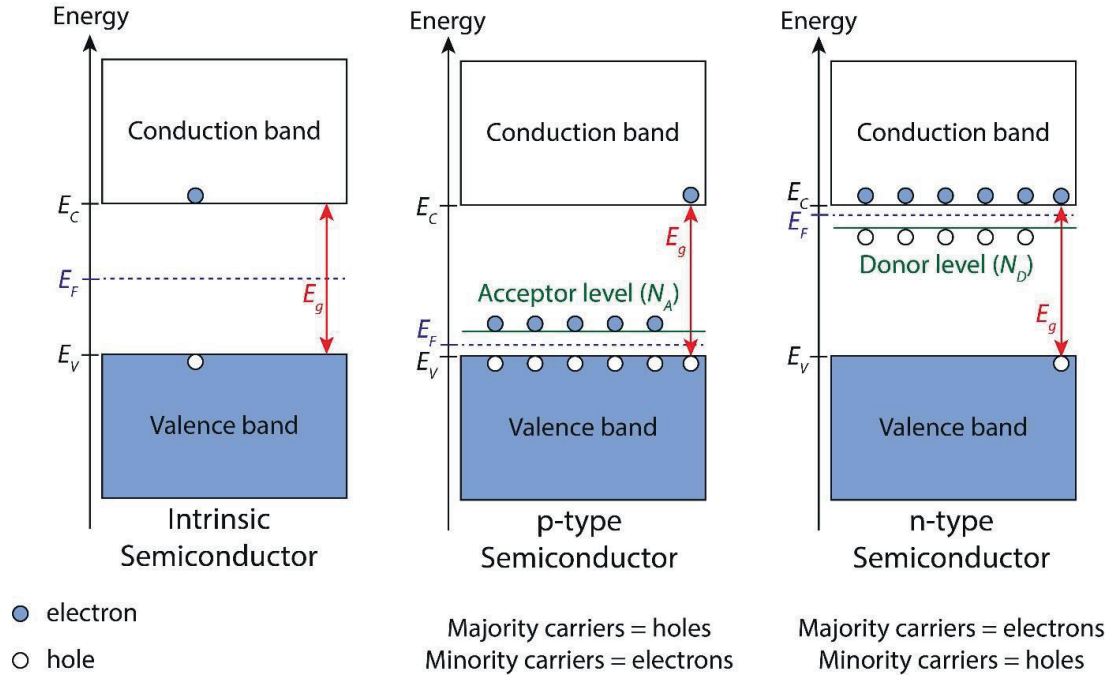


Figure 2.2 Simplified band diagram of an intrinsic, a p-type and an n-type semiconductors under thermal equilibrium. The acceptor and donor levels are represented after ionization. For p-type and n-type semiconductors, one type of charge carrier has a much higher concentration inside the bands, resulting in the existence of majority and minority carriers.

Similarly, for an n-type semiconductor, a donor level with a density N_D close to the conduction band will inject electrons inside of this conduction band, resulting, for fully ionized donors, in an electron density inside the conduction band of:

$$n_c = N_D \gg p_v \quad (2.11)$$

Therefore, for an n-type semiconductor, the Fermi level position is given by:

$$E_F = E_C - k_B T \ln \left(\frac{N_D}{N_C} \right) \quad (2.12)$$

As a result, while the concentration of holes and electrons were equal in an intrinsic – undoped – semiconductor, one can define majority and minority charge carriers in an extrinsic – doped – semiconductor. This discrepancy between the two types of charge carriers in a doped semiconductor is essential to the creation of a photoelectrode for PEC water splitting, as will be developed in the next section.

2.2 The semiconductor-liquid junction

PEC devices can achieve direct solar water splitting by the formation of a semiconductor-liquid junction (SCLJ) between a photoelectrode and water. As opposed to the PV + electrolyzer approach described in section 1.4, where the light-absorbing semiconductors are isolated from the aqueous electrolyte, the formation of a SCLJ stems from the direct electronic equilibration between a semiconductor and the electrolyte. This section describes the physico-chemical processes it involves.

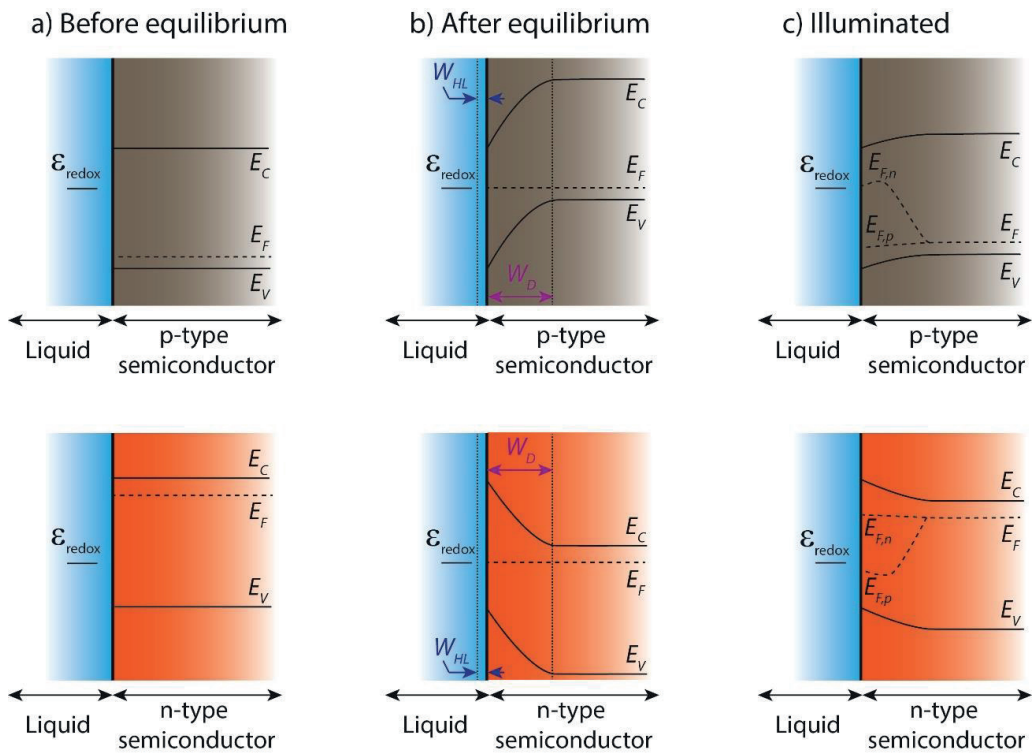


Figure 2.3 Formation of a SCLJ between a p-type (top row) or an n-type (bottom row) semiconductor and a liquid containing an electrolyte with a chemical potential E_{redox} . Before equilibrium (a) the bands of the semiconductor are flat. Once it is put in contact with the liquid phase, majority carriers flow from the semiconductor to the electrolyte until its Fermi level E_F equilibrates with E_{redox} , causing the formation of a depletion region of width W_D inside the semiconductor and of a Helmholtz layer of width W_{HL} inside the liquid. This results in a band bending in the depletion region of the semiconductor (downward in the p-type case or upward in the n-type case). c) Under illumination the production of photogenerated charge carriers induces the splitting of E_F into two quasi Fermi levels $E_{F,n}$ and $E_{F,p}$ for the electrons and holes respectively.

When a semiconductor is in contact with a liquid phase containing an electrolyte, the system reaches chemical equilibrium by equalization of the chemical potential

between the two phases. Inside the semiconductor, the chemical potential corresponds to E_F (see section 2.1), while in the liquid phase it is given by \mathcal{E}_{redox} ($\mathcal{E}_{redox} = -qE_{redox}$ where q is the elementary charge and E_{redox} is the redox potential of the electrolyte). To reach an equilibrium where these two quantities are equal, charges must flow between the semiconductor and the electrolyte, resulting in the formation of a SCLJ. The formation of this junction is illustrated in Figure 2.3. Typically, majority carriers flow from the semiconductor to the liquid phase, modifying the position of E_F until $E_F = \mathcal{E}_{redox}$, resulting in the formation of a depletion region of width W_D inside the semiconductor, empty of majority carriers. This depletion region is therefore charged (positively for an n-type semiconductor, and negatively for a p-type semiconductor) creating a potential barrier at the interface with the liquid and inducing a bending of the band edges – upward for an n-type semiconductor and downward for a p-type semiconductor. At the same time, the formation of this charged depletion region inside the semiconductor is screened by the formation of a charged layer of opposite sign by the ions present inside the liquid phase: the Helmholtz layer (HL) of width W_{HL} . A diffusive layer – the Gouy layer – can be added to the Helmholtz layer to describe more accurately the electrochemical double layer inside the liquid phase, but this secondary layer will be neglected in the following analysis.

This qualitative depiction can be improved by an analytical description of the main physico-chemical parameters defining the SCLJ. For this, we use the symbols and abbreviations recently proposed by Cendula *et al.*³ Moreover, considering the scope of the work presented in this manuscript, we limit the following description to p-type semiconductors, but equations describing n-type semiconductors can be found elsewhere.^{3,4} The derivations of the main result have been adapted from the book *Surface Electrochemistry* by John O'M. Bockris.⁴ Finally, the thermal contribution $\frac{k_B T}{q}$ is usually small in front of the other terms at room temperature, and will be neglected. The parametrization of the SCLJ under equilibrium is presented in Figure 2.4a.

The boundary conditions for the electrostatic potential ϕ are set as:

$$\text{Voltage drop in the HL:} \quad V_H = \phi(-W_{HL}) - \phi(0) = \phi_{el} - \phi_s \quad (2.13)$$

$$\text{Voltage drop in the semiconductor:} \quad V_{SC} = \phi(0) - \phi(W_D) = \phi_s - \phi_b \quad (2.14)$$

where ϕ_{el} is the electrostatic potential in the electrolyte is, ϕ_s is the electrostatic potential at the surface and ϕ_b is the electrostatic potential inside the bulk of the semiconductor.

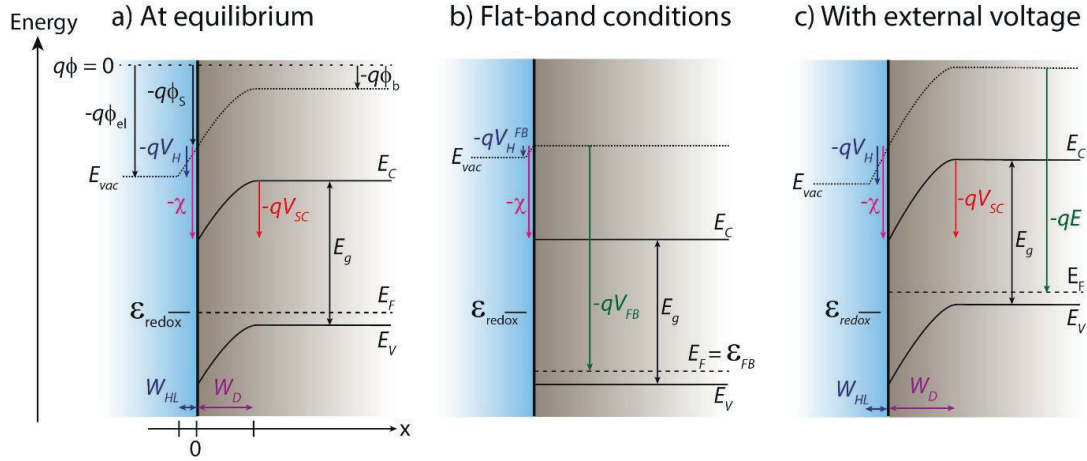


Figure 2.4 Parametrization of the SCLJ at equilibrium (a), under flat-band conditions (b), and under applied external voltage (c). Energies are referenced to the vacuum level (E_{vac}). The origin of potentials and the boundary conditions are represented only at equilibrium. E_C = conduction band edge; E_F = Fermi level; E_g = band gap, x = depth inside the semiconductor from the SCLJ.

Moreover, V_H and V_{SC} are related to the characteristics of the semiconductor, using Equation 2.10:

$$E_F = E_V + k_B T \ln \left(\frac{N_A}{N_V} \right) = qV_H - \chi + qV_{SC} - E_g + k_B T \ln \left(\frac{N_A}{N_V} \right) \quad (2.15)$$

where χ is the electron affinity of the semiconductor. A more convenient way to write this relationship is to refer to the flat-band energy (\mathcal{E}_{FB}), *i.e.* the value of E_F for which the bands are flat ($V_{SC} = 0$, see Figure 2.4b):

$$\mathcal{E}_{FB} = qV_H^{FB} - \chi - E_g + k_B T \ln\left(\frac{N_A}{N_V}\right) \quad (2.16)$$

Where V_H^{FB} is the voltage drop across the HL under flat-band conditions, which is *a priori* different than V_H . Therefore:

$$-qV_{SC} = \mathcal{E}_{FB} - E_F + q(V_H - V_H^{FB}) \quad (2.17)$$

Moreover $V_H, V_H^{FB} \ll V_{SC}$ for a typical SCLJ,⁵ therefore:

$$-qV_{SC} \approx \mathcal{E}_{FB} - E_F = \mathcal{E}_{FB} - \mathcal{E}_{redox} \quad (2.18)$$

Furthermore, the electrostatic potential ϕ and the electric field \mathcal{E} inside the semiconductor are obtained from the charge density ρ by solving Poisson's equation in one dimension:

$$\frac{d^2\phi}{dx^2} = -\frac{\rho(x)}{\epsilon_0\epsilon_r} \quad (2.19)$$

Where ϵ_0 is the vacuum permittivity and ϵ_r the dielectric constant of the semiconductor. For a p-type semiconductor with fully ionized acceptor sites, the charge density is zero in the bulk, as the hole concentration in the valence band is compensated by the ionized acceptor concentration, and is given by the ionized acceptor concentration in the depletion region, where majority carriers are considered uniformly negligible (abrupt conditions):

$$\begin{cases} \rho(x) = -qN_A & \text{for } 0 < x < W_D \\ \rho(x) = 0 & \text{for } x \geq W_D \end{cases} \quad (2.20)$$

Integrating Equation 2.19 twice, with the boundary conditions given in Equations 2.13 and 2.14 yields:

$$\begin{cases} \phi(x) = \frac{qN_A}{2\epsilon_0\epsilon_r}(x^2 - W_Dx) - \frac{V_{SC}x}{W_D} + V_{SC} + \phi_b & \text{for } 0 < x < W_D \\ \phi(x) = \phi_b & \text{for } x \geq W_D \end{cases} \quad (2.21)$$

Moreover, the electric field is given by:

$$\mathcal{E}(x) = -\frac{d\phi}{dx}(x) \quad (2.22)$$

$$\begin{cases} \mathcal{E}(x) = -\frac{qN_A}{2\epsilon_0\epsilon_r}(2x - W_D) + \frac{V_{SC}}{W_D} & \text{for } 0 < x < W_D \\ \mathcal{E}(x) = 0 & \text{for } x \geq W_D \end{cases} \quad (2.23)$$

Since the electric field has to be continuous in $x = W_D$, it comes that:

$$-\frac{qN_A}{2\epsilon_0\epsilon_r}W_D + \frac{V_{SC}}{W_D} = 0 \quad (2.24)$$

$$W_D = \sqrt{\frac{2V_{SC}\epsilon_0\epsilon_r}{qN_A}} \quad (2.25)$$

Therefore, under equilibrium the electric field expression is simplified to:

$$\begin{cases} \mathcal{E}(x) = -\frac{qN_A}{\epsilon_0\epsilon_r}(x - W_D) & \text{for } 0 < x < W_D \\ \mathcal{E}(x) = 0 & \text{for } x \geq W_D \end{cases} \quad (2.26)$$

And similarly, for the electrostatic potential profile:

$$\begin{cases} \phi(x) = \frac{qN_A}{2\epsilon_0\epsilon_r}(x - W_D)^2 + \phi_b & \text{for } 0 < x < W_D \\ \phi(x) = \phi_b & \text{for } x \geq W_D \end{cases} \quad (2.27)$$

It is furthermore possible to influence the band bending and the depletion width by applying an external voltage to the semiconductor, as illustrated in Figure 2.4c. This way, E_F is no longer in equilibrium with E_{redox} but rather with the applied external voltage E , and therefore:

$$E_F = -qV_{ext} \text{ hence } -qV_{SC} = \mathcal{E}_{FB} + qE \quad (2.28)$$

The space charge per unit area in the depletion region is given by:

$$Q_{SC} = -qN_A W_D = -\sqrt{2\epsilon_0\epsilon_r q N_A V_{SC}} \quad (2.29)$$

And the depletion layer capacitance per unit area is:

$$C_{SC} = \frac{\partial Q_{SC}}{\partial V'_{SC}} = -\sqrt{\frac{\epsilon_0\epsilon_r q N_A}{2V_{SC}}} \quad (2.30)$$

This yields the Mott-Schottky equation:

$$\frac{1}{C_{SC}^2} = \frac{2}{\epsilon_0\epsilon_r q N_A} V_{SC} \quad (2.31)$$

$$\frac{1}{C_{SC}^2} = -\frac{2}{\epsilon_0\epsilon_r q N_A} (E - E_{FB}) \quad (2.32)$$

Where V_{FB} is the flat-band potential ($E_{FB} = -\mathcal{E}_{FB}/q$). This equation is useful to determine V_{FB} experimentally (see chapters 4 and 6).

Under illumination, the semiconductor can absorb photons with an energy higher than E_g , thereby promoting electrons from the valence band to the conduction band. This

causes an increase in the population of electrons and holes at the SCLJ, and therefore the system reaches a different steady state, where the SCLJ is in equilibrium with the photon flux, resulting in the appearance of two different quasi Fermi levels for the electrons ($E_{F,n}$) and the holes ($E_{F,p}$). These quasi Fermi levels are related to the concentration of free carriers inside the depletion width:

$$n_c(x) = N_C \exp\left(-\frac{E_C(x) - E_{F,n}}{k_B T}\right) \quad (2.33)$$

$$p_v(x) = N_V \exp\left(-\frac{E_{F,p} - E_V(x)}{k_B T}\right) \quad (2.34)$$

Because majority carriers are repopulating the depletion region, the band bending is reduced under illumination. Importantly, photogenerated minority carriers are spontaneously driven towards the electrolyte under the influence of the built-in electric field at the SCLJ, while majority carriers are repelled. In the case of an n-type semiconductor, holes are driven towards the junction and eventually injected to the liquid phase to oxidize the electrolyte, forming a photoanode.

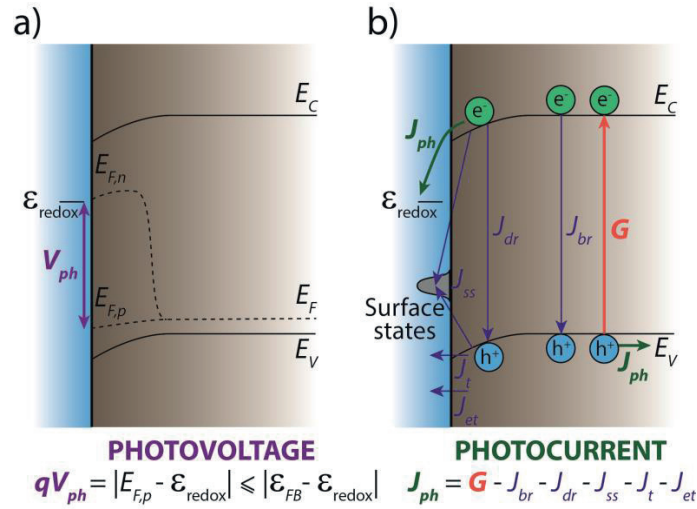


Figure 2.5 Illustration of the origin of (a) photovoltage and (b) photocurrent at the SCLJ. The photovoltage V_{ph} is defined by the splitting of quasi Fermi levels. It is maximum when the bands are fully flattened under illumination, and is then equal to $|\mathcal{E}_{FB} - \mathcal{E}_{redox}|/q$. The photocurrent J_{ph} is maximum and equal to the generation rate G when the junction is ideal. However, in practice it is hindered by recombination processes: bulk recombination (J_{br}), recombination in the depletion region (J_{dr}), tunneling through the SCLJ (J_t), thermionic emission through the SCLJ (J_{et}), and recombination at surface states (J_{ss}).⁶

Conversely, a p-type semiconductor in contact with a liquid will form a photocathode, where photogenerated electrons can reduce the electrolyte. Such a photoelectrode is characterized on one hand by its photovoltage V_{ph} (which corresponds to $|E_{F,p} - \mathcal{E}_{redox}|/q$, and is at best equal to $|\mathcal{E}_{FB} - \mathcal{E}_{redox}|/q$) and on the other hand, its photocurrent J_{ph} corresponding to the number of minority carriers transferred to the electrolyte (see Figure 2.5). Importantly, in Figure 2.3c and Figure 2.5a, the quasi Fermi level of minority carriers is shown to be in equilibrium with \mathcal{E}_{redox} for simplification. This represents the ideal case where there is no overpotential associated with the electrochemical reaction; however in practice, this overpotential η exists and therefore $|E_{F,p} - E_{F,n}| = |E_{F,p} - \mathcal{E}_{redox}| + \eta$.⁷ Similarly, in an ideal case, J_{ph} is equal to the rate of charge generation G , and to the flux of absorbed photon I_{abs} . However, in practice, a range of recombination currents can compete with charge injection to the electrolyte (J_{inj}), thereby reducing J_{ph} : bulk recombination (J_{br}), recombination in the depletion region (J_{dr}), tunneling through the SCLJ (J_t), thermionic emission through the SCLJ (J_{et}), and recombination at surface states (J_{ss}). These different competing kinetic pathways are illustrated in Figure 2.5b. For a more detailed analysis on the kinetics and thermodynamics of the SCLJ, one can refer to the work of P. Salvador.⁷

Thus, one can use the photovoltage and photocurrent produced by photoelectrodes to drive the water splitting reaction (Equation 1.1). This PEC water splitting is detailed in the next section.

2.3 Photoelectrochemical water splitting

PEC water splitting is realized by using one or two photoelectrodes inside a PEC cell. If a photoelectrode is irradiated with photons of energy $h\nu \geq E_g$, it will generate charges that can be used to perform the water splitting reaction. Thermodynamically, a PEC cell can perform solar water splitting if electrons are generated with an energy higher than $-qE^0(H^+/H_2)$ and holes are generated with an energy lower than $-qE^0(O_2/H_2O)$.⁸ The photocurrent produced by the PEC device determines its STH efficiency, given by the following formula:

$$\eta_{STH} = \frac{1.23 [V] \times J_{ph,op} [mA \cdot cm^{-2}] \times FE}{S [mW \cdot cm^{-2}]} \quad (2.35)$$

where $J_{ph,op}$ is the operating photocurrent, FE is the Faradaic efficiency (*i.e.* the conversion efficiency of free electrons to chemical product through the electrochemical reactions) and S is the total incident irradiance.

There are several possible approaches to perform direct water splitting using photoelectrodes, as illustrated in Figure 2.6. One possibility is to contact a single photoanode with water, oxidizing water on its surface, while the majority carriers are transferred to a “dark” electrode – typically a metal wire. This is the so-called single bandgap S2 approach (see Figure 2.6a) and it was historically employed in 1972 for the first successful demonstration of PEC water splitting by Fujishima and Honda, who used a n-TiO₂ photoanode and a Pt wire as the photoanode and cathode respectively.⁸

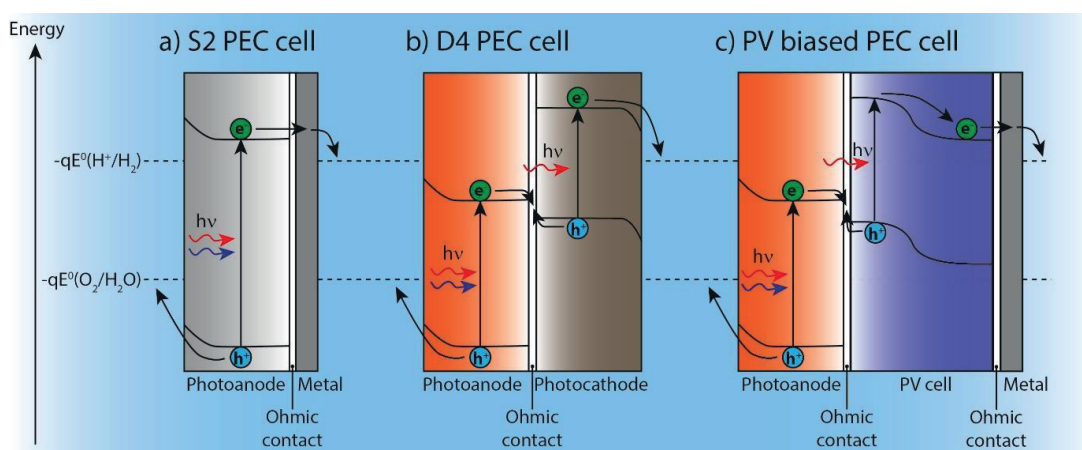


Figure 2.6 Band alignment of a) S2 PEC cell, b) D4 PEC cell and c) PV-biased PEC cell with the redox potentials of water for direct PEC water splitting. The light source is located on the left-hand side of each device: the blue arrow represent the high-energy photons of the incident light, while the red arrow represents the low-energy photons.

According to Equation 1.6, it is necessary for the system to produce a photovoltage higher than 1.23 V – due to transport and electrochemical overpotentials – to perform the water splitting process. In 2016, Fountaine *et al.* calculated that, in an ideal case, a single-junction device is expected to reach its highest efficiency (*ca.* 31%) for $E_g = 1.59$ eV.⁹ However, in the same study the authors stress that, in practice, necessary high overpotentials push the minimum photovoltage – and therefore the minimum E_g – much higher than this ideal value: typically a semiconductor with a bandgap of at least 2.0 eV (for a high-performance semiconductor) and more realistically higher than 2.5 eV is needed. A semiconductor with such a wide bandgap will only absorb the high-energy part

of the solar spectrum yielding a low G , and therefore a low $J_{ph,op}$, thereby limiting the STH efficiency of S2 PEC cell under AM 1.5 illumination to much lower values: 5.4% (for $E_g = 2.53$ eV) to 15% (for $E_g = 2.05$ eV). These calculations are also consistent with the values proposed in earlier studies.^{10–14}

Since two electrodes at least are necessary to perform PEC water splitting, one can replace the metal electrode in the S2 configuration by a light-absorbing photocathode, forming the so-called D4 configuration (see Figure 2.6b). In a D4 tandem cell, an n-type photoanode is connected in series – through an ohmic contact – to a p-type photocathode. The holes produced by the photoanode oxidize water, while the electrons produced by the photocathode reduce it. This structure allows distributing light absorption between the two photoelectrodes, and thereby using smaller band gaps than in the S2 configuration. Therefore, a D4 tandem cell can absorb a larger part of the solar spectrum resulting in a higher $J_{ph,op}$ than a S2 system, as illustrated in Figure 2.7a.

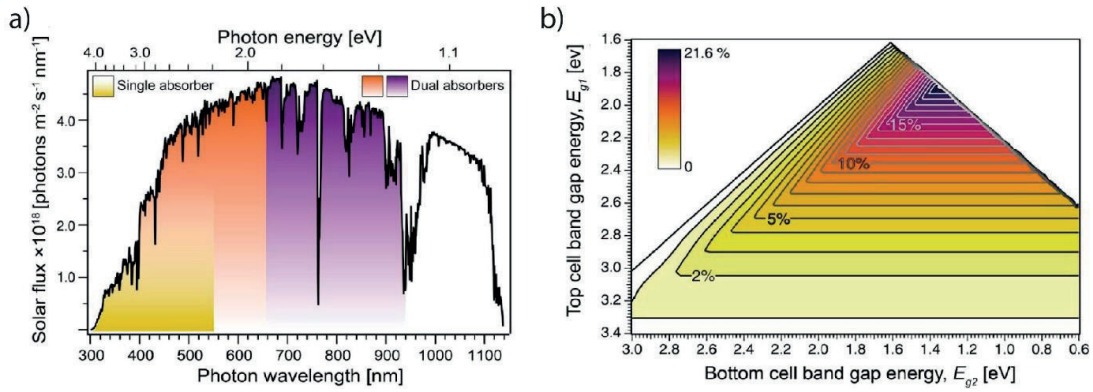


Figure 2.7 a) Comparison of the amount of light absorbed from the AM 1.5G solar spectrum by single-absorber vs dual-absorber configurations. The shading represents the photons that could be harvested and used to drive solar water splitting by an S2 PEC device (yellow) and a tandem D4 PEC device (brown and purple). b) Contour plot showing the maximum predicted STH efficiencies with AM 1.5G incident irradiation ($1000 \text{ W}\cdot\text{m}^{-2}$) and a total overpotential of 2 V for the water splitting reaction (1 V per photoelectrode) as a function of the chosen semiconductor bandgap energies with $E_{g1} > E_{g2}$. Reproduced from reference 1.

A D4 device can be formed by placing the two photoelectrodes side-by-side or one in front of the other (with respect to the direction of incident illumination). Calculations show that the latter configuration yields the highest maximum efficiency, and it is therefore the preferred approach: two photoelectrodes of similar surface area are stacked so that the incident light goes through each of them sequentially.¹⁰ The light is absorbed

first by the photoelectrode with the widest bandgap, so that the remaining low-energy light can be transmitted to the second photoelectrode with a smaller bandgap. Calculations further predict that such a D4 tandem cell with optimized E_g for the “top” and “bottom” photoelectrode can reach up to 40.0% in an ideal case⁹ and 16-29% STH efficiency using more realistic assumptions, depending on the considered overpotential,^{1,10–14} thus justifying its advantage over a single-absorber S2 configuration (see Figure 2.7b).

A third possibility is to use a PV cell instead of a photocathode to provide additional voltage to the photoelectrode, as shown in Figure 2.6c. This alternative approach – a compromise between the D4 and PV + electrolyzer architectures – is also widely investigated, and has already produced good STH efficiencies (up to ~ 12% for a single PV junction and ~ 17% for two PV junctions).^{15–19} However, it presents the disadvantage of requiring the presence of one or several additional so-called “buried junction” – inside the PV cell – compared to a D4 architecture, and also usually the careful encapsulation of the PV cell, due to its photo-instability if put in contact with a liquid electrolyte. This increased complexity in device manufacturing can negatively affect the resulting cost and lifetime of PV-biased systems if developed on a large scale and the scientific community is currently addressing these challenges. It is worth mentioning that this list of architectures is not exhaustive, and that any number of buried junction can be added to the system to improve its photovoltage, but at the cost of complicating the device architecture. Moreover, the role of photoanode and photocathode is interchangeable, as long as the overall photovoltage is sufficient to drive the water splitting reaction.

The work presented in the following chapters deals exclusively with the advancement of D4 tandem systems, which represent the most compact and robust architecture for direct solar water splitting, as will be detailed in the next section.

2.4 D4 tandem cells for PEC water splitting

A D4 tandem cell is realized by connecting an n-type photoanode and a p-type photocathode in series. In this configuration, the photovoltages of the two photoelectrodes add up while the same photocurrent must flow through both of them. The photogenerated electrons drift and diffuse towards the photocathode-liquid junction where they reduce H^+ to H_2 , while the holes drift and diffuse towards the photoanode-

liquid junction where they oxidize H₂O to O₂. The PEC behavior of each photoelectrode can be monitored in a three-electrode setup, yielding a current-potential curve (*J-V* curve), as pictured in Figure 2.8. The operation of a D4 cell can be determined by overlaying the *J-V* curves of each electrode: the crossing point of the two *J-V* curves gives the photocurrent $J_{ph,op}$ of the tandem cell, while its photovoltage V_{ph} is the sum of the photovoltages of the two photoelectrodes (see Figure 2.8).

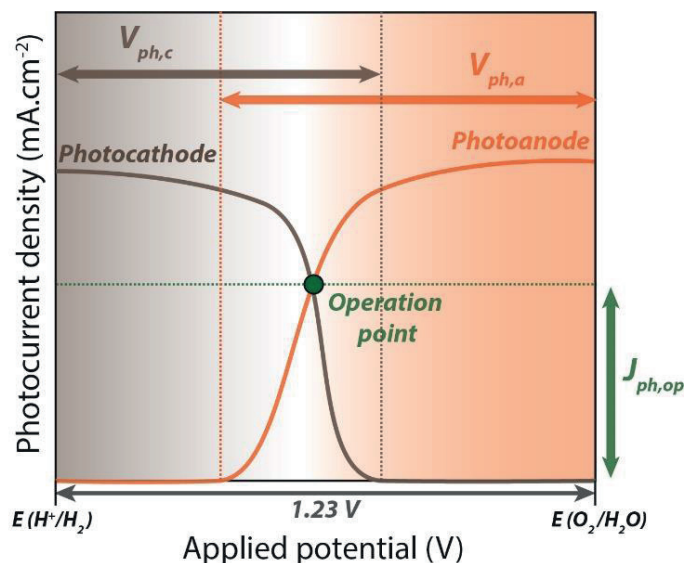


Figure 2.8 Overlaid *J - V* curves of a photocathode (brown) and a photoanode (orange). $J_{ph,op}$ is the photocurrent delivered by the tandem cell under operation, while $V_{ph,c}$ and $V_{ph,a}$ are the photovoltages delivered by the photocathode and the photoanode respectively.

While many n-type photoanodes have been studied for the water oxidation reaction, finding a material resilient to the highly oxidative conditions has been challenging but transition metal oxide semiconductors have excelled in terms of photostability. The prototype oxide photoanode has been TiO₂ for a long time, but, as mentioned in section 1.7, its wide bandgap limits its STH efficiency to around 2%.⁹ An early alternative to TiO₂ was WO₃, with a bandgap energy of 2.6 - 2.8 eV potentially allowing for conversion efficiencies up to about 5 - 6%. However, while it remains a good model compound, the high incident photon-to-current (IPCE, see Chapter 3, section 3.3.2) values reported suggest that further optimization is limited.²⁰ More recently, monoclinic bismuth vanadate (BiVO₄) has been proposed as photoanode candidate. With a smaller bandgap of about 2.4 eV, it can potentially provide STH efficiencies of over 9% in an optimized tandem PEC cell. In recent years, the performance of this material has been

substantially improved, with a record photocurrent of 6.7 mA.cm^{-2} – within 10% of the theoretical maximum efficiency.²¹ Finally, hematite ($\alpha\text{-Fe}_2\text{O}_3$), with a much smaller bandgap of 2.1 eV, could perform water oxidation with a maximum conversion efficiency of *ca.* 15%. Because of this very high value, and because it is made of two of the most abundant elements on Earth, it has been the focus of a lot of research work, especially over the last decade, reaching photocurrent densities of 4.3 mA.cm^{-2} at 1.23 V vs RHE and more than 6 mA.cm^{-2} at higher potentials.²² Overall, BiVO_4 and $\alpha\text{-Fe}_2\text{O}_3$ currently represent the best candidates for stable water oxidation under illumination, with performances continuously improving over time thanks to approaches like nanostructuring, surface passivation and catalytic overlayer deposition.

In comparison, little work has been done for the development of photocathodes for water reduction. Historically, p-type III-V semiconductors – GaP²³, InP²⁴, GaInP₂¹⁵ – have been used first, due to their good performance in PV devices. In fact, one of the highest STH efficiency for PEC water oxidation (12.4%) was obtained using a p-n GaAs buried junction in contact with a GaInP₂ photocathode.¹⁵ However, these materials are not ideal for large-scale production, due to the scarcity of their components, and their expensive deposition processes. Another class of material showing promising PEC performance is the one of p-type chalcopyrite: WS_2 ,²⁵ WSe_2 ,^{26,27} $\text{CuIn}_{1-x}\text{Ga}_x\text{Se}_2$ (CIGS)^{28–30} and $\text{Cu}_2\text{ZnSnS}_4$ (CZTS).^{31,32} These materials display promising short-term stability and photocurrents, but have either difficult processing conditions (WS_2 , WSe_2) or require the use of a toxic CdS overlayer (CIGS, CZTS). However, current research work in this field is yielding increasingly easy ways to overcome these limitations, and therefore chalcogenides represent a very important class of photocathode material. When considering large-scale production, an obvious candidate from the PV field is p-type Silicon. However, the necessity of creating a buried p-n junction, the poor stability of the material in aerated aqueous environments and its bandgap of 1.12 eV – limiting the STH efficiency of a tandem cell to below 15% (see Figure 2.7b) – question its choice as photocathode compared to other materials. Nonetheless, p-Si can produce high photocurrents over a short time,^{33,34} and efforts have been made to improve its stability through the deposition of conformal overlayers by atomic layer deposition.³⁵ Unfortunately, ALD is difficult to scale-up, and therefore p-Si processing remains too expensive for large-scale water splitting applications. Finally, prior to the work presented in this manuscript, several metal oxide photocathodes based on Cu(I) have been proposed: Cu_2O , CuBi_2O_4 and CuFeO_2 . While known for a long time for

its good transport properties and good absorption properties ($E_g=2.1$ eV), Cu₂O was neglected due to its high photo-instability in water. However, the deposition of conformal protecting layer by ALD (similar to the one for p-Si) has renewed interest in the material over the last five years.^{36–40} Very recently, ternary oxides CuBi₂O₄^{41,42} and CuFeO₂^{43,44} have been proposed as alternative candidates and, while CuBi₂O₄ suffers from the same instability than Cu₂O, the more robust CuFeO₂ displayed stability in aqueous environment for longer times.

More information on surface treatments for photoelectrode can be found in a review from Guijarro *et al.*⁴⁵ It is also noteworthy that very recently bipolar membranes have been introduced in the D4 architecture to overcome the incompatibility in pH and electrolyte that can occur between optimized photoanodes and photocathodes. These membranes afford dynamic sealing between the cathodic and anodic compartments of the cell, by transporting hydroxyl anions and protons only, while enabling minimal voltage losses through the system.^{46–48}

Overall, PEC water splitting – based on the formation of two SCLJ between phototelectrodes and water – has been established as a promising technology for a second generation of devices for solar fuel production. While photoanode materials have known fast improvements over the last decade, through nanostructuration and surface engineering, research on photocathode has comparably been sparser. In an effort to tackle this issue, the work presented here was devoted to the study and advancement of a novel photocathode material. Delafossite CuFeO₂, robust in aqueous media and made from Earth-abundant materials, represents a very attractive candidate for large-scale PEC water splitting application, and was chosen as the subject of study for the work presented in this thesis manuscript.

2.5 References

- (1) Prévot, M. S.; Sivula, K. *J. Phys. Chem. C* **2013**, *117* (35), 17879–17893.
- (2) Ashcroft, N. W.; Mermin, N. D. *Solid State Physics*; 1976.
- (3) Cendula, P.; Tilley, S. D.; Gimenez, S.; Bisquert, J.; Schmid, M.; Grätzel, M.; Schumacher, J. O. *J. Phys. Chem. C* **2014**, *118* (51), 29599–29607.
- (4) Bockris, J. O. *Surface Electrochemistry - A Molecular Level Approach*, Springer.; 1993.

- (5) Chandrasekaran, K.; Kainthla, R. C.; Bockris, J. O. *Electrochimica Acta* **1988**, *33* (3), 327–336.
- (6) Walter, M. G.; Warren, E. L.; McKone, J. R.; Boettcher, S. W.; Mi, Q.; Santori, E. A.; Lewis, N. S. *Chem. Rev.* **2010**, *110* (11), 6446–6473.
- (7) Salvador, P. J. *Phys. Chem. B* **2001**, *105* (26), 6128–6141.
- (8) Fujishima, A.; Honda, K. *Nature* **1972**, *238* (5358), 37–38.
- (9) Fountaine, K. T.; Lewerenz, H. J.; Atwater, H. A. *Nat. Commun.* **2016**, *7*, 13706.
- (10) Weber, M. F.; Dignam, M. J. J. *Electrochem. Soc.* **1984**, *131* (6), 1258–1265.
- (11) Bolton, J. R.; Strickler, S. J.; Connolly, J. S. *Nature* **1985**, *316* (6028), 495–500.
- (12) Hanna, M. C.; Nozik, A. J. *J. Appl. Phys.* **2006**, *100* (7), 074510.
- (13) Hu, S.; Xiang, C.; Haussener, S.; Berger, A. D.; Lewis, N. S. *Energy Environ. Sci.* **2013**, *6* (10), 2984–2993.
- (14) Seitz, L. C.; Chen, Z.; Forman, A. J.; Pinaud, B. A.; Benck, J. D.; Jaramillo, T. F. *ChemSusChem* **2014**, *7* (5), 1372–1385.
- (15) Khaselev, O.; Turner, J. A. *Science* **1998**, *280* (5362), 425–427.
- (16) Brillet, J.; Yum, J.-H.; Cornuz, M.; Hisatomi, T.; Solaraska, R.; Augustynski, J.; Graetzel, M.; Sivula, K. *Nat. Photonics* **2012**, *6* (12), 824–828.
- (17) Verlage, E.; Hu, S.; Liu, R.; Jones, R. J. R.; Sun, K.; Xiang, C.; Lewis, N. S.; Atwater, H. A. *Energy Environ. Sci.* **2015**, *8* (11), 3166–3172.
- (18) May, M. M.; Lewerenz, H.-J.; Lackner, D.; Dimroth, F.; Hannappel, T. *Nat. Commun.* **2015**, *6*, 8286.
- (19) Okamoto, S.; Deguchi, M.; Yotsuhashi, S. *J. Phys. Chem. C* **2017**, *121* (3), 1393–1398.
- (20) Solaraska, R.; Alexander, B. D.; Braun, A.; Jurczakowski, R.; Fortunato, G.; Stiefel, M.; Graule, T.; Augustynski, J. *Electrochimica Acta* **2010**, *55* (26), 7780–7787.
- (21) Pihosh, Y.; Turkevych, I.; Mawatari, K.; Uemura, J.; Kazoe, Y.; Kosar, S.; Makita, K.; Sugaya, T.; Matsui, T.; Fujita, D.; Tosa, M.; Kondo, M.; Kitamori, T. *Sci. Rep.* **2015**, *5*, 11141.
- (22) Kim, J. Y.; Magesh, G.; Youn, D. H.; Jang, J.-W.; Kubota, J.; Domen, K.; Lee, J. S. *Sci. Rep.* **2013**, *3*, 2681.
- (23) Ohashi, K.; Mccann, J.; Bockris, J. O. *Nature* **1977**, *266* (5603), 610–611.
- (24) Aharon-Shalom, E.; Heller, A. *J. Electrochem. Soc.* **1982**, *129* (12), 2865–2866.
- (25) Baglio, J. A.; Calabrese, G. S.; Harrison, D. J.; Kamieniecki, E.; Ricco, A. J.; Wrighton, M. S.; Zoski, G. D. *J. Am. Chem. Soc.* **1983**, *105* (8), 2246–2256.

- (26) McKone, J. R.; Pieterick, A. P.; Gray, H. B.; Lewis, N. S. *J. Am. Chem. Soc.* **2013**, *135* (1), 223–231.
- (27) Yu, X.; Prévot, M. S.; Guijarro, N.; Sivula, K. *Nat. Commun.* **2015**, *6*, 7596.
- (28) Kaneko, H.; Minegishi, T.; Nakabayashi, M.; Shibata, N.; Domen, K. *Angew. Chem. Int. Ed.* **2016**, *55* (49), 15329–15333.
- (29) Kaneko, H.; Minegishi, T.; Nakabayashi, M.; Shibata, N.; Kuang, Y.; Yamada, T.; Domen, K. *Adv. Funct. Mater.* **2016**, *26* (25), 4570–4577.
- (30) Guijarro, N.; Prévot, M. S.; Yu, X.; Jeanbourquin, X. A.; Bornoz, P.; Bourée, W.; Johnson, M.; Le Formal, F.; Sivula, K. *Adv. Energy Mater.* **2016**, *6* (7), n/a-n/a.
- (31) Rovelli, L.; Tilley, S. D.; Sivula, K. *ACS Appl. Mater. Interfaces* **2013**, *5* (16), 8018–8024.
- (32) Guijarro, N.; Prévot, M. S.; Sivula, K. *J. Phys. Chem. Lett.* **2014**, *5* (21), 3902–3908.
- (33) Boettcher, S. W.; Warren, E. L.; Putnam, M. C.; Santori, E. A.; Turner-Evans, D.; Kelzenberg, M. D.; Walter, M. G.; McKone, J. R.; Brunschwig, B. S.; Atwater, H. A.; Lewis, N. S. *J. Am. Chem. Soc.* **2011**, *133* (5), 1216–1219.
- (34) Seger, B.; Laursen, A. B.; Vesborg, P. C. K.; Pedersen, T.; Hansen, O.; Dahl, S.; Chorkendorff, I. *Angew. Chem. Int. Ed.* **2012**, *51* (36), 9128–9131.
- (35) Seger, B.; S. Tilley, D.; Pedersen, T.; K. Vesborg, P. C.; Hansen, O.; Grätzel, M.; Chorkendorff, I. *RSC Adv.* **2013**, *3* (48), 25902–25907.
- (36) Paracchino, A.; Laporte, V.; Sivula, K.; Grätzel, M.; Thimsen, E. *Nat. Mater.* **2011**, *10* (6), 456–461.
- (37) Tilley, S. D.; Schreier, M.; Azevedo, J.; Stefik, M.; Graetzel, M. *Adv. Funct. Mater.* **2014**, *24* (3), 303–311.
- (38) Bornoz, P.; Abdi, F. F.; Tilley, S. D.; Dam, B.; van de Krol, R.; Graetzel, M.; Sivula, K. *J. Phys. Chem. C* **2014**, *118* (30), 16959–16966.
- (39) Morales-Guio, C. G.; Liardet, L.; Mayer, M. T.; Tilley, S. D.; Grätzel, M.; Hu, X. *Angew. Chem. Int. Ed.* **2015**, *54* (2), 664–667.
- (40) Schreier, M.; Luo, J.; Gao, P.; Moehl, T.; Mayer, M. T.; Grätzel, M. *J. Am. Chem. Soc.* **2016**, *138* (6), 1938–1946.
- (41) Berglund, S. P.; Abdi, F. F.; Bogdanoff, P.; Chemseddine, A.; Friedrich, D.; van de Krol, R. *Chem. Mater.* **2016**, *28* (12), 4231–4242.
- (42) Sharma, G.; Zhao, Z.; Sarker, P.; Nail, B. A.; Wang, J.; Huda, M. N.; Osterloh, F. E. *J. Mater. Chem. A* **2016**, *4* (8), 2936–2942.
- (43) Read, C. G.; Park, Y.; Choi, K.-S. *J. Phys. Chem. Lett.* **2012**, *3* (14), 1872–1876.

- (44) Gu, J.; Wuttig, A.; Krizan, J. W.; Hu, Y.; Detweiler, Z. M.; Cava, R. J.; Bocarsly, A. B. *J. Phys. Chem. C* **2013**, *117* (24), 12415–12422.
- (45) Guijarro, N.; Prévot, M. S.; Sivula, K. *Phys. Chem. Chem. Phys.* **2015**, *17* (24), 15655–15674.
- (46) McDonald, M. B.; Ardo, S.; Lewis, N. S.; Freund, M. S. *ChemSusChem* **2014**, *7* (11), 3021–3027.
- (47) Vargas-Barbosa, N. M.; Geise, G. M.; Hickner, M. A.; Mallouk, T. E. *ChemSusChem* **2014**, *7* (11), 3017–3020.
- (48) Vermaas, D. A.; Sassenburg, M.; Smith, W. A. *J. Mater. Chem. A* **2015**, *3* (38), 19556–19562.

Chapter 3

Experimental methods

The experimental conditions used to produce the results presented in chapters 4 to 7 are gathered in this chapter. Rather than following a chronological order, the techniques used throughout the research work at hand are divided in three sections: synthetic methods, physical characterization methods, and photoelectrochemical methods for better clarity. For each method, a theoretical background is provided when appropriate, followed by experimental details.

Parts of this chapter have been adapted from the experimental sections of:

“Enhancing the Performance of a Robust Sol-Gel Processed p-Type Delafossite CuFeO₂ Photocathode for Solar Water Reduction” ¹ (Prévot, M.S; Guijarro, N.; Sivula, K., *ChemSusChem*, **2015**, 8, 1359-1367),

and “Improving Charge Collection with Delafossite Photocathodes: A Host-Guest CuAlO₂/CuFeO₂ approach” ² (Prévot, M.S.; Li, Y.; Guijarro, N.; Sivula, K., *J. Mater. Chem. A*, **2016**, 4, 3018-3026)

3.1 Synthetic methods

3.1.1 CuFeO₂ thin film preparation (Chapters 4 - 7)

In a typical experiment, Fe(NO₃)₃·9H₂O (0.808g, 2.00 mmol), Cu(NO₃)₂·3H₂O (0.482g, 2.00 mmol) and Citric acid (0.768g, 4.00 mmol) were mixed in 10 mL of ethanol and stirred overnight. Ethylene glycol (0.25 mL, 4.48 mmol) was then added to the mixture, which was further stirred for two hours.

The resulting solution was spin-coated, with a WS-650MZ-23NPP (Laurell) spin-coater onto clean Fluorine-doped tin oxide (FTO) substrates at 3000 rpm for 1 minute (Chapters 4 and 5) or 2000 rpm for 1 minute + 6000 rpm for 10 seconds (Chapters 6 and 7). Films were then dried on a hot plate at 100°C for 10 minutes before annealing in air at 450 °C in a Nabertherm LV5/11/B180 oven (ramp rate: 10°C min⁻¹) for 1h to remove all traces of organic material. Successive layers were then deposited on top of the first one following the same succession of steps. Finally, the film was annealed under argon flow (300 mL min⁻¹) at 700°C in an OTF-1200X oven (MTI corporation, ramp rate: 10°C min⁻¹) for 12h (Chapters 4 and 5) or 1h (Chapters 6 and 7).

To produce Mg-doped thin films, the composition of the precursor was modified by including Mg(NO₃)₂·6H₂O in the mixture and adjusting the Cu/Fe/Mg ratio at will. The deposition procedure was kept the same.

3.1.2 CuAlO₂ scaffold preparation (Chapter 5)

Al(NO₃)₃·9H₂O (1.500g, 4.00 mmol), Cu(NO₃)₂·3H₂O (0.964g, 4.00 mmol) and Citric acid (1.537g, 8.00 mmol) were mixed in 20 mL of ethanol. After stirring for 2 hours, Ethylene glycol (0.5 mL, 8.96 mmol) was added to the mixture, which was further stirred for 1 hour. The resulting solution was dried at 150 °C overnight. The resulting powder was grinded, and then annealed in air at 450 °C in a Nabertherm LV5/11/B180 oven (ramp rate: 10°C min⁻¹) for 5 h to remove all traces of organic material. The resulting powder was then annealed under argon flow (300 mL min⁻¹) at 1000 °C in an OTF-1200X oven (MTI corporation, ramp rate: 10°C min⁻¹) for 12 h. 200 mg of the resulting material was mixed with a 10% acetylacetone (acac) solution in isopropanol, and thoroughly grinded to break the aggregates. Then, 1 mL of a 1% acac solution in isopropanol was

added to the mixture and the resulting suspension was sonicated for 5 minutes. Finally, 1 mL of a 4% hydroxypropyl cellulose solution in isopropanol was added to the suspension, and the resulting paste was tape-casted onto FTO. The resulting films were heated at 700°C (ramp rate: 10°C min⁻¹) in Argon for 1 hour.

3.1.3 SiO₂ scaffold preparation (Chapter 5)

SiO₂ powder was prepared according to the following procedure. Cetyl trimethylammonium bromide (4.37 g, 12 mmol) was dissolved in 500 mL of deionized water. 15 mL of a 2 M NaOH solution was added and the resulting mixture was heated to 80°C. Tetraethyl orthosilicate (21.5 mL, 10 mmol) was added dropwise and the solution was stirred for three more hours. The resulting precipitate was filtered and dried in air. The powder was finally sintered at 500°C for 8 h to remove the surfactant. The obtained SiO₂ powder was casted on FTO using the same procedure than for the preparation of the CuAlO₂ scaffold.

3.1.4 Overlayer deposition (chapter 7)

On selected films Aluminum-doped ZnO and TiO₂ overlayers (15 nm/100nm) were deposited using a previously published procedure.³ A Pt co-catalyst was subsequently photodeposited using an Ar-purged aqueous solution of 1 mM H₂PtCl₆ and applying -0.4 V vs Ag/AgCl for 5 min under 1 sun illumination.

Amorphous gallium oxide overlayers were deposited through a sol-gel process. A solution of 0.15 M Gallium (III) isopropoxide and 0.15M ethanolamine in dry methoxyethanol was heated at 70°C for one hour. This precursor solution was then spin-coated on a CuFeO₂ thin film at 3000 rpm for 60 s. The deposition was repeated a second time to afford the final gallium precursor layer. The resulting thin-film was annealed at 300°C for 1 hour to form the final composite electrode. Pt nanoparticles were subsequently photoelectrodeposited from an Ar-purged aqueous solution of 1 mM H₂PtCl₆, by scanning the potential of the electrode between +0.4 V and 0 V vs Ag/AgCl under illumination.

3.2 Physical characterization methods

3.2.1 UV-Visible spectroscopy (Chapters 4 and 5)

a) Basic definitions

UV-visible (UV-Vis) spectroscopy is used to monitor change in light absorption or reflection caused by electronic transitions inside the material. The transmitted, absorbed and reflected light intensities (I_t , I_{abs} and I_r respectively) are related to the incident light intensity I_0 :

$$I_0 = I_t + I_{abs} + I_r \quad (3.1)$$

The transmittance T , absorbance A and reflectance R are defined as:

$$T = \frac{I_t}{I_0}; A = \frac{I_{abs}}{I_0}; R = \frac{I_r}{I_0} \quad (3.2)$$

The reflectance R can be further separated in two components – specular reflectance R_s and diffuse reflectance R_D – by using an integrating sphere (see Figure 3.1).

a) Absorption coefficient and bandgap determination

The absorption coefficient of a transparent material α is related to its thickness z by:

$$I_t = (I_0 - I_r) e^{-\alpha z} \Leftrightarrow \alpha = -\frac{1}{z} \times \ln\left(\frac{T}{1 - R}\right) \quad (3.3)$$

If the material is not transparent, the absorption coefficient is proportional to the Kubelka-Munk function $F(R_D)$ derived from the diffuse reflectance of the sample:

$$F(R_D) = \frac{(1 - R_D)^2}{2R_D} \quad (3.4)$$

UV-visible spectroscopy can be used to determine the bandgap of a semiconductor material with the Tauc relationship:

$$(\alpha h\nu)^{\frac{1}{n}} \propto (h\nu - E_g) \quad (3.5)$$

where h is the Planck's constant, ν is the frequency of the photon, α is the absorption coefficient, and n is a constant parameter linked to the nature of the bandgap transition.

$n = 1/2$ for direct allowed transition,
 $n = 3/2$ for direct forbidden transition,
 $n = 2$ for indirect allowed transition,
 $n = 3$ for indirect forbidden transition

The value of α can be extracted from Equation 3.3 or 3.4 depending on the transparency of the semiconductive sample. E_g is then determined by plotting $(\alpha h\nu)^{\frac{1}{n}}$ as a function of $h\nu$ in a so-called Tauc plot, and measuring the energy at which the linear part of the plot intercepts the x-axis.

a) Experimental setup and methods

UV-Visible spectrometry was performed with a UV-3600 (Shimadzu) Spectrometer, equipped with an integrating sphere. To determine the absorption of the different materials deposited on FTO-coated glass substrates, the following formulas, derived from Equations 3.1 and 3.2, were used:

$$A_{material} (\%) = 100 - T(\%) - R(\%) - A_{substrate}(\%) \quad (3.6)$$

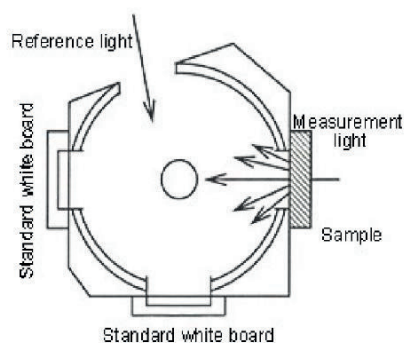
$$A_{substrate}(\%) = 100 - T_{substrate}(\%) - R_{substrate} \quad (3.7)$$

For each electrode, the total transmission T and the total reflectance R were measured, using an integrating sphere (see Figure 3.1). The absorption was then determined, using Equation 3.6 with the absorption of substrate being measured using Equation 3.7 on a blank substrate. Finally, the amount of light absorbed was calculated by integrating the product of the absorption spectrum by the AM 1.5 photon density between 300 and 900 nm.

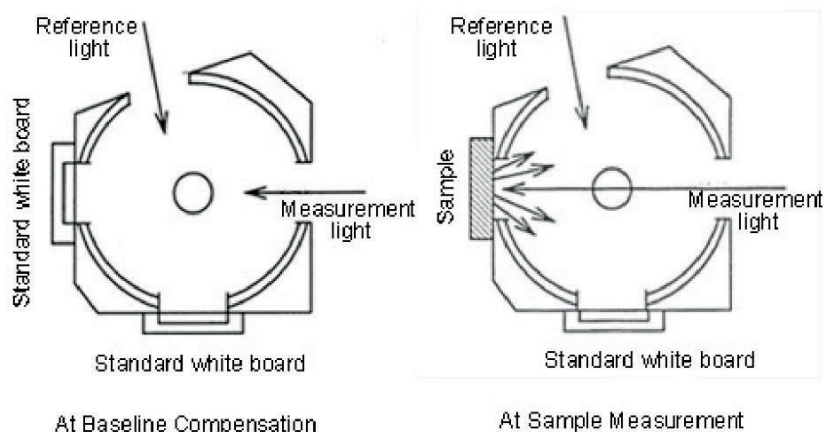
In chapter 4, the maximum photocurrent expected from the absorption spectrum of the photoelectrode has been calculated as follows. The absorptance was multiplied to the AM1.5G solar spectrum (in number of photons per second per m² per nm), available on the NREL website, to afford the number of photons absorbed per second at each wavelength, under AM 1.5 irradiation:

$$N_{photons}^{abs}(\lambda) = A * N_{photons}^{AM\ 1.5}(\lambda) \quad (3.8)$$

a) Transmittance measurement



b) Diffuse reflectance measurement



c) Total reflectance measurement

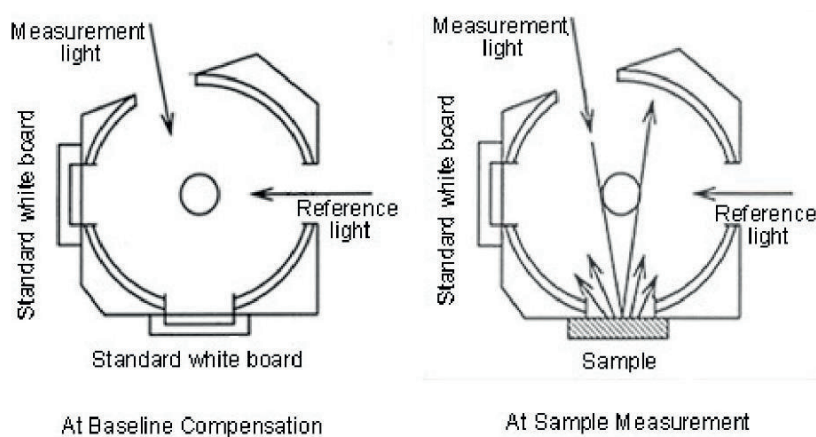


Figure 3.1 Integrating sphere configurations for the determination of the transmittance (a), diffuse reflectance (b) and total (diffuse + specular) reflectance (c) of a solid-state sample. Reproduced from the Shimadzu user manual.⁴

Assuming that each absorbed photon yields one electron, extracted from the electrode (100% internal conversion efficiency), the photocurrent density produced at each wavelength is given by:

$$j_{ph}(\lambda) = N_{photons}^{abs}(\lambda) * e \quad (3.9)$$

Therefore the total photocurrent that can potentially be produced by the material is given by:

$$j_{ph}^{tot} = \int_0^{\infty} j_{ph}(\lambda) d\lambda \quad (3.10)$$

In practice the photocurrent was integrated between 350 nm and 845 nm (the optical band gap of the material), which yielded 14.8 mA.cm⁻².

In chapter 5, the amount of CuFeO₂ in each composite electrode is estimated by measuring the absorbance of the film at 750 nm – proportional to the amount of CuFeO₂ according to the Beer-Lambert law (see Figure 5.11), using the formula:

$$\text{Absorbance} = -\log\left(\frac{I_t}{I_0 - I_r}\right) = -\log\left(\frac{T(\%)}{100 - R(\%)}\right) \propto \text{Amount of CuFeO}_2 \quad (3.11)$$

3.2.2 X-Ray diffraction measurements (Chapters 4 and 5)

a) Basic theory

X-Ray diffraction (XRD) is used to determine the crystal structure of a crystalline material. An incident beam of X-Rays is diffracted and reflected by the material of interest. The condition to observe constructive interferences in the diffracted beam is famously given by Bragg's law:

$$n\lambda = 2d \sin \theta \quad (3.12)$$

where λ is the wavelength of the incident beam, d is the distance between two crystallographic planes of the material, θ is the angle of incidence of the incident beam on the crystallographic plane, and n is an integer giving the order of the reflection. In other words, to get constructive interferences, the difference in optical path between two X-Ray beams has to be a multiple of the wavelength. A simple illustration of Bragg's law is provided in Figure 3.2a.

In practice, the wavelength of the X-Ray beam is kept constant, while the angle θ is varied. For each θ where the Bragg's law is verified, a peak is measured in the diffractogram, and a corresponding d can be determined.

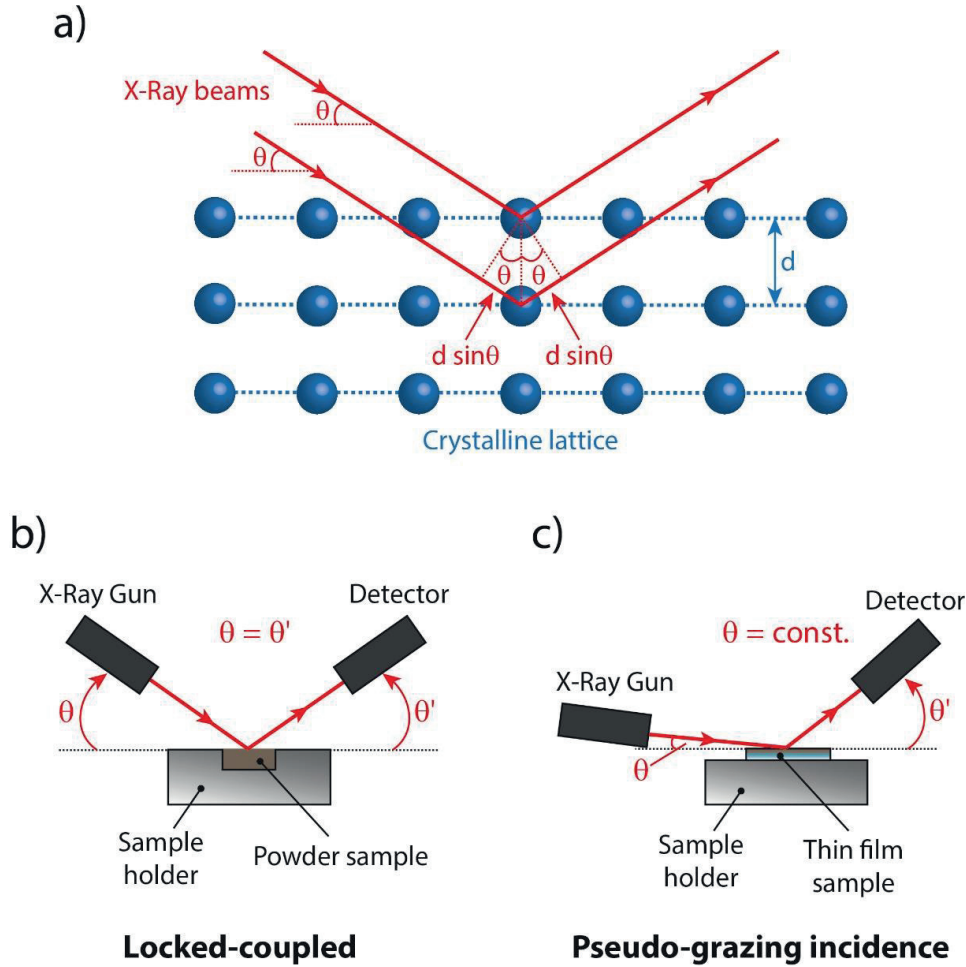


Figure 3.2 a) Illustration of the diffraction of X-Rays (red lines) by a crystalline lattice of ions (blue spheres). The difference in optical path between two beams reflected by two crystalline planes separated by a distance d is $2d \sin \theta$, and therefore constructive interferences between these two beams are obtained for $2d \sin \theta \propto \lambda$ (Bragg's law). b) Locked-couple configuration: the X-Ray gun and detectors have the same angle with respect to the surface of the sample at all time. c) Pseudo-grazing incidence configuration: the X-Ray gun forms a constant small angle with the surface of the sample, and only the detector is moving.

The entire set of peaks measured in the diffractogram can therefore be associated with the different crystalline planes of the material, and constitute an intrinsic signature of the crystal structure at hand. Each crystalline material therefore has a distinct diffractogram, which can be found in crystallographic databases. One can therefore identify the

crystalline structure of a sample by comparing its diffractogram with archived diffractograms from such databases. When several crystalline phases are present, the experimental diffractogram is the sum of the diffractograms of the different phases.

b) Experimental setup and methods

XRD was measured with a D8 Discovery (Bruker) diffractometer. For thin-film electrodes, the diffractometer was used in pseudo-grazing-incidence mode, while for powder samples it was used in the locked-coupled configuration. The difference between these two configurations is illustrated in Figure 3.2b and c, and can lead to differences in the final aspect of the diffractogram, as discussed in Chapter 4. For thin films, the pseudo-grazing incidence is preferred so that the signal of the thicker crystalline substrate (SnO₂) does not mask the signal of the material of interest.

3.2.3 Raman spectroscopy (Chapters 4 and 6)

Raman spectroscopy is a technique used to observe low-energy transitions, such as vibrational and rotational transitions. It relies on the inelastic scattering of a monochromatic laser: the laser interacts with the sample and its energy is shifted by vibrational or rotational modes inside the system. Commonly, Raman data is represented under the form of a spectrum as a function of the Raman shift Δw :

$$\Delta w = \frac{1}{\lambda_0} - \frac{1}{\lambda_1} \quad (3.13)$$

where λ_0 is the (excitation) wavelength of the incident light, and λ_1 is the wavelength monitored by the detector. When a mode is Raman active and shifts the incident wavelength from λ_0 to λ_1 , it translates into a peak in the Raman spectrum. If the range of scanned wavelengths (or wavenumbers) is large enough, a compound can be identified through its unique Raman spectrum (similar to XRD identification). Interestingly, Raman does not require the high degree of crystallinity needed in XRD, as it monitors short-range transitions (on the scale of chemical bonds). Moreover, the data presented in Chapters 4 and 6 were acquired using Raman microspectroscopy, which offers the added advantages of microscopy. The incident laser is focused on a micrometric volume, from which a Raman spectrum can be collected. This allows identifying materials on a small scale, and is very useful to test the final phase purity and homogeneity of a processed material.

Raman spectra presented in this manuscript were obtained with a LabRam spectrometer (Jobin Yvon Horiba). Excitation line was provided by an Ar laser (532.19 nm).

3.2.4 Optical microscopy & Scanning electron microscopy (Chapters 4 to 6)

a) Basic theory

Optical microscopy is an imagery technique using visible light and lenses to magnify images of microscopic samples. It can be used in reflective or transmittance mode (depending whether the incident and transmitted lights are emitted and collected on the same side of the sample). Moreover, its resolution d is limited by the range of wavelengths λ used to image the sample ($\sim 400 - 800$ nm for visible light) and the aperture of the microscope objective A following the formula:

$$d = \frac{\lambda}{2A} \quad (3.14)$$

Therefore, an optical microscope can only provide clear images of objects bigger than roughly 200 nm.

Scanning electron microscopy (SEM) is based on similar concepts of imaging an object through wave-matter interactions. However, instead of visible-light photons, electrons are beamed at the sample and collected after interaction. The De Broglie equation gives the wavelength λ_e of a (massive) electron for a given momentum p :

$$\lambda_e = \frac{h}{p} \quad (3.15)$$

Because electrons can be accelerated to high speeds in vacuum, they can reach wavelengths much lower than the ones of visible-light photons. This way, SEM can reach resolutions as low as a few nanometers, and can therefore be used to image nanoscopic objects. An important requirement to use SEM is that the sample is conductive enough to evacuate the electrons it receives from the beam. The semiconductors studied in the following chapters meet this requirement at low beam intensity. Therefore, optical microscopy and SEM can be used to visualize the morphology of semiconductor samples at different length scales (macroscopic to nanometric).

b) Experimental setup and methods

Optical microscopic images were obtained with a Nikon H550L. Micrographs were acquired in transmission mode, with the light shining under the sample (with respect to the objective). Scanning electron microscopy was performed with a Zeiss Merlin microscope equipped with a beam booster and an in-lens secondary electron detector.

3.2.5 Energy dispersive X-Ray spectroscopy (Chapter 7)

Energy dispersive X-Ray spectroscopy (EDX) is an analytical technique used for elemental analysis. It relies on the excitation of a sample with a beam of electrons, and the subsequent detection of its X-Ray emission spectrum. Indeed, once an element is excited by incoming energetic electrons, it can decay back to its ground state by emitting a spectrum of X-Rays with energies characteristic of its atomic structure. These emissions typically correspond to the K and L electronic transitions.

One can therefore collect the EDX spectrum of sample and detect the elements associated with the peaks present in it. Moreover, this technique is quantitative and can be used to measure the elemental composition of the sample by providing the respective amounts of each element. Finally, since the beam of electron is usually provided by the gun of an electron microscope, one can obtain an elemental mapping of the sample by simply scanning the sample with the electron beam.

EDX experiments were performed in a XLF-30 electron microscope equipped with a EDAX Si(Li) EDX detector with ultra-thin window for light element analysis.

3.2.6 Thermogravimetric analysis (Chapter 4)

Thermogravimetric analysis (TGA) is a technique used to monitor changes in physical and/or chemical properties of a material through associated variations in mass. Typically, a powder sample is deposited on top of microbalance and subjected to a temperature ramp: processes like gas desorption, phase transition, oxidation/reduction, etc. can then be detected as a function of the temperature. Another possibility is to monitor the variation in mass over time at a set temperature, giving information on the kinetics of a specific process. TGA can also be performed in air or under inert atmosphere. In the experiments presented here, TGA was performed with a Pyris 6 TGA (Perkin Elmer).

3.2.7 Time-resolved microwave conductivity measurement (Chapter 6)

a) Basic theory

Time-resolved microwave conductivity (TRMC) is a pump-probe spectroscopy technique. A semiconductor sample is excited by a light with an energy higher than its bandgap (the pump). This results in the creation of free charges inside the material, which modifies its conductivity. This change in conductivity translates into a change in absorption in the microwave range (the probe). A simplified illustration of the setup is shown in Figure 3.3.

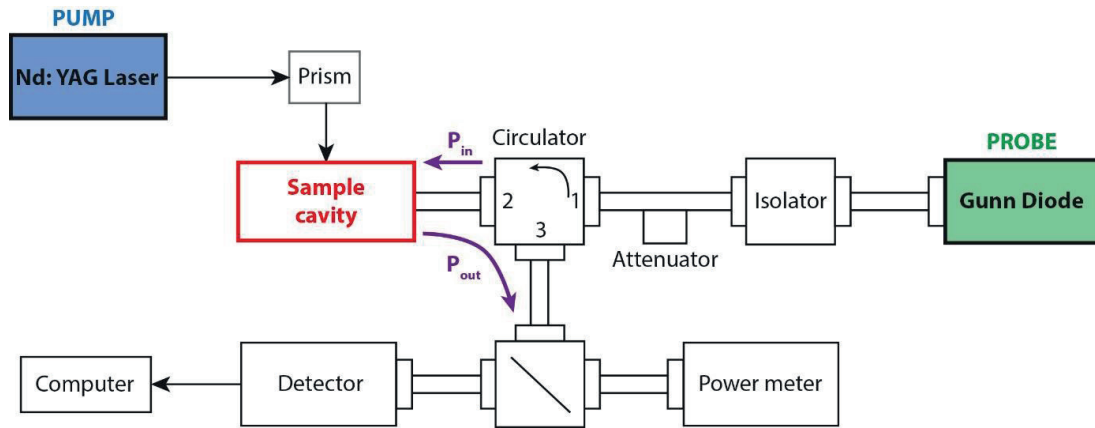


Figure 3.3 Simplified sketch of a TRMC setup. The Nd:Yag Laser provides the high-energy light to excite the sample (pump). The subsequent change in the reflective power of the sample is monitored with a microwave light provided by a Gunn diode (probe). P_{in} represents the power of the incident microwave signal, while P_{out} represents the power of the reflected light. A power meter and a detector are used to create the TRMC spectrum. Adpated from Killedar *et al.*⁵

When free charges couple to the electric field of microwaves, absorption occurs. This can be measured by monitoring the change in reflective power of the sample ΔP over time, which is directly proportional to the change in conductance ΔG of the sample:

$$\frac{\Delta P(t)}{P} = -K * \Delta G(t) \quad \text{and} \quad \Delta G(t) = \beta \int_0^L \Delta \sigma(z) dz \quad (3.16)$$

where P is the reflective power of the sample in the dark, K is the sensitivity factor of the cavity, β is a geometric constant linked to the dimensions of the waveguide, L is the absorption depth of the sample, z is the depth inside the sample and $\Delta \sigma$ is the variation in conductivity.

The change in conductivity $\Delta\sigma$ can be further linked to the concentration of free negative and positive charge carriers produced under illumination (Δn_n and Δn_p) and their mobilities (μ_n and μ_p):

$$\Delta\sigma = e(\Delta n_n \mu_n + \Delta n_p \mu_p) = e\Delta n \Sigma\mu \quad (3.17)$$

where $\Sigma\mu$ is the sum of mobilities of photogenerated carriers and $\Delta n = \Delta n_n = \Delta n_p$ since each electron promoted to the conduction band upon light absorption leaves a hole in the valence band. Considering that charges are created upon absorption of a light – with an incident flux I_0 – with a quantum yield Φ over a surface area A_{film} , then:

$$\int_0^L \Delta n(z) dz = \Phi I_0 A_{film} \quad (3.18)$$

Overall, the change in reflective power is tied to the sum of the mobilities of photogenerated free carriers inside the semiconductor:

$$\frac{\Delta P(t)}{P} = -K\beta e I_0 A_{film} \Phi \Sigma\mu \quad (3.19)$$

Since TRMC does not differentiate between the mobilities of the two types of charge carriers inside the semiconductor, one needs to know the relative effective masses of majority and minority carriers (m_v and m_c for holes and electrons respectively) inside the semiconductor in order to calculate the values of mobilities. Indeed, the ratio of mobilities is equal to the ratio of effective masses:

$$\frac{\mu_e}{\mu_h} = \frac{m_v}{m_c} \quad (3.20)$$

Therefore using $\Sigma\mu$ estimated from the TRMC data and Equation 3.19, and the relationship described in equation 3.20, one can determine the hole and electron mobilities inside the measured semiconductor. Finally, the diffusivity D_i ($i = n, p$) of each type of charge carrier is derived from the Einstein relationship:

$$D_i = \mu_i \times \frac{k_b T}{e} \quad (3.21)$$

Finally, measuring the decay of the TRMC signal over time yields an estimation of the lifetime of photogenerated charge carriers τ , which can be used to calculate diffusion length L_i ($i = n, p$) of charge carriers:

$$L_i = \sqrt{D_i \tau} \quad (3.22)$$

b) Experimental setup and methods

CuFeO₂ thin films prepared on fused quartz substrates were mounted in a microwave cavity cell and placed within a setup similar to the one described elsewhere.^{6,7} X-band (8.4-8.7 GHz) microwaves were generated using a Gunn diode. Experiments were carried out at 8.55 GHz, which was found to be the resonant frequency of the sample-loaded cavity. The sensitivity factor (K) of the sample-loaded cavity was calculated from the resonant characteristic using a sample dielectric constant value of 20, as reported elsewhere for CuFeO₂.^{8,9} During the TRMC measurements, the samples were excited by 6 ns FWHM pulses of a frequency-doubled Q-switched Nd:YAG laser at a wavelength of 355 nm (10 Hz repetition rate). The change in the microwave power reflected by the cavity upon excitation was monitored and correlated to the photoinduced change in conductance and the carrier mobility. The laser pulse intensities were adjusted using neutral density filters and varied from 3.3×10^{11} to 1.6×10^{14} photons pulse⁻¹ cm⁻².

For the determination of mobilities, diffusivities and diffusion lengths, a ratio of effective masses of $\frac{m_h^*}{m_e^*} = 0.8$ was used, a conservative estimation based on values reported for other cuprous delafossites^{10,11} and thickness studies presented in Chapter 4, section 4.3.3. This yielded $\mu_e \sim 0.1 \text{ cm}^2 \text{ V}^{-1} \text{ s}^{-1}$.

3.2.8 Atomic and Kelvin probe force microscopy (Chapter 6)

a) Basic theory

Atomic force microscopy (AFM) is a high-resolution imaging technique that relies on the atomic force that arise from the interaction of the surface of a sample and a sharp tip connected to a cantilever. The movement of the tip repulsed by the surface is measured by monitoring a laser reflected on its back. As opposed to optical microscopy and SEM, no wave-matter interaction is involved. AFM is used to probe the surface morphology of (conducting or insulating) samples and its resolution can be as low as a few nanometers.

Kelvin probe force microscopy (KPFM) is performed using the same experimental setup, and using a conductive metallic tip (typically made of platinum), electrically connected to the sample. With this technique, the surface chemical potential (i.e. its surface Fermi level) of a semiconductor can be measured. More precisely, when a

conductive AFM tip is brought close to the surface of the sample, an electrical force is generated between them due to the difference in energy between the Fermi level of the semiconductor ϕ_s and the workfunction of the metallic tip ϕ_t . Electrons therefore flow between the tip and the sample until $\phi_s = \phi_t$. After equilibration through electrical contact, the tip and the surface of the sample are therefore charged and a contact potential difference V_{CPD} is created:

$$V_{CPD} = \frac{\phi_t - \phi_s}{-q} \quad (3.23)$$

One can then apply an external bias (V_{DC}) between the tip and the sample to nullify the electric force due to V_{CPD} . In this situation, $V_{DC} = V_{CPD}$, so that V_{CPD} is known, and therefore one can measure ϕ_{SC} if ϕ_{tip} is known, according to equation 3.23. A simplified illustration of the energetics of the KPFM technique is shown in Figure 3.4. This technique can then be used to map the surface Fermi level of a semiconducting sample.

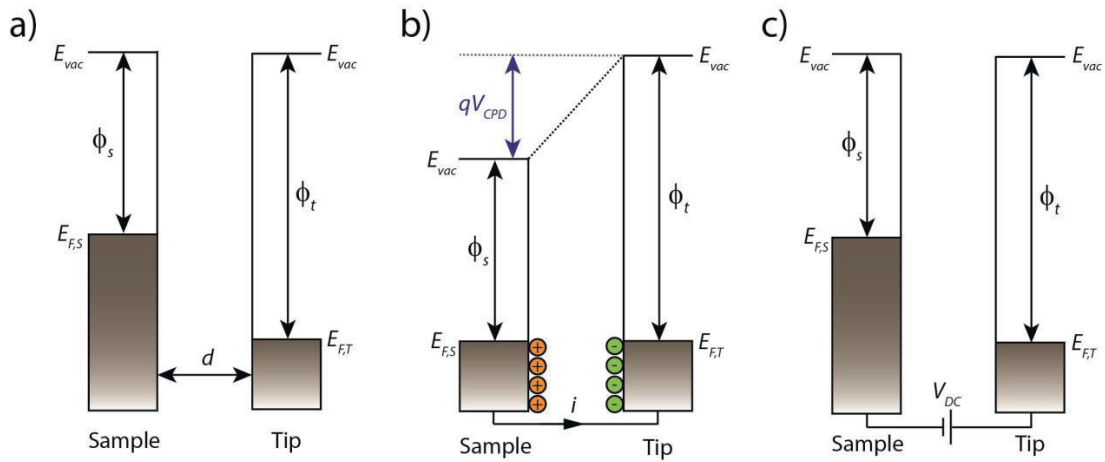


Figure 3.4 Electronic diagram of a sample and a conductive AFM tip in different situations: a) sample and tip separated by a distance d without electrical contact, b) sample and tip in electrical contact, resulting in V_{CPD} , c) sample and tip are in electrical contact and an external bias equal to V_{CPD} is applied to neutralize the electric field between the tip and the sample. E_{vac} is the vacuum energy, while E_{FS} and E_{FT} are the Fermi levels at the surface of the sample and the tip respectively. Adapted from Melitz *et al.*¹²

b) Experimental setup and methods

KPFM measurements were performed with a Cypher AFM (Asylum Research) using Pt:Ir-coated tips (AC240TM, Olympus).

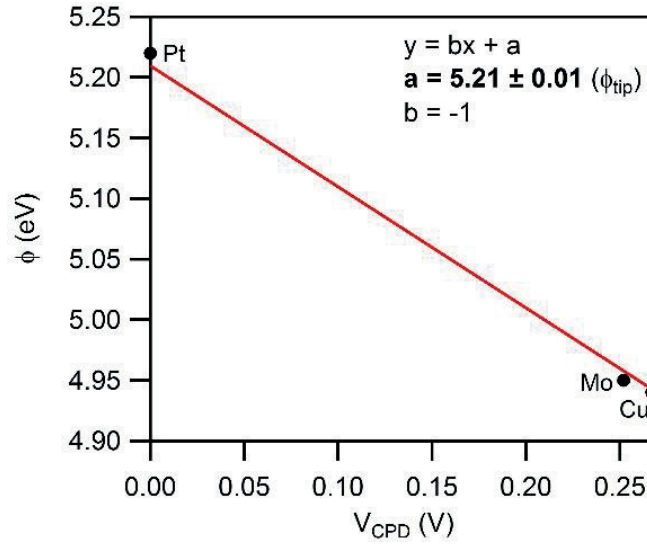


Figure 3.5 Calibration curve obtained for the conductive tip of the KPFM setup. The metals used for the calibration are indicated on the graph. The work function of the tip was taken as the intercept of the line with the y-axis.

The work function of the tip was calibrated using reference samples of Pt, Mo and Cu (see Figure 3.5). The surface morphology of the CuFeO_2 electrode and ϕ_{SC} were monitored on a $5 \mu\text{m} \times 5 \mu\text{m}$ surface area in the dark, and the change in ϕ_{SC} under illumination was measured over the same area, using a white light light-emitting diode positioned inside the chamber of the AFM.

3.2.9 X-Ray photoelectron spectroscopy (Chapter 6)

X-Ray photoelectron spectroscopy (XPS) is a quantitative surface spectroscopy technique consisting in shining a monochromatic X-Ray wave (typically produce by the K_α transition of Aluminium) of energy $E_{incident}$ on a sample – which will excite the core electrons of the surface atoms of the sample material and subsequently ionize these atoms – and monitoring the kinetic energy of the ejected electrons $E_{kinetic}$. Using this energy and the energy of the incident X-Ray beam, one can determine the binding energy of the electrons:

$$E_{binding} = E_{incident} - (E_{kinetic} + \phi) \quad (3.24)$$

where ϕ is a known offset coming from the absorption of the electron by the detector. A XPS spectrum will therefore show the electron counts as a function of their binding

energy, displaying peaks for $E_{binding}$ values characteristic of the atoms present in the sample and of their immediate environment. Another type of electrons detected by XPS corresponds to electrons emitted by Auger recombination: one electron excited upon X-Ray absorption will subsequently decay back to its ground state and transmit its energy to a more external electron that will be ejected from its orbital. In this case, the kinetic energy of the emitted electron does not depend on $E_{incident}$ but only on the energy of the orbital from where it is emitted (as opposed to the situation depicted by Equation 3.24).

The peaks observed in a XPS spectrum are characteristic of the examined material: binding energies and Auger transitions general locations can generally be associated with a precise element of the periodic table, while small changes in shape and/or position of the peaks can be linked to the chemical environment of this element inside the sample (*e.g.* oxidation state). Furthermore, if several elements are present in the material, their relative abundance can be measured by integration of their XPS signal, allowing determining an empirical chemical formula for the sample. Finally, it is possible to etch progressively the surface of the sample with a beam of Ar⁺ ions between XPS spectra acquisitions to get a cross-sectional profile of the elemental and chemical composition of the material.

In this study, XPS measurements were carried out using a PHI VersaProbe II scanning XPS microprobe (Physical Instruments AG, Germany). Analysis was performed using a monochromatic Al K α X-ray source of 24.8 W power with a beam diameter of 100 μ m. The spherical capacitor analyzer was set at 45° take-off angle with respect to the sample surface. The pass energy was 46.95 eV yielding a full width at half maximum of 0.91 eV for the Ag 3d 5/2 peak. For the depth profile analysis, the material was etched with a beam of Ar⁺. Curve fitting was performed using the PHI Multipak software.

3.3 Photoelectrochemical characterization methods

Photoelectrochemical (PEC) experiments refer to the measurements performed on the photoelectrode under operating conditions: the photoelectrode is probed using a three-electrode setup: typically the working electrode WE (*i.e.* the photoelectrode), the reference electrode (Ref) and the counter electrode CE are placed inside a “cappuccino cell” filled with the desired electrolyte (see Figure 3.6a) and connected to a potentiostat.

This way, the working electrode can be biased with respect to the reference electrode – which possesses a fixed potential – and the resulting current is measured between the working electrode and the counter electrode. Additionally, the working electrode can be illuminated by a solar simulator (built from a Xe arc lamp) either through a quartz window and the electrolyte (front illumination) or through the transparent substrate (back illumination) with a surface area of 0.238 cm² in contact with the electrolyte.

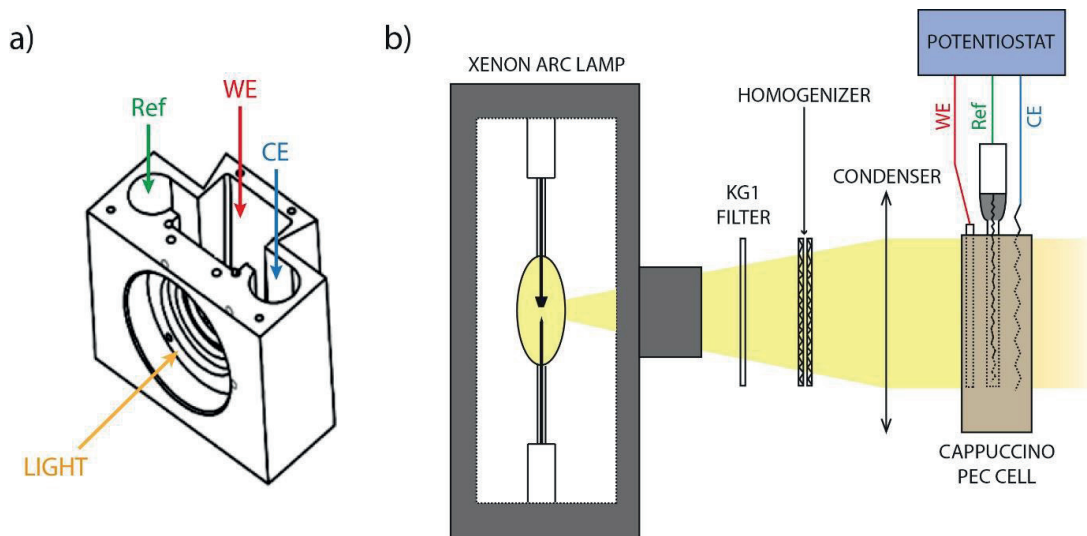


Figure 3.6 a) “Cappuccino” PEC cell design. The arrows indicate the positioning of the different electrodes and the path of the light through a quartz window. b) PEC setup used in this study: a solar simulator – made of a Xenon arc lamp and appropriate optics – produces the light illuminating the PEC cell connected to a potentiostat.

The PEC setup used for the research work presented in the following chapters is illustrated in Figure 3.6b. The counter electrode is typically a platinum wire, while the reference electrode is chosen as Ag/AgCl/KCl(sat.) for PEC experiments with aqueous electrolytes and as Ag⁺/Ag in acetonitrile. Moreover, when water splitting is studied in aqueous electrolytes, the potentials associated with water oxidation and water reduction undergo a Nernstian shift with the pH. Therefore, the PEC data are usually reported with respect to the Reversible Hydrogen Electrode (RHE), with a potential of:

$$E_{RHE}[V] = E_{Ag/AgCl}[V] - 0.21 - 0.059 \times \text{pH} \quad (3.25)$$

Therefore, the potential can be referenced to the RHE using the following relationship:

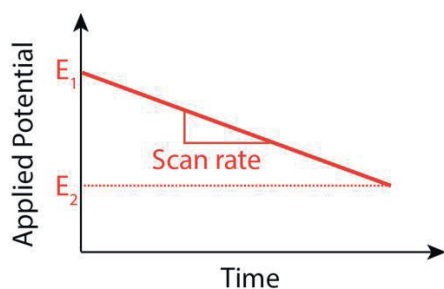
$$E [V \text{ vs RHE}] = E[V \text{ vs Ag/AgCl}] + 0.21 + 0.059 \times \text{pH} \quad (3.26)$$

On this scale, $E(\text{O}_2/\text{H}_2\text{O}) = 1.23 \text{ V vs RHE}$ and $E(\text{H}^+/\text{H}_2) = 0.00 \text{ V vs RHE}$ regardless of the pH. The different types of PEC measurements used in this manuscript are described in the following subsections. All of them were performed with a BioLogic SP-500 potentiostat.

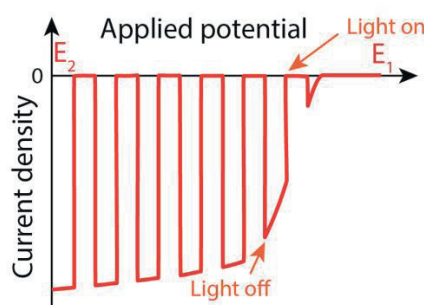
3.3.1 Voltammetry and chronoamperometry (Chapters 4 to 7)

Voltammetry refers to an electroanalytical method where the potential of the working electrode is varied over time, and the resulting change in electrical current flowing through the electrode is monitored. Two types of voltammetry are used in this manuscript: the linear sweep voltammetry (LSV) and the cyclic voltammetry (CV).

a) Linear Sweep Voltammetry

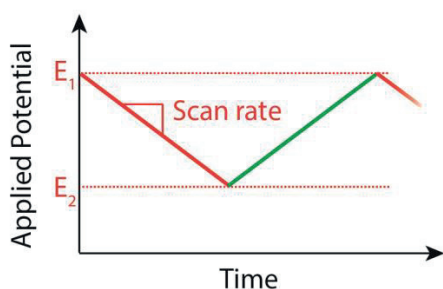


Input signal

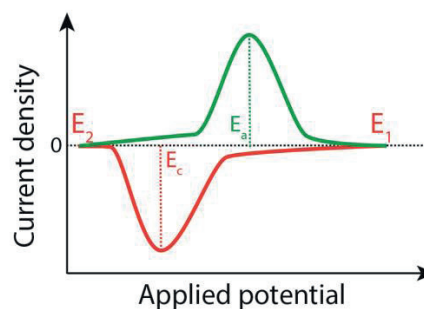


Typical output signal

b) Cyclic Voltammetry



Input signal



Typical output signal

Figure 3.7 a) Input signal and typical output signal of a LSV experiment conducted on a photocathode. The output current is modulated by chopped illumination of the electrode, as indicated by the orange arrows. b) Input signal and typical output signal of a CV experiment. The output curve corresponds to what is observed for a reversible redox couple with a peak reduction potential E_c and a peak oxidation potential E_a (only one cycle is represented). The value $E_{1/2} = (E_c + E_a)/2$ gives an estimation of the standard redox potential of the electrolyte.

In a LSV, the potential of the working electrode is swept linearly between two potential values (referenced to the reference electrode), yielding a current-potential curve of the electrode. Moreover, the change in current brought by illumination – the photocurrent J_{ph} – can be monitored by providing an intermittent illumination of the sample while the voltage is swept. An illustration of the procedure and of a typical output curve is shown in Figure 3.7a.

The CV is essentially a series of LSV carried out sequentially: the voltage is now swept linearly between two values but once the second voltage is reached, the voltage of the working electrode is swept in the opposite direction towards its initial value. This procedure is cycled several times, and is typically used to monitor the reversibility and thermodynamic potential of redox processes or the stability of a material towards electrochemical cycling. An illustration of the CV method and a resulting curve is shown in Figure 3.7b.

Chronoamperometry refers to a technique where the potential of the working electrode is held constant and the electrical current is monitored over time. This technique is used to test the stability of the photoelectrode under operating conditions – by measuring the stability of the output photocurrent over time – or to measure the Faradaic efficiency of the PEC process (see section 3.3.7).

3.3.2 Incident photon-to-electron conversion efficiency (Chapters 4 and 5)

The incident photon-to-electron conversion efficiency (IPCE) is a measure of the quantum efficiency of light-to-current conversion for a photoactive material at a given wavelength. In the case of a photoelectrode it is given by:

$$IPCE(\lambda) = \frac{N_e(\lambda)}{N_{hv}(\lambda)} = \frac{J_{ph}(\lambda) [A.m^{-2}] \times hv [J]}{I_\lambda(\lambda) [W.m^{-2}] \times e [C]} \quad (3.27)$$

where $N_e(\lambda)$ and $N_{hv}(\lambda)$ are the number of generated electrons and the number of incident photons respectively, and $I_\lambda(\lambda)$ is the incident light flux of wavelength λ . Plotting the IPCE as a function of the wavelength informs on the ability of the photoelectrode to convert sunlight into free charges as a function of the incident-light energy. To perform the IPCE measurement, the photocurrent produced by the photoelectrode was monitored in a three-electrode PEC setup under monochromatic light illumination provided by a 75

W Xe Tunable PowerArc Illuminator (Optical Building Blocks). The wavelength of the incident light was varied by increments of 5 nm between 900 and 300 nm.

3.3.3 Lamp calibration

The shape of the lamp spectrum was recorded using an OceanOptics USB2000+XR1 ES spectrometer with a Spectralon cosine corrector, which provided a relative measure of the number of photons created by the lamp at each wavelength. This spectrum was adjusted for the AM 1.5 spectrum, so that, when integrated between 300 nm and 850 nm, both spectra gave the same number of photons, as shown in Figure 3.8a. The calibrated spectrum corresponds to the spectrum of the Xenon arc lamp providing as many photons as the AM 1.5 spectrum between 300 nm and 850 nm.

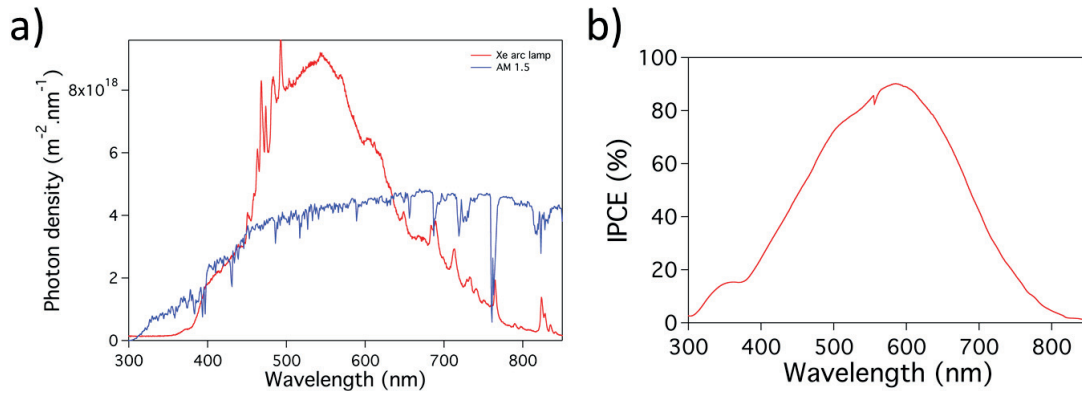


Figure 3.8 a) Xe arc lamp emission spectrum (red line) calibrated with the solar AM 1.5 spectrum (blue line) for the number of incident photons between 300 nm and 850 nm. b) IPCE of the silicon photodiode as a function of the incident wavelength.

On the other hand, the IPCE spectrum of a Silicon photodiode was recorded (Figure 3.8b). The IPCE was multiplied by the previously calibrated lamp spectrum, to afford the expected photocurrent produced by the diode under illumination by the calibrated Xe arc lamp, using the formula:

$$j_{ph}^{tot} = \int_{300}^{850} [IPCE(\lambda) * N_{photons}^{AM\ 1.5}(\lambda) * e] d\lambda \quad (3.28)$$

Finally, the samples were placed at the position where the photodiode provided the previously calculated photocurrent.

3.3.4 Electrochemical impedance spectroscopy (Chapters 4 to 6)

Electrochemical impedance spectroscopy (EIS) is a method that consists in probing the response of an electrode to a sinusoidal modulation of its potential at different frequencies. Typically, the electrode is biased with a constant *dc* voltage, to which is added a small *ac* perturbation of frequency ω :

$$\hat{E}(t) = E_0 + E_1 e^{j\omega t} \quad (3.29)$$

If E_1 is small (< 10 mV), the response of the electrode to this perturbation can be considered linear as it induces a sinusoidal current of same frequency and with a potential phase shift ϕ :

$$\hat{I}(t) = I_0 + I_1(\omega) e^{j(\omega t - \phi(\omega))} \quad (3.30)$$

The electrochemical impedance of the system is then defined as:

$$\hat{Z}(\omega) = \frac{E_1 e^{j\omega t}}{I_1(\omega) e^{j(\omega t - \phi(\omega))}} = \frac{E_1}{I_1}(\omega) e^{j\phi(\omega)} = |\hat{Z}(\omega)| e^{j\phi(\omega)} \quad (3.31)$$

It can also be expressed as a function of its real and imaginary parts (Z' and Z'' respectively):

$$\hat{Z}(\omega) = Z'(\omega) + j Z''(\omega) \quad \text{with} \quad \begin{cases} Z'(\omega) = |\hat{Z}(\omega)| \cos[\phi(\omega)] \\ Z''(\omega) = |\hat{Z}(\omega)| \sin[\phi(\omega)] \end{cases} \quad (3.32)$$

There are two complementary ways to visualize the impedance behavior of a system: the Bode plot representing $|\hat{Z}(\omega)|$ and $\phi(\omega)$ as a function of $\log \omega$, and the Nyquist plot representing $Z''(\omega)$ vs $Z'(\omega)$. For an electrical circuit, the shape of these plots is characteristic of the electrical arrangement of the components of this circuit (resistor, capacitor, inductance), as shown in Figure 3.9.

In an EIS experiment, the Bode and Nyquist plots of an electrode are collected for a given E_0 and a 50 mHz – 1 MHz frequency range, using a three-electrode setup and a BioLogic SP-500 potentiostat. These plots are then fitted using an equivalent electrical circuit, which components are associated to charge transfer processes occurring inside the electrode under operation. For instance, the double layer at the SCLJ can be modeled by a capacitance (associated with the depletion and Helmholtz layers of opposite charge) in parallel with a resistance (associated with the charge transfer across the SCLJ). Once

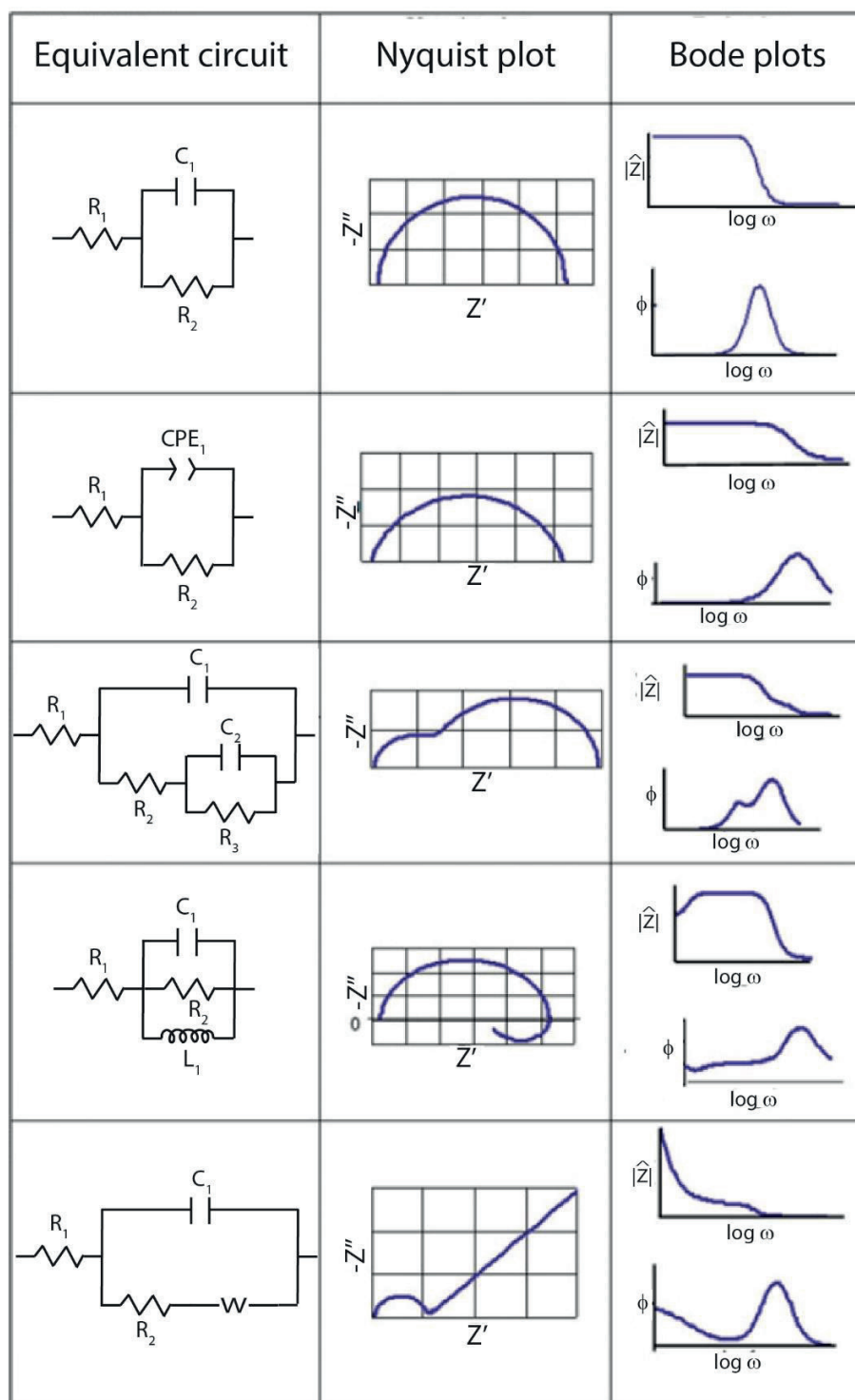


Figure 3.9 Equivalent circuits commonly used in EIS and typical shapes of the associated Nyquist and Bode plots. The charge carrier pathway inside the electrode is modeled using electrical components: resistors (R), capacitors (C), constant phase elements (CPE), inductance (L) or Warburg element (W, for diffusion processes). Adapted from Cesiulis *et al.*¹³

the EIS data of the electrode is correctly fitted with an equivalent circuit, one can therefore quantify the different processes occurring on different timescales (*i.e.* different ω) inside the electrode. In particular, this technique can be used to measure the capacitance of the depletion layer inside a semiconductor electrode at different E_0 and to produce a Mott-Schottky plot of this electrode (see Equation 2.32). This plot can then be used to extract the majority carrier density and the flat-band potential of the semiconductor.

3.3.5 Electrolyte preparation (Chapter 6)

Materials: Potassium ferricyanide (III) (99+%, Sigma-Aldrich), Potassium hexacyanoferrate (II) hydrate (99+%, Sigma-Aldrich), Tris(2-4-pentanedionato)-ruthenium (III) (TCI), Hexaamineruthenium (III) chloride (98%, Sigma-Aldrich), Hexaamineruthenium (II) chloride (99,9%, abcr), Methyl Viologen hydrate (98%, Acros), Ferrocene (98%, Acros), Chloranil (98%, TCI), Bis(pentamethylcyclopentadienyl)Iron (99%, abcr), Potassium phosphate monobasic (99+%, Acros), Potassium phosphate dibasic trihydrate (99+%, Acros), Sodium tetraborate decahydrate (99,5%, Sigma-Aldrich), Tetrafluoroboric acid (48 wt% in H₂O, Sigma-Aldrich), and *p*-benzoquinone (98+%, Alfa Aesar) were all purchased from their respective suppliers. Aqueous redox electrolytes were prepared by dissolving the corresponding oxidant and reductant salts in equal quantities, in the desired buffer. The buffer solutions were prepared according to the following recipes in 100 mL of deionized water:

- pH 4: 38.6 mL of 0.2 M K₂HPO₄ + 61.4 mL of citric acid;
- pH 5: 51.4 mL of 0.2 M K₂HPO₄ + 48.6 mL of citric acid;
- pH 6: 87.7 mL of 0.2 M KH₂PO₄ + 12.3 mL of 0.2 M K₂HPO₄;
- pH 7: 39 mL of 0.2 M KH₂PO₄ + 61 mL of 0.2 M K₂HPO₄;
- pH 8: 5.3 mL of 0.2 M KH₂PO₄ + 94.7 mL of 0.2 M K₂HPO₄;
- pH 9: 50 mL of 0.025 M borax + 5 mL of 0.1 M HCl, completed to 100 mL with water,
- pH 10: 50 mL of 0.025 M borax + 18 mL of 0.1 M NaOH, completed to 100 mL with water;
- pH 11: 25 mL of 0.1 M K₂HPO₄ adjusted with 0.1 M NaOH;
- pH 12: 0.01 M NaOH in 0.1M Na₂SO₄.

After the preparation, the pH was measured using a pH-meter. The organic electrolytes were prepared by dissolving the desired equal quantities of salts in 0.1 M tetrabutylammonium perchlorate in acetonitrile.

FeCp_2^+ and $\text{Fe}(\text{C}_5\text{Me}_5)_2^+$ were prepared by oxidation of FeCp_2 and $\text{Fe}(\text{C}_5\text{Me}_5)_2$ using hexafluoroboric acid and p-benzoquinone, following a previously reported procedure¹⁴. All the oxidation states unavailable for direct purchase were produced in situ by reduction/oxidation of the corresponding species in deaerated solutions. The process was stopped when the potential of the electrolyte, measured at a Pt wire was equal to $E_{1/2}$.

3.3.6 Gartner model for the estimation of photocurrent (Chapter 6)

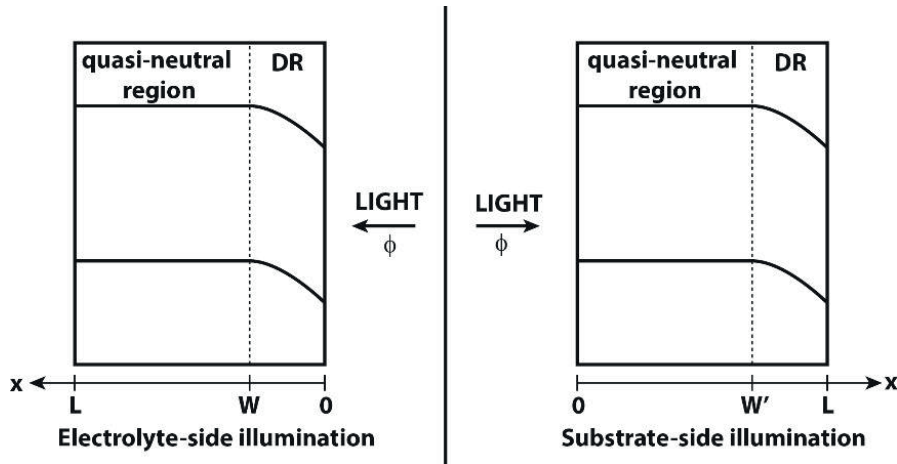


Figure 3.10 Parametrization of the system for Electrolyte-side and Substrate-side illuminations (left-hand side and right-hand side respectively).

This model has been proposed by Gartner¹⁵ and refined by others.^{16–18} It consists in calculating the total photocurrent as the sum of the photocurrent generated in the depleted region (DR) J_{ph}^{DR} and the photocurrent provided by diffusion in the quasi-neutral region J_{ph}^{diff} :

$$J_{ph}^{tot} = J_{ph}^{DR} + J_{ph}^{diff} \quad (3.33)$$

The first term is equal to:

$$J_{ph}^{DR} = q\Phi (1 - e^{-\alpha W}) \quad (3.34) \quad \text{for electrolyte-side illumination}$$

$$J_{ph}^{DR} = q\Phi (e^{-\alpha W'} - e^{-\alpha L}) \quad (3.35) \quad \text{for substrate-side illumination}$$

Where q is the elementary charge, Φ is the photon flux in the incoming light, α is the absorption coefficient of the semiconductor, W or $L - W'$ is the depletion width

(depending on the illumination side, see Figure 3.10), L is the thickness of semiconductor (taken as 200 nm).

The second term is obtained by solving the diffusion equation in the quasi-neutral region:

$$\frac{d^2 \Delta n}{dx^2} - \frac{\Delta n}{L_n^2} + \frac{\alpha \Phi}{D_n} e^{-\alpha x} = 0 \quad (3.36)$$

Δn is the density of photogenerated electrons, L_n is the diffusion length of electrons (taken as 300nm), D_n is the diffusion coefficient (taken as $10^{-7} \text{ m}^2 \cdot \text{s}^{-1}$).

This yields:

$$\Delta n(x) = C_1 e^{\frac{x}{L_n}} + C_2 e^{-\frac{x}{L_n}} + \frac{\alpha \Phi L_n^2}{D_n(1 - \alpha^2 L_n^2)} e^{-\alpha x} \quad (3.37)$$

And finally:

$$J_{ph}^{diff} = -q D_n \left. \frac{d\Delta n}{dx} \right|_{x=W \text{ (or } x=W')} \quad (3.38)$$

With the boundary conditions:

$$\begin{cases} \Delta n(W) = n_0 \exp\left(\frac{qV_{ph}}{k_B T}\right) \\ \frac{d\Delta n}{dx}(L) = 0 \end{cases} \quad (3.39) \quad \text{for electrolyte-side illumination}$$

$$\begin{cases} \Delta n(W') = n_0 \exp\left(\frac{qV_{ph}}{k_B T}\right) \\ \frac{d\Delta n}{dx}(0) = 0 \end{cases} \quad (3.40) \quad \text{for substrate-side illumination}$$

3.3.7 Gas chromatography and Faradaic efficiency measurement (Chapter 7)

Gas chromatography (GC) was used to analyze the composition of the gas produced in photoelectrochemical experiments. Argon was used as a carrier gas (or mobile phase), and the amounts of H_2 , O_2 and N_2 in the Ar stream were measured after interaction with a chromatography column (the stationary phase). In the experiment presented in chapter 6, the GC setup was directly connected to the PEC cell subjected to a chronoamperometry measurement to analyze the product composition *in situ*. A simplified sketch of the setup is shown in Figure 3.11. The three-electrode cell was filled with aqueous electrolyte (0.5 M Na_2SO_4 buffered to pH 6.1), subsequently sealed, and continuously Ar-bubbled at $5 \text{ mL} \cdot \text{min}^{-1}$ to purge the solution and carry the H_2 generated toward the chromatograph.

After purging the solution for 1 h, the photo electrode was held at a constant potential and illuminated. After 30 min of illumination to ensure steady-state operation, the concentration of H₂ generated was measured by injecting 0.5 mL of the output gas into the column (held at 50°C).

To determine the Faradaic efficiency (*FE*) of a photoelectrode, the H₂ production under illumination was measured by integrating the corresponding peak in the chromatograph. The GC setup was calibrated using a Pt electrode – which has a 100% *FE* for H₂ production – at different currents (see Figure 3.11b). The amount of H₂ produced by the photoelectrode is then compared to this calibration curve to determine the corresponding *FE*.

A Gas Chromatograph Clarus 480 (Perkin Elmer) equipped with a molecular sieves column (5A) and a plasma emission detector (PlasmaDetek) coupled to a modified “cappuccino” PEC cell was utilized with an area of 0.238 cm² of the electrode exposed to the electrolyte.

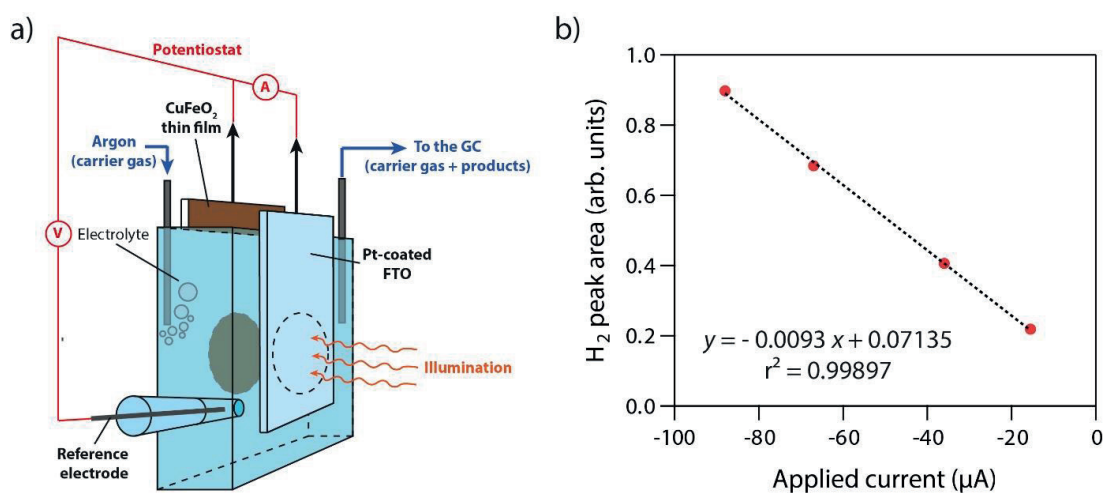


Figure 3.11 a) Sketch of the configuration used to measure the *FE* of CuFeO₂ photoelectrodes. The PEC cell was hermetically sealed to avoid contamination from the outer atmosphere, and a trap was setup on the output gas line to avoid the introduction of liquid electrolyte inside the GC. B) Calibration curve obtained with a platinum foil showing the area of the H₂ peak on the output chromatogram as a function of the current flowing through the Pt foil.

3.4 References

- (1) Prévot, M. S.; Guijarro, N.; Sivula, K. *ChemSusChem* **2015**, 8 (8), 1359–1367.
- (2) Prévot, M. S.; Li, Y.; Guijarro, N.; Sivula, K. *J. Mater. Chem. A* **2016**, 4 (8), 3018–3026.
- (3) Paracchino, A.; Laporte, V.; Sivula, K.; Grätzel, M.; Thimsen, E. *Nat. Mater.* **2011**, 10 (6), 456–461.
- (4) Diffuse Reflectance Measurement: SHIMADZU (Shimadzu Corporation)
http://www.shimadzu.com/an/molecular_spectro/uv/accessory/solid/sample/solid.html (accessed Apr 22, 2017).
- (5) Killedar, V. V.; Rajpure, K. Y.; Patil, P. S.; Bhosale, C. H. *Mater. Chem. Phys.* **1999**, 59 (3), 237–241.
- (6) Kroeze, J. E.; Savenije, T. J.; Warman, J. M. *J. Am. Chem. Soc.* **2004**, 126 (24), 7608–7618.
- (7) Savenije, T. J.; Ferguson, A. J.; Kopidakis, N.; Rumbles, G. *J. Phys. Chem. C* **2013**, 117 (46), 24085–24103.
- (8) Kimura, T.; Lashley, J. C.; Ramirez, A. P. *Phys. Rev. B* **2006**, 73 (22), 220401.
- (9) Terada, N.; Nakajima, T.; Mitsuda, S.; Kitazawa, H.; Kaneko, K.; Metoki, N. *Phys. Rev. B* **2008**, 78 (1), 014101.
- (10) Godinho, K. G.; Morgan, B. J.; Allen, J. P.; Scanlon, D. O.; Watson, G. W. *J. Phys. Condens. Matter* **2011**, 23 (33), 334201.
- (11) Suzuki, I.; Nagatani, H.; Kita, M.; Iguchi, Y.; Sato, C.; Yanagi, H.; Ohashi, N.; Omata, T. *Inorg. Chem.* **2016**, 55 (15), 7610–7616.
- (12) Melitz, W.; Shen, J.; Kummel, A. C.; Lee, S. *Surf. Sci. Rep.* **2011**, 66 (1), 1–27.
- (13) Cesiulis, H.; Tsyntsar, N.; Ramanavicius, A.; Ragoisha, G. *Nanostructures and Thin Films for Multifunctional Applications - Chapter 1: The Study of Thin Films by Electrochemical Impedance Spectroscopy*; Springer, 2016.
- (14) Gray, H. B.; Hendrickson, D. N.; Sohn, Y. S. *Inorg. Chem.* **1971**, 10 (8), 1559–1563.
- (15) Gärtner, W. W. *Phys. Rev.* **1959**, 116 (1), 84–87.
- (16) Reichman, J. *Appl. Phys. Lett.* **1980**, 36 (7), 574–577.
- (17) Allongue, P.; Cachet, H.; Horowitz, G. *J. Electrochem. Soc.* **1983**, 130 (12), 2352–2357.
- (18) Choo, S. C.; Tan, L. S.; Quek, K. B. *Solid-State Electron.* **1992**, 35 (3), 269–283.

Chapter 4

CuFeO₂: a promising photocathode material for solar hydrogen production

Iron and copper are respectively the fourth and twenty-sixth most abundant elements in the Earth crust, and respectively the first and eight most industrially produced element in the world. This, coupled with the fact that these metals are non-toxic, makes CuFeO₂ a material of choice for a potential global-scale production and application. It was discovered in 1873 in Siberia by the French mineralogist Charles Friedel (1838-1899), and was named in honor of other French mineralogist Gabriel Delafosse (1796-1878). In this chapter, the structural and optoelectronic properties of CuFeO₂ are presented, followed by the several possible routes used to process the material. Then seminal attempts to use this material as photocathode in PEC water splitting are described. Finally, an original sol-gel processing approach is presented, along with the PEC performance of the resulting photoelectrode.

The last part has been adapted from “Enhancing the Performance of a Robust Sol-Gel Processed p-Type Delafossite CuFeO₂ Photocathode for Solar Water Reduction” (Prévot, M.S; Guijarro, N.; Sivula, K., *ChemSusChem*, **2015**, 8, 1359-1367).

4.1 Structural and opto-electronic properties of CuFeO₂

Delafossite CuFeO₂ gives its name to the family of crystal structure it belongs to. Delafossite compounds are ternary oxides of general formula ABO₂. In the associated crystal structure, described for instance by Marquardt *et al.*,¹ the metal cation A has a (+I) oxidation state and is linearly coordinated to two oxygen ions. Typically, A cations can be Pd⁺, Pt⁺, Cu⁺ or Ag⁺. The other metal cation B has a (+III) oxidation state and is located at the center of distorted edge-shared BO₆ octahedra. B cations can be *p*-block metal ions (Ga³⁺, In³⁺, Al³⁺), transition metal ions (Fe³⁺, Co³⁺, Y³⁺), or rare-earth metal ions (La³⁺, Nd³⁺, Eu³⁺). The resulting crystal structure has a layered configuration, alternating monolayers of A cations and layers of BO₆ octahedra. The stacking of these layers gives rise to two polytypes: the 3*R* polytype of $R\bar{3}m$ symmetry, and the 2*H* polytype of $P6_3/mmc$ symmetry. These structures are shown in Figure 4.1a and b. CuFeO₂, like most of the delafossite materials, belongs to the space group $R\bar{3}m$.²

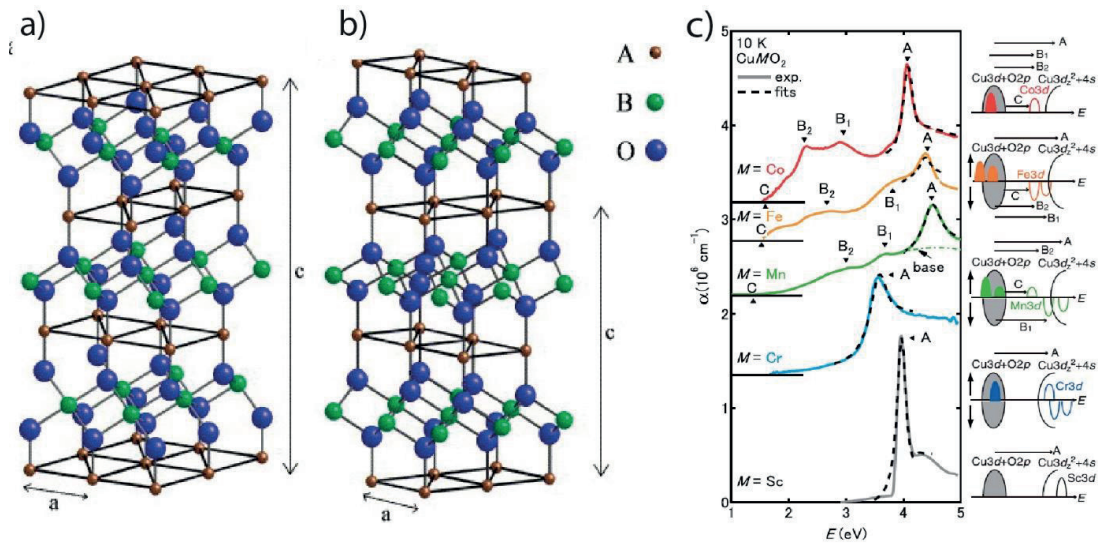


Figure 4.1 The 3*R* polytype (a) and 2*H* polytype (b) of the delafossite structure ABO₂, reproduced from reference 1, with permission of Elsevier. c) Absorption spectra (solid lines) of CuMO₂ (M = Sc, Cr, Mn, Fe, and Co) thin films measured at 10 K. Dashed lines represent fits of the experimental data based on a modified Elliott model. Schematic energy diagrams, derived from first-principles calculations, are shown in the right panel. Arrows indicate transitions corresponding to the observed absorption peaks. Reproduced from reference 7 with permission of the American Physical Society.

Cuprous delafossites – of general formula CuMO₂ – are semiconductors, which valence band is composed of hybridized Cu 3*d* states and O 2*p* states. This allows the

formation of holes upon oxidation of $3d^{10}$ Cu(I) to $3d^9$ Cu(II) in the presence of excess oxygen, giving these materials p-type conductivity – much like in p-type Cu_2O .³⁻⁷ Moreover, in the case of CuFeO_2 , its low-lying conduction band, based on Fe $3d$ states, yields an optical bandgap of 1.15-1.5 eV,^{3,8-12} providing absorption of a significant part of the visible light (see Figure 4.1c). This bandgap energy is attributed to an indirect transition, as shown by Tauc plot analysis,^{10,11} which is therefore relatively weak, while a stronger direct transition occurs for energies higher than 3.1 eV. Further discussion about the absorption spectrum of CuFeO_2 can be found in section 4.3.1. Moreover, as already described in Chapter 2, the valence and conduction bands of CuFeO_2 are adequately positioned in energy for photoelectrochemical water reduction. Finally, conductivity measurements performed on CuFeO_2 yielded widely different values depending on the processing method: 1 mS.cm^{-1} for rf-sputtered thin films,¹³ 0.4 S.cm^{-1} for sol-gel-deposited thin films,¹¹ 1.5 S.cm^{-1} for sintered pellets,¹⁴ and 2 S.cm^{-1} for single crystals.¹⁵ This shows that even solution-processed CuFeO_2 thin films can reach conductivities high enough for PEC applications. Overall CuFeO_2 possesses the required p-type conductivity and band alignment to perform solar water reduction, in addition of being made of earth-abundant elements.

4.2 Early reports of CuFeO_2 photocathodes

The group of M. Trari made the first PEC characterizations of CuFeO_2 in 2008-2009. In a series of papers, they explored the synthesis of CuFeO_2 powder through a nitrate solid-state route¹⁶ and a sol-gel approach¹⁷ as well as the production of single-crystalline CuFeO_2 by a flux method.⁸ These papers demonstrated that the material produced a reduction photocurrent under illumination, confirming its capability to operate as a photocathode, although the extracted currents were modest, due to the lack of optimization for the studied systems.

The most common way to prepare CuFeO_2 consists in reacting Cu_2O or CuO and Fe_2O_3 powders. If the synthesis is performed in air, it has to be carried out at very high temperature ($> 1000^\circ\text{C}$),¹⁸ while it can be done at slightly lower temperatures under inert atmosphere (typically *ca.* 850°C) to produce a powder of CuFeO_2 , as shown by Gu *et al.* in 2013.¹⁹ In their study, they pressed the resulting powder into a pellet, onto which they coated a 100 nm-thick layer of gold by sputtering. The resulting photoelectrode was then

tested for PEC CO₂ reduction: it produced photocurrents on the order of hundreds of $\mu\text{A}\cdot\text{cm}^{-2}$, with an apparent photovoltage of *ca.* 0.45V. The IPCE was modest as it was measured to be under 15% in the whole visible range, and the Faradaic efficiency for CO₂ reduction was limited to less than 10%, due to competition with water reduction. The authors further pointed out the formation of Cu (0) at the surface of the electrode during the PEC process, questioning the stability of the photocathode under operating conditions.

The same year, Read et al. reported the electrochemical synthesis of CuFeO₂ photocathodes.⁹ They used an electrolyte containing 1mM Cu(NO₃)₂ and 3mM Fe(ClO₄)₃ in 0.1 M KClO₄ in dimethylsulfoxide. They then performed the electrodeposition of a thin film of Cu-Fe oxide on Fluorine-doped tin oxide (FTO) from this electrolyte. The poor conductivity of the resulting amorphous ternary oxide thin film made the process self-limiting and prevented the deposition of thicknesses higher than 130 nm. Finally, this amorphous material was converted to CuFeO₂ by annealing the film at 650°C under Ar for one hour. The final electrode was then tested for PEC water reduction: it produced a small and unsustainable photocurrent of *ca.* 80 $\mu\text{A}\cdot\text{cm}^{-2}$ at 0.6 V vs RHE in 1M NaOH – quickly decreasing to a steady-state value of *ca.* 15 $\mu\text{A}\cdot\text{cm}^{-2}$ – and associated with a large apparent photovoltage of *ca.* 0.7 V. When oxygen was bubbled in the electrolyte – and used as a sacrificial electron scavenger – the photocurrent was decoupled and reached a stable value of 0.16 mA $\cdot\text{cm}^{-2}$ at 0.6 V vs RHE. The IPCE remained below 5% over the visible range, even in the presence of O₂. Importantly, the presence of small amounts of H₂ were detected by GC analysis in the presence of O₂, demonstrating the capacity of CuFeO₂ to reduce water to a certain extent.

Overall, these early studies established the possibility of using CuFeO₂ as a photocathode in a PEC setup. Although the photocurrents were low, the photovoltage was promising, and the detected reduction products (formate from CO₂ or hydrogen from water) confirmed the adequate band positioning of CuFeO₂ for driving direct water photoreduction with this material. However, the difficult processing conditions used in these reports likely prevented further optimization of the performance of the material. The next sections describe the original research work accomplished during the PhD thesis presented in this manuscript.¹⁰

4.3 A robust sol-gel-processed CuFeO₂ photocathode

In an attempt to overcome issues with controllable film deposition and improve electrode performance, a simple and scalable solution-processed route to stable p-CuFeO₂ thin-film photocathodes is presented, using cheap and abundant precursors. CuFeO₂ thin films are made directly on transparent conductive FTO substrates, and, through optimization and photoelectrochemical characterization, are shown to be very promising photocathodes for water reduction.

4.3.1 Thin-film preparation and characterization

Delafossite thin films were synthesized by a citrate-nitrate sol-gel method,²⁰ whereby metal nitrates salts were mixed with citric acid and ethylene glycol in ethanol. A first layer of this precursor solution was deposited on FTO coated aluminoborosilicate glass by spin-coating. The obtained film was dried, and annealed at 450°C in air for one hour. This temperature was found to be high enough to remove any organic material, but low enough to keep the atoms from crystallizing and segregating in different oxide domains. This procedure could then be repeated to increase the thickness of the precursor layer. In a last step, the films were annealed at 700°C, under Argon flow for 12h, to afford a dark brown film of CuFeO₂.

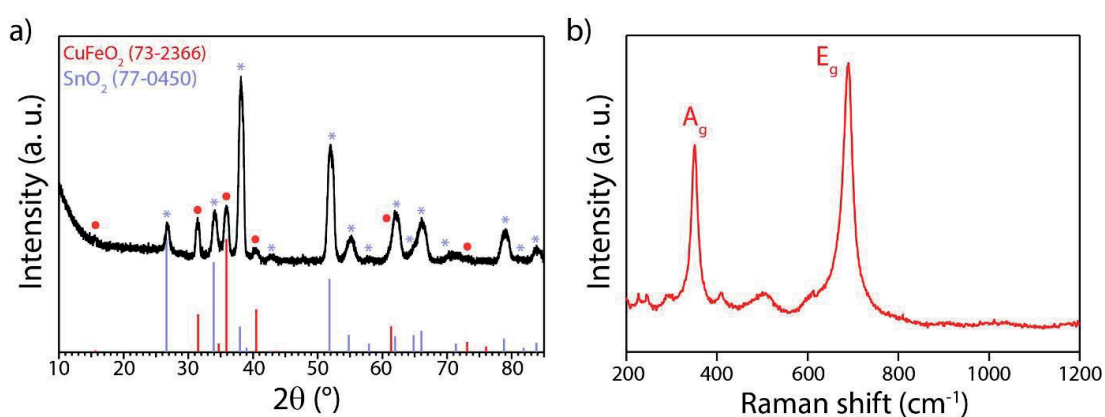


Figure 4.2 a) XRD trace of a CuFeO₂ thin film deposited on FTO collected under pseudograzing incidence geometry. Blue and red lines correspond to SnO₂ and CuFeO₂ signals, respectively, from the ICDD database. b) Surface Raman spectrum of the same film.

The presence of the delafossite phase in the final films was confirmed by XRD and Raman spectroscopy presented in Figure 4.2. The XRD trace is consistent respectively

with the ICDD database and to previous reports,²¹ and no unexpected peaks were observed, indicating that other crystalline iron or copper compounds were not present. The wide shape of the XRD peaks is caused by the pseudo-grazing incidence configuration of the diffractometer used to enhance reflections from the thin film (see Chapter 3, section 3.2.2). Roughly the same relative intensities between the diffraction peaks were observed in the spectrum of powder prepared by the same route, indicative of no preferential orientation in the thin film. The Raman spectrum displays the expected two Raman-active phonon modes at 351 cm⁻¹ and 692 cm⁻¹, respectively corresponding to A_g and E_g symmetries in the C_{3v} point group.²¹

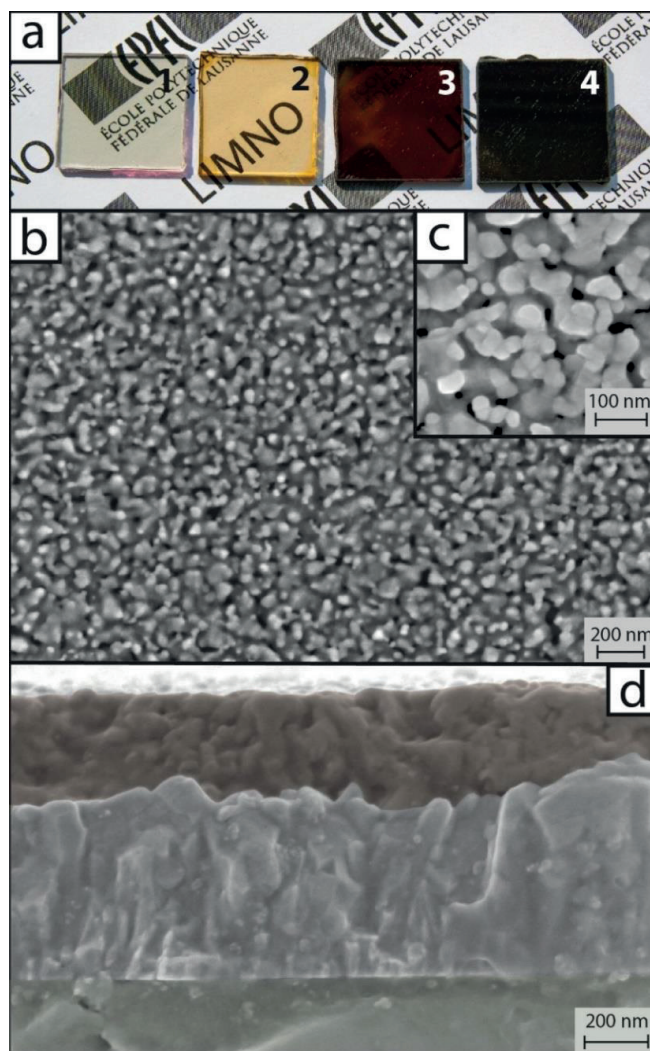


Figure 4.3 a) Optical images of the FTO substrate (1), one layer of the dried gel (2), a six-layer film annealed at 450°C in air for one hour (3), and the final six-layer CuFeO₂ film annealed at 700°C in argon for 12 hours (4). SEM top (b and c) and cross-sectional (d) views of a six-layer CuFeO₂ film on FTO.

Optical photographs of the films during different stages of the deposition process are shown in Figure 4.3a, and give a suggestion of the drastic change of light absorption the film exhibits after annealing at 700°C (*i.e.* from sample 3 to sample 4). The temperature of 700°C was found to be the lowest at which the delafossite crystal phase was formed in the experimental conditions at hand (in a 51 mm diameter tube furnace under Ar flow at 300 mL min⁻¹). When annealed at lower temperatures, a lighter material was formed, which proved to be unstable, while annealing at higher temperatures did not bring significant improvement. Importantly, it was not possible to anneal the film higher than 800°C due to the loss of conductivity of the FTO substrate at these temperatures. Scanning electron micrographs of the resulting CuFeO₂ films are shown in Figure 4.3. The low magnification micrograph shown in Figure 4.3b revealed a good coverage of the substrate surface, while close-up views, such as the one displayed in Figure 4.3c, showed the nanoporous morphology of the film. Before annealing the material at 700°C, the films were smooth and compact with no apparent phase segregation. The nano-features observed in the final films therefore arose from sintering the material at high temperature. Moreover, a cross-sectional image, shown in Figure 4.3d, indicated that the films prepared with six spin-coated layers had an average thickness of about 290 nm. This thickness was found to be an optimal compromise between the absorption properties and the photo-activity of the film (*vide infra*).

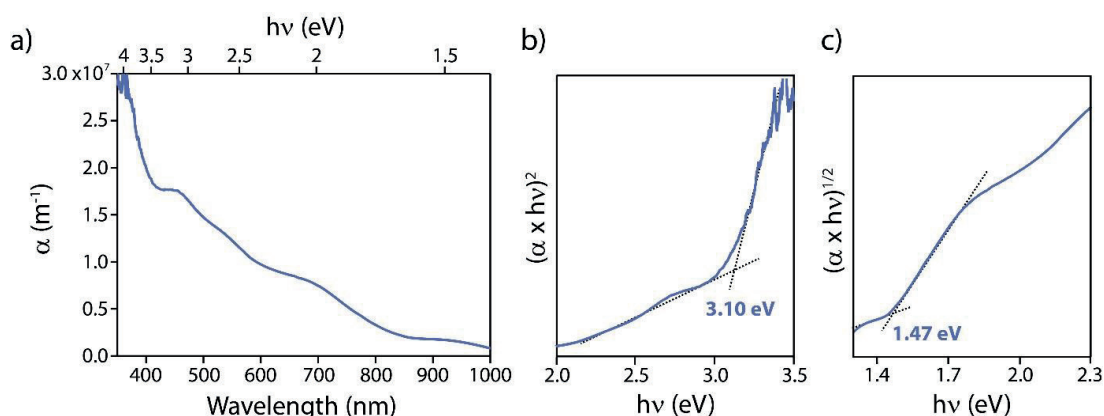


Figure 4.4 a) UV-vis absorption spectrum of a CuFeO₂ film on FTO, corrected for the substrate. Corresponding direct (b) and indirect (c) Tauc plots for optical transition determination.

Films of this thickness did indeed absorb a significant portion of the solar spectrum as suggested by the optical photograph (Figure 4.3a). The UV-vis-NIR absorbance revealed three optical transitions occurred, as shown in Figure 4.4. The nature of these

transitions was further investigated using a Tauc plot analysis. Tauc plots of $(\alpha h\nu)^n$ vs $h\nu$ are shown in Figure 4.4b and c, where $n = 1/2$ for an indirect optical transition, and $n = 2$ for a direct one. CuFeO₂ thin films exhibited an indirect optical gap at 1.47 eV, and a direct transition at 3.1 eV. The third transition located at 2.1 eV could be considered either direct or indirect. These values are consistent with previous experimental reports^{11,12} and theoretical calculations^{7,22} on CuFeO₂ (see Figure 4.1c). Importantly, the absorption coefficient of CuFeO₂ thin films was found to be three orders of magnitude higher than Cu₂O thin films.²³

4.3.2 Photoelectrochemical characterization

The delafossite films were subsequently tested for their activity in PEC water reduction. To do so, they were inserted in a PEC cell and illuminated with a spectrally matched Xe arc lamp with a calibrated light intensity of 100 mW cm⁻², corresponding to the standard value of 1 sun (see Chapter 3, section 3.3.3). Linear sweep voltammetry (LSV) was performed in 1M NaOH electrolyte against an Ag/AgCl reference electrode and reported potential against the RHE scale. LSV curves of a delafossite thin film under front-side illumination are shown in Figure 4.5a (red curve). When the electrolyte was purged with argon and under chopped illumination, the electrode produced low steady-state photocurrents of about 25 $\mu\text{A cm}^{-2}$ at +0.4 V vs RHE. High cathodic transient current spikes, with short lifetimes, corresponded to the onset of illumination.

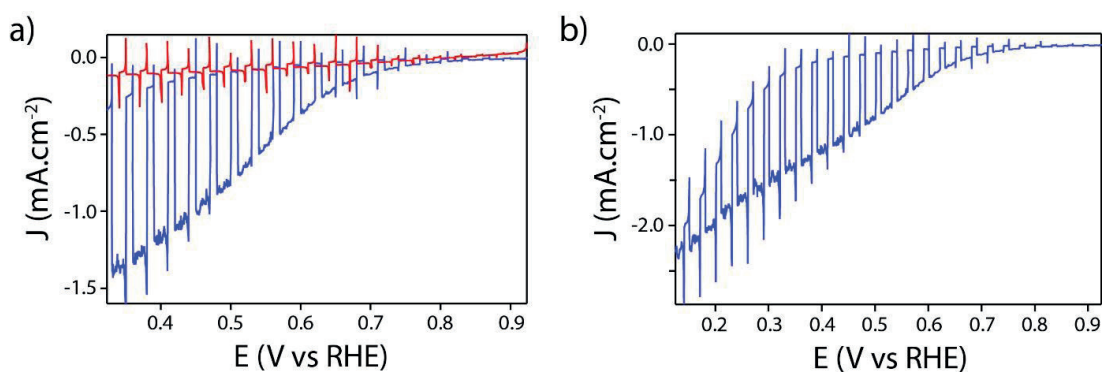


Figure 4.5 a) LSV of a ~ 300 nm-thick CuFeO₂ photocathode in 1M NaOH under intermittent one sun illumination, with argon-purged electrolyte (red trace) and oxygen-saturated electrolyte (blue trace). b) Wider potential range scan in oxygen-saturated electrolyte. The sweep rate was 10 mV.s⁻¹ towards negative potentials.

The observation of a corresponding anodic current spike upon turning off the illumination strongly suggests that charge accumulation is occurring at the semiconductor liquid junction (SCLJ) under these conditions,²⁴ and indicates that charge injection into the electrolyte is limiting the steady state photocurrents. In order to probe the maximum photocurrent that could be produced by these CuFeO₂ electrodes, they were then evaluated in the presence of a sacrificial electron acceptor dissolved in the electrolyte. In general sacrificial agents allow the separate investigation of charge separation efficiency and charge injection efficiency in photo-electrodes for water splitting.²⁵ Sacrificial electron acceptors such as O₂,⁹ Eu³⁺,²⁶ or MV²⁺²⁷ have been shown to exhibit faster reduction kinetics compared to water for p-type cathodes. In this work and in accordance with previous investigations,⁹ an electrolyte saturated with O₂ was used. As shown in Figure 4.5a (blue curve), when saturated O₂ was used, steady-state photocurrents rose drastically to about 1.05 mA.cm⁻² for a ~ 300 nm-thick electrode at +0.4 V vs RHE, while transient currents were reduced, as the kinetics were less limited by charge transfer across the SCLJ. Alkaline conditions were chosen because they produced the highest photocurrent for O₂ reduction at the CuFeO₂ photocathode, and the bubbling rate of O₂ was adjusted so no diffusion-limited photocurrent (characterized by a slow decay over time) was observed. Interestingly, the photocathode showed a decreasing photocurrent when scanned negative of ca. +0.3 V vs RHE (see Figure 4.5b). Despite this unexpected photocurrent decrease, the electrode displayed a highly anodic photocurrent onset, located around +0.9 V vs RHE, making it potentially compatible with previously reported photoanodes, such as n-BiVO₄,²⁸ or n-WO₃,²⁹ in a complete photoelectrochemical tandem cell for water splitting.

4.3.3 Thickness optimization and performance consistency

Because the use of the sacrificial (O₂ purged) electrolyte allowed the measurement of meaningful photocurrents, the influence of the thickness of the delafossite film on the electrode performance could be rigorously investigated. Figure 4.6a shows the average photocurrents obtained at +0.4 and +0.6 V vs RHE for films of different thicknesses, under front (electrolyte side) illumination. At +0.4V the photocurrent produced by the electrode initially increased with the thickness and reached a maximum value for a thickness of 300 nm. Further increasing the thickness resulted in a decrease in photocurrent. The optimal thickness of 300 nm accords well to the penetration depth of photons implied by Figure

4.4 ($\alpha^{-1} = 200$ nm for $\lambda=700$ nm) suggesting a trade-off between light absorption and majority carrier transport through the bulk of the film. In contrast, the behavior at +0.6 V does not exhibit the same trend. Here the smaller and relatively constant value of the photocurrent suggests that charge separation is limiting the photocurrent at this potential. In addition, there is a clear discrepancy between the magnitude of the optimized photocurrent and the number of photons absorbed. Indeed, calculations based on the standard AM 1.5G solar photon flux, indicate a theoretical maximum photocurrent of 14.8 mA.cm⁻², assuming 100% internal quantum efficiency (calculation details are given in Chapter 3, section 3.2.1). This large discrepancy, even in the presence of an electron acceptor, indicates that charge separation within the material is limiting the performance. This view is supported by the back illumination study (*i.e.* through the glass substrate), where photocurrents were found to steadily decrease with increasing thickness for all thicknesses measured (see Figure 4.6b). In addition, for electrodes thicker than 100 nm, electrolyte-side illumination afforded higher photocurrent than substrate-side illumination. This further suggests that the charge harvesting depth (*i.e.* the space-charge layer width plus the diffusion length of minority carriers) is relatively thin compared to the semiconductor layer thickness.

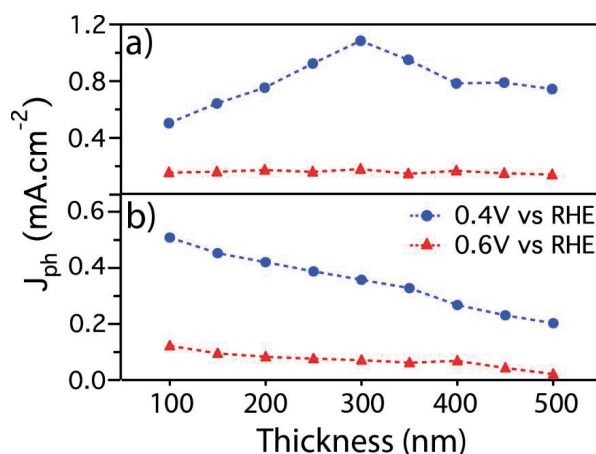


Figure 4.6 Photocurrent densities obtained with electrodes of varying thicknesses at 0.4 V vs RHE (blue markers) and 0.6 V (red markers) vs RHE under electrolyte-side (a) and substrate-side (b) illumination. The data was recorded in oxygen-purged 1M NaOH.

Despite relatively low photocurrents compared to the light absorption, this sol-gel method consistently produced electrodes of similar photoactivity. Among the ten 300 nm-thick CuFeO₂ films tested for this work, samples displayed photocurrents of 1.05 ± 0.06

mA cm^{-2} at 0.4 V vs RHE, and $0.31 \pm 0.05 \text{ mA.cm}^{-2}$ at 0.6 V vs RHE. When this research was carried out, this value of the photocurrent surpassed other reports using sacrificial agents with CuFeO_2 .⁹ In an effort to verify the magnitude of the photocurrent produced by the best electrode and quantify the spectral response the IPCE spectra was evaluated next. A typical IPCE of an optimized CuFeO_2 electrode, at +0.4 V vs RHE, is plotted as a function of wavelength in Figure 4.7. IPCE values monotonously increased with decreasing wavelength, exceeding 10% at 400nm. The spectrum also exhibited shoulders at wavelengths matching the optical transitions of the film. The onset of the response was found at around 830 nm (1.49 eV), affirming that a large portion of the solar spectrum, up to the near IR, can be absorbed and converted to useful free charges by CuFeO_2 .

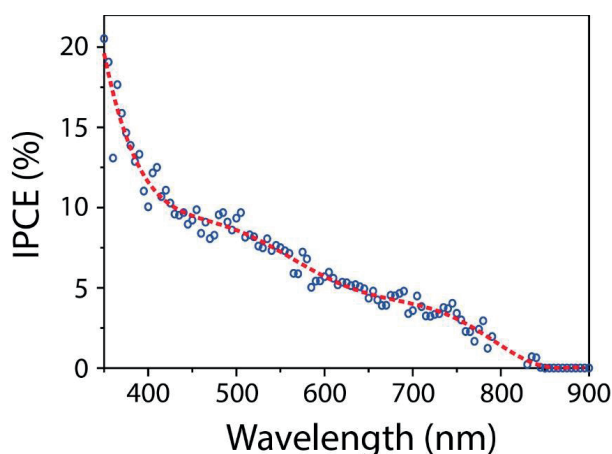


Figure 4.7 IPCE measurement performed on an optimized CuFeO_2 electrode in O_2 -purged 1M NaOH electrolyte. The blue circles represent experimental data, while the broken red trace represents the smoothed curve obtained from these data.

Importantly, the IPCE measurement was performed on an electrode, improved by extrinsic O_2 doping – a technique described in Chapter 5 of this manuscript. Therefore, integrating the IPCE multiplied by the standard solar spectrum AM 1.5G, 100 mW cm^{-2} , afforded an expected photocurrent density of 1.48 mA cm^{-2} , in agreement with the photocurrents measured for such an electrode under simulated solar illumination (see Chapter 5, section 5.1.1), but higher than the one reported in Figure 4.5.

4.3.4 Electrochemical Impedance spectroscopy

The electronic characteristics of the electrode were next examined by means of EIS. Nyquist plots of the electrodes were acquired for potentials close to the onset of

photocurrent and for frequencies in the 100 mHz – 1 MHz range. The high-frequency part of the data was fitted with a simple Randles equivalent circuit shown in Figure 4.8. From the fit, the space-charge capacitance (C_{SC}) was extracted. This capacitance is linked to the applied voltage through the Mott-Schottky relationship for a p-type semiconductor (Equation 2.32). Figure 4.8 displays the corresponding Mott-Schottky diagram, where C_{SC}^{-2} is plotted against E for a CuFeO₂ electrode.

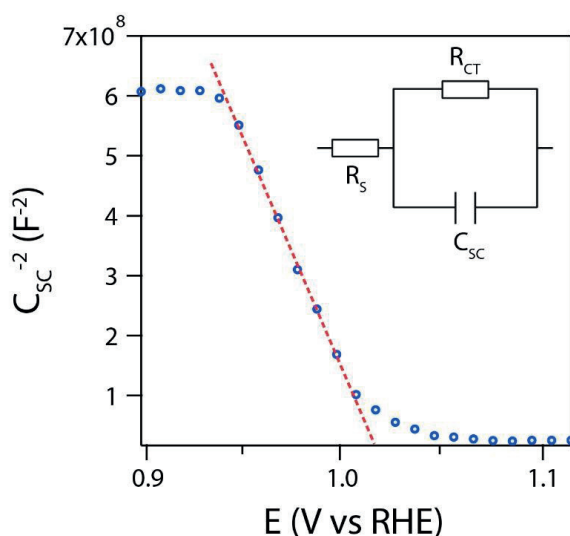


Figure 4.8 Mott-Schottky diagram of a CuFeO₂ thin film on FTO in O₂-saturated 1M NaOH. The red line indicates the linear region that corresponds to the depletion regime of the semiconductor: it intercepts the x -axis at E_{FB} . The equivalent circuit used to extract the values of C_{SC} is represented in the top-right corner.

From the linear region attributed to the depletion region of CuFeO₂ (represented by the red line in Figure 4.8) a flat-band potential $E_{FB} = +1.01$ V vs RHE was obtained, in agreement with previous reports.^{9,19} This very anodic flat-band potential explains the favorable photocurrent onset observed in the J-V curve. Moreover, a relatively high acceptor density, in the order of 10^{18} cm⁻³, was calculated. This value was obtained assuming a roughness factor of 50, roughly estimated from SEM pictures of the film, and previously reported roughness factors for nanoporous films,³⁰ and using a value of 20 for the dielectric constant of the material, as reported elsewhere.³¹

While this model was sufficient to fit the behavior of CuFeO₂ electrodes close to V_{FB} – and therefore allowed to estimate E_{FB} and N_A – it failed on a wider potential range. A more general and more accurate EIS analysis of CuFeO₂ electrodes is proposed in Chapter 6 to overcome the shortcomings of the Randle circuit proposed here.

4.3.5 Photoelectrode stability

As the stable operation of any photocathode is of fundamental interest to its potential application in a PEC device, the stability of the CuFeO_2 photoelectrodes was tested. To investigate the stability of the bare CuFeO_2 , cyclic voltammetry (without illumination) over the potential range from +0.3 to +0.9 V vs RHE in 1 M NaOH (the conditions studied in Figure 4.5a) was performed. The results (Figure 4.9a and b) are consistent with a stable electrode (red trace). Moreover, Raman spectra taken before and after the CV showed no change (see Figure 4.9c).

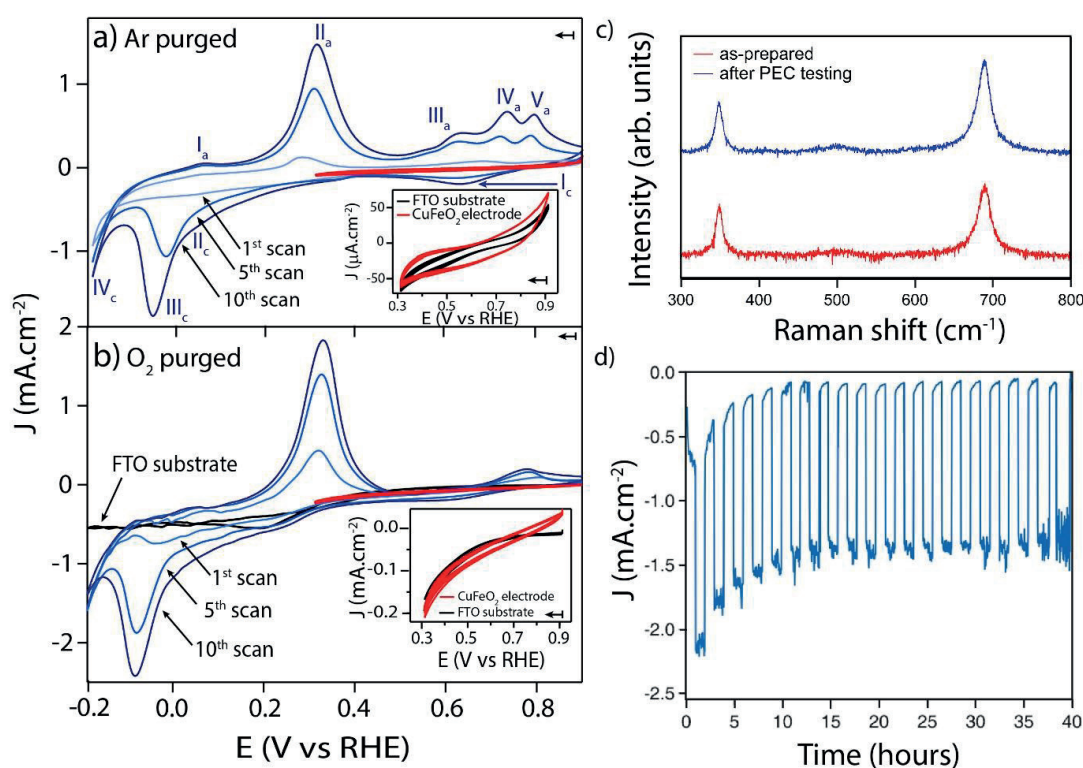


Figure 4.9 Cyclic voltammograms of a CuFeO_2 electrode in Ar-purged (a) and O_2 -purged (b) 1M NaOH (scan rate: 10 mV/s). The arrows indicate the starting voltage and the direction of the voltage scans. The blue trace shows the evolution of the voltammogram over 10 scans between +0.9 V and -0.2 V vs RHE. The red trace corresponds to the same evolution between +0.9 V and +0.3 V vs RHE. The insets show a comparison of the latter and the bare FTO substrate under the same conditions. The redox peak in (a) are labeled and identified in Table 4.1. c) Raman spectra of a CuFeO_2 electrode before (red trace) and after (blue trace) being subjected to a voltage sweep from 0.9 to 0.3 V vs RHE in O_2 -purged 1M NaOH under 1 sun illumination. d) Chronoamperometry of a CuFeO_2 electrode during 40 hours at +0.4 V vs RHE in 1M NaOH under O_2 bubbling and chopped illumination. Oxygen bubbles caused the noise present when the electrode was under illumination.

A longer demonstration of the operational stability was obtained by subjecting a bare CuFeO₂ electrode to a chronoamperometric scan at +0.4 V vs RHE, for 40 h in O₂ purged electrolyte (under 1 sun illumination with a 30 min light chopping frequency). The resulting chronoamperogram (Figure 4.9d) showed no sign of degradation (after an initial drop of about 10% in the first two hours). The noise appearing in the chronoamperogram when the electrode is illuminated is a result of interference from bubbles of the purge gas. Overall these results show that the bare CuFeO₂ is stable under polarization from +0.3 to +0.9 V vs RHE in 1 M NaOH, which is a suitable range for application in a PEC tandem cell. However, when scanning to more negative potentials, redox peaks develop that are consistent with copper and iron reduction/re-oxidation in an alkaline electrolyte (see Figure 4.9a and b, and Table 4.1). In addition, when subjected to a voltage more negative than +0.1 V vs RHE, the electrode showed visible signs of decomposition consistent with the reduction of the copper and iron inside the film.

Table 4.1 Identified peaks on the CV (Figure 4.9a). The copper peaks are taken from reference and while the iron peaks are from reference

Peak	Redox process
I _c	Cu(II) → Cu(I)
II _c	Cu(I) → Cu(0)
III _c	Fe(III) → Fe(II)
IV _c	Fe(II) → Fe(0)
I _a	Fe(0) → Fe(II)
II _a	Fe(II) → Fe(III)
III _a	Cu(0) → Cu(I)
IV _a	Cu(0) → Cu(II)
V _a	Cu(I) → Cu(II)

4.4 Conclusions

Delafossite material CuFeO₂ presents attractive structural and opto-electronic properties for use as photocathode for solar hydrogen production. Early work on the material performed between 2009 and 2013 established its capacity to produce photocurrents with a high apparent photovoltage. In the original work presented in

section 4.3 of this chapter, a sol-gel based technique is used to prepare thin films of p-type delafossite CuFeO₂ on FTO glass. This citrate-nitrate route displays several advantages compared to previously reported techniques, such as the straightforward solution processing of the films, the relatively low annealing temperature required to attain the delafossite phase, and the ability to tune the layer thickness. Physical characterization of the films confirmed the purity and crystal phase. CuFeO₂ films displayed good band edge positioning, with an optical band gap energy potentially allowing high efficiency water splitting in an integrated tandem device. LSV curves of unmodified CuFeO₂ electrodes revealed record photocurrent densities – at the time – for the bare films using sacrificial electron acceptors and an advantageous photocurrent onset at +0.9 V vs RHE, while the IPCE onset of the material was found to be around 830 nm. These electrodes were further found to be stable for time periods of days under operating conditions, making CuFeO₂ an exception among photocathodes, which usually require protective coatings to resist corrosion under reductive conditions.

While this work demonstrates that CuFeO₂ is a promising photocathode material for solar water reduction, it cannot perform water reduction on its own, and suffers from poor charge separation, as evidenced by the large discrepancy between measured photocurrents and what is expected based on the high absorption coefficient of the material. The next chapter will therefore describe the efforts undertaken to overcome these major limitations.

4.5 References

- (1) Marquardt, M. A.; Ashmore, N. A.; Cann, D. P. *Thin Solid Films* **2006**, 496 (1), 146–156.
- (2) Shannon, R. D.; Rogers, D. B.; Prewitt, C. T. *Inorg. Chem.* **1971**, 10 (4), 713–718.
- (3) Galakhov, V. R.; Poteryaev, A. I.; Kurmaev, E. Z.; Anisimov, V. I.; Bartkowski, S.; Neumann, M.; Lu, Z. W.; Klein, B. M.; Zhao, T.-R. *Phys. Rev. B* **1997**, 56 (8), 4584–4591.
- (4) Buljan, A.; Alemany, P.; Ruiz, E. J. *Phys. Chem. B* **1999**, 103 (38), 8060–8066.
- (5) Kandpal, H. C.; Seshadri, R. *Solid State Sci.* **2002**, 4 (8), 1045–1052.
- (6) Scanlon, D. O.; Walsh, A.; Watson, G. W. *Chem. Mater.* **2009**, 21 (19), 4568–4576.
- (7) Hiraga, H.; Makino, T.; Fukumura, T.; Weng, H.; Kawasaki, M. *Phys. Rev. B* **2011**, 84 (4), 041411.

- (8) Omeiri, S.; Bellal, B.; Bouguelia, A.; Bessekhoud, Y.; Trari, M. *J. Solid State Electrochem.* **2009**, *13* (9), 1395–1401.
- (9) Read, C. G.; Park, Y.; Choi, K.-S. *J. Phys. Chem. Lett.* **2012**, *3* (14), 1872–1876.
- (10) Prévot, M. S.; Guijarro, N.; Sivula, K. *ChemSusChem* **2015**, *8* (8), 1359–1367.
- (11) Chen, H.-Y.; Wu, J.-H. *Appl. Surf. Sci.* **2012**, *258* (11), 4844–4847.
- (12) Chen, H.-Y.; Wu, J.-H. *Thin Solid Films* **2012**, *520* (15), 5029–5035.
- (13) Barnabé, A.; Mugnier, E.; Presmanes, L.; Tailhades, P. *Mater. Lett.* **2006**, *60* (29–30), 3468–3470.
- (14) Benko, F. A.; Koffyberg, F. P. *J. Phys. Chem. Solids* **1987**, *48* (5), 431–434.
- (15) Shannon, R. D.; Rogers, D. B.; Prewitt, C. T.; Gillson, J. L. *Inorg. Chem.* **1971**, *10* (4), 723–727.
- (16) Omeiri, S.; Gabès, Y.; Bouguelia, A.; Trari, M. *J. Electroanal. Chem.* **2008**, *614* (1–2), 31–40.
- (17) Bassaid, S.; Chaib, M.; Omeiri, S.; Bouguelia, A.; Trari, M. *J. Photochem. Photobiol. Chem.* **2009**, *201* (1), 62–68.
- (18) Amrute, A. P.; Łodziana, Z.; Mondelli, C.; Krumeich, F.; Pérez-Ramírez, J. *Chem. Mater.* **2013**, *25* (21), 4423–4435.
- (19) Gu, J.; Wuttig, A.; Krizan, J. W.; Hu, Y.; Detweiler, Z. M.; Cava, R. J.; Bocarsly, A. B. *J. Phys. Chem. C* **2013**, *117* (24), 12415–12422.
- (20) Kakihana, M. *J. Sol-Gel Sci. Technol.* **1996**, *6* (1), 7–55.
- (21) Pavunny, S. P.; Kumar, A.; Katiyar, R. S. *J. Appl. Phys.* **2010**, *107* (1), 013522.
- (22) Ong, K. P.; Bai, K.; Blaha, P.; Wu, P. *Chem. Mater.* **2007**, *19* (3), 634–640.
- (23) Paracchino, A.; Brauer, J. C.; Moser, J.-E.; Thimsen, E.; Graetzel, M. *J. Phys. Chem. C* **2012**, *116* (13), 7341–7350.
- (24) Le Formal, F.; Sivula, K.; Grätzel, M. *J. Phys. Chem. C* **2012**, *116* (51), 26707–26720.
- (25) Dotan, H.; Sivula, K.; Grätzel, M.; Rothschild, A.; Warren, S. C. *Energy Environ. Sci.* **2011**, *4* (3), 958–964.
- (26) Ikeda, S.; Nonogaki, M.; Septina, W.; Gunawan, G.; Harada, T.; Matsumura, M. *Catal. Sci. Technol.* **2013**, *3* (7), 1849–1854.
- (27) Bookbinder, D. C.; Lewis, N. S.; Bradley, M. G.; Bocarsly, A. B.; Wrighton, M. S. *J. Am. Chem. Soc.* **1979**, *101* (26), 7721–7723.

- (28) Abdi, F. F.; Han, L.; Smets, A. H. M.; Zeman, M.; Dam, B.; van de Krol, R. *Nat. Commun.* **2013**, *4*.
- (29) Amano, F.; Li, D.; Ohtani, B. *Chem. Commun.* **2010**, *46* (16), 2769–2771.
- (30) Kim, S. H.; Choi, J. B.; Nguyen, Q. N.; Lee, J. M.; Park, S.; Chung, T. D.; Byun, J. Y. *Phys. Chem. Chem. Phys.* **2013**, *15* (16), 5782–5787.
- (31) Kimura, T.; Lashley, J. C.; Ramirez, A. P. *Phys. Rev. B* **2006**, *73* (22), 220401.

Chapter 5

Improving charge separation and collection in sol-gel CuFeO₂ photocathodes

Delafossite CuFeO₂ has been established in Chapter 4 as a promising photocathode candidate. However, optimization of the CuFeO₂ layer thickness suggested that the charge harvesting depth (i.e. the space-charge layer at the interface plus the diffusion length of minority carriers) was relatively thin compared to the semiconductor thickness required for good light harvesting (based on the absorption coefficient). This discord between carrier transport and light absorption can be addressed in several ways. First, the transport of charges inside the material can be improved by extrinsic doping, thereby reducing charge recombination due to poor transport inside the bulk of the material. Second, charge collection can be promoted by introducing a charge-collecting layer inside a “host-guest” architecture. Both of these approaches were applied to the sol-gel CuFeO₂ electrode presented in Chapter 4 and the resulting improvements are reported in this chapter.

This chapter has been adapted from “Enhancing the Performance of a Robust Sol-Gel Processed p-Type Delafossite CuFeO₂ Photocathode for Solar Water Reduction” ¹ (Prévot, M.S; Guijarro, N.; Sivula, K., *ChemSusChem*, **2015**, 8, 1359-1367),

and from “Improving Charge Collection with Delafossite Photocathodes: A Host-Guest CuAlO₂/CuFeO₂ approach” ² (Prévot, M.S.; Li, Y.; Guijarro, N.; Sivula, K., *J. Mater. Chem. A*, **2016**, 4, 3018-3026)

5.1 Extrinsic doping of CuFeO₂ photocathodes

Extrinsic p-type doping of CuFeO₂ results in a higher acceptor density, which in turn yields a higher majority carrier conductivity and a higher photocurrent by increasing the charge separation efficiency. Traditionally, two types of dopants have been used for CuFeO₂: O intercalation in the Cu layers of the structure^{3–5} and substitution of Fe³⁺ ions by Mg²⁺ ions.^{6–8} Both of these approaches were tested on the CuFeO₂ photocathodes described in Chapter 4, section 4.3.

5.1.1 Oxygen intercalation

To probe oxygen intercalation in CuFeO₂, thermogravimetric analysis (TGA) was performed (under O₂ flow) on a CuFeO₂ powder obtained through the same citrate-nitrate route. The resulting curve, shown in Figure 5.1, displayed a small increase in mass starting from 300°C, and ending with a shoulder around 450°C, that was attributed to oxygen intercalation, followed by a much bigger increase in mass, corresponding to the progressive oxidation of the delafossite CuFeO₂ into the spinel CuFe₂O₄, in good agreement with previous studies.^{4,5} According to this curve, it should be possible to thermally intercalate oxygen inside the delafossite structure by heating it between 300°C and 450°C.

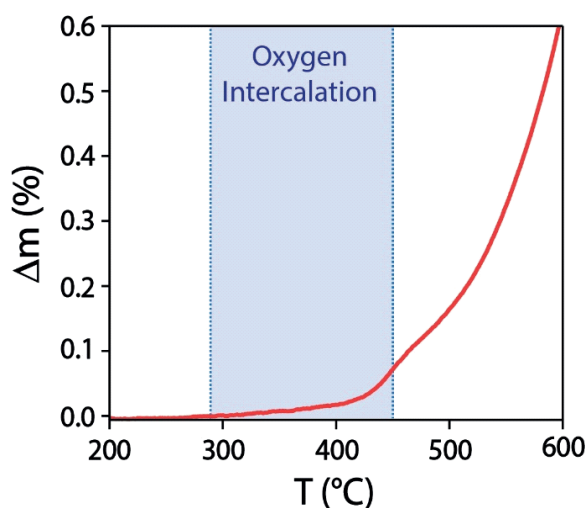


Figure 5.1 Thermogravimetric analysis of CuFeO₂ powder in air, showing the percentage of mass variation as a function of the temperature

To study the influence of oxygen intercalation on the performance of the films, freshly prepared electrodes were cut in half; one side of each sample was tested without further modification, while the other one was submitted to an additional annealing step in air. CuFeO₂ thin films were found to withstand thermal treatment in air up to 350°C, and started to change in color at higher temperature, indicating a chemical modification of the material. PEC measurements showed that films heated at temperatures higher than 350°C did not produce any photocurrent and were unstable. The fact that thin films degraded at lower temperature than the powder was attributed to the presence of the substrate in the former case, which could induce additional strain on the crystal structure, thus making it easier to oxidize.

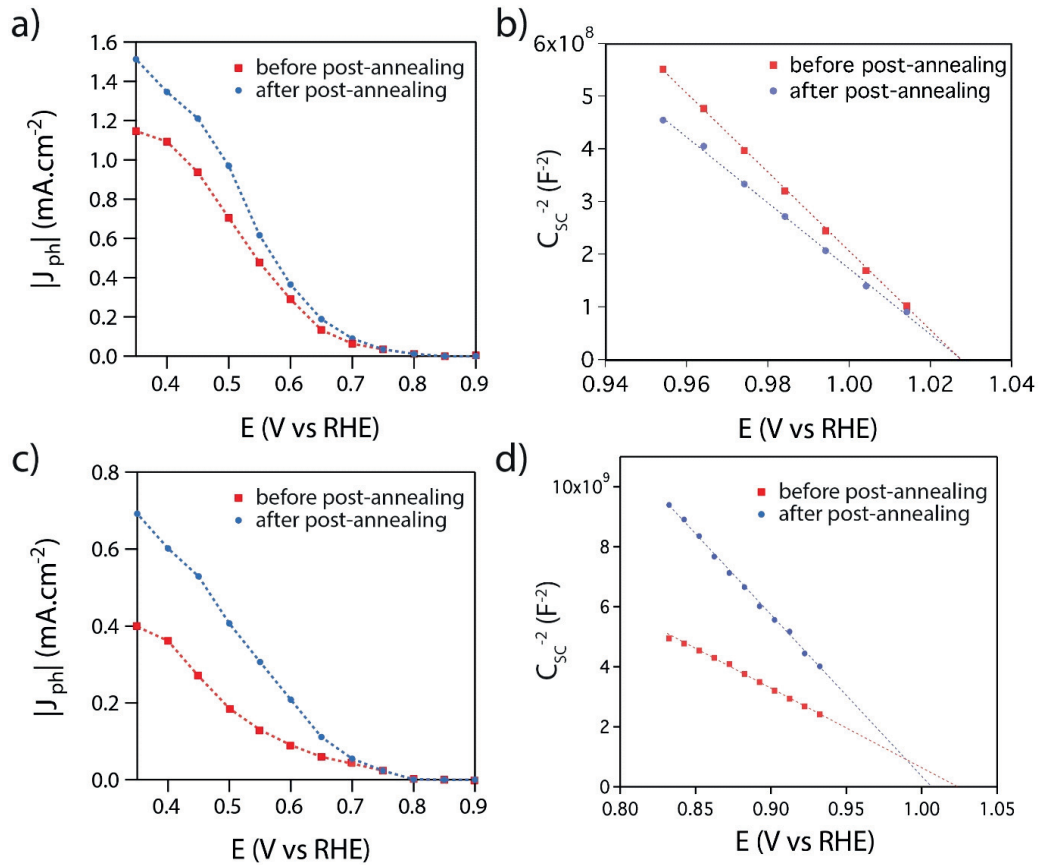


Figure 5.2 a) Absolute photocurrent (total current minus dark current) density $|J_{ph}|$ as a function of applied potential for a 300 nm-thick CuFeO₂ thin films on FTO in O₂-saturated 1M NaOH under one sun illumination before (red) and after (blue) post-annealing at 300°C in air. b) Linear regions of the Mott-Schottky diagram for the same electrodes under the same conditions. c) and d) represent the same data than a) and b) respectively, but for a 100 nm-thick electrode.

On the other hand, exposing the electrodes to air at 300°C for only one hour caused measureable improvement in the magnitude of the photocurrents produced by the electrode, indicating a positive effect of this treatment on the photocurrents of the material in O₂ saturated electrolyte. Figure 5.2 shows typical improvements of the photocurrent for a 300 nm and a 100 nm-thick electrode. Photocurrents increased over the entire potential range by 20 to 25% for the 300 nm-thick film (Figure 5.2a) and by 50% to 100% for the 100 nm-thick film (Figure 5.2c). The best performing electrode, from the series studied in this work, displayed photocurrents of 1.51 mA cm⁻² at +0.35 V vs RHE, under front illumination and in O₂-purged 1M NaOH. XRD spectra taken before and after annealing in air showed no difference (see Figure 5.3), suggesting no phase change is occurring. The effect of oxygen intercalation on the film doping density was investigated by plotting the Mott-Schottky relationship for the material before and after annealing in air. From the resulting linear fits, shown in Figure 5.2, acceptor densities were compared. The acceptor density rose by 20% for the 300 nm-thick film (Figure 5.2b) and doubled for the 100 nm-thick film (Figure 5.2d), matching the magnitude of the photocurrent increase. While the impact of oxygen on the dopant density may seem modest, it was consistently observed on multiple samples, and since it was more pronounced with thinner samples, allows further insight into the limitations in the photocurrent.

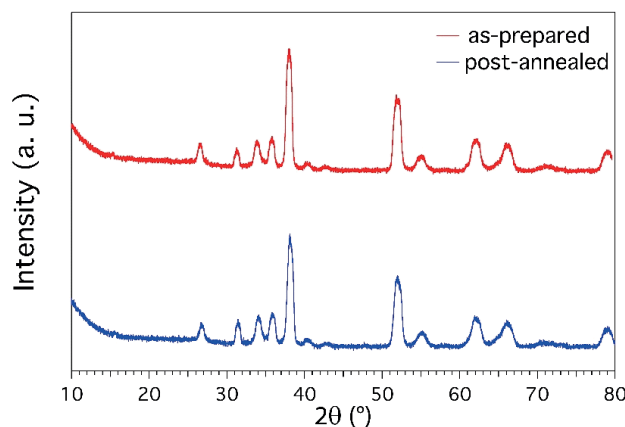


Figure 5.3 XRD traces of a CuFeO₂ thin film on FTO before (red trace) and after (blue trace) post-annealing at 300°C in air. The diffractograms were collected under pseudo-grazing incidence.

A possible explanation is that, as the doping density increases, the electric field in the space charge region correspondingly increases, resulting in better charge separation in the depletion layer of the material. The fact that thinner samples exhibit a larger

response to this treatment suggests that majority carrier transport remains a limitation in the thicker films. Thus, further increase in the majority carrier concentration should further increase the charge collection efficiency. Overall the O₂ intercalation results demonstrate an easy way to improve the properties of CuFeO₂ as a photocathode, but more importantly, indicate that further increase in the p-type doping of the material could translate to further improvement of photocurrent.

5.1.2 Iron substitution by Mg²⁺

A better-controlled way of doping CuFeO₂ is by substituting a fraction of its Fe(III) ions by Mg²⁺. To study the effect of this substitution on the PEC performance of the CuFeO₂ thin films, Mg(NO₃)₂ was incorporated with varying quantities to the sol-gel precursor. The total quantity of metal ions in the precursor was kept constant and the relative amounts of the different metals were Cu: Fe : Mg = 1 : 1-X : X with 0 < X < 0.05. The procedure to prepare the electrode from the precursor solution was unchanged. Similar to oxygen intercalation, replacing a small fraction of the iron ions by magnesium ions had a measureable effect on the PEC behavior of the photocathode in O₂-purged electrolyte.

Photocurrents measured in the presence of O₂ and under one sun illumination for nine photoelectrode compositions are displayed in Figure 5.4a. Contrary to oxygen intercalation, these measurements were performed with a constant film thickness of *ca.* 300 nm. A clear effect of the composition on the photocurrent magnitude was observed: increasing the Mg content of the film initially improved the photocurrent density, but after an optimum was reached, further increasing the amount of Mg inside the film yielded decreasing performance. Except for high amounts of Mg ($X_{\text{Mg}} > 2\%$), no clear influence on the photocurrent onset (*i.e.* the apparent photovoltage) was observed. For better clarity, $|J_{ph}|$ values measured at 0.4 and 0.6 V vs RHE for each composition are shown in Figure 5.4b. The poor performance of the film containing 5% of Mg was omitted to better emphasize the photocurrent variation at low doping densities. The optimum photocurrent density was obtained for $X_{\text{Mg}} = 0.125\%$, at both potentials, reaching *ca.* 1.4 mA.cm⁻² at 0.4 V vs RHE. Interestingly, this optimized film produced more than 1.5 mA.cm⁻² at 0.35 V vs RHE – a performance similar to the optimized O-doped film presented in section 3.1.1. The increase in dopant density was monitored by plotting Mott-Schottky diagrams of the undoped and optimized doped film (see Figure 5.4c). From the linear part

of these plots, a threefold increase in acceptor density was measured for the doped film vs the bare CuFeO₂, while the photocurrent only increased by about 50%. This is in contrast with the result obtained for oxygen intercalation, where the increase in dopant density was similar to the increase in photocurrent. This indicates a different effect of doping by substitution vs doping by intercalation on the PEC performance of the film. Finally, the result of this experiment shows that substitutional doping can only provide at best a 50% increase in photocurrent, and therefore is not sufficient to solve the charge recombination issues observed in Chapter 4, section 4.3.

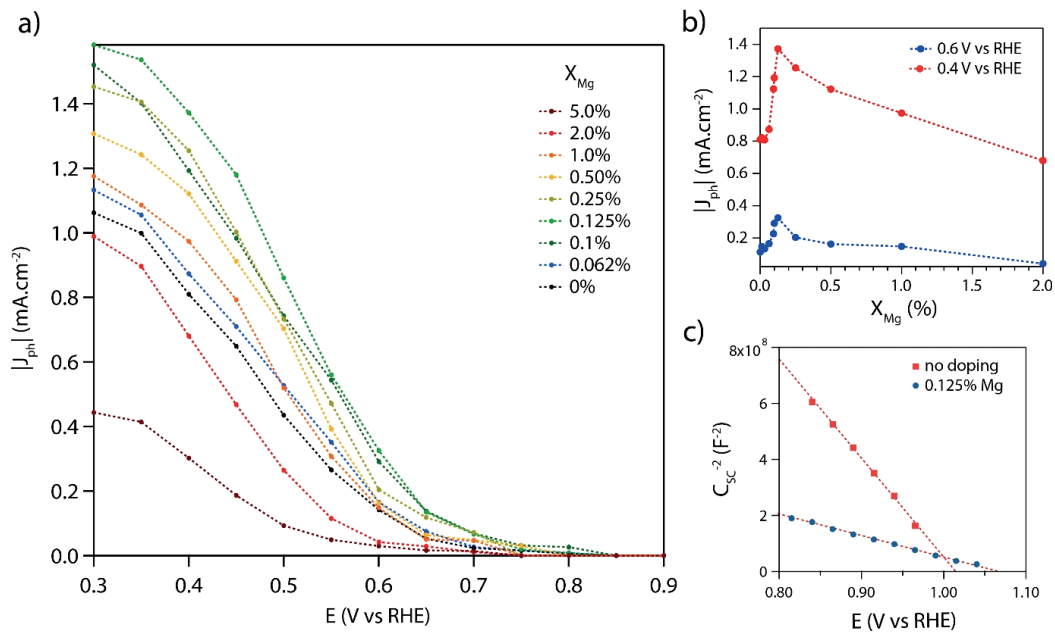


Figure 5.4 a) Absolute photocurrent (total current minus dark current) density $|J_{ph}|$ as a function of applied potential under one sun illumination for nine different atomic ratios of Mg in the precursor (see caption). b) Measured photocurrent density at 0.4 V vs RHE (blue) and 0.6 V vs RHE (red) under one sun illumination as a function of the atomic ratio of Mg. c) Mott-Schottky diagram of an undoped electrode (red) and an electrode doped with 0.125% of Mg. All three graphs were obtained for = 300 nm-thick CuFeO₂ thin films on FTO in O₂-saturated 1M NaOH.

Overall, extrinsic doping of CuFeO₂ by oxygen intercalation or Fe (III) substitution by Mg (II) both improved the photocurrent of the photocathode by 50%. This modest improvement was attributed to better charge separation at the SCLJ, due to a stronger built-in electric field (see Equation 2.23). However, increasing the dopant density also reduces the depletion width (see Equation 2.25), and therefore enlarges the neutral bulk region inside the semiconductor, and reduces the already thin charge harvesting depth of

the SCLJ. This means that majority carriers must diffuse for a longer time before being extracted at the $\text{CuFeO}_2/\text{FTO}$ interface, further increasing the chances of bulk recombination. This could partly explain why even doped electrodes only produce a fraction of the photocurrent anticipated from CuFeO_2 band positioning and absorption properties. Therefore, efforts to improve majority carrier collection at the back of the electrode are presented in the next section.

5.2 A Host-Guest $\text{CuAlO}_2/\text{CuFeO}_2$ photocathode

Optimization of the CuFeO_2 layer thickness suggested that the charge harvesting depth was relatively thin compared to the semiconductor thickness required for good light harvesting (based on the absorption coefficient). This discord between carrier transport and light absorption has been previously addressed with hematite photoanodes using the host-guest approach – where an extremely thin layer of the hematite light absorber was deposited on a high surface area scaffold with suitable electronic properties – resulting in the ability to decouple light absorption and charge transfer, reduce charge carrier recombination, and attain higher photocurrents.⁹⁻¹²

In order to apply this approach to CuFeO_2 , a p-type material must be identified to satisfy four basic criteria: (i) high transparency (large E_g), (ii) high p-type (hole) conductivity, (iii) valence and conduction band energy levels both higher, respectively, than CuFeO_2 , (to block back electron transfer and facilitate hole transfer from the absorber to the scaffold) and (iv) suitable stability in the conditions for the preparation of CuFeO_2 and for PEC testing. Unfortunately, only a few p-type scaffold candidates have been reported in the literature to date. NiO is by far the most commonly used, and has been sensitized with molecular dyes or quantum dots in photovoltaic¹³⁻¹⁵ or photoelectrosynthetic¹⁶⁻¹⁸ devices. However, despite its prevalence, NiO presents the drawbacks of significant visible light absorption and low hole mobility. Moreover, Nickel oxide is not stable at 700°C under inert atmosphere, as shown in the Ellingham diagram of the metal. This makes this material incompatible with the conditions necessary for the formation of p- CuFeO_2 . On the other hand, in recent reports, transparent delafossite materials, such as CuGaO_2 ¹⁹⁻²¹ and CuAlO_2 ²²⁻²⁴ have been suggested as attractive replacements for NiO . Indeed these materials have favorable light absorption properties and can display high charge carrier mobility, making them suitable candidates as

transparent conductive oxides (TCOs)^{25–27}. In addition, the stability of these Cu-based delafossites in aqueous environments make them attractive for applications in solar water splitting. Therefore, in this chapter, it is demonstrated that CuAlO₂, with a band gap of 3.5 eV, can be used as a low-cost solution-processed mesoporous scaffold in a host-guest configuration with CuFeO₂.

5.2.1 CuAlO₂/CuFeO₂ electrode preparation

To demonstrate the host-guest approach with CuFeO₂, the sol-gel synthesis of CuFeO₂ thin films presented in Chapter 4 was employed. While CuAlO₂ is a promising host material for CuFeO₂, it requires temperatures higher than 1000°C to form the delafossite phase. This prevents the direct formation of the material by a sol-gel method on the FTO substrate, thus the synthetic approach had to be adapted accordingly, i.e. using preformed CuAlO₂ nanoparticles. A fine powder of CuAlO₂ was prepared using an adapted sol-gel approach as described in the experimental section (Chapter 3, section 3.1.2) and X-Ray diffraction confirmed that the final powder was the desired pure crystalline delafossite phase (see Figure 5.5).

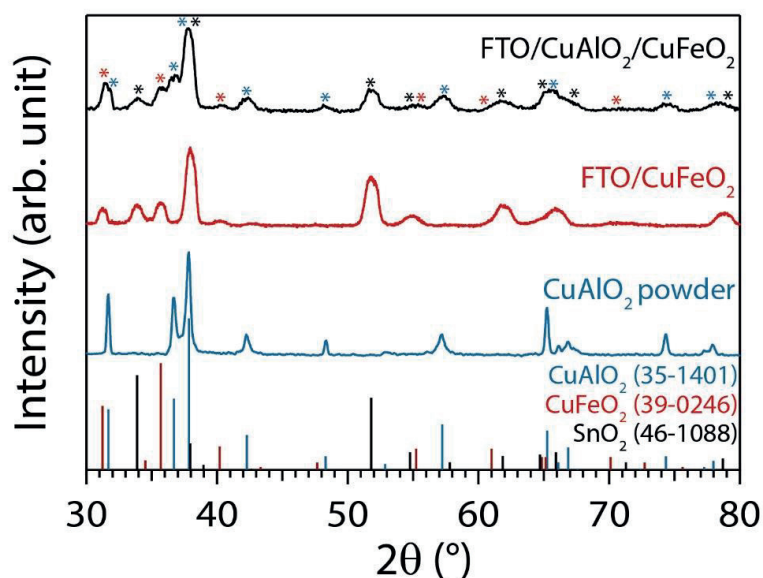


Figure 5.5 XRD spectra of CuAlO₂ powder (blue trace), CuFeO₂ film on FTO (red trace) and CuAlO₂/CuFeO₂ film on FTO (black trace). Films on FTO were measured under pseudo grazing incidence, whereas the CuAlO₂ powder was measured under locked-coupled conditions, causing a difference in peak broadness. Corresponding peak signals from the IPCC database are shown at the bottom of the figure.

In order to create high-surface area, porous thin films of the scaffold material on FTO, a viscous dispersion was prepared by grinding the powder with acetylacetone and hydroxypropyl cellulose (HPC). Acetylacetone was used as a surface ligand to increase dispersion stability and to enhance shear forces when grinding (wet grinding), which aids aggregate separation,²⁸ while HPC was used as the organic porogen and a rheology additive. This final dispersion had the consistency of a paste and was tape-cast onto FTO substrates. The resulting film was annealed at 450°C to remove the HPC and afford a mesoporous CuAlO_2 film.

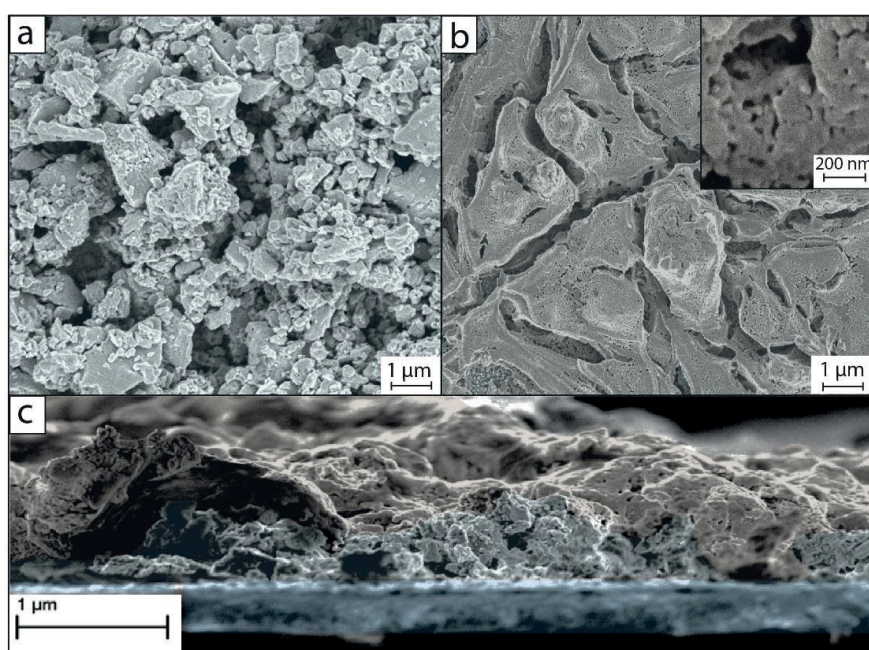


Figure 5.6 a) Top-view scanning electron micrograph of a 2 μm -thick CuAlO_2 scaffold on FTO. b) Top-view micrograph of the same electrode after the deposition of 6 layers of CuFeO_2 on the CuAlO_2 scaffold. Inset: zoomed-in top view of the same sample. c) Cross-sectional view of the same $\text{CuAlO}_2/\text{CuFeO}_2$ composite electrode. In each micrograph, CuAlO_2 is colorized in grey and CuFeO_2 is colorized in brown.

A scanning electron micrograph of a typical CuAlO_2 scaffold deposited on FTO is shown in Figure 5.6a. It shows a very rough morphology with a wide range of grain size: from 100 to 1000 nm. At the same time, a good coverage of the FTO substrate by the scaffold was observed. The thickness of the film was estimated using a profilometer, and could be varied between 500 and 2500 nm by controlling the concentration of the paste. To afford the final host/guest electrode the CuFeO_2 material was then deposited onto the CuAlO_2 scaffold. Optimization of the quantities for the two materials will be discussed

later. For the case of a CuAlO₂ scaffold of ca. 2 μm thick covered by 6 successive spin coating depositions of CuFeO₂, the resulting morphology is shown in Figure 5.6b. It appears that the CuFeO₂ completely covers the scaffold while retaining a mesoporous morphology (see Figure 5.6b inset). Finally, a cross-sectional view of the composite electrode, presented in Figure 5.6c, confirmed the existence of a high-surface area interface between CuFeO₂ and CuAlO₂. Finally, the composition of the host-guest electrode was investigated by XRD, and the resulting spectrum, shown in Figure 5.5, confirmed the presence of the desired crystalline phases only. The spectrum of a control electrode made of a thin film of CuFeO₂ on FTO is added for comparison. Having established the ability to fabricate the desired host/guest electrode it is next important to verify that the CuAlO₂ satisfies the basic criteria for performance as an effective host. First, UV-vis spectroscopy (see Figure 5.7) shows that the CuAlO₂ has a direct optical band gap of 3.51 eV and is thus transparent in the range from 1.45 to 3.1 eV where both the CuFeO₂ absorbs and there is an appreciable number of solar photons.

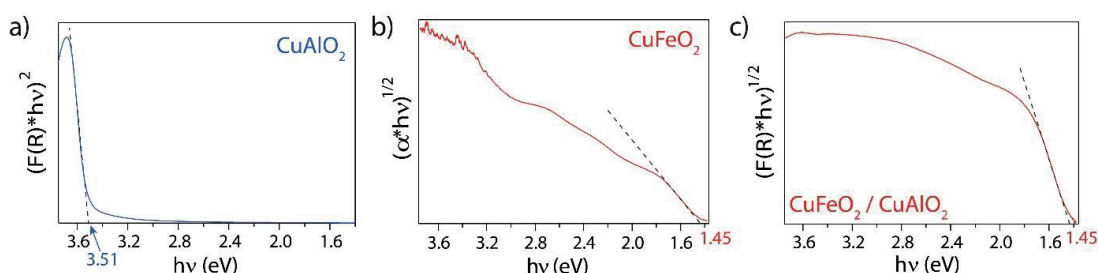


Figure 5.7 Tauc plots of the CuAlO₂ scaffold (a), a bare CuFeO₂ film (b) and a CuFeO₂/CuAlO₂ electrode (c)

5.2.2 Electrochemical Impedance spectroscopy

To verify that the electronic energy levels are suitable to accept majority carriers from the CuFeO₂ and block minority carriers, EIS was used to determine the position of the flat-band potential of CuAlO₂ and CuFeO₂. Nyquist plots of each material were acquired between 100 mHz and 100 kHz at different voltages—between +1.2 and +0.5 V vs RHE—and each the Nyquist plot was then fitted with a Randles circuit shown in Figure 5.8a – similar to the one used in Chapter 4. From the fit, a value of the space charge capacitance, C_{sc} , was calculated at each voltage, and used in the resulting Mott-Schottky plots displayed in Figure 5.8a. This yielded

flat-band potentials of +0.93 V vs RHE and +1.01 V vs RHE for CuAlO₂ and CuFeO₂, respectively.

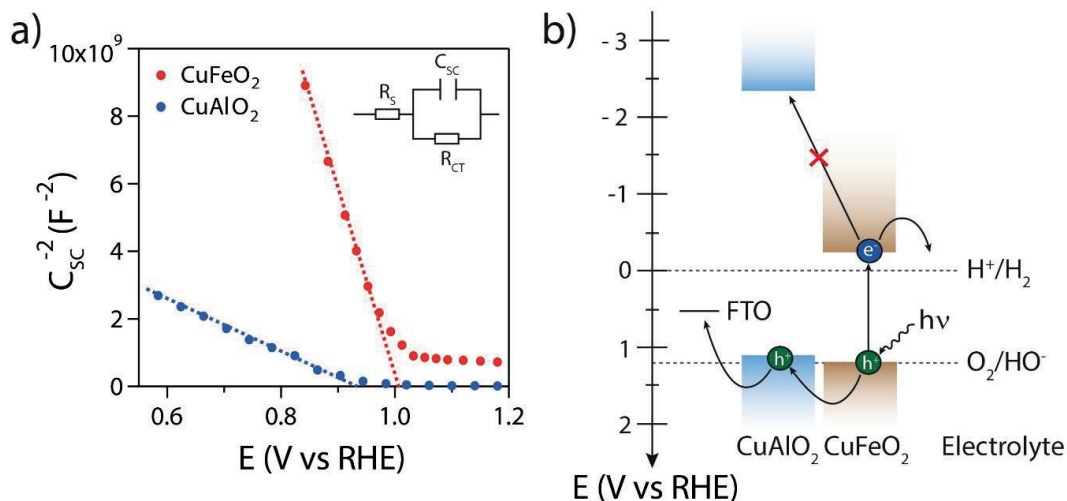


Figure 5.8 a) Mott-Schottky plot obtained for CuAlO₂ (blue trace) and CuFeO₂ (red trace) on FTO. The measurement was done in 1M NaOH, using the equivalent circuit shown in the top right corner. b) Simplified energy diagram of the host-guest CuAlO₂/CuFeO₂ electrode. Colorized areas represent energy bands, arrows indicate spontaneous charge transfer under illumination, and dashed lines mark the position of the water redox couples.

As expected, these potentials were relatively similar for the two materials, as their valence bands are both based on hybridized O(2p) and Cu(3d) orbitals, but not equal, as Al and Fe have different neighboring effects on the copper orbitals. In fact, CuAlO₂ was found to have a flat-band potential higher in energy than CuFeO₂. Since the valence band energy in both delafossites are likely offset by a similar amount from the Fermi level (given the absence of extrinsic dopants) this implies that the spontaneous transfer of holes from CuFeO₂ to CuAlO₂ is possible. A simplified sketch of the position of the energy levels is displayed in Figure 5.8b, as well as the corresponding spontaneous charge transfer that is expected to occur upon light absorption by the CuFeO₂ layer (recombination pathways are not represented). Valence bands of the two materials were positioned roughly 0.2 eV below their flat-band potential,²⁹ and the position of the corresponding conduction bands were estimated using the optical band gap of each materials (see Figure 5.7). The resulting sketch illustrates the role of CuAlO₂ as a viable hole-acceptor in the host-guest electrode.

5.2.3 Photoelectrochemical characterization

Given the favorable optoelectronic properties of the CuAlO₂/CuFeO₂ combination, the electrodes were subsequently submitted to photoelectrochemical evaluation. Electrodes were inserted in a PEC cell and illuminated by simulated sunlight. In an effort to keep the system as simple as possible, and since the aim of this work was to examine the influence of the scaffold on the light harvesting and charge separation properties of the electrode, the photoelectrochemical behavior was evaluated in the presence of O₂ as a sacrificial electron scavenger. A comparison of the LSV curves obtained under intermittent illumination with the best performing host-guest composite electrode (2 μ m scaffold/6 layers of CuFeO₂) and an optimized control CuFeO₂ electrode (ca. 300 nm layer without scaffold) is shown in Figure 5.9a.

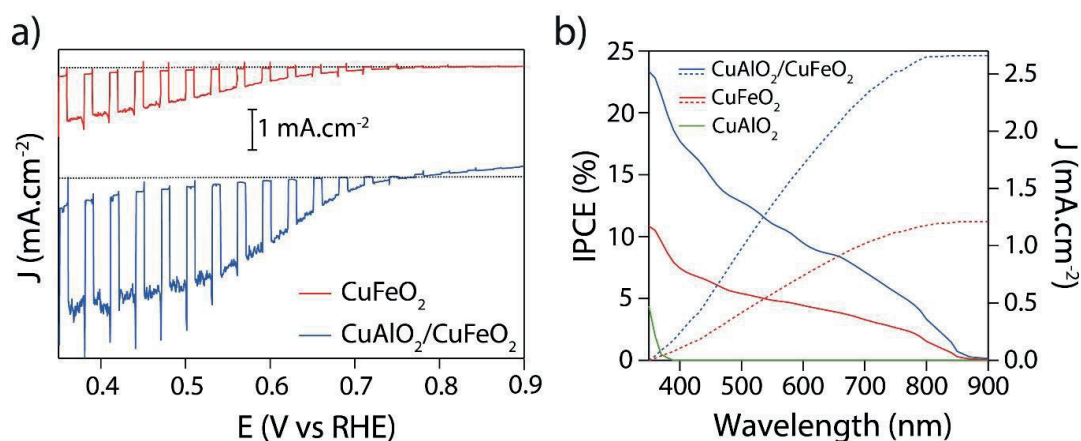


Figure 5.9 a) Comparison of LSV curves obtained for optimized CuAlO₂/CuFeO₂ (blue trace) and CuFeO₂ (red trace) electrodes, under O₂ bubbling. Electrolyte: 1M NaOH, scan rate: 10 mV.s⁻¹, illumination : 1 sun. b) IPCE spectra of CuAlO₂ (green solid line), CuFeO₂ (red solid line), and CuFeO₂/CuAlO₂ (blue solid line) electrodes. Corresponding integrated photocurrents are represented by the dotted lines, and referenced to the right-hand side y-axis.

Clearly, introducing the scaffold afforded an increase in photocurrent over the entire potential range scanned, while maintaining a good photocurrent onset potential of +0.75 V vs RHE of the bare material. Indeed, for the particular electrodes shown in Figure 5.9a, the photocurrent at +0.35 V vs RHE was improved from 1 mA cm⁻² for the control electrode to 2.4 mA cm⁻² for the composite one. More generally, averaged over a series of 5 electrodes prepared at each condition, the photocurrent delivered at +0.4 V vs RHE was

1.95 ± 0.25 mA cm⁻² for the host-guest electrode while the optimized control electrode delivered 0.98 ± 0.07 mA cm⁻² at the same potential. Notably the different uncertainty in the values of the composite electrode's average photocurrent compared to the control is evidence of increased variation in morphology between replicate electrodes. Nevertheless a clear enhancement in photocurrent was observed across the series. In addition it was observed that a bare CuAlO₂ electrode (without CuFeO₂) produced a very small photocurrent of only 0.13 mA.cm⁻² at +0.4 V vs RHE² (not shown here). This suggest that the photocurrent enhancement was due to an improved performance of the CuFeO₂ when the scaffold is employed.

To understand the origin of the photocurrent enhancement and to better quantify the benefit of the scaffold, the IPCE was measured for control electrodes consisting of only CuAlO₂ or CuFeO₂ and a host-guest CuAlO₂/CuFeO₂ electrode to determine how much of the incident light spectrum was productive in generating the observed photocurrents. The resulting spectra, shown in Figure 5.9b, reveal that CuAlO₂ itself only produces photocurrent at wavelengths lower than 400 nm with a small IPCE (green trace), consistent with small photocurrent observed. Importantly, an increase in IPCE was observed with the composite electrode (blue trace) over the entire wavelength range compared to the control CuFeO₂ electrode (red trace). Integrating these spectra with the standard AM 1.5G solar spectrum yielded predicted photocurrent densities of 1.2 and 2.6 mA.cm⁻² for the control and the host-guest electrodes respectively. These values are consistent with the photocurrent densities observed in the J-V curves (Figure 5.9a), given the small mismatch between the simulated sunlight and the AM 1.5G spectrum (see Chapter 3, section 3.3.3).

5.2.4 Thickness optimization

Further insight into the limitations and maximum extent of the photocurrent enhancement using the scaffold approach can be gained by independently varying the thickness of the host and guest layers. Given the consistent shape of the J-V curve, the photocurrent densities, J_{ph} at +0.4 V vs RHE can be used as a performance metric. Moreover, since the CuAlO₂ scaffold had the advantage of being transparent in the visible range, it was possible to compare the behavior of the electrodes under front (electrolyte-side) and back (substrate-side) illumination. A series of electrodes was prepared, where

the thickness of the scaffold was varied between 0.5 and 2.5 μm , and the number of CuFeO₂ deposition steps by spin coating were varied between 2 and 10 (each spin coating layer gives ca. 50 nm of CuFeO₂ on a bare FTO substrate, see Chapter 4). The results of this series of experiments are summarized in Figure 5.10. The photocurrent initially increased with the thickness of the scaffold for all CuFeO₂ thicknesses until a maximum at a scaffold thickness of 2 μm . Further increase in CuAlO₂ thickness caused the photocurrent to decrease. This trend was identical under front and back illumination, and was rationalized as follows: initially increasing the thickness of the CuAlO₂ film is beneficial as it increases the roughness of the electrode, but eventually at a certain thickness, the conductivity of the scaffold limits the current density, causing the photocurrent to decrease with increasing scaffold thickness. It was also observed that photocurrents were consistently higher when the electrode was under front illumination, suggesting that minority carrier transport was limiting in all cases.

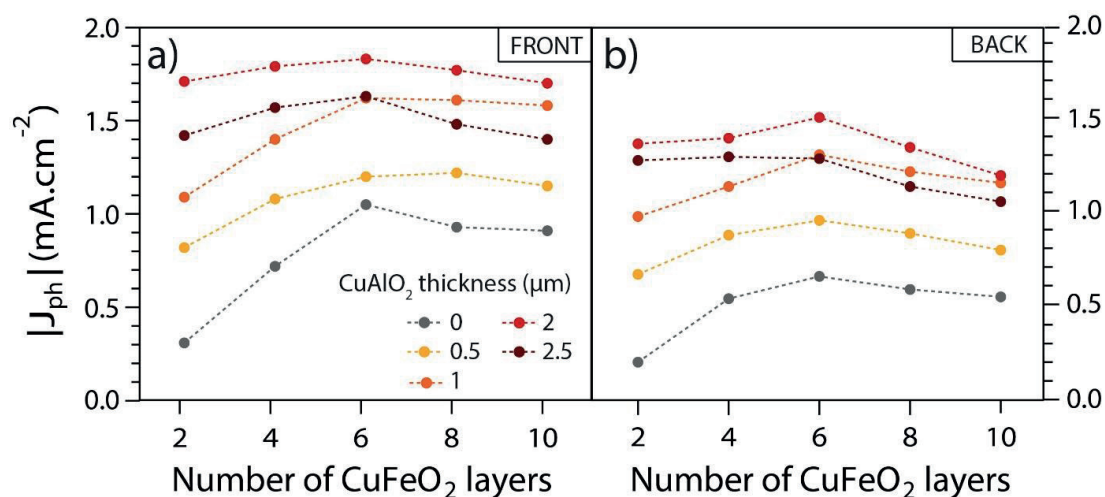


Figure 5.10 Photocurrent densities obtained for composite electrodes with several CuAlO₂ and CuFeO₂ contents, under front (a) and back (b) illumination and under an applied bias of +0.4 V vs RHE. Electrolyte: 1M NaOH purged with O₂, illumination: 1 sun.

The optimal CuFeO₂ loading was reached after 6 successive depositions regardless of the CuAlO₂ thickness. This is surprising as the quantity of CuFeO₂ deposited for each deposition step was expected to depend on the thickness of the CuAlO₂ scaffold. Assuming a constant void fraction, a higher amount of precursor material should be retained in thicker scaffolds after spin coating, resulting in a higher amount of CuFeO₂ for thicker CuAlO₂ scaffolds. To estimate and compare the relative amounts of CuFeO₂ between

different samples light absorbance measurements were done at 750 nm, since CuAlO₂ does not absorb at this wavelength. In order to estimate only the amount of light absorbed by the layer of CuFeO₂, the light reflected by the scaffold was removed from the incident beam in the calculations. The resulting measurements are shown in Figure 5.11a. The amount of CuFeO₂ after 6 successive spin coating depositions was observed to increase linearly with the thickness of the CuAlO₂ scaffold as expected (see Figure 5.11b). Based on these measurements the best performing host-guest electrode—prepared by 6 successive depositions on a 2 μ m CuAlO₂ scaffold—contained about 2.2 times more CuFeO₂ than the best performing bare CuFeO₂ electrode (prepared by 6 successive depositions directly on FTO).

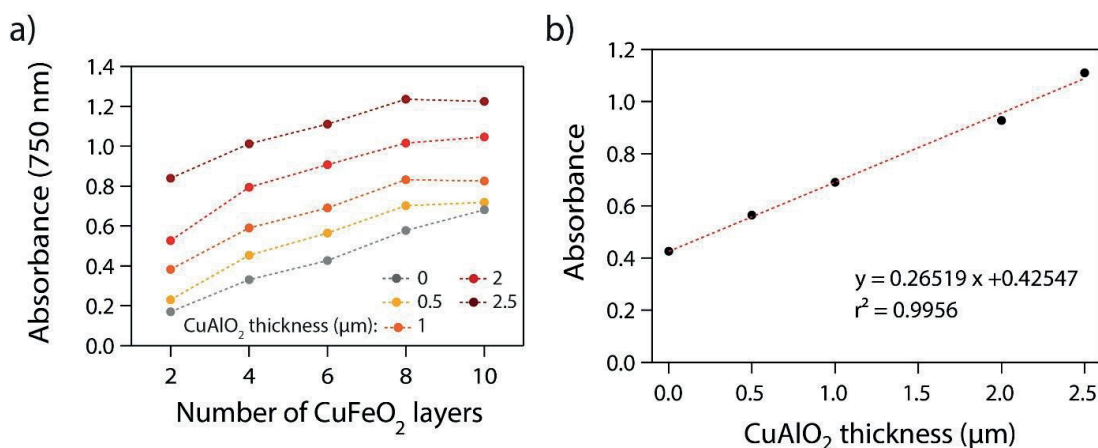


Figure 5.11 a) Absorbance of composite electrodes with several CuAlO₂ and CuFeO₂ contents at 750 nm. c) Dependence of the absorbance of composite electrodes made with 6 successive depositions of CuFeO₂ as a function of the scaffold thickness.

Clearly, the fact that the optimized composite electrode contains more than twice the amount of CuFeO₂ compared to the optimized control CuFeO₂ electrode suggests that the host-guest architecture is successful at increasing the amount of absorbing material without increasing the rate of recombination inside the film. This is consistent with the observed morphology, where the CuFeO₂ layer remains thin enough for efficient charge separation, but enables a higher absorber loading due to the roughness of the mesoporous scaffold. Indeed, the host/guest morphology increases the number of photons that are absorbed within the charge-separating layer at the CuFeO₂/electrolyte interface compared to the control case. It is therefore plausible that the enhancement of photocurrent in the composite electrode is merely due to this morphological effect, rather than to enhanced hole extraction from CuFeO₂.

5.2.5 Origin of photocurrent enhancement

To examine whether the photocurrent is enhanced due to a decreased recombination in the CuFeO₂ associated with hole injection into the CuAlO₂, the electrode light absorption was next investigated in detail to determine if the difference in total light absorption between the control CuFeO₂ and the composite CuAlO₂/CuFeO₂ electrode was commensurate with the difference in the photocurrents they produced. In this case, instead of performing the absorption measurement only at 750 nm (as was previously done to estimate the amount of CuFeO₂ in the electrode), here the entire wavelength range was examined and the reflective scattering induced by the CuAlO₂ substrate was also considered. For each electrode, the total transmission, as well as the total and diffuse reflectance were recorded with an integrating sphere. Using this data (see Appendix – Figure A1), the amount of light absorbed in each case was evaluated (see details in Chapter 3, section 3.2.1) and graphed in Figure 5.12 (solid lines).

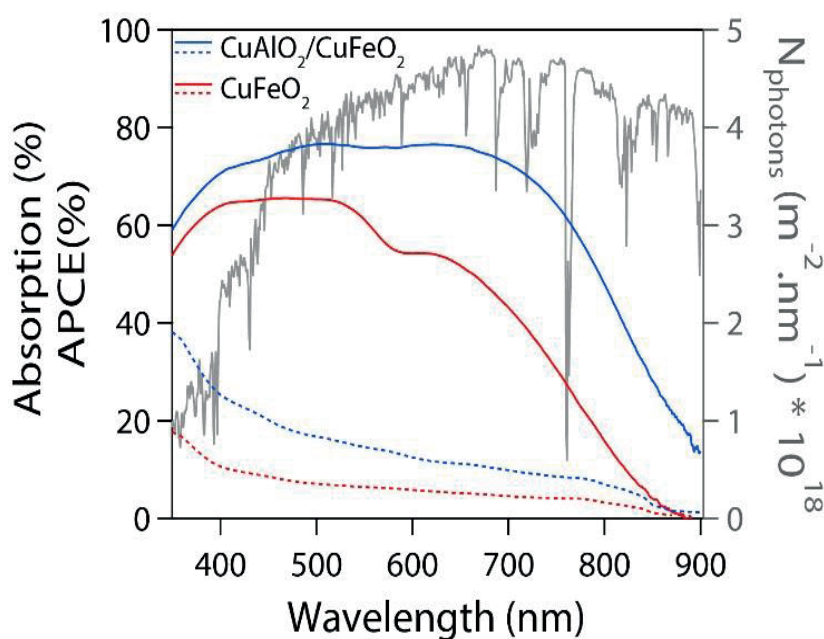


Figure 5.12 Absorption spectra of CuAlO₂/CuFeO₂ (blue solid line) and CuFeO₂ (red solid line) electrodes, and the associated APCE spectra (dotted lines), superimposed with the solar emission spectrum in photon density. Electrolyte: 1M NaOH purged with O₂, illumination: 1 sun.

Integrating the absorption spectra with the photon flux density under AM 1.5G conditions (100 mW.cm⁻²) indicated that the composite electrode absorbed 56% more photons than the control electrode over the entire wavelength range. While this increase

in absorption brought by the host-guest configuration was significant, it does not account for the entire photocurrent enhancement observed in the J-V curve (a factor of 2.4 increase). Indeed, the absorbed photon-to-current efficiency (APCE), also shown in Figure 5.12 (dotted lines), shows a uniform increase in internal quantum efficiency of CuFeO_2 in the composite electrode over the entire wavelength range. Importantly, in the case that morphology alone was responsible for the increase, one would expect to see a comparatively higher quantum efficiency near the absorption edge of the absorbing layer for the composite electrode⁹ due to the increased absorption depth of photons near the band edge. However in the normalized quantum efficiency (presented in Figure 5.12) the traces have an identical shape. This suggests that a combination of an increased light absorption – resulting in a higher number of photogenerated carriers and a reduction in recombination due to hole injection from the CuFeO_2 into the CuAlO_2 – were responsible for the improved photocurrents produced by the composite electrode.

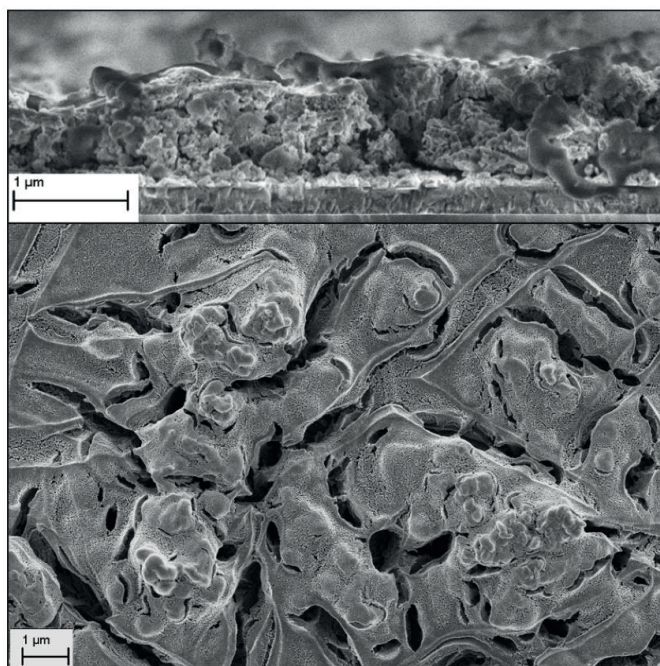


Figure 5.13 Cross-sectional and top views of a $\text{SiO}_2/\text{CuFeO}_2$ composite electrode

However, it is important to point out that, due to the highly porous morphology of the host-guest electrode, a non-negligible portion of CuFeO_2 is expected to be in direct contact with the FTO substrate. Additionally as pointed out previously, the higher photocurrents obtained under front illumination for all the

electrodes shown in Figure 5.10 suggest that minority carrier transport is limiting. Therefore, the possibility that majority carrier transport occurs completely inside the CuFeO₂ cannot be excluded. This prompted us to investigate the path taken by the photogenerated holes to reach the substrate. An obvious way to confirm that charges pass through CuAlO₂ would be to make a CuAlO₂/CuFeO₂ bilayer device where direct contact between the CuFeO₂ and FTO is eliminated. However, due to the high temperature treatment needed for CuAlO₂ processing, it was not possible to deposit a compact thin layer of this material directly on the substrate.

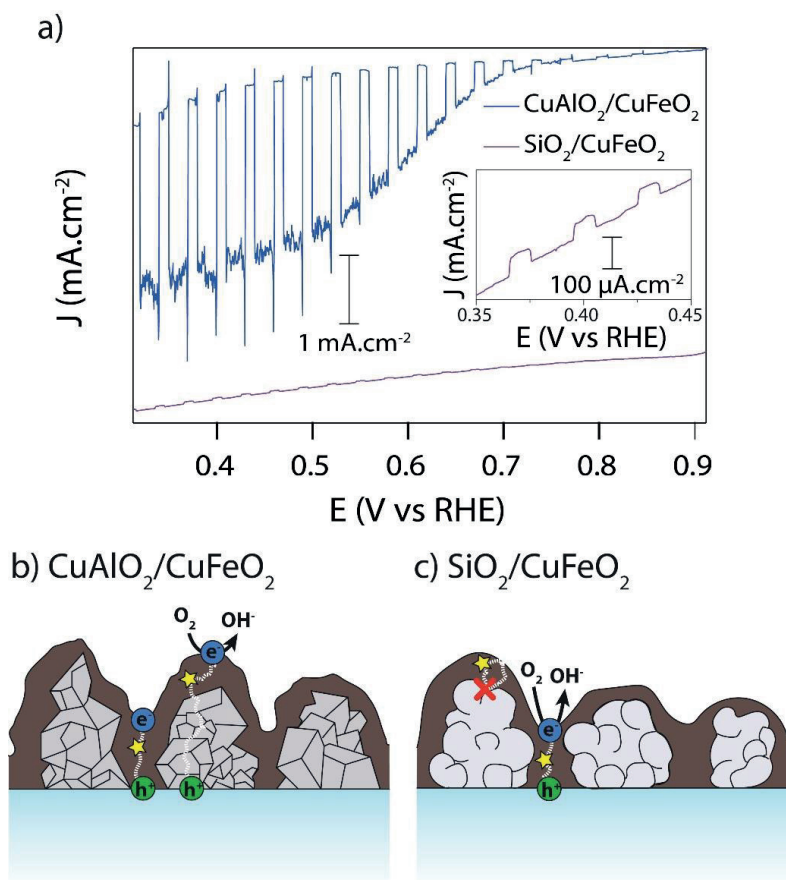


Figure 5.14 a) Comparison of J-V curves obtained for optimized CuAlO₂/CuFeO₂ (blue trace) and SiO₂/CuFeO₂ (black trace) electrodes, under O₂ bubbling. Electrolyte: 1M NaOH, scan rate: 10 mV.s⁻¹, illumination: 1 sun. The inset provides a detail on the J-V curve of the SiO₂/CuFeO₂ electrode for the potential range 0.35-0.45 V vs RHE b) Scheme of the possible pathways that photogenerated charges can take inside a CuAlO₂/CuFeO₂ electrode. The brown layer represents CuFeO₂. Holes can travel either inside the CuFeO₂ layer or through the CuAlO₂ scaffold. c) Scheme of the possible pathways that photogenerated charges can take inside a SiO₂/CuFeO₂ electrode. Holes are blocked at the surface of the insulating SiO₂ that acts as a recombination center. The only possible pathway for holes to reach the substrate is to travel exclusively inside the CuFeO₂ layer.

Instead the p-type mesoporous CuAlO_2 scaffold was replaced by an insulating SiO_2 scaffold prepared in a similar fashion and exhibiting a comparable morphology (see SEM images in Figure 5.13 and electrode sketches in Figure 5.14). This new electrode was then submitted to PEC testing in 1M NaOH in the presence of O_2 . The resulting J-V data are shown in of Figure 5.14a in comparison to the $\text{CuFeO}_2/\text{CuAlO}_2$ host-guest electrode. While a small photocurrent is observed in the $\text{SiO}_2/\text{CuFeO}_2$ electrode (see inset of Figure 5.14a), corresponding to the direct hole transfer from CuFeO_2 to the FTO, it is evident that replacing the p- CuAlO_2 scaffold by an insulating SiO_2 scaffold decreased the performance of the electrode dramatically. This result therefore confirms that photogenerated holes move through the p- CuAlO_2 scaffold in the host-guest electrode (as shown in Figure 5.14b), and also that a good band alignment between the host and guest materials is necessary to promote hole transfer towards the substrate. Otherwise, given the relatively poor conductivity of the CuFeO_2 , photogenerated holes will recombine before travelling through the CuFeO_2 to the substrate.

5.3 Conclusions

In a first study, it was demonstrated that the extrinsic doping of CuFeO_2 could improve its majority carrier conductivity and therefore its PEC performance. Both optimized thermal oxygen intercalation and Fe^{3+} substitution by Mg^{2+} resulted in a 50% increase in photocurrent for 300 nm-thick CuFeO_2 thin films, in the presence of an electron scavenger. While a noticeable increase in performance was noted, the highest photocurrent measured in this study was still far below the value anticipated from the good absorption properties of CuFeO_2 . This was rationalized in a thickness-dependence study where the existence of a low charge-harvesting depth was evidenced, hinting that increasing hole-extraction at the back of the electrode would help to further improve the photocurrent.

Therefore, in a second study, a host-guest composite electrode was presented, where the CuFeO_2 layer was supported by a hole-extracting p-type CuAlO_2 scaffold. CuAlO_2 displayed favorable optoelectronic properties in this configuration: it was transparent in the visible range ($E_g = 3.5$ eV) and its flat band potential was around 0.1 eV higher in energy than the one of CuFeO_2 suggesting

selective extraction photogenerated holes towards the substrate at the CuFeO₂/CuAlO₂ interface was possible. The solution-based deposition allowed for optimization of the composition of the host-guest electrode under front (electrolyte-side) and back (substrate side) illumination, during photoelectrochemical testing. Optimized CuAlO₂/CuFeO₂ electrodes consistently produced higher photocurrents than their optimized CuFeO₂ electrode counterparts, with photocurrents measured to be up to 2.4-fold higher for the composite electrode. This improvement in performance was found to be not only due to better charge separation but also to an improved morphology – a thin layer of CuFeO₂ on top of a highly porous CuAlO₂ scaffold – where a higher amount of CuFeO₂ could be incorporated to the electrode before reaching minority carrier transport limitations. Furthermore, using a control electrode in which CuAlO₂ was replaced by insulating SiO₂, it was concluded that most of the photogenerated holes effectively travelled through the scaffold, since only very little photocurrent was observed with the insulating scaffold. This study therefore demonstrated that CuAlO₂ and CuFeO₂ formed an efficient host-guest system, displaying higher photocurrents, stemming from better charge separation and charge transport properties than for the bare CuFeO₂ material. Based on its optoelectronic properties and the chemical stability, it is also expected that CuAlO₂, as a p-type transparent conductive oxide, should be a suitable hole-extracting scaffold for a variety of p-type photocathode materials.

Overall, extrinsic doping and the host-guest architecture provided two different and complementary avenues for improving the PEC performance of CuFeO₂: doping could help charge separation at the SCLJ, while using a thin film of CuFeO₂ on top of a mesostructured hole-accepting underlayer could help majority carrier transport and extraction. These approaches tested with an electron scavenger show that by combining morphological and electronic approaches, a CuFeO₂ photoelectrode with sufficient performance for use in an all-oxide tandem cell for solar hydrogen production should be feasible, once the issue of poor charge transfer to the electrolyte is solved. This particular issue will therefore be the focus of the next sections.

5.4 References

- (1) Prévot, M. S.; Guijarro, N.; Sivula, K. *ChemSusChem* **2015**, *8* (8), 1359–1367.
- (2) Prévot, M. S.; Li, Y.; Guijarro, N.; Sivula, K. *J. Mater. Chem. A* **2016**, *4* (8), 3018–3026.
- (3) Zhao, T.-R.; Hasegawa, M.; Takei, H. *J. Cryst. Growth* **1997**, *181* (1), 55–60.
- (4) Mugnier, E.; Barnabé, A.; Tailhades, P. *Solid State Ion.* **2006**, *177* (5–6), 607–612.
- (5) Lalanne, M.; Barnabé, A.; Mathieu, F.; Tailhades, P. *Inorg. Chem.* **2009**, *48* (13), 6065–6071.
- (6) Lalanne, M.; Demont, P.; Barnabé, A. *J. Phys. Appl. Phys.* **2011**, *44* (18), 185401.
- (7) Deng, Z.; Fang, X.; Wu, S.; Zhao, Y.; Dong, W.; Shao, J.; Wang, S. *J. Alloys Compd.* **2013**, *577*, 658–662.
- (8) Gu, J.; Wuttig, A.; Krizan, J. W.; Hu, Y.; Detweiler, Z. M.; Cava, R. J.; Bocarsly, A. B. *J. Phys. Chem. C* **2013**, *117* (24), 12415–12422.
- (9) Sivula, K.; Formal, F. L.; Grätzel, M. *Chem. Mater.* **2009**, *21* (13), 2862–2867.
- (10) Lin, Y.; Zhou, S.; Sheehan, S. W.; Wang, D. *J. Am. Chem. Soc.* **2011**, *133* (8), 2398–2401.
- (11) Hisatomi, T.; Dotan, H.; Stefiak, M.; Sivula, K.; Rothschild, A.; Grätzel, M.; Mathews, N. *Adv. Mater.* **2012**, *24* (20), 2699–2702.
- (12) Wang, L.; Palacios-Adrós, A.; Kirchgeorg, R.; Tighineanu, A.; Schmuki, P. *ChemSusChem* **2014**, *7* (2), 421–424.
- (13) Gibson, E. A.; Smeigh, A. L.; Le Pleux, L.; Fortage, J.; Boschloo, G.; Blart, E.; Pellegrin, Y.; Odobel, F.; Hagfeldt, A.; Hammarström, L. *Angew. Chem. Int. Ed.* **2009**, *48* (24), 4402–4405.
- (14) Nattestad, A.; Mozer, A. J.; Fischer, M. K. R.; Cheng, Y.-B.; Mishra, A.; Bäuerle, P.; Bach, U. *Nat. Mater.* **2010**, *9* (1), 31–35.
- (15) Barceló, I.; Guillén, E.; Lana-Villarreal, T.; Gómez, R. *J. Phys. Chem. C* **2013**, *117* (44), 22509–22517.
- (16) Li, L.; Duan, L.; Wen, F.; Li, C.; Wang, M.; Hagfeldt, A.; Sun, L. *Chem. Commun.* **2012**, *48* (7), 988–990.
- (17) Ji, Z.; He, M.; Huang, Z.; Ozkan, U.; Wu, Y. *J. Am. Chem. Soc.* **2013**, *135* (32), 11696–11699.
- (18) Yang, H. B.; Miao, J.; Hung, S.-F.; Huo, F.; Chen, H. M.; Liu, B. *ACS Nano* **2014**, *8* (10), 10403–10413.
- (19) Yu, M.; Natu, G.; Ji, Z.; Wu, Y. *J. Phys. Chem. Lett.* **2012**, *3* (9), 1074–1078.

- (20) Renaud, A.; Chavillon, B.; Pleux, L. L.; Pellegrin, Y.; Blart, E.; Boujtita, M.; Pauporté, T.; Cario, L.; Jobic, S.; Odobel, F. *J. Mater. Chem.* **2012**, *22* (29), 14353–14356.
- (21) Renaud, A.; Cario, L.; Deniard, P.; Gautron, E.; Rocquefelte, X.; Pellegrin, Y.; Blart, E.; Odobel, F.; Jobic, S. *J. Phys. Chem. C* **2014**, *118* (1), 54–59.
- (22) Nattestad, A.; Zhang, X.; Bach, U.; Cheng, Y.-B. *J. Photonics Energy* **2011**, *1* (1), 011103-011103-9.
- (23) Ahmed, J.; Blakely, C. K.; Prakash, J.; Bruno, S. R.; Yu, M.; Wu, Y.; Poltavets, V. V. *J. Alloys Compd.* **2014**, *591*, 275–279.
- (24) Yu, M.; Draskovic, T. I.; Wu, Y. *Phys. Chem. Chem. Phys.* **2014**, *16* (11), 5026–5033.
- (25) Kawazoe, H.; Yasukawa, M.; Hyodo, H.; Kurita, M.; Yanagi, H.; Hosono, H. *Nature* **1997**, *389* (6654), 939–942.
- (26) Scanlon, D. O.; Walsh, A.; Watson, G. W. *Chem. Mater.* **2009**, *21* (19), 4568–4576.
- (27) Herraiz-Cardona, I.; Fabregat-Santiago, F.; Renaud, A.; Julián-López, B.; Odobel, F.; Cario, L.; Jobic, S.; Giménez, S. *Electrochimica Acta* **2013**, *113*, 570–574.
- (28) Ito, S.; Chen, P.; Comte, P.; Nazeeruddin, M. K.; Liska, P.; Péchy, P.; Grätzel, M. *Prog. Photovolt. Res. Appl.* **2007**, *15* (7), 603–612.
- (29) Read, C. G.; Park, Y.; Choi, K.-S. *J. Phys. Chem. Lett.* **2012**, *3* (14), 1872–1876.

Chapter 6

Evaluating charge carrier transport and surface states in CuFeO₂ photocathodes

In Chapter 4, two major limitations of CuFeO₂ photocathodes are described: poor charge transport and separation on one hand, and poor charge injection to the electrolyte to perform the electrochemical reduction of water. The first type of limitation is addressed in Chapter 5, where electronic and morphological tuning is employed to improve the PEC performance of CuFeO₂ photocathodes in the presence of an electron scavenger. However, after optimization, the final photocurrent observed with these electrodes remains lower than 3 mA.cm⁻², far below the 15 mA.cm⁻² expected from light absorption measurements. This observation and the absence of photocurrent in the absence of electron scavenger warrants a more in-depth investigation of charge transport and charge transfer processes in the bulk of photocathode and at the SCLJ. In this chapter, a detailed investigation relying on spectroscopic and PEC techniques, aims at clarifying the bulk and surface electronic properties of CuFeO₂ in order to explain the reason for these limitations. This represents the first in-depth study of a CuFeO₂ photocathodes, and it should provide guidelines for future research work aimed at improving the PEC performance of the material.

This chapter has been adapted from “Evaluating Charge Carrier Transport and Surface States in CuFeO₂ Photocathodes”¹ (Prévot, M.S. *et al.*, *Chem. Mater.*, **2017**, 29, 4952-4962)

6.1 Thin film preparation and phase-purity assessment

The CuFeO₂ thin films investigated in this study were prepared using the Pechini-type sol-gel method reported in Chapter 4.² Importantly, for this study, the examined films were slightly thinner than the ones presented in previous chapter, using less deposition steps for the sake of faster film processing – as thickness did not appear to have a major effect on the limitations identified in CuFeO₂ photocathodes.

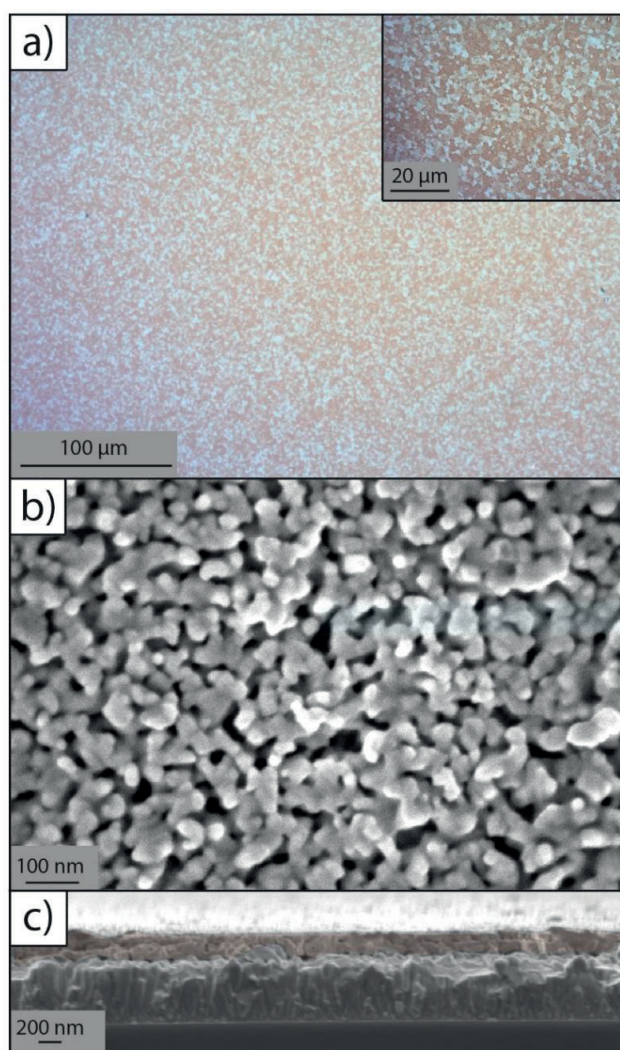


Figure 6.1 a) Optical microscope image of a typical CuFeO₂ electrode. The inset shows an image obtained at higher magnification. Both images were obtained in transmission (the incident light was going through the transparent sample). No presence of bright red hematite was observed. b) Top view SEM image of the surface of the same electrode c) Cross-sectional SEM image of the same electrode: the CuFeO₂ layer is colored in brown.

The morphology of the resulting film was monitored by optical microscopy and SEM, as shown in Figure 6.1. The expected nanoporous morphology was observed, arising from the crystallization at high temperature, along with a film thickness of 200 nm (vs. 300 nm for previous chapter).

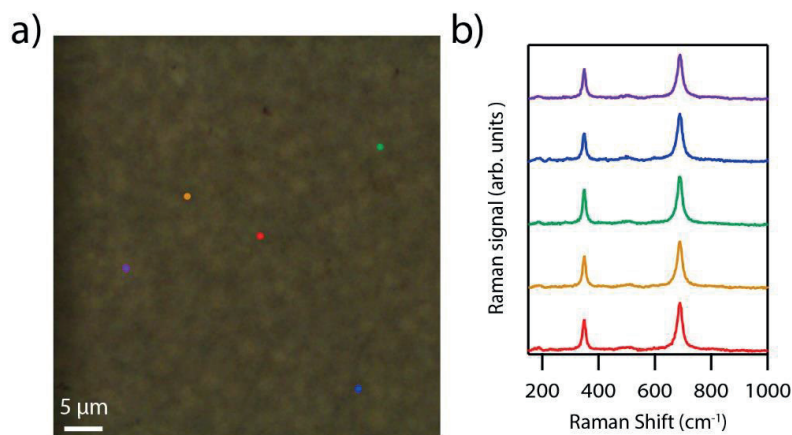


Figure 6.2 a) Optical microscope image of the surface of a CuFeO_2 thin film. The colored dots indicate the locations at which the Raman spectra displayed in (b) were acquired. For each of the five measurements, only the two peaks associated with CuFeO_2 were observed, with no trace of secondary phase.

One concern with the sol-gel processing of CuFeO_2 thin films is the potential creation of secondary phases, such as hematite or CuO .³ Therefore, the preparation conditions were carefully optimized to ensure that no secondary phase were present, as supported by microscopy (Figure 6.1a and c) and Raman data (Figure 6.2) – where only the vibration peaks corresponding to CuFeO_2 were observed.

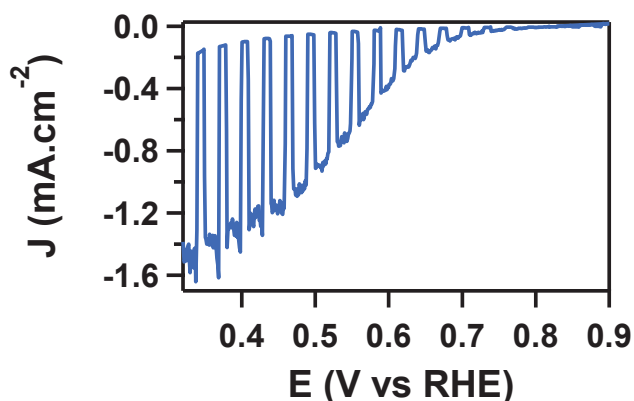


Figure 6.3 Typical LSV curve obtained for a CuFeO_2 photocathode under chopped 1 sun illumination in O_2 -purged 1M NaOH. Scan rate: 10 mV/s.

A typical linear sweep voltammetry (LSV) curve of the CuFeO₂ electrode (on FTO coated glass) in O₂-purged 1M NaOH (Figure 6.3) illustrates the PEC performance for sacrificial O₂ reduction. The observed photocurrent is reproducible in the 1.3-1.5 mA cm⁻² range at 0.4 V vs RHE.

These verifications confirmed that the electrodes studied in this section, although thinner, were performing with similar (even slightly better) performance than the electrodes of the initial study reported in Chapter 4. Moreover no secondary phase was visible by microscopy or spectroscopy, discounted this possible reason for the observed low performance. From there, this low PEC performance – reminiscent from the ones observed for instance in pyrite⁴ or hematite⁵⁻⁸ – can be rationalized by the presence of either surface or bulk defect states that promote charge recombination. There is an important distinction between these two possibilities, as bulk and surface defects require different treatment strategies. While a high density of bulk defects based on intrinsic properties can permanently prevent application of a material as a photoelectrode, surface states are arguably easier to tackle with adequate post-processing treatments such as applying overlayers⁹ or etch/regrowth¹⁰ repairing techniques. Therefore, in order to clarify whether the low performance observed in CuFeO₂ originates from bulk or surface defects, a comprehensive investigation based on a variety of PEC, microscopic and spectroscopic techniques, is presented in the next sections.

6.2 Time-resolved microwave conductivity

As a first step, it was investigated whether the performance of CuFeO₂ is limited by its intrinsic bulk properties using time-resolved microwave conductivity (TRMC). TRMC is a contactless technique that can be used to monitor charge carrier mobility and lifetime in inorganic or organic semiconductors.¹¹⁻¹³ In this pump-probe method, a nanosecond laser pulse first excites the material, and the resulting transient of the reflected microwave power is subsequently probed. The measured change in reflected power is directly proportional to the sum of the mobilities $\Sigma\mu$ of free carriers in the film. We note that, while TRMC does not offer a direct way to discriminate between the mobilities of majority and minority carriers, it is possible to separate them using their difference in effective masses (see Chapter 3, section 3.2.6 for more explanation). TRMC transients were collected for a typical CuFeO₂ film at different pulse intensities (see Figure 6.4a). For

each transient TRMC signal, the peak value corresponds to a lower bound of $\Phi\Sigma\mu$, where Φ represents the quantum yield of photogenerated charges, considering the charge recombination within the pulse is not measured. This peak value of $\Phi\Sigma\mu$ is plotted against the photon flux of the pulse in Figure 6.4b for two similarly absorbing CuFeO₂ films (Figure 6.4a) prepared on quartz substrates.

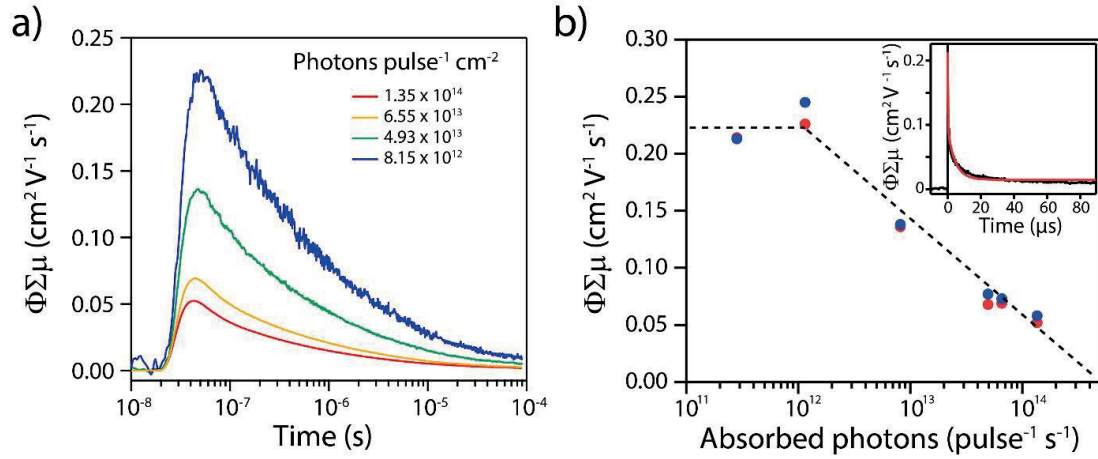


Figure 6.4 a) TRMC spectra obtained for a CuFeO₂ thin film for different pump intensities. b) Peak TRMC signal values measured for two duplicate CuFeO₂ thin films (red and blue markers, respectively), at different flux of incident photons per pulse. Inset: typical TRMC signal produced by a thin film of CuFeO₂ after a pulse of 8.15×10^{12} photons cm^{-2} . The red trace represents the biexponential fit. The pulse wavelength was 330 nm for all measurements. AM1.5 illumination is equivalent to $\sim 10^9 \text{ cm}^{-2} \text{ pulse}^{-1}$.

At high photon densities, $\Phi\Sigma\mu$ decreases with the log of photon density, due to fast non-geminate electron-hole recombination. The slope of the plot in this range ($\Phi\Sigma\mu \propto I_{\text{abs}}^{\alpha-1}$, with α the reciprocal of the order of recombination¹³) yields $\alpha = 0.7$, indicating a combination of first and second order recombination at high illumination intensities. On the other hand, at lower photon densities, $\Phi\Sigma\mu$ is approximately constant, indicating a first order recombination, and thus corresponds to the intrinsic bulk properties of the absorbing CuFeO₂ layer. In this range of photon densities, $\Phi\Sigma\mu$ was found to have a value of about $0.225 \text{ cm}^2 \text{V}^{-1} \text{s}^{-1}$ (average over the two samples measured), which gives us a lower estimate for $\Sigma\mu$ in the film. This value is in agreement with previously reported Hall measurements for CuFeO₂,¹⁴ is one order of magnitude lower than for WO₃ and Cu₂O, one order of magnitude higher than for BiVO₄ and similar to that of α -Fe₂O₃.¹¹ Moreover, the time constant associated with the decay is a direct measure of the lifetime of photogenerated carriers inside the active layer. This decay was fit with a biexponential model (see inset of Figure 6.4b), which yielded time constants of $\tau_1 = 200 \text{ ns}$ and $\tau_2 =$

4 μ s. For comparison, the lifetime of charge carriers in Cu₂O and α -Fe₂O₃ were reported to be only on the order of picoseconds,^{15,16} while τ can reach a few tens of nanoseconds in BiVO₄.¹⁷ Therefore, these results indicate that charge carriers are relatively long lived in CuFeO₂. Given that τ_2 is typically attributed to trapped carriers, an estimated free carrier diffusion length, L , can be calculated using τ_1 as $L = (D\tau_1)^{1/2} = 225$ nm, where $D = k_B T \mu / e$ is the diffusion coefficient of the charge carriers, k_B is Boltzmann's constant, T is the temperature and e is the elementary charge. This diffusion length is in good agreement with the optimum film thickness of ~ 300 nm previously reported for this material (see Chapter 4).²

Finally, the results of the TRMC measurement could further be used to get an estimation of the upper limit for the photovoltage achievable by CuFeO₂, according to the relation proposed by Lewis:¹⁸

$$V_{OC,max} \cong \frac{k_B T}{e} \ln \left(\frac{J_{ph} L_n N_A}{e D_n n_i^2} \right)$$

where J_{ph} the photocurrent measured at 0 V vs the reversible hydrogen electrode (RHE), L_n the diffusion length of electrons, N_A the acceptor density, D_n the diffusivity of electrons and n_i is the density of thermally produced charge carriers inside the film. Using the most conservative estimations for the different parameters (see Chapter 3, section 3.2.6 for details): $D_n = 2.5 \times 10^{-3} \text{ cm}^2 \text{ s}^{-1}$, $n_i^2 \cong 8.76 \times 10^{11} \text{ cm}^{-6}$, $L_n = 225$ nm, $J_{ph} = 0.6 \text{ mA cm}^{-2}$, $N_A = 10^{18} \text{ cm}^{-3}$, a maximum expected open-circuit potential of 1.1 V is found (in absence of surface recombination or shunting across the potential barrier at the junction). Since the water reduction potential is reported at roughly 300 mV below the conduction band edge of CuFeO₂,² a photovoltage of around 0.8 V for water reduction at the surface of a CuFeO₂ photocathode is reasonably expected.

It is important to note that this analysis assumes a value for D_n based on an estimated mobility of electrons, μ_e , of $0.1 \text{ cm}^2 \text{ V}^{-1} \text{ s}^{-1}$ (see Chapter 3, section 3.2.6). While this values accords with the TRMC measurement presented here and other reports as mentioned, an early report suggests an extremely low electron mobility for Sn-doped n-type CuFeO₂ ($10^{-6} \text{ cm}^2 \text{ V}^{-1} \text{ s}^{-1}$).¹⁹ However, the recent calculations performed on other p-type copper-based delafossites^{20,21} suggest similar effective masses and therefore similar mobility for holes and electrons (within one order of magnitude). This is

supported by the thickness-dependence study detailed in Chapter 4², which implies that photogenerated electrons can diffuse hundreds of nanometers and produce a photocurrent under substrate-side illumination. The very low electron mobility in the Sn doped samples could be due to detrimental effects of cation substitution on the crystal structure. Overall, the conservative photovoltage value of 0.8 V reported here indicates that bulk processes should not drastically limit the performance of CuFeO₂, and rather suggests that interfacial recombination plays a predominant role in the system at hand. In the following sections, we use a variety of methods to characterize this phenomenon.

6.3 Photoelectrochemical properties

A convenient method to investigate the SCLJ is to photoelectrochemically “map” the bandgap of the semiconducting electrode using a series of redox species with electrochemical potentials varying from the valence band edge potential to the conduction band edge potential.^{22–26} In order to apply this approach to CuFeO₂ we relied on a series of fast outer-sphere electron transfer-based redox couples to reduce the influence of charge transfer kinetics as much as possible. These couples, used either in water or in acetonitrile are shown schematically in Figure 6.5 with respect to their redox potentials relative to the position of the bands of CuFeO₂ under flat-band conditions.

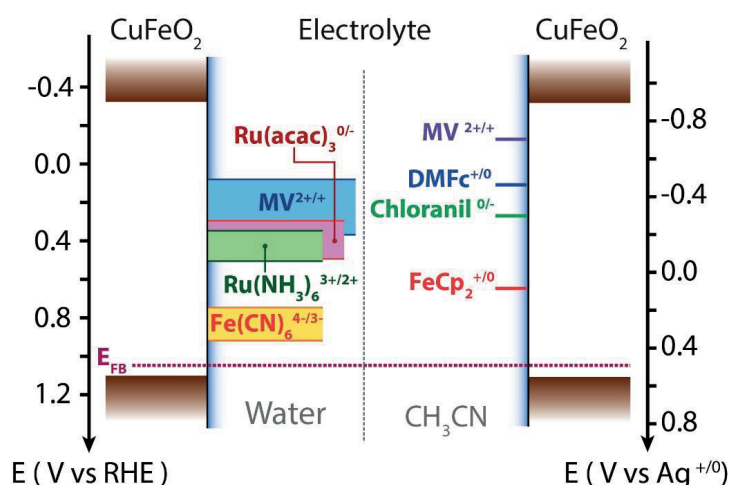


Figure 6.5 Schematic representation of the potential regions probed by the different redox couples used in this study shown next to the band position of CuFeO₂, under flat-band conditions, in water (left side) and in acetonitrile (right side). Note: the band bending induced by the junction is not represented. MV = Methyl Viologen, DMFc = decamethylferrocene, E_{FB} = Flat-band potential of CuFeO₂.

Note that in the case of aqueous electrolytes, ranges of potentials are shown rather than a single value. This is due to a change in electrolyte pH, and because the band edges of oxide semiconductors including CuFeO₂ display a Nernstian behavior with the pH at the SCL: $E(\text{pH}) = E(\text{pH } 0) - 0.059 \times \text{pH} [\text{V}]$ at 25°C. Since none of the redox couples used herein involve the transfer of protons (and are thus not sensitive to pH), by increasing the pH of the electrolyte by one unit the redox $E_{1/2}$ effectively shifts by + 59 mV with respect to the band edges of the semiconductor. Consequently varying the pH allows to probe a range of potentials using a single aprotic redox couple.²⁶ The values of $E_{1/2}$ for each electrolyte were measured by cyclic voltammetry: for a reversible electron transfer, $E_{1/2}$ is given by the arithmetic mean of the oxidative peak and reductive peak potentials (see Figure 6.6).

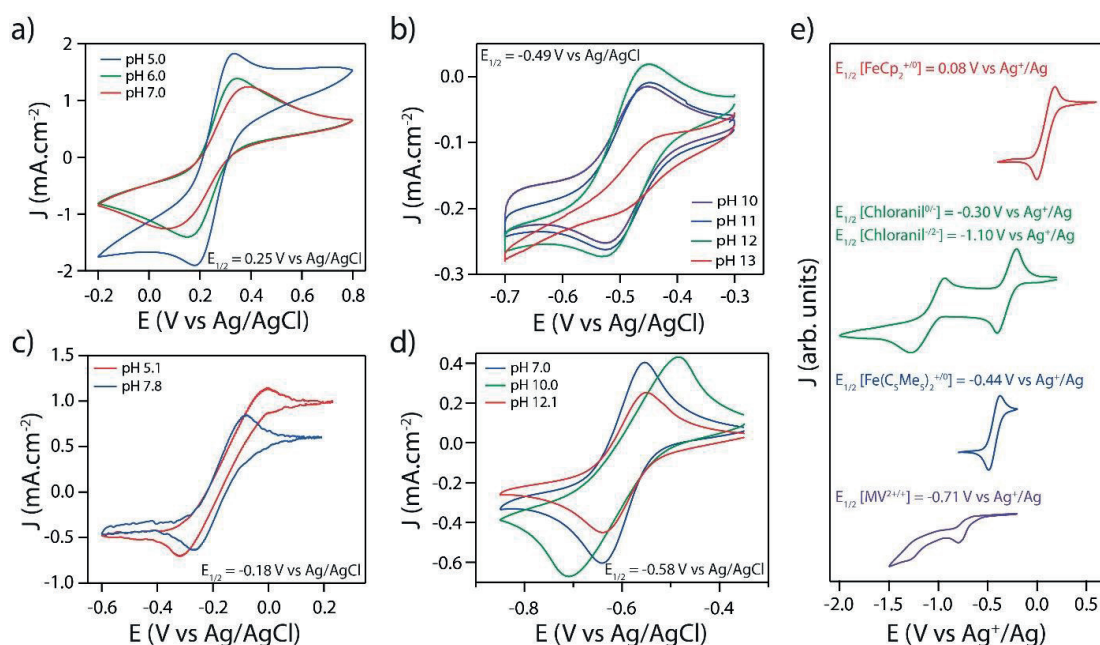


Figure 6.6 Cyclic voltammograms obtained at different pH (indicated on each graph) in water for a) 0.05 M Fe(CN)₆^{3-/4-} b) 0.001 M Ru(acac)₃^{0/-}, c) 0.005 M Ru(NH₃)₆^{3+/2+} and d) 0.01 M MV^{2+/+}. e) Cyclic voltammograms obtained for 0.01 M FeCp₂^{+/0}, 0.01 M Chloranil^{0/2-}, 0.003 M Fe(C₅Me₅)^{+/0} and 0.001 M MV^{2+/+} in 0.1 M TBAP/CH₃CN. All the scans were obtained on a Pt electrode at 5 mV/s.

6.3.1 Linear Sweep Voltammetry measurements

In a first series of measurements, CuFeO₂ (on FTO) was put in contact with two different redox couples in water: Fe(CN)₆^{3-/4-} ($E_{1/2} = 0.25 \text{ V vs Ag/AgCl}$) and Ru(acac)₃^{0/-} ($E_{1/2} = -0.49 \text{ V vs Ag/AgCl}$). The resulting LSV curves for CuFeO₂ under intermittent (1

sun) illumination are shown in Figure 6.7a and b with respect to $E_{1/2}$ (where the red star symbols on each curve represent a fixed potential on the RHE scale as indicated). When using $\text{Fe}(\text{CN})_6^{3-/4-}$ between pH 5 and 7 (i.e. when varying $E_{1/2}$ between 0.75 and 0.87 V vs RHE), we observed a clear shift in onset potential for the photocurrent with respect to $E_{1/2}$. However, the onset of photocurrent occurred at a constant potential vs RHE (around 1.0 V vs RHE), in good agreement with the flat-band potential, E_{FB} , of 1.01 V vs RHE previously reported for CuFeO_2 .²

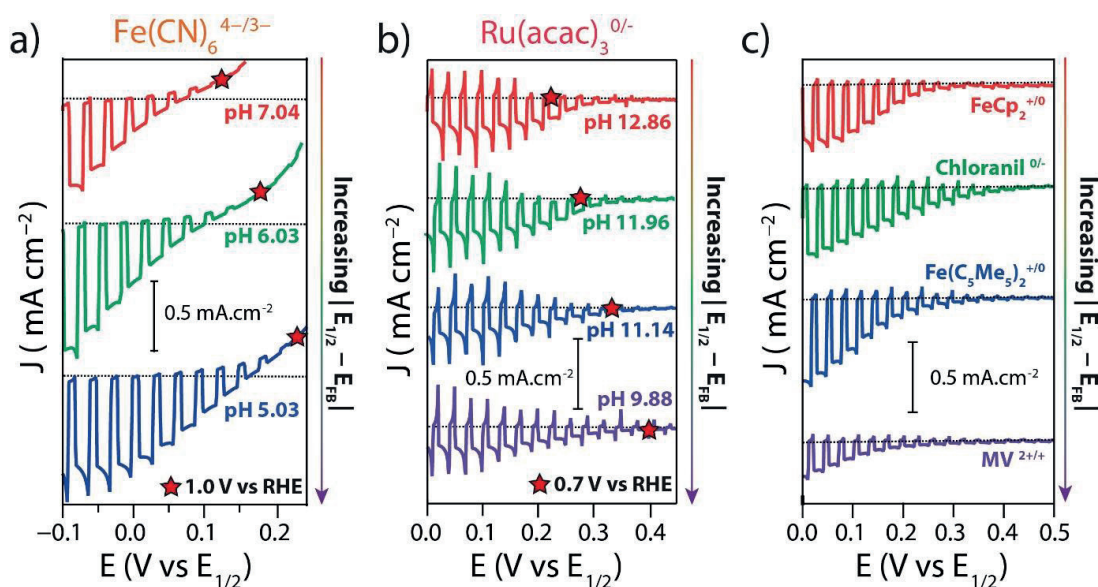


Figure 6.7 LSV curves of CuFeO_2 under intermittent 1 sun illumination (10 mV s^{-1} scan) in a) 50mM $\text{Fe}(\text{CN})_6^{4-/3-}$ and b) $\sim 1 \text{ mM}$ $\text{Ru}(\text{acac})_3^{0/-}$ (saturated) at different pH, referenced to the redox potential of the electrolyte. For each curve, the red star represents a fixed potential on the RHE scale, to help visualize the apparent FLP. For c) the LSV curves were obtained for different redox systems at concentration 0.01 M in CH_3CN , except for $\text{MV}^{2+/+}$ which saturated at $\sim 1 \text{ mM}$.

Since the photovoltage can be approximated from the potential difference between $E_{1/2}$ and the photocurrent onset (see Chapter 2, Figure 2.8), and is directly proportional to $|E_{1/2} - E_{\text{FB}}|$, in this case, for a $\sim 180 \text{ mV}$ potential range negative of E_{FB} , we deduce that the CuFeO_2 SCLJ behaves as expected in this range. Conversely, when tested with $\text{Ru}(\text{acac})_3^{0/-}$ between pH 10 and 13 (i.e. when varying $E_{1/2}$ between 0.31 and 0.49 V vs RHE, see Figure 6.5), a shift in the photocurrent onset was observed vs RHE, while the onset appeared unchanged vs $E_{1/2}$. We note that the smaller photocurrent magnitude in this case was due to the relatively poor solubility of $\text{Ru}(\text{acac})_3$ in water, yielding a diffusion-limited photocurrent, as evidenced by the transient photocurrent spikes. More

importantly, in this potential range (between 0.56 and 0.74 V negative of E_{FB}), the constant photocurrent onset at ca. + 0.35 V vs $E_{1/2}$ observed indicates a photovoltage independent of $|E_{1/2} - E_{FB}|$, in contrast with the linear dependence expected for an ideal SCLJ. In order to probe whether the observed behavior of the photovoltage was sensitive to the aqueous nature of the electrolyte, *e.g.* through protonation/deprotonation of the surface of the semiconductor, a similar experiment was performed in MeCN with different redox species: $\text{FeCp}_2^{+/0}$ ($E_{1/2} = 0.08$ V vs Ag^+/Ag), Chloranil $^{0/-}$ ($E_{1/2} = -0.30$ V vs Ag^+/Ag), $\text{Fe}(\text{C}_5\text{Me}_5)_2^{+/0}$ ($E_{1/2} = -0.44$ V vs Ag^+/Ag) and $\text{MV}^{2+/+}$ ($E_{1/2} = -0.71$ V vs Ag^+/Ag). Again, $E_{1/2}$ was measured by CV for each redox couple (see Figure 6.6). The resulting LSV curves (under intermittent illumination) are shown in Figure 6.7c. Note that the lower photocurrents obtained with $\text{MV}^{2+/+}$ are due to its solubility in MeCN (inferior to 1 mM). Nonetheless, the onset of photocurrent is seen clearly to be located at ~ 0.35 V vs $E_{1/2}$ for each redox couple despite their different $E_{1/2}$. This consistent behavior compared with the aqueous redox couples suggests that the observed photovoltage limitation is independent of the aqueous nature of the electrolyte.

6.3.2 Open-circuit potential measurements

An arguably more accurate method to investigate the photovoltage is to directly monitor the shift in open-circuit potential (OCP) caused by illumination of the electrode. In the dark at equilibrium the Fermi level of the semiconductor is aligned with the Redox potential of the electrolyte even in the presence of intra-bandgap surface states, in which case the Fermi level of the semiconductor is aligned with the surface states, themselves in equilibrium with the electrolyte.^{24,27} The measured shift in open-circuit potential under high-intensity illumination (ΔOCP) is a direct measure of the shift in Fermi level, and therefore a measure of the photovoltage at the junction, assuming no voltage loss through the film. Three redox couples were used to “map” the bandgap of the CuFeO₂ electrode with this method: $\text{Fe}(\text{CN})_6^{3-/4-}$ ($E_{1/2} = 0.25$ V vs Ag/AgCl), $\text{Ru}(\text{NH}_3)_6^{3+/2+}$ ($E_{1/2} = -0.18$ V vs AgCl/Ag) and $\text{MV}^{2+/+}$ ($E_{1/2} = -0.55$ V vs Ag/AgCl). By using a range of pH for each couple (limited by the chemical stability of the molecules involved), we were able to scan the following potential ranges: 0.77 V to 0.90 V vs RHE (using $\text{Fe}(\text{CN})_6^{3-/4-}$ between pH 5.2 and 7.5), 0.33 V to 0.49 V vs RHE (using $\text{Ru}(\text{NH}_3)_6^{3+/2+}$ between pH 5.0 and 7.9) and 0.07 V to 0.38 V vs RHE (using $\text{MV}^{2+/+}$ between pH 6.8 and 12.1). The open-circuit potentials collected in the dark and under illumination for each condition (Figure 6.8a-c) show

equilibration at $E_{1/2}$ in the dark as expected. Furthermore, in the potential range scanned using $\text{Fe}(\text{CN})_6^{3-/4-}$ (the closest to E_{FB}), we observed a linear progression of OCP under illumination with the pH. The associated slope was found to be -60 mV pH^{-1} , confirming the Nernstian behavior of the electronic bands of CuFeO_2 over the potential range of 0.77 V to 0.90 V vs RHE. On the contrary, in the potential ranges scanned with the two other redox species, no linear behavior was observed. In the case of $\text{Ru}(\text{NH}_3)_6^{3+/2+}$, a constant OCP was obtained under illumination, independent of the pH, while, in the case of $\text{MV}^{2+/+}$, the OCP also showed very little variation.

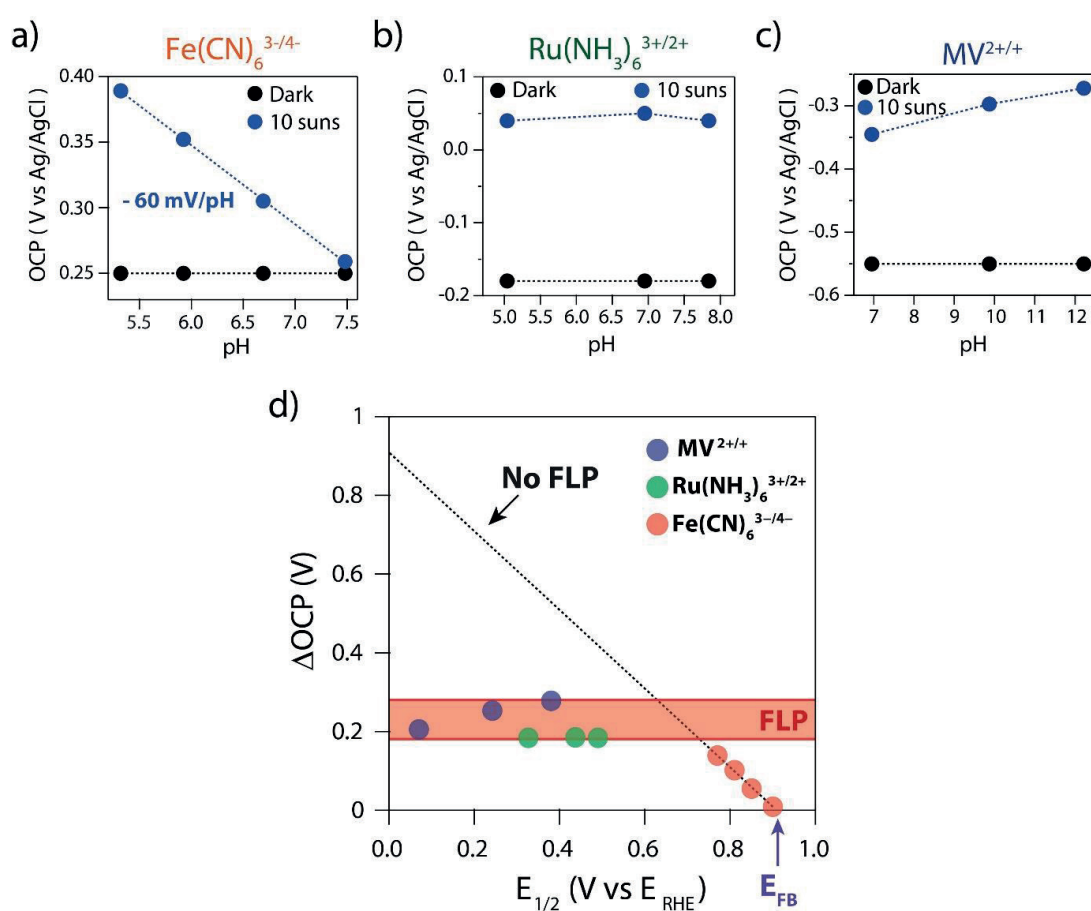


Figure 6.8 OCP measured in the dark and under 10 suns front illumination at different pH for a CuFeO_2 electrode in contact with a) 50 mM $\text{Fe}(\text{CN})_6^{3-/4-}$, b) 1 mM $\text{Ru}(\text{NH}_3)_6^{3+/2+}$ and c) 10 mM $\text{MV}^{2+/+}$ (see Chapter 3, section 3.3.5 for details on the concentration of the buffers). d) $\Delta\text{OCP} = \text{OCP}_{10\text{suns}} - \text{OCP}_{\text{dark}}$ measured as a function of the redox potential of the electrolyte, referenced to the RHE. The expected ΔOCP value, in absence of FLP, is shown as the dotted line that intercepts the x-axis at $E = E_{\text{FB}}$.

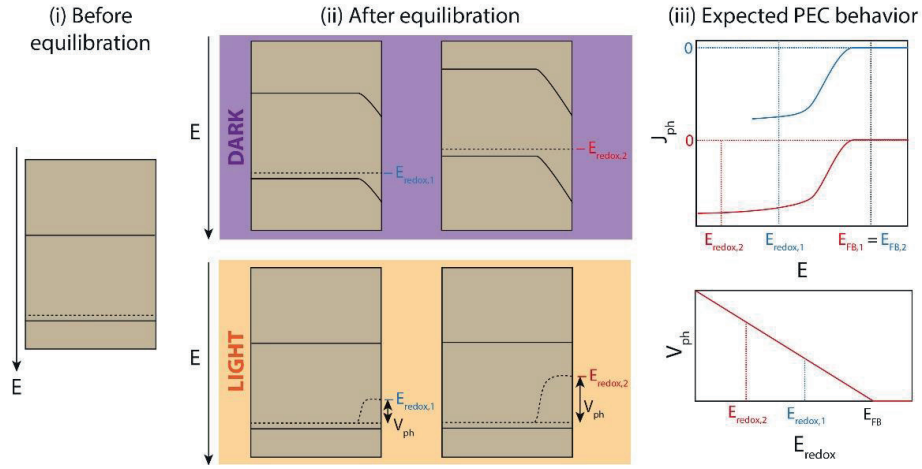
An overview of the OCP measurements is represented in Figure 6.8d, where ΔOCP is plotted against $E_{1/2}$, referenced to the RHE. Clearly, a plateau in photovoltage was observed for $E_{1/2}$ more negative than 0.7 V vs RHE, with a generally constant ΔOCP of $\sim 0.18 - 0.28$ V in this region.

A potential explanation for the observed dependence of the photovoltage on $|E_{1/2} - E_{\text{FB}}|$ would be the presence of surface trap states with energy levels inside the band gap. A sufficient density of these states located close to the valence band edge prevent the photovoltage from reaching the value anticipated from an ideal SCLJ (represented by the dotted line in Figure 6.8d) as the Fermi energy in the bulk of the semiconductor equilibrates with the energy of these states rather than with the electrolyte, causing a so-called Fermi level pinning (FLP).^{22,23,25,27} In this situation, the barrier height at the junction is no longer related to $E_{1/2}$. Rather since E_{F} is pinned to the surface states, any additional voltage provided by a more negative $E_{1/2}$, or by an external applied potential, results in the charging of the surface states rather than an increase in band bending in the semiconductor. An illustration of the evolution of the band system of a photocathode at the SCLJ in the presence and absence of surface states is provided in Figure 6.9. Overall, the photoelectrochemical measurements presented in this section suggest the presence of FLP-causing surface states located roughly 0.35 V negative to E_{FB} . However, the density and the chemical nature of the surface states remain unknown. Since the relative density of surface states compared to the density of bulk carriers primarily determines the extent of FLP, the next sections are devoted to additional techniques to evaluate the concentration and distribution of these states.

6.4 Electrochemical impedance spectroscopy

Although EIS data has been reported before for CuFeO₂ (see Chapters 4 and 5)^{2,28}, only the dielectric capacitance^{29,30} corresponding to the space-charge layer present at the SCLJ has been evaluated. On the contrary, the existence of any chemical capacitance associated to the accumulation/transfer of charges through potential surface states – manifested by a small deviation of the fitting of EIS data from experimental values at lower frequencies – has been neglected. Here, the initially-reported model (a Randles circuit) is refined to include the contribution of the surface states suggested by the observation of

a) No surface state



b) With surface states

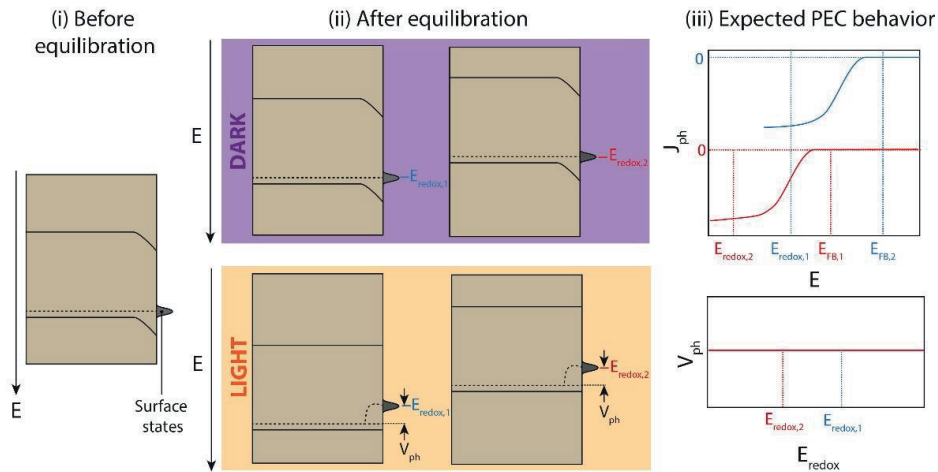


Figure 6.9 Sketches of the band energies of a p-type semiconductor a) without surface states and b) with surface states, referenced to the potential scale (E). In each case, three situations are depicted: (i) band diagram before the semiconductor is put in contact with the electrolyte, (ii) band diagram after equilibration between the semiconductor and two different electrolytes of different redox potentials – such that $E_{redox,1} > E_{redox,2}$ in the dark (top) and under illumination (bottom), and (iii) Expected evolution of photocurrent (J_{ph}) with the applied potential (top) E and of the photovoltage V_{ph} with the redox potential of the electrolyte (bottom). In the absence of surface states, as the redox potential of the electrolyte becomes more negative (*i.e.* higher in energy), the band bending at equilibrium increases, and so does the photovoltage under illumination. On the contrary, when surface states are present with a high density, the Fermi level is pinned to their energy, and therefore the band bending and the photovoltage are independent of the potential of the electrolyte. As a result, if the surface states are close to the conduction band, a constant and small photovoltage is measured, and any additional voltage provided to the system occurs inside the electrolyte (across the Helmholtz layer) until the strap states are completely full or empty.

FLP. Photoelectrodes displaying surface states have been studied with EIS before, and are typically modeled by the equivalent circuit. The following elements are included (following previously established nomenclature⁵): a series resistance R_s associated with charge transfer through the external circuit and the bulk of the semiconductor, a capacitance C_{bulk} , such as $C_{bulk}^{-1} = C_{SC}^{-1} + C_H^{-1}$, where C_{SC} corresponds to the depletion layer inside the semiconductor and C_H to the Helmholtz layer inside the electrolyte, a parallel resistance $R_{trapping}$, associated with charge trapping/detrapping at surface states, and a pair $C_{trap}/R_{ct,trap}$ corresponding respectively to the capacitive effect induced by the accumulated charges in surface states and to the resistance of charge transfer to the electrolyte through the surface states. Direct electron transfer from the conduction band to the electrolyte is not considered in this model.³¹

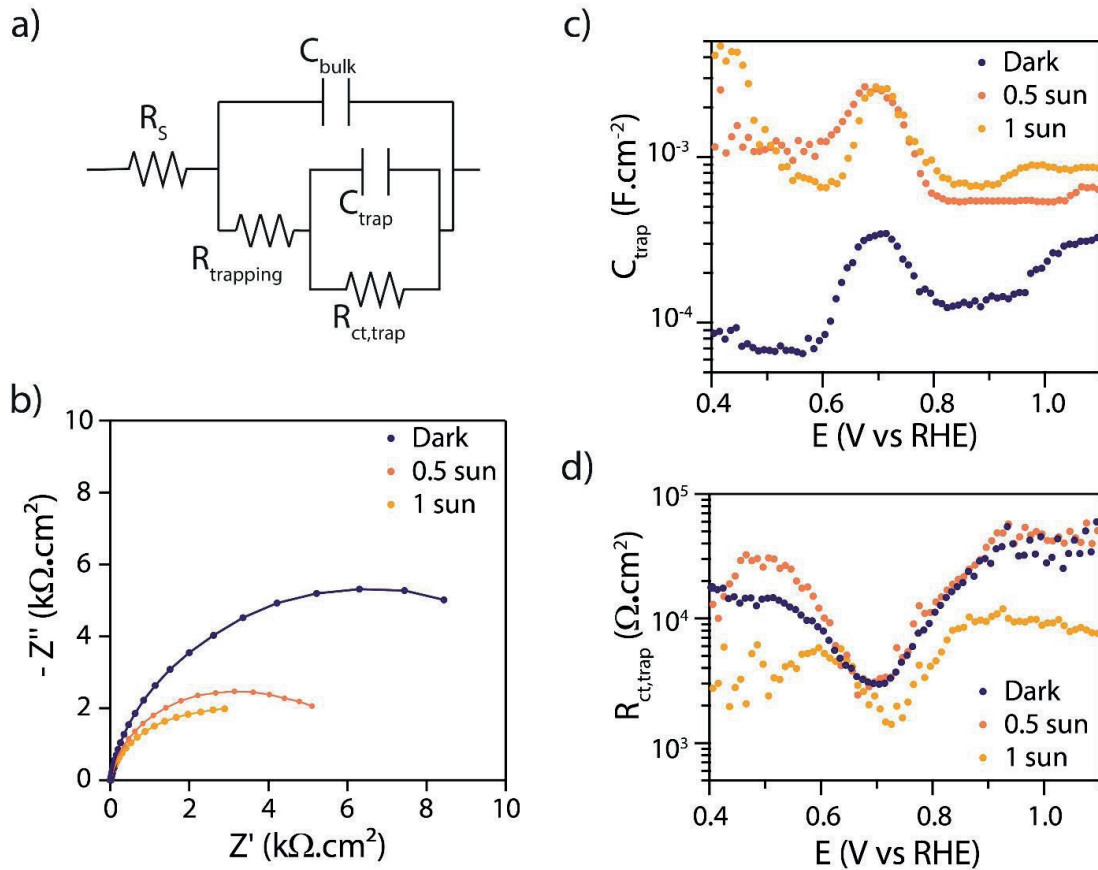


Figure 6.10 a) Equivalent circuit used to fit the EIS data. b) Typical Nyquist plots representing EIS data for a CuFeO₂ electrode collected at 0.7 V vs RHE, in 1M NaOH, in the dark, under 0.5 sun and 1 sun illumination. Markers represent experimental data, and lines represent the fit. c) and d) Plots of the extracted values of C_{trap} and $R_{ct,trap}$ respectively, as a function of the applied potential, referenced to the RHE.

Typical Nyquist plots obtained in 1M NaOH, at 0.7 V vs RHE, in the dark and under two different illumination intensities, are shown in Figure 6.10b. In all cases, the entire plot could not be properly fit with only one semicircle (i.e. with a simple Randles circuit), hence justifying the use of the model chosen in the present study (see also Appendix – Figure A2). Increasing the light intensity induces a decrease in the size of the semicircles in the Nyquist plot, indicating a lower value of $R_{trapping} + R_{ct,trap}$, due to the CuFeO₂ photoconductivity. To obtain more insight into the trapping of charges at the surface, the values of the parameters C_{trap} , and $R_{ct,trap}$ extracted from the model are displayed in Figure 6.10c and d. In the dark, the presence of a Gaussian peak in the plot of C_{trap} , is observed to coincide with a drop in $R_{ct,trap}$. The same behavior was observed under illumination, although C_{trap} was one order of magnitude higher. There is no clear influence of the light intensity on the parameters associated with charge transfer from the trap, similar to what was previously observed with hematite photoanodes.⁵ Regardless, the measurements of C_{trap} confirms the presence of the previously hypothesized density of surface states, located around 0.7 V vs RHE, and the model involving transfer across the SCLJ occurs through these surface states fits appropriately the experimental data.

On the other hand, to examine the behavior of C_{bulk} with potential we used the Mott-Schottky relationship, which relates the change in C_{SC}^{-2} with the applied potential to the acceptor density N_A and E_{FB} (see Chapter 2, Equation 2.32). The Mott-Schottky plots in the dark, as well as under illumination, are shown in Figure 6.11a. All plots showed a similar behavior: as the potential was scanned in the negative direction, C_{SC}^{-2} first increased, as expected in the depletion region, but quickly reached a peak value before decreasing back to its initial value. This decrease is characteristic of the presence of an inversion regime, due to the accumulation of minority carriers (electrons) at the SCLJ, causing an inversion of the polarity of the surface of the semiconductor.³² Using the linear part of the Mott-Schottky plot, it was possible to estimate the bulk acceptor density and the flat-band potential under each conditions, using $\epsilon = 20$ ^{33,34} and an electrode roughness $f_r = 18 \pm 3$ (calculated on three samples by Orange II adsorption, following a method previously reported for Fe₂O₃ thin films³⁵). While the experimental data yields an estimation of C_{bulk}^{-1} , the measured value of C_{bulk}^{-1} was taken as equal to C_{SC}^{-1} , as the assumption that $C_H \gg C_{SC}$ generally holds true for semiconductors due to their low dielectric constant and low carrier density.²⁷ Regarding the inversion region of the Mott-

Schottky plot, in all cases the potential range over which the inversion occurred coincided with the energetic distribution of the surface states, DOS, suggested by C_{trap} (as $DOS = C_{trap}/e$) represented in Figure 6.11b with baseline correction by removing the background capacitance.

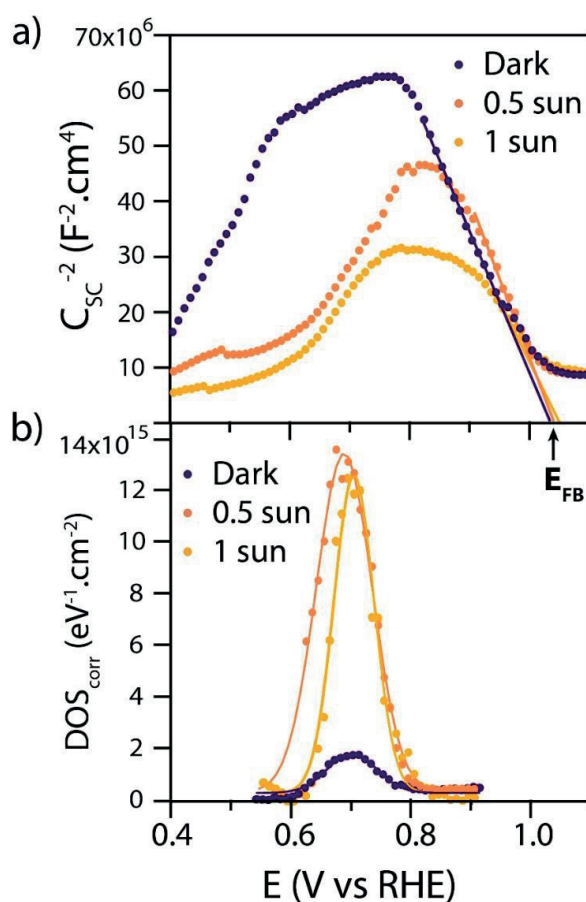


Figure 6.11 a) Mott-Schottky plots of a CuFeO₂ electrode in 1M NaOH in the dark, as well as under half a sun and 1 sun illuminations. b) Corresponding plot of the corrected density of surface states (DOS) extracted from C_{trap} after removal of the background capacitance.

The total density of surface states, N_{SS} , was calculated by integrating the curves shown in Figure 6.11b, again taking into account f_r . To obtain accurate estimations of the parameters E_{FB} , N_A and N_{SS} the EIS measurements were performed on three replicate samples. Average values are summarized in Table 6.1. No significant influence of the illumination intensity on the measured flat-band potential ($E_{FB} \sim 1.05$ V vs RHE), nor on the measured acceptor density ($N_A \sim 10^{18}$ cm⁻³) is observed. These values are in agreement with the previous report using the Randles circuit.² Interestingly, a significant

density of surface states ($\sim 10^{13} \text{ cm}^{-2}$) was measured in the dark, contrary to what was reported for hematite,^{5,36} where the surface states were only accessible under illumination.

Table 6.1 CuFeO₂ semiconductor parameters derived from EIS data^a

Illumination (sun)	E _{FB} (V vs RHE)	N _A (10 ¹⁸ cm ⁻³)	N _{SS} (10 ¹³ cm ⁻²)
0	1.05 ± 0.01	1.20 ± 0.42	0.74 ± 0.64
0.5	1.06 ± 0.01	1.24 ± 0.60	6.39 ± 0.46
1	1.07 ± 0.01	1.49 ± 0.84	6.80 ± 0.51

E_{FB}: flat-band potential; N_A: bulk acceptor density; N_{SS}: surface state density

^a Taking $\epsilon = 20$ and $f_r = 18$

This is consistent with the observed inversion region in the dark Mott-Schottky plot. In addition, under illumination N_{SS} is one order of magnitude higher ($\sim 10^{14} \text{ cm}^{-2}$) compared to the dark, suggesting that the majority of the states are accessible under illumination only. Overall the EIS results reinforce the energetic position of the surface states at +0.7 V vs RHE, and give an estimation of their density at $\sim 10^{14} \text{ cm}^{-2}$. This density is two orders of magnitude higher than the minimal density of surface states considered necessary to induce FLP with a bulk acceptor density of 10^{18} cm^{-3} .²² Thus the inversion observed in the EIS and the limited photopotential of $\sim 0.3 \text{ V}$ are likely caused by these surface states.

6.5 Surface analysis

Further information regarding the physiochemical nature of the surface states was next sought using Kelvin Probe Force Microscopy (KPFM) and X-Ray Photoelectron Spectroscopy (XPS).

6.5.1 Kelvin probe force microscopy

KPFM afforded the mapping of the Fermi Level position at the surface³⁷ in both dark and illuminated conditions on CuFeO₂ electrodes in air. As shown in Figure 6.12b, a 5 μm by 5 μm surface scan revealed a relatively homogeneous surface potential (root mean square deviation of 8 meV) compared to the surface roughness (Figure 6.12a, RMS deviation of 13 nm). In the dark the Fermi Level at the surface was calibrated to -5.20 eV

vs vacuum (see Chapter 3, section 3.2.7), which is equivalent to +0.70 V vs NHE, and consistent with the results obtained by EIS assuming FLP at the surface states.

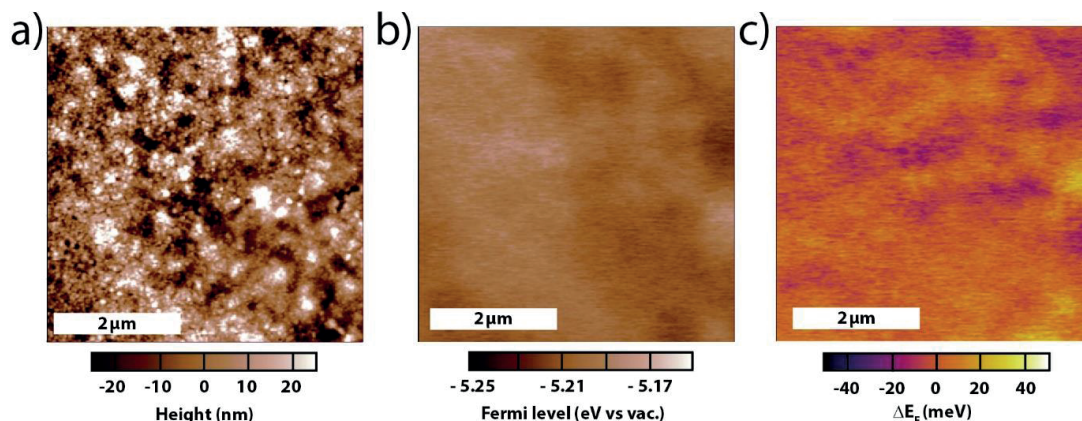


Figure 6.12 KPFM measurements. a) Height image of the surface of a bare CuFeO₂ electrode by AFM b) Dark KPFM mapping of the value of E_F at the surface for the same region. c) Shift in E_F ($\Delta E_F = E_{F,\text{light}} - E_{F,\text{dark}}$) measured upon illumination of the surface of the sample.

Illumination of the sample did not induce significant shift in average surface potential in the range of light intensity experimentally available (up to ca. 0.1 Sun), but the surface remained equally homogeneous (Figure 6.12c), suggesting a uniform distribution of the surface states on the CuFeO₂ and casting doubt on the possibility that the surface states are due to isolated domains of secondary phases.

6.5.2 X-Ray Photoelectron Spectroscopy

XPS data for Fe, Cu and O recorded on a pristine thin film of CuFeO₂ at different etching depths are shown in Figure 6.13. The Cu 2p signal (shown in Figure 6.13a) is consistent with the signature expected for Cu(I),³⁸ with two peaks at 932.4 eV and 952.4 eV, and showed no change as a function of depth. No Cu(II) could be detected at the CuFeO₂ surface or inside the film given the absence of the signature satellite peak between 940 and 945 eV. However, we note that it is not possible to discriminate between Cu(I) and Cu(0) based on the 2p signal. However, the Cu LMM signature has been reported to be significantly different for Cu(I) and Cu(0).³⁸ Spectra in this range (Figure 6.13b) showed changes with the depth of the measurement: near the surface, a single peak was observed with a kinetic energy of 916.7 eV. With increasing depth this peak progressively shifted towards a slightly sharper peak at 918.9 eV. This indicates a change in the chemical

environment of the copper centers between the surface and the bulk of the material, supporting the presence of surface states. However, the Cu LMM spectra did not present the features characteristic of Cu(0), i.e. a well-defined peak at 918.7 eV and two well defined smaller peaks *ca.* 916.7 eV and 921.8 eV. Thus rather than Cu(0), the surface states are reasonably Cu(I) centers with a different chemical environment than the Cu(I) in the bulk CuFeO₂.

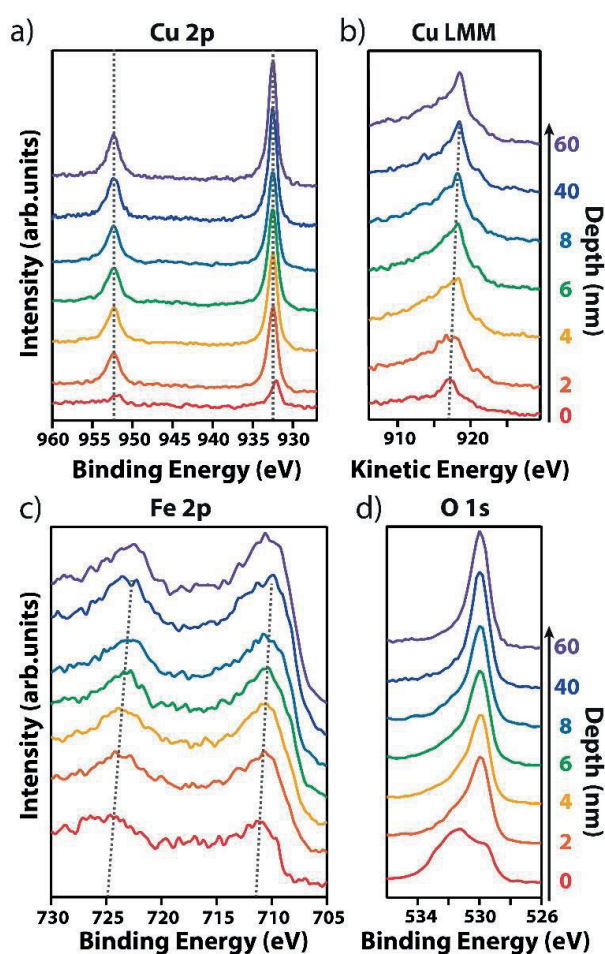


Figure 6.13 a) XPS spectra as a function of depth of Cu 2p. b) XPS spectra as a function of depth of Cu LMM. c) XPS spectra as a function of depth of Fe 2p. d) XPS spectra as a function of depth of O 1s. The scans were performed at 0 nm, 2 nm, 4 nm, 6 nm, 8 nm, 40 nm and 60 nm from the surface of the sample, starting from the bottom scan (red trace).

Similarly, the signals for Fe and O (Figure 6.13c and d respectively) show a clear change with the depth. The Fe 2p signature on the surface showed the two features characteristic of Fe(III), with binding energies of 711.2 eV and 724.8 eV, but upon etching these peaks progressively shifted to lower energies of 710.2 eV and 722.6 eV, indicating

an analogous change in the environment of the Fe atoms. Moreover, while the signature of the oxygen showed two peaks at the surface (at 529.8 eV 531.6 eV), the peak at 531.6 eV progressively decreased in intensity as the depth increased, ultimately vanishing in the bulk. In contrast, the peak at 529.8 eV progressively increased in intensity. This signal is similar to the signature of oxygen in other oxides, consistent with metal-oxygen bonding, while the signal at 531.6 eV can be attributed to metal-hydroxyl groups M-OH.^{38,39} Moreover, the shift in energy in the Fe signal is consistent with the presence of disordered Fe(III)-OH near the surface of the electrode, suggesting a disruption in the bulk crystal structure—where iron and oxygen are organized in FeO₆ octahedra.^{39,40} We note that the presence of hydroxide species near the surface could also explain the shift observed in the Cu(I) signal, but the presence of Cu(I)-OH group is difficult to assess due to the lack of reports on the XPS signature of this particular chemical group. Overall the XPS analysis suggests that the electronic surface states detected in PEC experiments are likely related to the presence of ~ 10 nm-thick hydroxide layer at the surface of the electrode, while the presence of Cu(0), Cu(II) or Fe(II) was discounted.

6.6 Discussion

The different measurements presented in this chapter and their interpretation can be summarized in a semi-quantitative description of the electronic configuration and charge transport properties of CuFeO₂ thin film electrodes. Figure 6.14 shows a band diagram displaying the key features established in this work. Firstly, TRMC data revealed a relatively long photogenerated carrier lifetime of 200 ns and an estimated electron diffusion length of 300 nm. Furthermore, detailed EIS measurements yielded an acceptor density of $N_A \sim 10^{18} \text{ cm}^{-3}$ and a flat-band potential E_{FB} at 1.05 V vs RHE (-5.55 eV vs vacuum). Considering an effective density of states in the valence band on the order of 10^{19} cm^{-3} ,⁴¹ the difference in energy between the valence band edge E_{VB} and the Fermi level E_F in the bulk is estimated to be ~ 60 meV at 298 K (see Equation 2.10).⁴²

On the other hand, PEC measurements reveal the presence of surface states (located roughly 0.35 eV negative of E_{FB}) that induce Fermi level pinning at the SCLJ. Interestingly, although the conclusions drawn from the OCP and LSV are generally identical, ΔOCP measurements (see Figure 6.8d) yielded a photovoltage value of about 200 mV, 150 mV lower than suggested by the LSV data (see Figure 6.7). This discrepancy

could be due to voltage losses between the SCLJ (where ΔOCP is produced) and the back of the electrode (where potential is measured) in the absence of current flow. To support this explanation we note that the value of E_{FB} extracted from the plot in Figure 6.8d (i.e. where ΔOCP extrapolates to zero) is close to 0.9 V vs RHE, which is also 150 mV lower than E_{FB} extracted from MS (see Figure 6.11a). Bulk defects such as grain boundaries may be the physical origin of this loss as they could prevent the complete flattening of the bands even at high light intensity. For this reason, our most confident assessment of the surface state position is centered at -5.2 eV vs vacuum (from LSV and EIS data).

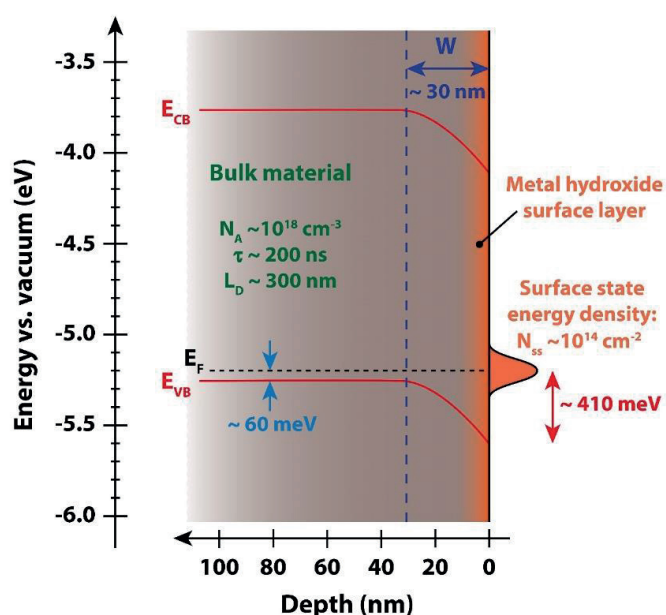


Figure 6.14 Proposed energy band diagram for an isolated CuFeO_2 electrode in the dark. E_{CB} = Conduction band edge, E_{VB} = Valance band edge, E_{F} = Fermi level, N_{A} = Acceptor density, τ = carrier lifetime, L_{D} = carrier diffusion length, W = depletion width, N_{SS} = density of surface states.

The KPFM measurements support this value and, together with the PEC measurements in different electrolytes, the KPFM further indicates that the presence of surface states was not related to the presence of the electrolyte. XPS analysis rather suggests that the possible nature of these surface states is metal hydroxyl groups, while KPFM indicates their homogeneous surface distribution. As hydroxyl groups have been invoked in the past to explain surface trapping in other oxides,^{36,43,44} we suggest the presence of a continuous 10 nm layer of metal hydroxide or oxyhydroxide on the surface of the CuFeO_2 . It is worth noting that photoluminescence measurements employed to

verify the lifetime of photogenerated charges independently from the TRMC measurement were unsuccessful due to the lack of measurable luminescence in the range of accessible conditions. This is consistent with the presence of a homogeneous layer of surface traps that effectively quenches luminescence from the bulk.

EIS analysis further indicated that the surface states act as electron traps (as an inversion regime observed is reasonably due to electrons accumulating in the surface traps) and gave an energetic distribution and density of the surface states that confirms the existence of FLP when comparing to the bulk acceptor density. Due to the equilibrium of the bulk E_F with the surface states the depletion width is limited to 30 nm (see SI for calculation)⁴² and the photovoltage is limited to 0.35 V. The limited depletion width of 30 nm is small compared to the penetration depth of the light in CuFeO₂ ($\delta_p = 1/\alpha \approx 100$ nm for visible photons). Therefore, a significant portion of the charges will be generated outside the depletion width, even under front (electrolyte side) illumination. An estimate of the maximum photocurrent expected considering this aspect was calculated using the model developed by Gartner and others.^{45–48} Using appropriate boundary conditions for either substrate-side or electrolyte-side illumination (see Chapter 3, section 3.3.6), the maximum photocurrent produced by a 200 nm-thick CuFeO₂ layer at different photovoltages was estimated the absence of recombination. Under front illumination, with a photovoltage of 350 mV, and an associated depletion width of 30 nm, one can expect a photocurrent of *ca.* 6 mA cm⁻². In contrast, the case of an ideal junction with water, yielding a photovoltage of 0.8 V, and a depletion width of 45 nm, gives a maximum photocurrent of *ca.* 9 mA cm⁻². On the contrary, substrate-side illumination greatly limits the photocurrent, as experimentally observed previously (see Chapter 4),² and in the case of a SCLJ with Fe(CN)₆^{3-/4-}, the expected photocurrent is no higher than 1.5 mA cm⁻² in the absence of recombination, which is reasonable compared the experimental value of 0.7 mA.cm⁻² reported in Figure 6.7 considering the likely presence of recombination outside the depletion region due to the absence of a charge accelerating electric field. It is worth mentioning that substrate-side illumination was employed in this work due to the varying visible light absorption properties of the redox couples used. Overall, the simple photocurrent model discussed here indicates that if the surface states were successfully passivated or removed, a photovoltage of 0.8 V and reduced surface recombination would

reasonably give photocurrents approaching 9 to 10 mA cm⁻² at one sun illumination under electrolyte-side illumination in the absence of bulk recombination.

6.7 Conclusion

The results of a variety of photoelectrochemical, microscopy and spectroscopy techniques were used to explore and characterize a thin-film CuFeO₂ photocathode. Overall, the study conducted in this chapter allowed to get a semi-quantitative picture of the transport and recombination of charge carriers inside the material and at the SCLJ. A high density of surface states ($N_{ss} \sim 10^{14}$ cm⁻²) was measured, compared to the bulk acceptor density ($N_A \sim 10^{18}$ cm⁻³), which is believed to cause Fermi Level pinning at the SCLJ, drastically limiting the photovoltage to roughly 0.35 V, regardless of the electrolyte used to create the junction. The conclusion is that these states act as electron traps, causing an inversion of the depletion layer upon filling, both in the dark and under illumination thereby promoting charge recombination at the surface. On the other hand, TRMC measurements suggested that the bulk material presented good transport properties, including a very long lifetime for photogenerated charge carriers (~ 200 ns). With an associated diffusion length of about 300 nm, and known good absorption properties and high stability of the material under operating conditions, CuFeO₂ remains attractive for use as a photocathode, as this study indicates that its bulk properties are not the limiting factor for PEC performances. Importantly, if this were to be achieved, the estimated maximum photovoltage the electrode could reach for water reduction is roughly 0.8 V, based on the TRMC measurements, making it, eventually, a strong candidate for a combination with an oxide photoanode, based on BiVO₄ or Fe₂O₃, for the creation of an earth-abundant, solution-processed, all-oxide tandem photoelectrochemical cell.

6.8 References

- (1) Prévot, M. S.; Jeanbourquin, X. A.; Bourée, W. S.; Abdi, F.; Friedrich, D.; van de Krol, R.; Guijarro, N.; Le Formal, F.; Sivula, K. *Chem. Mater.* **2017**, 29 (11), 4952–4962.
- (2) Prévot, M. S.; Guijarro, N.; Sivula, K. *ChemSusChem* **2015**, 8 (8), 1359–1367.
- (3) Bourée, W. S.; Prévot, M. S.; Jeanbourquin, X. A.; Guijarro, N.; Johnson, M.; Formal, F. L.; Sivula, K. *Adv. Mater.* **2016**, 28 (42), 9308–9312.

- (4) Cabán-Acevedo, M.; Kaiser, N. S.; English, C. R.; Liang, D.; Thompson, B. J.; Chen, H.-E.; Czech, K. J.; Wright, J. C.; Hamers, R. J.; Jin, S. *J. Am. Chem. Soc.* **2014**, *136* (49), 17163–17179.
- (5) Klahr, B.; Gimenez, S.; Fabregat-Santiago, F.; Hamann, T.; Bisquert, J. *J. Am. Chem. Soc.* **2012**, *134* (9), 4294–4302.
- (6) Du, C.; Zhang, M.; Jang, J.-W.; Liu, Y.; Liu, G.-Y.; Wang, D. *J. Phys. Chem. C* **2014**, *118* (30), 17054–17059.
- (7) Iandolo, B.; Hellman, A. *Angew. Chem. Int. Ed.* **2014**, *53* (49), 13404–13408.
- (8) Le Formal, F.; Pendlebury, S. R.; Cornuz, M.; Tilley, S. D.; Grätzel, M.; Durrant, J. R. *J. Am. Chem. Soc.* **2014**, *136* (6), 2564–2574.
- (9) Formal, F. L.; Tétreault, N.; Cornuz, M.; Moehl, T.; Grätzel, M.; Sivula, K. *Chem. Sci.* **2011**, *2* (4), 737–743.
- (10) Jang, J.-W.; Du, C.; Ye, Y.; Lin, Y.; Yao, X.; Thorne, J.; Liu, E.; McMahon, G.; Zhu, J.; Javey, A.; Guo, J.; Wang, D. *Nat. Commun.* **2015**, *6*, 7447.
- (11) Brenot, R.; Vanderhaghen, R.; Drevillon, B.; French, I.; Roca i Cabarrocas, P. *Thin Solid Films* **1997**, *296* (1), 94–97.
- (12) Dicker, G.; de Haas, M. P.; Siebbeles, L. D. A.; Warman, J. M. *Phys. Rev. B* **2004**, *70* (4), 045203.
- (13) Abdi, F. F.; Savenije, T. J.; May, M. M.; Dam, B.; van de Krol, R. *J. Phys. Chem. Lett.* **2013**, *4* (16), 2752–2757.
- (14) Chen, H.-Y.; Wu, J.-H. *Appl. Surf. Sci.* **2012**, *258* (11), 4844–4847.
- (15) Cherepy, N. J.; Liston, D. B.; Lovejoy, J. A.; Deng, H.; Zhang, J. Z. *J. Phys. Chem. B* **1998**, *102* (5), 770–776.
- (16) Paracchino, A.; Brauer, J. C.; Moser, J.-E.; Thimsen, E.; Graetzel, M. *J. Phys. Chem. C* **2012**, *116* (13), 7341–7350.
- (17) Ravensbergen, J.; Abdi, F. F.; van Santen, J. H.; Frese, R. N.; Dam, B.; van de Krol, R.; Kennis, J. T. M. *J. Phys. Chem. C* **2014**, *118* (48), 27793–27800.
- (18) Lewis, N. S. *J. Electrochem. Soc.* **1984**, *131* (11), 2496–2503.
- (19) Benko, F. A.; Koffyberg, F. P. *J. Phys. Chem. Solids* **1987**, *48* (5), 431–434.
- (20) Godinho, K. G.; Morgan, B. J.; Allen, J. P.; Scanlon, D. O.; Watson, G. W. *J. Phys. Condens. Matter* **2011**, *23* (33), 334201.
- (21) Suzuki, I.; Nagatani, H.; Kita, M.; Iguchi, Y.; Sato, C.; Yanagi, H.; Ohashi, N.; Omata, T. *Inorg. Chem.* **2016**, *55* (15), 7610–7616.

- (22) Bard, A. J.; Bocarsly, A. B.; Fan, F. R. F.; Walton, E. G.; Wrighton, M. S. *J. Am. Chem. Soc.* **1980**, *102* (11), 3671–3677.
- (23) Kelly, J. J.; Memming, R. *J. Electrochem. Soc.* **1982**, *129* (4), 730–738.
- (24) Baglio, J. A.; Calabrese, G. S.; Harrison, D. J.; Kamieniecki, E.; Ricco, A. J.; Wrighton, M. S.; Zoski, G. D. *J. Am. Chem. Soc.* **1983**, *105* (8), 2246–2256.
- (25) Lewerenz, H. J. *J. Electroanal. Chem.* **1993**, *356* (1), 121–143.
- (26) Warren, E. L.; Boettcher, S. W.; Walter, M. G.; Atwater, H. A.; Lewis, N. S. *J. Phys. Chem. C* **2011**, *115* (2), 594–598.
- (27) Nagasubramanian, G.; Wheeler, B. L.; Bard, A. J. *J. Electrochem. Soc.* **1983**, *130* (8), 1680–1688.
- (28) Jang, Y. J.; Park, Y. B.; Kim, H. E.; Choi, Y. H.; Choi, S. H.; Lee, J. S. *Chem. Mater.* **2016**, *28* (17), 6054–6061.
- (29) Bisquert, J. *Phys. Chem. Chem. Phys.* **2003**, *5* (24), 5360–5364.
- (30) Bisquert, J. *Phys. Chem. Chem. Phys.* **2008**, *10* (1), 49–72.
- (31) Bertoluzzi, L.; Lopez-Varo, P.; Tejada, J. A. J.; Bisquert, J. *J. Mater. Chem. A* **2016**, *4* (8), 2873–2879.
- (32) Sato, N. *Electrochemistry at Metal and Semiconductor Electrodes*; Elsevier, 1998.
- (33) Kimura, T.; Lashley, J. C.; Ramirez, A. P. *Phys. Rev. B* **2006**, *73* (22), 220401.
- (34) Terada, N.; Nakajima, T.; Mitsuda, S.; Kitazawa, H.; Kaneko, K.; Metoki, N. *Phys. Rev. B* **2008**, *78* (1), 014101.
- (35) Kay, A.; Cesar, I.; Grätzel, M. *J. Am. Chem. Soc.* **2006**, *128* (49), 15714–15721.
- (36) Klahr, B.; Hamann, T. *J. Phys. Chem. C* **2014**, *118* (19), 10393–10399.
- (37) Melitz, W.; Shen, J.; Kummel, A. C.; Lee, S. *Surf. Sci. Rep.* **2011**, *66* (1), 1–27.
- (38) Poulston, S.; Parlett, P. M.; Stone, P.; Bowker, M. *Surf. Interface Anal.* **1996**, *24* (12), 811–820.
- (39) Mansour, A. N.; Brizzolara, R. A. *Surf. Sci. Spectra* **1996**, *4* (4), 357–362.
- (40) Grosvenor, A. P.; Kobe, B. A.; Biesinger, M. C.; McIntyre, N. S. *Surf. Interface Anal.* **2004**, *36* (12), 1564–1574.
- (41) Krishnan Rajeshwar. In *Encyclopedia of Electrochemistry*; Wiley-VCH Verlag GmbH & Co. KGaA, 2007.
- (42) Cendula, P.; Tilley, S. D.; Gimenez, S.; Bisquert, J.; Schmid, M.; Grätzel, M.; Schumacher, J. O. *J. Phys. Chem. C* **2014**, *118* (51), 29599–29607.
- (43) Di Valentin, C.; Pacchioni, G.; Selloni, A. *Phys. Rev. Lett.* **2006**, *97* (16), 166803.

- (44) Sivula, K.; Zboril, R.; Le Formal, F.; Robert, R.; Weidenkaff, A.; Tucek, J.; Frydrych, J.; Grätzel, M. *J. Am. Chem. Soc.* **2010**, *132* (21), 7436–7444.
- (45) Gärtner, W. W. *Phys. Rev.* **1959**, *116* (1), 84–87.
- (46) Reichman, J. *Appl. Phys. Lett.* **1980**, *36* (7), 574–577.
- (47) Allongue, P.; Cachet, H.; Horowitz, G. *J. Electrochem. Soc.* **1983**, *130* (12), 2352–2357.
- (48) Choo, S. C.; Tan, L. S.; Quek, K. B. *Solid-State Electron.* **1992**, *35* (3), 269–283.

Chapter 7

Surface modification of CuFeO₂ photocathodes.

In the previous chapter, CuFeO₂ photoelectrodes were shown to exhibit a high density of surface states energetically close to the valence band of the material. The presence of these intra-bandgap surface states induces a low photovoltage and is also likely the cause for the absence of photocurrent observed in Chapter 4 for photoelectrodes measured in Ar-purged aqueous electrolyte. The detrimental effects of surface states in other oxide photoelectrodes have previously been addressed by the deposition of optimized overlayers, as presented in the first part of this chapter. These layers can either remove the existence of the surface states (passivating effect) or kinetically favor minority carrier injection to the electrolyte (catalytic or extraction effect). In the following parts of this chapter, catalytic/extraction and passivating surface modifications or CuFeO₂ photocathodes are explored and their effect on the PEC performances are reported.

Part of this chapter has been adapted from “Enhancing the Performance of a Robust Sol-Gel Processed p-Type Delafossite CuFeO₂ Photocathode for Solar Water Reduction”¹ (Prévot, M.S; Guijarro, N.; Sivula, K., *ChemSusChem*, **2015**, 8, 1359-1367).

7.1 Surface modification of oxide photoelectrodes

Surface trapping states are a common source of voltage losses and recombination in oxide photoelectrodes, where the atomic lattice is interrupted at the semiconductor surface and dangling bonds are present, which leads to the creation of chemical defects in the structure. To tackle this problem, one can modify the surface of the photoelectrode with a thin overlayer of another semiconductor material, which can act either as a charge-extracting layer for minority carriers and prevent their recombination at the surface states, or directly as a passivating layer, removing the presence of surface states. A good semiconductor overlayer should meet the following requirements: (i) stability under operating conditions, (ii) homogeneous (or even conformal) coating of the photoactive layer, (iii) reduced lattice mismatch with the photoactive layer, (iv) transparency in the visible range (to limit parasitic absorption losses), and (v) selectivity for photogenerated minority carriers. This last requirement entails that an adequate photocathode overlayer should form a type-II heterojunction with the light-absorbing layer, where the band system of the overlayer is lower in energy, so that (for protecting a p-type photocathode) photogenerated electrons are injected into its low-lying conduction band, whereas its low-lying valence band blocks photogenerated holes. Finding a material and a morphology meeting all these requirements is challenging, but several candidates have been shown to notably improve the performance of oxide photoelectrodes when used as overlayers.

Thin layers of TiO₂ represent the most commonly studied type of photocathode overlayer, due to its excellent stability in water and favorable band alignment, with a conduction band *ca.* 0.25 eV higher in energy than the reduction potential of water. It has been successfully used on a wide variety of photocathodes, such as InP,² Si,³ GaP,⁴ and Cu₂O.^{5–7} Furthermore, Al-doped ZnO (AZO) has been identified as an efficient buffer layer in photovoltaic cells based on a Cu₂O absorbing layer,^{8–10} and was also adopted for Cu₂O photocathodes, where a TiO₂ was additionally employed as a protecting layer. This yielded the final architecture FTO/Au/Cu₂O/AZO/TiO₂ that performs with one of the highest photocurrents produced by an oxide photocathode for water reduction, when combined with Pt or RuO₂ as electrocatalyst.^{5,11} Importantly, because Cu₂O photocorrodes under operating conditions when in contact with water, the AZO/TiO₂ overlayer has to be deposited by atomic layer deposition (ALD), which provides a conformal coating fully

isolating Cu₂O from the electrolyte. However, the presence of this overlayer also limits the photovoltage of the Cu₂O photocathode to about 0.4 V, much lower than what is anticipated from the 2.0 eV bandgap of Cu₂O and this was attributed to the misalignment of the semiconductor band systems in the Cu₂O/AZO type-II heterojunction.^{6,9,12} This is why, more recently, Ga₂O₃ has been presented as a better alternative overlayer candidate for Cu₂O photocathodes, producing photovoltages as high as 1 V for water splitting¹³ (and 1.2 V in solar cells¹⁴). This was attributed to the favorable band alignment of the buried Cu₂O/Ga₂O₃ junction. Interestingly, the best performance were again obtained when a TiO₂ overlayer was retained on top of the Ga₂O₃ layer.¹³ It is worth mentioning that Ga₂O₃¹⁵ and Al₂O₃¹⁶ have also been successfully used as passivating for α -Fe₂O₃ photoanodes that present surface states akin to the ones evidenced in Chapter 6 for CuFeO₂. In both cases a cathodic shift in the onset of photocurrent for water oxidation, *i.e.* an improvement of the photovoltage, was observed after introduction of the passivating layer and was attributed to the removal of surface states responsible for the low photovoltage of the bare material. Overall, semiconducting/insulating overlayers such as TiO₂, AZO, Ga₂O₃ and Al₂O₃ have been shown to successfully enhance stability and/or photovoltage of oxide photoelectrodes, and should be investigated as candidates for overcoming the photovoltage limitations of CuFeO₂.

Another common way to improve PEC performances of photoelectrodes is to favor minority carrier injection to the electrolyte by depositing catalyst nanoparticles at the surface of the electrode. In contrast to a semiconductor overlayer a catalyst will not directly block corrosion or the transfer of majority carriers, but serves to accelerate the extraction of minority carriers for electrochemical reaction. Indeed, the electrochemical process usually represents a kinetic bottleneck for the overall PEC process, resulting in the accumulation of charge carriers at the surface of the photoelectrode, and favoring charge recombination. On the contrary, if an adequate electrocatalyst is present at the SCLJ, the electrochemical reaction can perform with a high rate, favoring charge injection into the electrolyte over charge recombination. For PEC water reduction, Pt is usually used as it is the best metallic hydrogen evolution catalyst and it can be easily photoelectrodeposited from an H₂PtCl₆ solution directly on the surface of the photoelectrode, but is worth mentioning that more earth-abundant catalysts – such as MoS₂, CoP or Ni₂P – are actively developed to ultimately replace Pt in large-scale applications.^{17,18}

A more extensive review of surface modification of photoelectrodes (not limited to oxide materials) can be found in an article by Guijarro *et al.*¹⁹ Overall, semiconductor overlayers and electrocatalyst deposition are two proven ways to improve the performance of photoelectrodes, and are in fact usually used in combination in state-of-the-art devices, where enhanced charge separation, surface-state passivation and fast electrochemical kinetics benefit the extracted photovoltage and photocurrent. Therefore, these approaches were applied to the CuFeO₂ electrode developed in the previous chapters and the results are described in the following sections.

7.2 CuFeO₂ modification with a AZO/TiO₂/Pt overlayer

Initial attempts to attach noble metal electrocatalysts directly to the surface of the CuFeO₂ following standard approaches gave inconsistent results. Attempts were made to directly photoelectrodeposit Pt or Au from an H₂PtCl₆ electrolyte or an HAuCl₄ electrolyte respectively. In both cases, there was very little photocurrent associated with the deposition (on the $\mu\text{A}\cdot\text{cm}^{-2}$ scale) resulting in a very poor deposition of the catalyst. Even after prolonged deposition, the modified electrode did not show any improvement in performance. Spin-coating of a dilute solution of the metal salts onto a CuFeO₂ photoelectrode, followed by annealing under Ar/H₂ atmosphere, also failed to yield any increase in photocurrent. Finally, citrate colloids of Pt and Au nanoparticles were synthesized and deposited on the surface of the photocathode but, once again, did not improve the PEC behavior of the material. Overall, these negative results suggested that directly depositing metal catalysts on the surface of CuFeO₂ was not a good strategy to reduce charge recombination at the SCLJ.

To tackle the problem, further engineering of the surface of the material was therefore necessary. As mentioned in section 7.1, AZO has been used as a buffer layer in Cu₂O-based PV and PEC devices. The Cu₂O and AZO layers form a buried type II heterojunction (*i.e.* the bandgaps of the materials are staggered), allowing for better charge separation. Because ZnO is unstable under illumination in water, a protecting layer of TiO₂ has to be added on top of it for PEC water splitting applications. Once the absorbing layer is coated with this buffer layer, one can deposit a metal catalyst on the surface of the electrode to improve the kinetic of

water reduction at the SCLJ. This strategy has been applied to the CuFeO_2 photocathode developed during the PhD thesis at hand: a layer of AZO and a layer of TiO_2 were sequentially deposited on the CuFeO_2 layer by ALD, and the resulting electrode was then coated with Pt nanoparticles by photoelectrodeposition from a 2 mM H_2PtCl_6 solution. The resulting architecture of the electrode is depicted alongside the predicted energetic band alignment of the different layers in Figure 7.1. Importantly, the surface trap states discussed in Chapter 6 are considered passivated/inactive in this diagram.

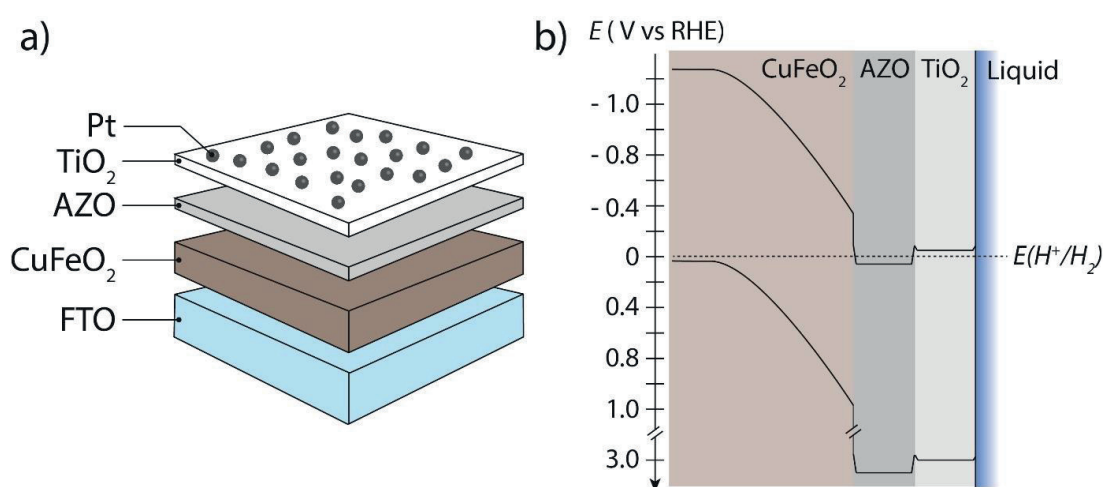


Figure 7.1 a) Sketch of the structure of the layered $\text{CuFeO}_2/\text{AZO}/\text{TiO}_2/\text{Pt}$ electrode. The relative thicknesses of the layers are not to scale. b) Predicted band alignment of the semiconducting layers of the electrode in equilibrium with the reduction potential of water. The structure exhibits a buried $\text{CuFeO}_2/\text{AZO}$ type-II p-n heterojunction, a buried AZO/TiO_2 type-II n-n heterojunction, and a SCLJ. The band structure of AZO and TiO_2 are reproduced from Paracchino *et al.*⁷

A composite electrode made of a 300 nm-thick CuFeO_2 layer coated with an AZO/TiO_2 overlayer was then tested for PEC water reduction in pH 6. The LSV curves obtained under chopped illumination before and after Pt deposition are shown in Figure 7.2a. The photocurrents measured after introduction of the oxide overlayer were still quite low (black trace), but interestingly, the electrochemical wave assigned to the reduction of Cu(I) to Cu(0) in CuFeO_2 is not observed anymore at ~ -0.1 V vs RHE (see Chapter 4, Figure 4.9a). This indicates that the conformal ALD-coated oxide overlayer protected the CuFeO_2 from corrosion by physically isolating it from the electrolyte. When put in a 2mM H_2PtCl_6 , the composite electrode produced photocurrents in the range of hundreds of $\mu\text{A}\cdot\text{cm}^{-2}$, making the photoelectrodeposition of Pt possible. After Pt

deposition, the photocurrents produced by the photocathode dramatically increased to reach 0.4 mA.cm⁻² at 0 V vs RHE and 0.8 mA.cm⁻² at -0.2 V vs RHE. This is a clear improvement over the bare CuFeO₂ photocathode, which does not produce any photocurrent in water (see Chapter 4, Figure 4.5a). However, the onset of photopotential is located at ~ 0.4 V vs RHE, *ca.* 600 mV negative to E_{FB} . This can have different origins: (i) the surface states detailed in Chapter 6 are not efficiently passivated by the overlayer and still induce FLP at the CuFeO₂/AZO junction; (ii) a different kind of trap states is introduced at the CuFeO₂/AZO junction (as the Cu₂O/AZO is known to be defective); (iii) the misalignment of the conduction bands of CuFeO₂ and AZO induce a drop in photovoltage and favors charge recombination at the junction. This issue warrants further study, but was not investigated further during the thesis at hand.

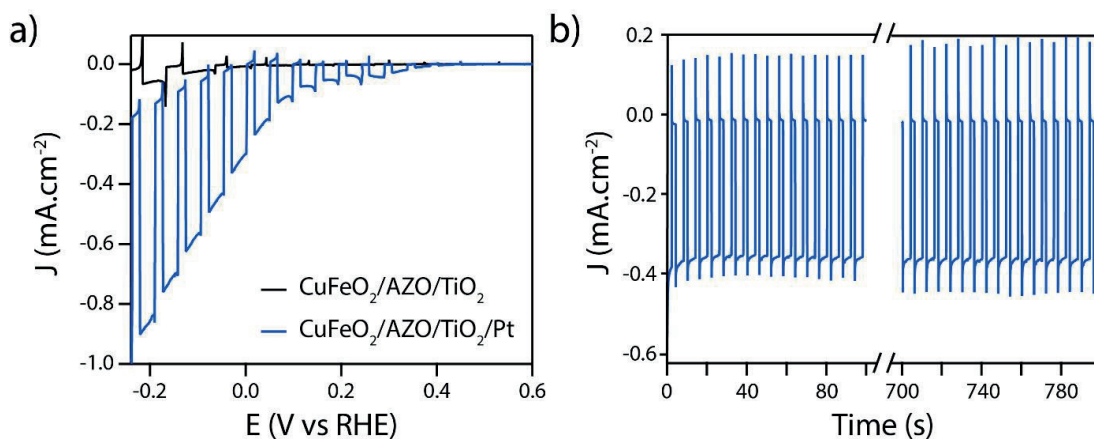


Figure 7.2 a) LSV curves obtained under chopped 1 sun illumination for a 300 nm-thick CuFeO₂ electrode ALD-coated with an AZO/TiO₂ overlayer before (black trace) and after (blue trace) Pt deposition. Scan rate: 10 mV.s⁻¹. Electrolyte: 0.5 M Na₂SO₄ buffered at pH 6.1. b) Stability measurement performed for 800 seconds at 0 V vs RHE in the same electrolyte and under chopped 1 sun illumination.

Regardless, for the first time, the sol-gel CuFeO₂ photocathode produced a photocurrent stable over time at 0 V vs RHE (see Figure 7.2b). To determine if this current was exclusively associated with the production of H₂ from water reduction, the *FE* of the photoelectrode was measured. To do so, the PEC cell was connected to a GC in order to monitor the quantities of evolved gases, and to compare them with the photocurrent produced by the photocathode in real time. Details of the experiment are provided in Chapter 3, section 3.3.7. During the measurement, the photocurrent was stable, with an average absolute value of *ca.* 0.0597 mA (see Figure 7.3), and the H₂ peak on the

chromatogram had an area of 0.6279 (arbitrary units). Based on the calibration curve provided in section 3.3.7, the *FE* was equal to $100\% \pm 0.5\%$ for water reduction. Importantly, this work represents the only report of quantitative PEC water reduction by a CuFeO_2 electrode.

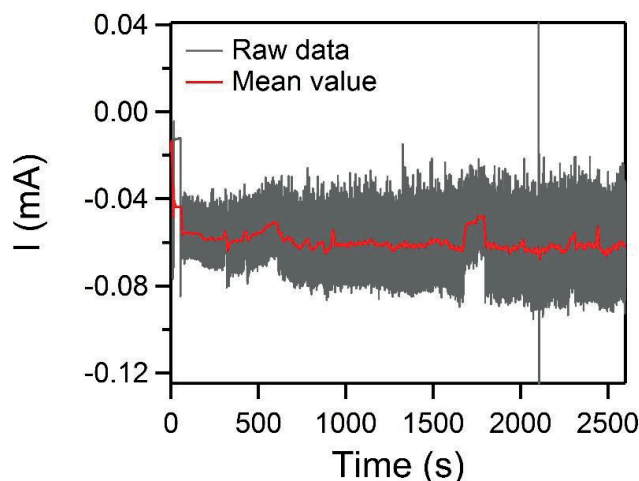


Figure 7.3 Chronoamperometry of a $\text{CuFeO}_2/\text{AZO}/\text{TiO}_2/\text{Pt}$ electrode at -0.2 V vs RHE under constant illumination in Ar-purged pH 6.1 buffered electrolyte. The effective illumination of the photoelectrode was well below 1 sun illumination as the light has to pass through the CE before reaching the WE (as described in Chapter 3 section 3.3.7). The intense noise in the data was due to Ar purging of the electrolyte, and a mean value of the current is therefore provided. The illuminated surface area of the photoelectrode was 0.238 cm^2 .

While the above-described ALD/catalysis approach provides a solution to the absence of electron injection from bare CuFeO_2 photocathode to the water, an important drawback of this strategy is the cathodic shift of the photocurrent onset. While the exact origin of this loss in photovoltage has not been investigated for the system at hand, replacing the complicated and hardly scalable ALD-coated AZO/TiO_2 overlayer with a different passivating layer could be the key to further progress in performance.

7.3 CuFeO_2 modification with a GaO_x/Pt overlayer

Since gallium oxide has been shown to advantageously replace AZO as a buffer layer in Cu_2O -based PV and PEC devices, it was also tested on CuFeO_2 photocathodes developed in this study. Furthermore, because the ALD process is not easy to scale up, and

is only necessary if the active layer of the photoelectrode is unstable under operating conditions, a sol-gel process was used for the deposition of gallium oxide on CuFeO₂ electrode (see Chapter 3). Briefly, a precursor based on gallium (III) isopropoxide was spin-coated onto a 200 nm-thick CuFeO₂ photoelectrode and the resulting film was subsequently annealed at 300°C for one hour, resulting in the formation of a thin layer of gallium (III) oxide. Considering that Ga₂O₃ crystal phases are typically formed at temperatures higher than 400°C, the films produced in this study were likely amorphous.^{20,21} The morphology of the resulting electrode was observed by SEM, and revealed that the amorphous GaO_x coating was quite homogeneous and thin enough to retain most of the nanoporosity of the CuFeO₂ layer (see Figure 7.4b). Moreover, the homogeneity of the gallium-based overlayer was confirmed by EDX analysis, revealing a full coverage of the surface of the electrode (see Figure 7.4c). This morphology is beneficial for two reasons: it preserves a high surface area of contact with the electrolyte and it limits the resistive losses in the poorly conductive amorphous overlayer.

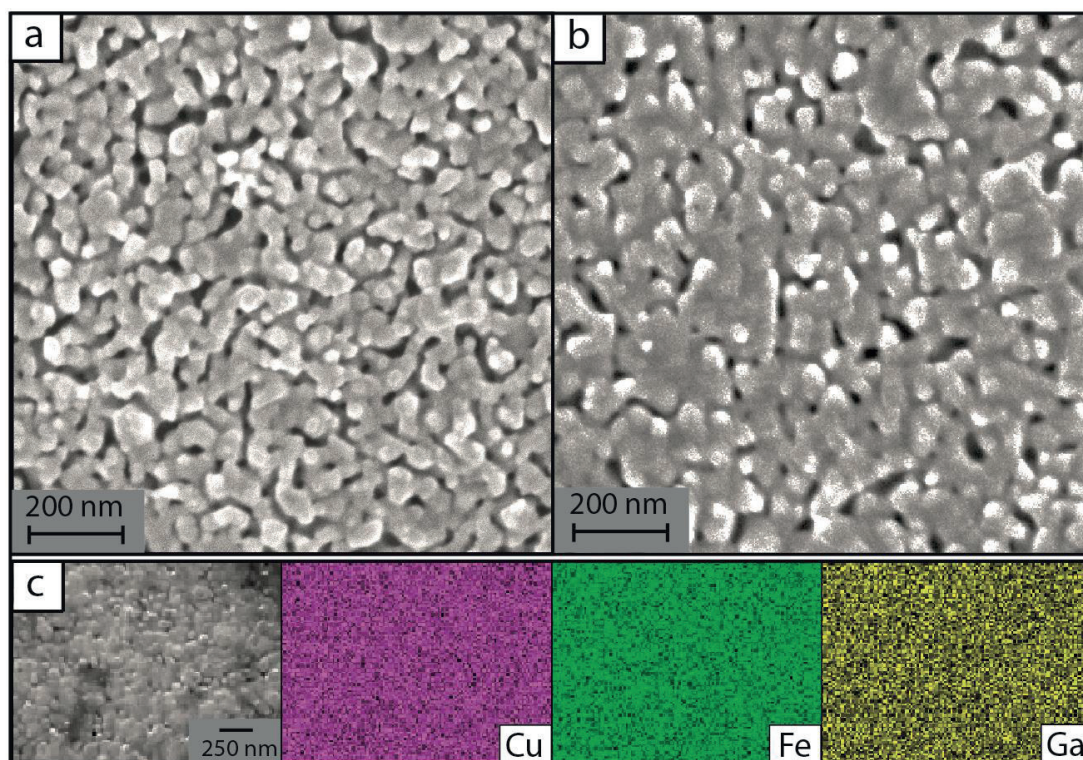


Figure 7.4 SEM pictures of a) a bare 200 nm-thick CuFeO₂ thin film on FTO and b) the same electrode after GaO_x coating. c) EDX elemental mapping of the same electrode for Cu, Fe and Ga.

The 200 nm-thick CuFeO_2 thin film coated with GaO_x was then tested for PEC water splitting in 0.5 M Na_2SO_4 buffered at pH 6. The resulting LSV is shown in Figure 7.5 (black trace): a very faint p-type behavior was observed, with no measurable improvement in performance over the bare CuFeO_2 electrode. It is however worth pointing out that – similarly to the ALD-coated overlayer of section 7.2 – no reductive wave was observed at potential lower than 0 V vs RHE, indicating that the sol-gel GaO_x overlayer is conformal enough to protect the CuFeO_2 layer from dark corrosion. Once the photoelectrode was coated with GaO_x , it was possible to photoelectrodeposit Pt on its surface from an H_2PtCl_6 solution. Similarly to what was observed for the AZO/TiO_2 overlayer in section 7.2, the photocurrent increased dramatically after the electrocatalyst deposition (see blue trace in Figure 7.5) reaching $1.8 \text{ mA}\cdot\text{cm}^{-2}$ at 0 V vs RHE and over $2 \text{ mA}\cdot\text{cm}^{-2}$ at -0.1 V vs RHE.

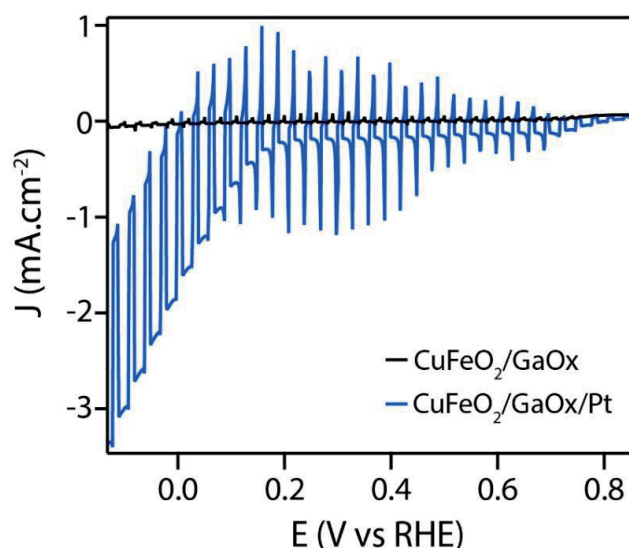


Figure 7.5 LSV curves obtained under chopped 1 sun illumination for a 200 nm-thick CuFeO_2 electrode coated with a GaO_x overlayer before (black trace) and after (blue trace) Pt deposition. Scan rate: $10 \text{ mV}\cdot\text{s}^{-1}$. Electrolyte: 0.5 M Na_2SO_4 buffered at pH 6.0.

These photocurrents were significantly higher than the ones obtained with the AZO/TiO_2 overlayer, even considering that the CuFeO_2 layer was thinner (200 nm vs 300 nm) and therefore absorbed less light. On the contrary, the onset of photocurrent is still located around +0.2 V vs RHE, indicating no clear improvement in photovoltage. However, as opposed what was observed with the AZO/TiO_2 overlayer (see Figure 7.1), the electrode modified with GaO_x and Pt displayed transient photocurrents up to +0.85 V vs RHE, suggesting a different origin for the limitation in performance, as discussed hereinafter.

Furthermore, the high dark current observed negative to 0 V vs RHE is likely to originate from Pt particles deposited on the FTO substrates, as the GaO_x overlayer is not as conformal as the one deposited by ALD in the previous section. Finally, another issue encountered with this system was the poor mechanical adherence of the Pt particles on the GaO_x overlayer. As a result, photocurrents decreased over time, due to detachment of the catalyst from the surface of the electrode and although they can be regenerated by redeposition of the Pt, this prevented any accurate *FE* or stability measurements

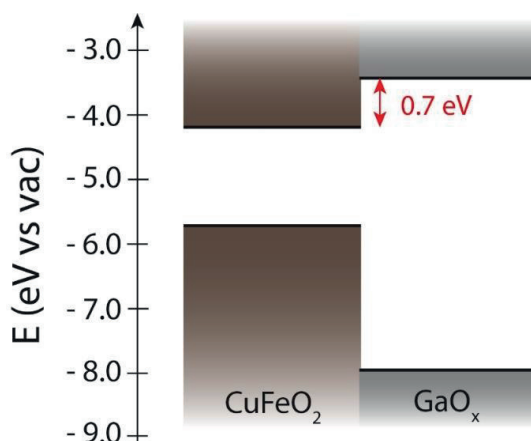


Figure 7.6 Predicted electronic band alignment for the CuFeO₂/GaO_x heterojunction before equilibration, based on the study presented in Chapter 6 for CuFeO₂ and on a previous report by Lee *et al.* for GaO_x.¹⁴ It reveals that, instead of forming the desired type-II heterojunction, CuFeO₂ and GaO_x are more likely to form a type-I heterojunction, with an offset of ~ 0.7 eV between the conduction band edges.

The fact that transient photocurrents much slower than the ones observed for the bare material (see Chapter 4, Figure 4.5) were measured up to almost the E_{FB} (*i.e.* + 1.01 V vs RHE) suggests that the recombination at surface states discussed in Chapter 6 is at least slowed down by the GaO_x overlayer. It is therefore more likely that the poor onset in photocurrent originates from a different source within the CuFeO₂/GaO_x junction. One important difference between CuFeO₂ and Cu₂O – which forms a good type-II heterojunction with gallium oxide overlayers – is the position of their conduction band. Indeed, the conduction band of CuFeO₂ lies about 0.9 eV lower in energy than the one of Cu₂O, and it is therefore possible that CuFeO₂ and GaO_x are not able to form a proper type-II heterojunction, based on the band position reported for ALD-coated GaO_x layers (see Figure 7.6). Indeed, the conduction band of GaO_x is likely to be positioned *ca.* 0.7 eV higher in energy than the one of CuFeO₂, based on energies reported for ALD-grown Ga₂O₃ thin films.¹⁴ This band misalignment could cause the GaO_x layer to block minority carriers at

the junction with the CuFeO₂, and could explain the necessity to considerably bias the photoelectrode towards cathodic potentials (lower than +0.2 V vs RHE) to allow them to flow through the junction and produce high photocurrents. To verify this assumption, additional experiments, such as EIS, UV-vis absorption and XPS analysis are needed and are currently under way.

Because this configuration generates the highest, albeit still unstable photocurrent for the CuFeO₂ electrodes developed through the thesis at hand, and because it only requires scalable solution-based deposition techniques, it is still considered promising for the advancement of CuFeO₂ PEC performance and, as such, is under optimization and deeper investigation at the moment of writing of this thesis manuscript.

7.4 Conclusion

While direct deposition of catalyst nanoparticles on the surface of CuFeO₂ failed to affect its PEC properties, two types of overlayer were found to have a beneficial effect on the performance of the photocathode. The ALD-processed AZO/TiO₂ and sol-gel-processed GaO_x overlayers presented in this chapter both improved the stability of the CuFeO₂ layer, as evidenced by the suppression of the reduction wave associated with Cu reduction in the LSV data. Furthermore, coating CuFeO₂ with any of these layers enabled the efficient photoelectrodeposition of Pt nanoparticles, something that was not possible on the bare electrode. The final photoelectrodes including a semiconducting overlayer coated with electrocatalytic nanoparticles, two traditionally synergetic and efficient approaches to improve performances in PEC applications.

While both overlayers fail to generate the photovoltage anticipated from the study presented in Chapter 6 (~ 0.8 V), they still present some differences. GaO_x is easier to process and yields higher photocurrents than AZO/TiO₂. It also does not suppress transient photocurrent at potentials close to E_{FB} , therefore showing a more promising behavior. However, it appears that Pt adherence on GaO_x is poor compared to TiO₂, as the catalyst quickly falls off under operating conditions. A possible reason for the behavior observed with GaO_x could be its band misalignment with CuFeO₂, causing electron trapping and recombination at the interface.

Overall, GaO_x seems the most promising approach investigated during this work, and avenues to improve it are currently explored. One way to prevent charge recombination at the CuFeO₂/GaO_x interface could be to reduce the thickness of the GaO_x overlayer until electrons can tunnel through it and reach the electrolyte. Another possibility could be to dope extrinsically the GaO_x layer to drive its band system lower in energy. The mechanical instability of Pt particles could be tackled by adding a thin TiO₂ overlayer on top of GaO_x, or even to replace Pt with another hydrogen evolution electrocatalyst, such as amorphous molybdenum sulfide. Based on the study detailed in Chapter 6 and the preliminary results presented in this chapter, the use of an optimized surface treatment should enable to extract a high photovoltage and eventually high photocurrents from CuFeO₂, which will ultimately lead to its inclusion inside a fully functional tandem PEC device.

7.5 References

- (1) Prévot, M. S.; Guijarro, N.; Sivula, K. *ChemSusChem* **2015**, 8 (8), 1359–1367.
- (2) Lee, M. H.; Takei, K.; Zhang, J.; Kapadia, R.; Zheng, M.; Chen, Y.-Z.; Nah, J.; Matthews, T. S.; Chueh, Y.-L.; Ager, J. W.; Javey, A. *Angew. Chem. Int. Ed.* **2012**, 51 (43), 10760–10764.
- (3) Seger, B.; Pedersen, T.; Laursen, A. B.; Vesborg, P. C. K.; Hansen, O.; Chorkendorff, I. *J. Am. Chem. Soc.* **2013**, 135 (3), 1057–1064.
- (4) Malizia, M.; Seger, B.; Chorkendorff, I.; Vesborg, P. C. K. *J. Mater. Chem. A* **2014**, 2 (19), 6847–6853.
- (5) Paracchino, A.; Laporte, V.; Sivula, K.; Grätzel, M.; Thimsen, E. *Nat. Mater.* **2011**, 10 (6), 456–461.
- (6) Paracchino, A.; Brauer, J. C.; Moser, J.-E.; Thimsen, E.; Graetzel, M. *J. Phys. Chem. C* **2012**, 116 (13), 7341–7350.
- (7) Paracchino, A.; Mathews, N.; Hisatomi, T.; Stefik, M.; David Tilley, S.; Grätzel, M. *Energy Environ. Sci.* **2012**, 5 (9), 8673–8681.
- (8) Izaki, M.; Shinagawa, T.; Mizuno, K.-T.; Ida, Y.; Inaba, M.; Tasaka, A. *J. Phys. Appl. Phys.* **2007**, 40 (11), 3326.
- (9) Seog Lee, Y.; Heo, J.; Cheng Siah, S.; P. Mailoa, J.; E. Brandt, R.; Bok Kim, S.; G. Gordon, R.; Buonassisi, T. *Energy Environ. Sci.* **2013**, 6 (7), 2112–2118.
- (10) Nishi, Y.; Miyata, T.; Minami, T. *Thin Solid Films* **2013**, 528, 72–76.

- (11) Tilley, S. D.; Schreier, M.; Azevedo, J.; Stefik, M.; Graetzel, M. *Adv. Funct. Mater.* **2014**, *24* (3), 303–311.
- (12) Scheer, R. *J. Appl. Phys.* **2009**, *105* (10), 104505.
- (13) Li, C.; Hisatomi, T.; Watanabe, O.; Nakabayashi, M.; Shibata, N.; Domen, K.; Delaunay, J.-J. *Energy Environ. Sci.* **2015**, *8* (5), 1493–1500.
- (14) Lee, Y. S.; Chua, D.; Brandt, R. E.; Siah, S. C.; Li, J. V.; Mailoa, J. P.; Lee, S. W.; Gordon, R. G.; Buonassisi, T. *Adv. Mater.* **2014**, *26* (27), 4704–4710.
- (15) Hisatomi, T.; Formal, F. L.; Cornuz, M.; Brillet, J.; Tétreault, N.; Sivula, K.; Grätzel, M. *Energy Environ. Sci.* **2011**, *4* (7), 2512–2515.
- (16) Formal, F. L.; Tétreault, N.; Cornuz, M.; Moehl, T.; Grätzel, M.; Sivula, K. *Chem. Sci.* **2011**, *2* (4), 737–743.
- (17) McCrory, C. C. L.; Jung, S.; Ferrer, I. M.; Chatman, S. M.; Peters, J. C.; Jaramillo, T. F. *J. Am. Chem. Soc.* **2015**, *137* (13), 4347–4357.
- (18) Morales-Guio, C. G.; Tilley, S. D.; Vrubel, H.; Grätzel, M.; Hu, X. *Nat. Commun.* **2014**, *5*, 3059.
- (19) Guijarro, N.; Prévot, M. S.; Sivula, K. *Phys. Chem. Chem. Phys.* **2015**, *17* (24), 15655–15674.
- (20) Ristić, M.; Popović, S.; Musić, S. *Mater. Lett.* **2005**, *59* (10), 1227–1233.
- (21) Kumar, S. S.; Rubio, E. J.; Noor-A-Alam, M.; Martinez, G.; Manandhar, S.; Shutthanandan, V.; Thevuthasan, S.; Ramana, C. V. *J. Phys. Chem. C* **2013**, *117* (8), 4194–4200.

Chapter 8

Final comments and outlook

The work conducted during this PhD thesis and presented in this manuscript aimed at exploring and advancing a novel photocathode material for direct solar water splitting. The research work accomplished in this field over the last decades showed that finding materials meeting the criteria of processability, stability and efficiency required for the large-scale development of photoelectrochemical hydrogen production was a challenging task. While most photoelectrodes studied up to now were based on binary compounds and have come short on at least one of these criteria, multinary materials are now attracting a lot of attention if only for the gigantic number of possible combinations involving two or more *d*-block transition metals. This approach has for instance successfully led to the development of BiVO₄, which is arguably currently one of the most promising photoanode material. However, while a lot of progress has been and is being made on photoanode development and optimization, photocathode development has been slower and is only starting to expand to less traditional materials.

The study conducted on CuFeO₂ and presented here falls within this context, and is part of the current efforts made by the solar fuel research community to produce a p-type photocathode material that could be combined with a state-of-the-art photoanode inside a photoelectrochemical tandem cell. In this chapter, the main challenges tackled during this work are listed and commented on, and finally an opinion and outlook on the future of CuFeO₂ photocathodes is provided.

8.1 Processing of thin-film CuFeO₂ photoelectrodes

While CuFeO₂ as a material presents attractive properties – its intrinsic p-type conductivity, its good stability in aqueous environments and its good absorption in the visible range – processing it into a good thin-film photoelectrode is a challenge. Here, a sol-gel approach – presented in Chapter 4 – was adopted because of its versatility, scalability and good reproducibility. Moreover, it allows for a high number of electrodes to be processed from a single solution batch under the same conditions, making comparison studies easy. However, this sol-gel method still presents several drawbacks. First, it requires an intermediate annealing step in air that, if not controlled properly, could lead to the formation of undesirable oxide phases, such as CuFe₂O₄, CuO or Fe₂O₃. Ideally, this annealing process needs to degrade organic residues from the gel while keeping the metal atoms inside an amorphous oxide phase. Second, the precursor film needs to be annealed at elevated temperature (700°C) under Argon. These conditions are too harsh for most conductive substrates, as metal substrate will tend to oxidize at the interface with the precursor film or even diffuse into it, modifying its composition, and indium-doped tin oxide (ITO) will lose its conductivity. Even FTO is barely able to withstand this temperature without losing its conductivity. This effectively limits the deposition of CuFeO₂ thin films to FTO substrates so far, preventing any in-depth study of the effect of the workfunction and nature of the substrate at the back contact with the absorbing layer. Finally, as this work was carried out, it appeared that the phase purity of the final photoelectrode was sensitive to the composition of the precursor solution¹ but also to the presence of small amounts of O₂ in the oven during the last annealing step. This last parameter can be hard to control and requires a thorough purge of the oven with inert gas so that it does not interfere with the final film composition.

Overall, CuFeO₂ can be easily solution-processed but the conditions required to produce this metastable phase are not completely satisfactory yet, especially regarding substrate stability. Forming the right crystal structure at temperatures of 700°C or lower – as has been reported elsewhere² – is challenging due to the sensitivity of the process towards the presence of impurities such as O₂ or NaCl that favor the formation of α -Fe₂O₃ inside the film.³ Moreover, during this project, evidence was found that FTO itself could favor the development of α -Fe₂O₃, at elevated temperatures although the reason for this was unclear. This is important because an impure CuFeO₂ film could contain photoactive

but not photostable Cu_2O or CuO phases, potentially yielding to incorrect attribution of observed photocurrents in PEC characterization. For instance, in a recent report, CuFeO_2 thin films were processed at 700°C but displayed a light brown/orange color, questioning the phase purity of these samples, where Cu (II) was detected.² For these reasons, it is crucial to carefully probe the phase purity of CuFeO_2 electrodes after processing through XRD and/or Raman spectroscopy. Finally, the development of alternative processing techniques, such as spray pyrolysis or hydrothermal synthesis of CuFeO_2 electrodes could benefit the research field by introducing additional handles to control the material properties.

8.2 Photoelectrochemical properties of thin-film CuFeO_2 photocathodes

Bare CuFeO_2 photocathodes can produce photocurrent densities on the mA.cm^{-2} scale in the presence of electron scavengers such as O_2 (as shown in Chapter 4) or MV^{2+} . This is still one order of magnitude lower than what is expected from the absorption properties of the material, and for what is necessary to reach high STH efficiencies, but it still represents an interesting starting point for the material. Moreover, its flat-band potential was calculated to lie around $\sim 1 \text{ V}$ vs RHE, promising the possibility to develop a high photovoltage from the SCLJ between CuFeO_2 and water. Finally, CuFeO_2 electrodes displayed long-term stability in aqueous and non-aqueous (acetonitrile-based) electrolytes. This represents one of their most attractive properties, since stability has been a long-term issue for most photocathodes, which tend to either photocorrode under illumination, from the generation of a high density of minority carriers inside the absorbing semi-conductor (*e.g.* photogenerated electrons will reduce Cu (I) to Cu (0) in Cu_2O), or to naturally oxidize by contact with water (*e.g.* the formation of an amorphous silicon oxide layer at the surface of a Si photoelectrode placed in water).

The PEC properties of CuFeO_2 were significantly improved by extrinsic doping and the introduction of a mesostructured hole-accepting scaffold between the absorbing CuFeO_2 layer and the conductive substrate – as shown in Chapter 5. In particular, the structuring approach allowed to multiply the output photocurrent by 2.5, while also seemingly improving the shape of the LSV close to the onset of photocurrent. Therefore,

this approach seems to have a good potential to reach high PEC performance with CuFeO₂ photocathodes and deserves to be further investigated in future works.

Unfortunately, as-prepared CuFeO₂ photoelectrode did not display any measurable sustained photocurrent when tested in Ar-purged aqueous electrolyte. Importantly, because the material is good at photoreducing O₂ in water, it is crucial to make sure that any trace of it is removed from the electrolyte – for instance by thoroughly purging it with Ar – before any PEC testing is performed. Another quick and effective way to make sure that the observed photocurrents are not coming from O₂ reduction is to perform a chronoamperometry over at least tens of minutes and check whether the photocurrent is stable, or decrease due to the consumption of dissolved O₂. Finally, the best method to make sure that observed photocurrents are coming from the reduction of water into H₂ by CuFeO₂ is to measure the Faradaic efficiency of the electrode over time. Since CuFeO₂ is stable for days under operating conditions (see Chapter 4) it should be possible to measure a 100% Faradaic efficiency over extended periods using an Ar-purged electrolyte. Importantly, this has never been achieved for systems where CuFeO₂ is put directly in contact with water, suggesting that water reduction is intrinsically limited on the surface of CuFeO₂. Making sure the electrolyte is completely O₂-free is therefore important to consider for future work on the material, so that PEC results are not misleading.

8.3 Surface states characterization and surface treatments of thin-film CuFeO₂ electrodes

The absence of report for CuFeO₂ photoelectrodes able to perform PEC water reduction with a 100% efficiency despite their established stability under operating conditions added to their observed mediocre performance in Ar-purged electrolyte reported here (see Chapter 4) suggested some sort of intrinsic limitation to the material. Since no in-depth material and electrochemical study of CuFeO₂ was available before the project presented in this manuscript, it was decided to answer this shortcoming by submitting CuFeO₂ electrodes to a wide range of physico-chemical tests. The results of these tests, presented in Chapter 6, led to the conclusion that a large density of electronic trap states was present at the surface of the photoelectrode, preventing the formation of a good SCLJ with the water, and inducing charge recombination at the interface. This type

of recombination has been studied in-depth for other (n-type) materials such as Fe_2O_3 ,⁴⁻⁶ BiVO_4 ⁷ or FeS_2 ,⁸ and seem to be a limitation commonly found in oxide or chalcogenide semiconductors. However, while the presence of surface states is commonly observed in varied materials, the study reported here is the only one where these surface states led to an apparent inversion regime upon trapping of the charge carriers. This intriguing result warrants a deeper investigation of the material, and to do so one could rely on the numerous *in-operando* techniques currently developed in the field: electrochemical surface probing with a bi-potentiostat, intensity-modulated photocurrent spectroscopy (IMPS), *in-situ* infrared/Raman spectroscopy... These more advanced techniques could shed some more light on the origin and behavior of the surface states measured in the current study.

Traditionally surface states have been rather successfully tackled by using appropriate passivating or catalytic overlayers. Finding one for CuFeO_2 proved difficult, although some progress was made, as presented in Chapter 7. Depositing catalytic particles directly on the surface of the photocathode failed to improve its PEC performance, but first depositing a thin oxide overlayer on the surface of CuFeO_2 before decorating it with Pt nanoparticles was more successful. Using an ALD-processed AZO/ TiO_2 overlayer coating led to the first observation of H_2 production with a 100% Faradaic efficiency at the surface of a CuFeO_2 photocathode, but the overall PEC performance was still low. Replacing this overlayer with a thin amorphous gallium oxide layer allowed to push the photocurrents higher than 2 mA.cm^{-2} in an Ar-purged electrolyte, but failed to fix the poor onset of photocurrent, possibly due to band misalignment at the $\text{CuFeO}_2/\text{GaO}_x$ heterojunction. However, the incremental progress made with oxide overlayers during this thesis are promising and, clearly, finding and optimizing a better surface treatment should be the next major step towards the development of efficient CuFeO_2 photocathode for direct water splitting.

8.4 Outlook

The work performed during this PhD thesis established that CuFeO_2 has attractive features as a novel photocathode material for water reduction. In particular, the abundance of its constituent elements and its robustness under operating conditions should facilitate a potential future large-scale development. However, before reaching

this stage, the PEC performances of CuFeO_2 have to be significantly improved. While this has proven quite challenging over the course of the work exposed in this manuscript, the exploratory studies developed in Chapters 5 and 7 showed promising results. The LSV measured in the presence of O_2 for $\text{CuAlO}_2/\text{CuFeO}_2$ composite photocathodes in Chapter 5 would in fact already be good enough for inclusion into a functional D4 tandem cell, if similar performance were achieved for water reduction. This is illustrated in Figure 8.1, where the LSV of the $\text{CuAlO}_2/\text{CuFeO}_2$ photocathode (blue trace) is overlaid with the LSV of the best-performing oxide photoanode reported so far (yellow trace):⁹ the crossing point between these two curves yields a $J_{ph,op}$ of ca. 2.5 mA.cm^{-2} , which would translate into a η_{STH} of about 3%.

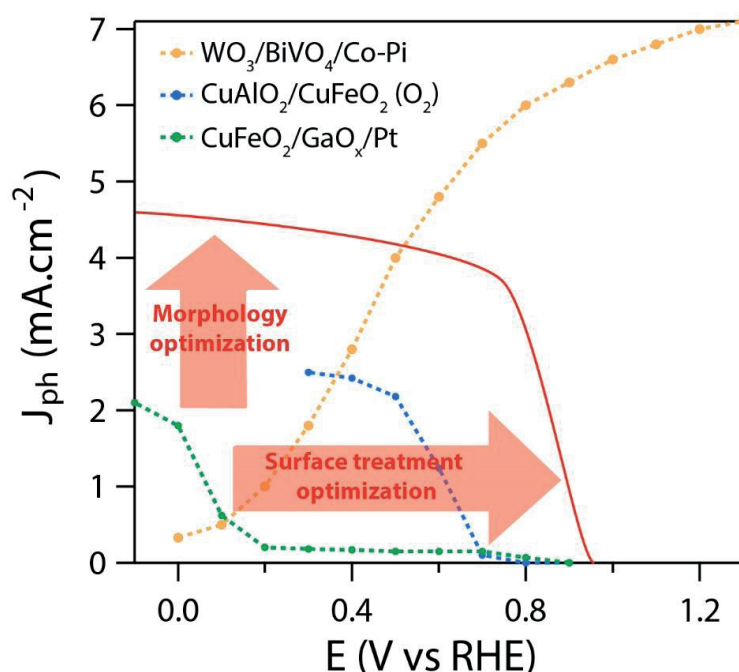


Figure 8.1 LSV curves of the best-performing CuFeO_2 photocathode developed during this PhD thesis in the presence of O_2 as an electron scavenger (blue trace, Chapter 5) and in deaerated electrolyte (green trace, Chapter 7). These curves are overlaid with the LSV of the best performing oxide photoanode reported in the literature⁹ (yellow trace). The red trace represents the LSV needed for an optimized CuFeO_2 photocathode to reach about 5% STH conversion efficiency when combined with this photoanode. To reach this target, surface engineering could help improve the photovoltage (*i.e.* the onset of photocurrent), while morphology control (*e.g.* nanostructuring) could benefit the photocurrent densities.

The knowledge gained through the in-depth study presented in Chapter 6 and the initial attempts at surface modification presented in Chapter 7 seem to indicate that

developing an optimal surface treatment could be the key towards better performance for CuFeO₂ photoelectrodes, and in particular its photovoltage. This is illustrated in Figure 8.1, where the current best PEC performance of the sol-gel CuFeO₂ photocathode (green trace) is represented alongside the performance needed to reach a η_{STH} of about 5%, which could be achieved using efficient morphology and surface treatment optimization. Because this type of treatment is the focus of major efforts in the field, and because CuFeO₂ is getting increasing attention from the community, the work presented in here will certainly serve as a foundation for the development of efficient advanced CuFeO₂ photoelectrodes and their incorporation into tandem PEC device for solar fuel production in the near future.

The work presented in here provides a small contribution towards the development of an inexpensive and sustainable global energy model based on renewable sources and in particular solar energy. These are exciting times for scientific research, as humanity is facing its biggest energy transition since the Industrial Revolution of the 18th century, and has to accomplish it as soon as possible. As Thomas Edison once said more than 85 years ago:

“I’d put my money on the sun and solar energy. What a source of power! I hope we don’t have to wait until oil and coal run out before we tackle that.”

And it feels like we are finally getting there.

8.5 References

- (1) Bourée, W. S.; Prévot, M. S.; Jeanbourquin, X. A.; Guijarro, N.; Johnson, M.; Formal, F. L.; Sivula, K. *Adv. Mater.* **2016**, *28* (42), 9308–9312.
- (2) Jang, Y. J.; Park, Y. B.; Kim, H. E.; Choi, Y. H.; Choi, S. H.; Lee, J. S. *Chem. Mater.* **2016**, *28* (17), 6054–6061.
- (3) Li, Y.; Guijarro, N.; Zhang, X.; Prévot, M. S.; Jeanbourquin, X. A.; Sivula, K.; Chen, H.; Li, Y. *ACS Appl. Mater. Interfaces* **2015**, *7* (31), 16999–17007.
- (4) Klahr, B.; Gimenez, S.; Fabregat-Santiago, F.; Hamann, T.; Bisquert, J. *J. Am. Chem. Soc.* **2012**, *134* (9), 4294–4302.
- (5) Klahr, B.; Hamann, T. *J. Phys. Chem. C* **2014**, *118* (19), 10393–10399.

- (6) Le Formal, F.; Pendlebury, S. R.; Cornuz, M.; Tilley, S. D.; Grätzel, M.; Durrant, J. R. *J. Am. Chem. Soc.* **2014**, *136* (6), 2564–2574.
- (7) Ma, Y.; Pendlebury, S. R.; Reynal, A.; Formal, F. L.; Durrant, J. R. *Chem. Sci.* **2014**, *5* (8), 2964–2973.
- (8) Cabán-Acevedo, M.; Kaiser, N. S.; English, C. R.; Liang, D.; Thompson, B. J.; Chen, H.-E.; Czech, K. J.; Wright, J. C.; Hamers, R. J.; Jin, S. *J. Am. Chem. Soc.* **2014**, *136* (49), 17163–17179.
- (9) Pihosh, Y.; Turkevych, I.; Mawatari, K.; Uemura, J.; Kazoe, Y.; Kosar, S.; Makita, K.; Sugaya, T.; Matsui, T.; Fujita, D.; Tosa, M.; Kondo, M.; Kitamori, T. *Sci. Rep.* **2015**, *5*, 11141.

Appendix

Additional UV-vis data (Chapter 5)

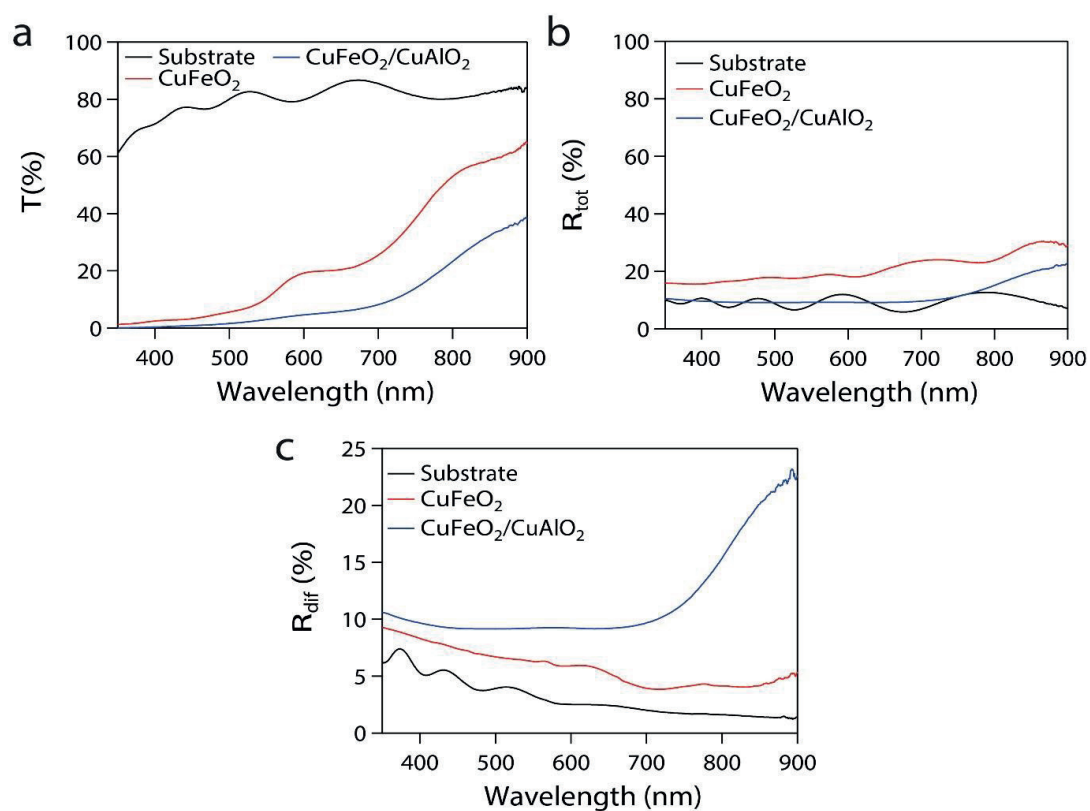


Figure A1 Transmission (a), total reflectance) (b) and diffuse reflectance (c) spectra of the substrate (black trace), the bare CuFeO_2 electrode (red trace) and the $\text{CuFeO}_2/\text{CuAlO}_2$ electrode (blue trace)

Additional EIS fitting data (Chapter 6)

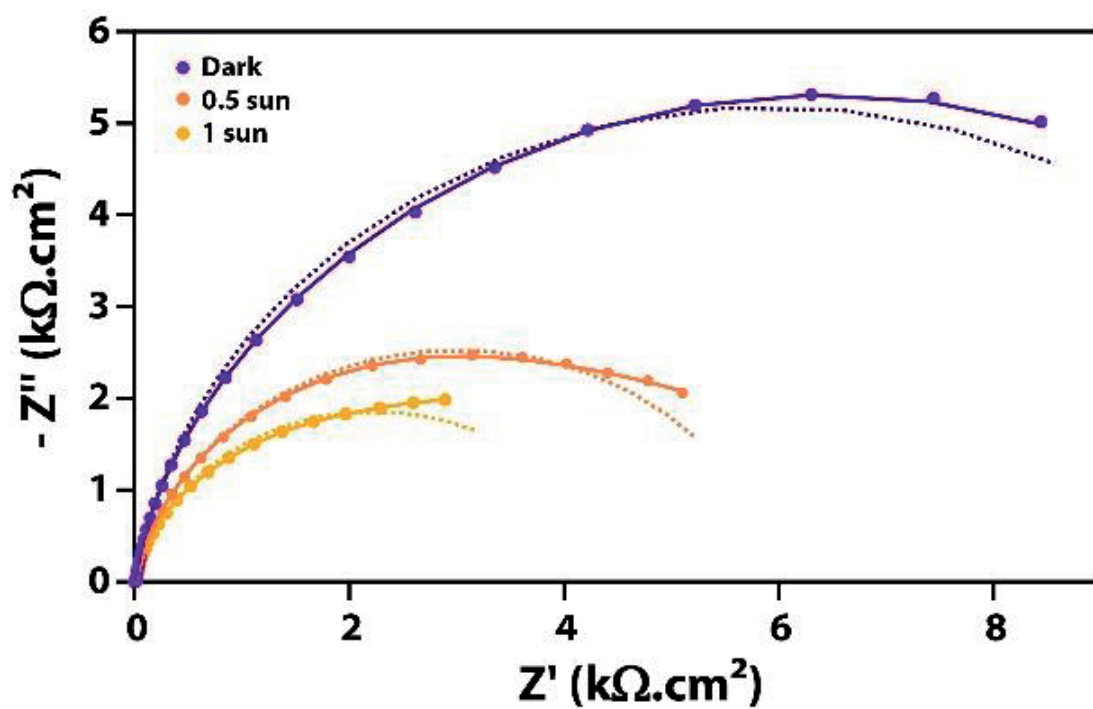


Figure A2 Typical Nyquist plots representing EIS data for a CuFeO_2 electrode collected at 0.7 V vs RHE, in 1M NaOH, in the dark, under 0.5 sun and 1 sun illumination. Markers represent experimental data, dotted lines represent the fit obtained with a simple Randles circuit, and solid lines represent the fit obtained with the model used in chapter 6.

Curriculum Vitae

MATHIEU S. PRÉVOT

mathieu.prevot@epfl.ch | École Polytechnique Fédérale de Lausanne, Switzerland

Date of birth: July 6th, 1990

Nationality: French, American

Research Experience

PhD project under the supervision of Prof. Kevin Sivula Oct 2012 – Jun 2017

École Polytechnique Fédérale de Lausanne, Switzerland

Thesis: Investigating and controlling charge carrier behavior in delafos-site p-type CuFeO₂ photocathodes for solar fuel production.

Master project under the supervision of Prof. Curtis Berlinguette Jan 2012 – Jul 2012

University of Calgary, Canada

Thesis: Development of mixed metal oxide thin films created by photo-chemical metal-organic decomposition as catalysts for the water oxidation reaction.

Research Internship under the supervision of Prof. Curtis Berlinguette Apr 2011 – Jun 2011

University of Calgary, Canada

Topic: Investigation of iron oxide thin films created by photochemical metal-organic decomposition as catalysts for the water oxidation reaction.

Research Internship under the supervision of Prof. Chantal Andraud

Jun 2010

École Normale Supérieure de Lyon, France

Topic: Synthesis of organic push-pull structures applied to non-linear optical microscopy.

Higher Education

PhD studies – École Polytechnique Fédérale de Lausanne, Switzerland Apr 2013 - current

Faculty of Basic Sciences – Dpt. of Chemistry & Chemical Engineering

Master studies – École Normale Supérieure de Lyon, France Sept 2009 – Aug 2012

Master degree in “Science of Matter” – option Chemistry

Obtained with distinction (Très Bien)

Bachelor studies – École Normale Supérieure de Lyon, France Sept 2008 – Aug 2009

Bachelor degree in “Science of Matter” – option Chemistry

Obtained with distinction (Bien)

Teaching Experience

Master thesis supervision

3 students

Oxide Thin film optimization, Design of composite nanoparticles

**Introduction to chemical engineering – Lab course
(Teaching Assistant)**

2 semesters

2nd year Bachelor – Chemistry Students

Chemical Engineering: Transport phenomena (Teaching Assistant)

6 semesters

3rd year Bachelor – Chemical Engineering Students

Interdisciplinary project (Supervision of the experimental work)

8 weeks

Synthesis of supported nanoparticle catalysts for biomass conversion

1st year Master – Chemistry Students

Technical Expertise

- **Synthesis:** Solution-processing of semiconducting oxide and chalcogenide thin films (sol-gel, collo-idal, spray pyrolysis, electrodeposition, PMOD). Templating and nanostructuring of thin films.
Organic synthesis: regular coupling reactions, column chromatography, recrystallization.
- **Electrochemistry:** Electrochemical characterization (voltammetry, amperometry). Photoelectrochemical characterization of semiconductor-liquid junctions. Incident photon-to-current efficiency measurement. Electrochemical Impedance Spectroscopy (Mott-Schottky analysis of semiconductors).
- **Physical Characterization:** Scanning electron microscopy. Atomic Force Microscopy. X-ray diffraction (1D). UV-vis spectrometry. IR & Raman spectrometry. Gas Chromatography. Profilometry. Thermogravimetric Analysis. NMR.
Basic experimental knowledge: Transmission electron microscopy, BET adsorption, Zeta potential measurement, X-Ray Photoelectron Spectroscopy.

Peer-reviewed Scientific Publications

H-index: 11 – 1109 citations (16th May 2017, Google Scholar)

▪ Selected publications

1. Evaluation of charge carrier behavior in CuFeO₂ photocathodes: the influence of surface recombination.
M.S. Prévot, X.A. Jeanbourquin, W.S. Bourrée, N. Guijarro, F. Le Formal, F. Abdi, K. Sivula, *Chem. Mater.*, 2017, **29**, 4952 .
2. Improving charge collection with delafossite photocathodes: a host-guest CuAlO₂/CuFeO₂ approach.
M.S. Prévot, Y. Li, N. Guijarro, K. Sivula, *J. Mater. Chem. A*, 2016, **4**, 3018
3. Self-assembled 2D WSe₂ thin films for photoelectrochemical hydrogen production.
X. Yu*, M.S. Prévot*, N. Guijarro, K. Sivula, *Nature Commun.*, 2015, **6**, 7596
*These authors contributed equally to this work
4. Enhancing the performance of a robust sol-gel-processed p-type delafossite CuFeO₂ photocathode for solar water reduction.
M.S. Prévot, N. Guijarro, K. Sivula, *ChemSusChem*, 2015, **8**, 1359
5. Photoelectrochemical tandem cells for solar water splitting.
M.S. Prévot, K. Sivula, *J. Phys. Chem. C*, 2013, **117**, 17879
6. Water oxidation catalysis: electrocatalytic response to metal stoichiometry in amorphous metal oxide films containing Iron, Cobalt, and Nickel.
R.D.L. Smith, M.S. Prévot, R.D. Fagan, S. Trudel, C.P. Berlinguette, *J. Am. Chem. Soc.*, 2013, **135**, 11580
7. Photochemical route for accessing amorphous metal oxide materials for water oxidation catalysis.
R.D.L. Smith, M.S. Prévot, R.D. Fagan, Z. Zhang, P.A. Sedach, M.K.J. Siu, S. Trudel, C.P. Berlinguette, *Science*, 2013, **340**, 60

▪ Other publications

1. CuInGaS₂ photocathodes treated with SbX₃ (X=Cl, I): the effect of the halide on solar water splitting performance. (Invited paper)
N. Guijarro, M.S. Prévot, M. Johnson, X. Yu, W.S. Bourée, X.A. Jeanbourquin, P. Borno, F. Le Formal, K. Sivula, *J. Phys. D: Appl. Phys.*, 2017, **50**, 044003

2. Switchable photoelectrodes: robust hierarchically structured biphasic ambipolar oxide photo-electrode for light-driven chemical regulation and switchable logic applications.
W.S. Bourée, M.S. Prévot, X.A. Jeanbourquin, N. Guijarro, M. Johnson, F. Le Formal, K. Sivula, *Advanced Materials*, 2016, **28**, 9308

3. A Gibeon meteorite yields a high-performance water oxidation electrocatalyst. (*Nature highlight*)
F. Le Formal, N. Guijarro, W.S. Bourée, A. Gopakumar, M.S. Prévot, A. Daubry, L. Lombardo, C. Sornay, J. Voit, A. Magrez, P.J. Dyson, K. Sivula, *Energy Environ. Sci.*, 2016, **9**, 3448

4. A bottom-up approach towards all-solution-processed high-efficiency Cu(In,Ga)S₂ photocathodes for water splitting.
N. Guijarro, M.S. Prévot, X. Yu, X.A. Jeanbourquin, P. Borno, W.S. Bourée, M. Johnson, F. Le Formal, K. Sivula, *Adv. Energy Materials*, 2016, **6**, 1501949

5. Challenges towards economic fuel generation from renewable electricity: the need for efficient electrocatalysts.
F. Le Formal, W.S. Bourée, M.S. Prévot, K. Sivula, *CHIMIA*, 2015, **69**, 789

6. Direct light-driven water oxidation by a ladder-type conjugated polymer photoanode.
P. Borno, M.S. Prévot, X. Yu, N. Guijarro, K. Sivula, *J. Am. Chem. Soc.*, 2015, **137**, 15338

7. Autodecomposition approach for the low-temperature mesostructuring of nanocrystal semi-conductor electrodes.
N. Guijarro, M.S. Prévot, X.A. Jeanbourquin, X. Yu, K. Sivula, *Chem. Mater.*, 2015, **27**, 6337

8. Templating sol-gel hematite films with sacrificial copper oxide: enhancing photoanode performance with nanostructure and oxygen vacancies.
Y. Li, N. Guijarro, X. Zhang, M.S. Prévot, X.A. Jeanbourquin, K. Sivula, H. Chen, Y. Li, *ACS Appl. Mater. Interfaces*, 2015, **7**, 16999

9. Surface modification of semiconductor photoelectrodes.
N. Guijarro, M.S. Prévot, K. Sivula, *Phys. Chem. Chem. Phys.*, 2015, **17**, 15655

10. Enhancing the charge separation in nanocrystalline Cu₂ZnSnS₄ photocathodes for photoelectro-chemical application: the role of surface modification.
N. Guijarro, M.S. Prévot, K. Sivula, *J. Phys. Chem. Lett.*, 2014, **5**, 3902

11. Multiflake thin film electronic devices of solution-processed 2D MoS₂ enabled by sonopolymer- assisted exfoliation and surface modification.
X. Yu, M.S. Prévot, K. Sivula, *Chem. Mater.*, 2014, **26**, 5892

Presentations

1. Characterization of defect states responsible for the low photovoltage in p-type CuFeO₂ photocathodes (Poster)
SwissPEC Symposium. Lausanne, Switzerland. Nov 11th, 2016
2. Earth-abundant solution-processed CuFeO₂ photocathode for water reduction (Poster)
Gordon Research Conference – Solar Fuels. Luca, Italy. Feb 27th – Mar 3rd, 2016
3. Earth-abundant solution-processed photocathodes for water reduction (Oral presentation)
European Material Research Society – Fall Meeting. Warsaw, Poland. Sep 15th – Sep 18th, 2015
4. Identifying limitations and enhancing photocurrent in solution-processed p-type CuFeO₂ photo-cathodes (Oral presentation)
Material Research Society – Fall Meeting. Boston, MA, USA. Nov 30th – Dec 5th, 2014
5. Identifying limitations and enhancing photocurrent in solution-processed p-type CuFeO₂ photo-cathodes for solar hydrogen production (Oral presentation)
European Material Research Society – Spring Meeting. Lille, France. May 26th – May 30th, 2014

References

Prof. Kevin Sivula – École Polytechnique Fédérale de Lausanne, Switzerland
Prof. Curtis Berlinguette – University of British Columbia, Vancouver, Canada
Prof. Simon Trudel – University of Calgary, Canada
Dr. Néstor Guijarro – École Polytechnique Fédérale de Lausanne, Switzerland

